Upconversion Luminescence in ZnO-TiO_2 Composite Doped with Rare Earth Elements

September 2018

Department of Science and Advanced Technology
Graduate School of Science and Engineering
Saga University

Krisana Kobwittaya

Upconversion Luminescence in ZnO-TiO_2 Composite Doped with Rare Earth Elements

By

Krisana Kobwittaya

A dissertation submitted in partial fulfillment of

the requirements for the degree of

Doctor of Philosophy (Ph.D.)

in

Chemical Engineering

Department of Science and Advanced Technology

Graduate School of Science and Engineering

Saga University

Japan

September 2018

CERTIFICATE OF APPROVAL

This is to certify that the dissertation submitted by

Krisana KOBWITTAYA

titled "**Upconversion Luminescence in ZnO-TiO_2 Composite Doped with Rare Earth Elements**" has been approved by the dissertation committee for the partial fulfillment of the requirements for the degree of ***Doctor of Philosophy (Ph.D.)*** in Chemical Engineering at September 2018.

Dissertation Committee:

_____ *Date* _____
Dr. Yushi OISHI (Supervisor)
Professor, Department of Chemistry and Applied Chemistry,
Graduate School of Science and Engineering, Saga University

_____ *Date* _____
Dr. Takanori WATARI (Member)
Professor, Department of Advanced Technology Fusion,
Graduate School of Science and Engineering, Saga University

_____ *Date* _____
Dr. Yasunori YAMADA (Member)
Professor, Department of Chemistry and Applied Chemistry,
Graduate School of Science and Engineering, Saga University

_____ *Date* _____
Dr. Takayuki NARITA (Member)
Associate Professor, Department of Chemistry and Applied Chemistry,
Graduate School of Science and Engineering, Saga University

ACKNOWLEDGEMENTS

First and foremost, I would like to express my heartfelt gratitude and sincere appreciation to my supervisor, Professor Dr. Yushi Oishi, for his invaluable guidance, endless assistance and support, and encouragement throughout my study at Saga University.

It gives me immense pleasure and privilege to express my profound gratitude to Professor Dr. Takanori Watari, for giving me the opportunity to carry out this research project and always having time for insightful scientific discussions, continuous guidance, and constructive suggestions, including astute criticism during the research project planning, and later during the preparation of scientific papers and this dissertation.

I would like to extend my appreciation to my committee members, Professor Dr. Yasunori Yamada and Associate Professor Dr. Takayuki Narita, for their kind cooperation and suggestions. I am grateful to Associate Professor Dr. Mitsunori Yada and Dr. Hom Nath Luitel (Toyota Central R&D Labs., Inc., Aichi, Japan) for their support and generous help in various aspects. I would also like to express my thanks to Associate Professor Dr. Masanao Era and Professor Dr. Keisuke Ohto, who took care of me when I first arrived at Saga University. I wish to express my deep gratitude to Associate Professor Dr. Sanya Sirivithayapakorn and Associate Professor Patcharaporn Suwanvitaya (Kasetsart University, Bangkok, Thailand), who recommended me to Saga University for doctoral course in the year of 2015.

My sincere appreciation is extended to Professor Emeritus Dr. Masaki Yoshio for giving me the great opportunity to develop my research skills by working as research assistant. Special thanks are given to technical assistant, Mr. Toshio Torikai, who not only taught me how to use and maintain the laboratory equipment, but also helped me solving the problems regarding my research works. Also, I would like to convey my special thanks to my scholarship provider, *The Saga University Scholarship for Strategic International Postgraduate Program (SIPOP)*, for granting me the occasion to achieve the doctorate degree.

Last but not least, I would like to give a big thanks to my beloved parents and friends who have always encouraged and supported me to make my dreams come true.

Krisana Kobwittaya
September 2018
Saga University, Saga, Japan

ABSTRACT

In this dissertation, the upconversion (UC) phosphor fabricated using a new UC host material, ZnO-TiO_2 composite, is implemented. The practicable routes namely solid-state reaction and powder-solution mixing methods are contemplated for the synthesis of ZnO-TiO_2 composite UC phosphor activated with rare earth elements. This dissertation comprises of six chapters that cover essential background of UC phosphors, crucial aspects of three basic sensitizer-activator pairs of ions which are normally used for making UC phosphors, and the interesting and important results regarding the site preference of rare earth ions in the UC host material under the situation that the crystal structure of UC host material is the complex crystal matrix and the Rietveld refinement cannot be applied to estimate the substitution position of rare earth ions within target host crystal matrix. Initially, a brief and general background of phosphors, focusing mainly on fundamental knowledge of UC phosphor, mechanism models of the generation of UC luminescence (UCL), and the methods of preparation of UC phosphors are given in the first chapter. For the detailed research works, there are two main topics based on the synthetic route which can be described as follows.

Firstly, the pellet form of Ho^{3+} and Yb^{3+} co-doped ZnO-TiO_2 composite phosphor prepared by solid-state reaction method was successfully synthesized at 1200 °C for 4 h. The effect of synthesis parameters like UCL characteristics, ZnO/TiO_2 mixing ratios, and Ho^{3+} and Yb^{3+} concentrations were studied in detail. The most efficient product, ZnO:TiO_2 = 1:1 (in mole) doped with 0.05 mol% Ho^{3+} and 9 mol% Yb^{3+}, exhibited the green emission under a 980-nm laser excitation. The UC mechanism of this UC phosphor system was also suggested and discussed in detail based on the pump power dependent studies.

Secondly, the powder form of ZnO-TiO_2 composite phosphors containing different pairs of rare earth ions (Er^{3+}/Yb^{3+}, Ho^{3+}/Yb^{3+}, and Tm^{3+}/Yb^{3+}) prepared by a new synthetic method, namely powder-solution mixing method, was successfully carried out. In this research, the effect of firing temperature, ZnO/TiO_2 mixing ratio, and dopant concentration ranges on structural and UCL properties under a 980-nm laser excitation was investigated. The simple chemical formula equations, for explaining the site preference of rare earth ions in host crystal matrix, were generated by considering the target host crystal structure, its crystal properties, and the effect of dopants to its crystal matrix. Under optimum firing temperature (1300 °C) and fixed firing time (1 h), the most effective product of these three systems was ZnO:TiO_2 = 1:1

(in mole) doped with 3 mol% Er^{3+} and 9 mol% Yb^{3+} emitting bright red emission, ZnO:TiO_2 = 1:1 (in mole) doped with 0.03 mol% Ho^{3+} and 9 mol% Yb^{3+} exhibiting bright green emission, and ZnO:TiO_2 = 1:1 (in mole) doped with 0.125 mol% Tm^{3+} and 15 mol% Yb^{3+} emitting nearly pure NIR emission. The dependence of UC emission intensity on the excitation power was studied, and the UC mechanism was proposed and discussed in detail. Additionally, the comparison of UC emission intensity of the phosphor prepared by different synthetic methods was also investigated.

In conclusion, it is believed that ZnO-TiO_2 composite phosphors containing Er^{3+}/Yb^{3+}, Ho^{3+}/Yb^{3+}, and Tm^{3+}/Yb^{3+} pairs of ions have the potential to be an effective UC phosphor not only because of the good properties of target host material but also the emission color and emission intensity observed. In addition, the new preparation method, powder-solution mixing, provides the homogeneous phase of the product which gives rise to the higher regularity of the distribution of UC emission intensity than the product synthesized by solid-state reaction method. Hence, this method might be one of the appropriate techniques for the fabrication of efficient UC phosphors.

TABLE OF CONTENTS

LIST OF FIGURES

LIST OF TABLES

Chapter I

Introduction

1.1 General introduction

The development of new strategies in the fabrication of optical materials including the enhancement in their properties for both physical and chemical has dramatically expanded in recent years, especially in the field of upconversion (UC) luminescence material (or called UC phosphor) [1-3]. UC phosphors have become one of the most investigated forms of luminescent materials because of the potential uses in the field of biomedical sciences [3-5]. Apart from the biomedical applications, they have also been used in many fields of research, for example display technologies, renewable technologies, and photocatalysis due to its unique properties like high color purity, sharp emission bandwidths, high photochemical stability, and long emission lifetimes [5-7]. Theoretically, upconversion luminescence (UCL) can be simply described as the light conversion which converts near infrared (NIR) light into visible (VIS) or ultraviolet (UV) light. In consequent of the absorption of at least two photons, a higher energy photon is emitted [8]. Since the UCL was discovered in the 1960s until nowadays, trivalent rare earth (RE^{3+}) ions are employed as UCL center because of their energy levels structure. The luminescence emission from RE^{3+} ions mainly occurs due to its particular 4*f* transitions, giving rise to sharp emissions and narrow emission bands [9-11].

The fundamental structure of UC phosphors consists of a host material and RE^{3+} dopants. Typically, the emission emitted by UC phosphors is in the term of sensitized luminescence because there are two working types of RE^{3+} dopants added into the host material. One is employed as luminescent center which emits the radiation and is called an "*activator*", and the other one harvests the excited energy efficiently and then transfers that energy to the activator and is called a "*sensitizer*". Therefore, the well-organized UCL can be fundamentally observed in RE^{3+} activator-sensitizer combination-based UC phosphor [1]. For the activator, Er^{3+}, Ho^{3+}, and Tm^{3+} are the most extensively used due to their plentiful electronic energy levels to adapt

UCL [11-14]. Also, these ions are the main activator for fabricating red, green, and blue emitting UC phosphors. Additionally, by the combination of these activator ions (at least two ions e.g. Er^{3+}/Tm^{3+}), suitable sensitizer ion (e.g. Yb^{3+}), stable inorganic crystal, and eventually tuning dopants concentration ratio, the UC phosphor can provide a variety of UCL colors including white emission [15].

Among many efficient UC phosphors, fluoride-based UC phosphors have received much attention because, in general, fluorides demonstrate high chemical stability and low phonon energy around 350 cm^{-1} (low phonon energy is the considerable criteria for selecting UC host material) [16]. However, their applications are still limited due to their hygroscopic and instability. In comparison, oxide-based materials demonstrate higher chemical and thermal stability, but their drawback is phonon energy (~ 550 cm^{-1}) which is relatively high when compared to fluorides [17]. Taking into account potential applications as priority, appropriate oxides with low or intermediate phonon energy may have more promising applications than using fluorides as UC host material.

Nowadays, many new applications and technologies require a variety of properties of material which traditional materials have limited applicability. Composite materials, which comprise of the combination of two phases or more with different physical or chemical properties, have gained much attention in recent years because this type of material is typically light weight, flexible, high corrosion resistance, and impact strength. Because of these properties, composite materials have been considered as a replacement of classical materials used in aerospace industry, construction, and electrical and electronics [18]. With the prominent points of oxide-based material and composite material, the combination of ZnO and TiO_2 as composite material is one of the appropriate choices because each composition demonstrates the properties which are required in many technologies and applications like low-cost, non-toxic, environmental benign, high photosensitivity, high physical and chemical stability, and easy synthesis [19-22]. Additionally, ZnO-TiO_2 mixed oxide has been much studied for applying in various applications such as photocatalysis [23], fabrication of dowconversion phosphor [24], and optical temperature sensing [25].

In the ZnO-TiO_2 composite system, it has been reported that three main compounds exist, consisting of spinel-type Zn_2TiO_4 (cubic), Ilmenite-type $ZnTiO_3$ (hexagonal), and $Zn_2Ti_3O_8$

(cubic, low temperature form of $ZnTiO_3$). The existence of each compound depends on ZnO/TiO_2 mixing ratio and firing temperature used. Among these compounds, the noteworthy product is Zn_2TiO_4 that is a high thermal stability phase due to its inverse spinel structure. Besides, Zn_2TiO_4 is a steady phase (from room temperature to its melting point (1550 °C [26])) and easily formed by the reaction between ZnO and TiO_2, even if the system has low amount of ZnO [27]. In addition, Zn_2TiO_4 shows great potential for being the good optical host because it has high value of refractive index n = 2.1 [28] and low phonon energy around 721 cm^{-1} [29], which control part of energy losses in the electron toward phonon energy transfer and other non-radiative processes [30]. Therefore, Zn_2TiO_4 phase could be one of the candidate hosts for the fabrication of efficient UC phosphor.

Up to now, UCL from ZnO-TiO_2 composite phosphors has been rarely studied and has just been the topic of investigations in the last few years [31-36]. In addition, a series of reports regarding UCL from ZnO-TiO_2 composite phosphor shows only certain results in green and red emission bands which are observed from Er^{3+}/Yb^{3+} co-doped ZnO-TiO_2 composite prepared by solid-state reaction and metal-organic decomposition methods. Due to the lack of research about other basic dopant systems like Ho^{3+}/Yb^{3+} and Tm^{3+}/Yb^{3+}, ZnO-TiO_2 composite phosphor containing these dopants should be examined. Focusing on the preparation method, conventional solid-state reaction method can provide the product in two forms; powder and pellet, but it is well-known that the pellet form shows better luminescence properties because the bulk density of raw product, which depends on how intimately individual particles pack together, is higher which this characteristic directly affects the formation process of phosphor and its luminescence efficiency. Basically, the formation process of the products prepared by this method is diffusion process which the main problem is the diffusion limited. This problem leads to incomplete reaction, some loss of reactants, and compositionally inhomogeneous products [16]. In the field of UC phosphor, these will cause the irregularity of the distribution of UCL intensity. For metal-organic decomposition, the product is in the form of thin films and there are many criteria needed to be controlled, for example deposition rate, film uniformity, quality of film, and type of substrate, leading to a much wider variation in performance of UC phosphor thin films before obtaining the excellent one [37,38]. Thus, this method is not appropriate to explore the properties and performance of new fabricated materials. With these reasons, plenty of challenges regarding the preparation method of ZnO-TiO_2 composite UC phosphor are required

to find out the method that can produce UC phosphor with homogenous phase and high regularity of the distribution of UCL intensity for both powder and pellet forms.

According to all existed reports regarding UCL properties of ZnO-TiO_2 composite phosphors, the fundamental parameters like effect of firing temperature, ZnO/TiO_2 mixing ratio, RE^{3+} ion doping concentrations and their ratios on the crystal phase, and UCL properties were investigated [31-36]. However, the obvious result about the potential site preference of RE^{3+} ions in host crystal matrix has not been reported so far because ZnO-TiO_2 composite doped with RE elements shows the complex products in the form of multiphase coexistence (Zn_2TiO_4, TiO_2, and $RE_2Ti_2O_7$) and its XRD results show many overlapping peaks in which some peaks are nebulous and hard to define the phase of such peak position, causing to uncertain investigation on finding out actual position of RE^{3+} ions in host crystal matrix. Commonly, Rietveld refinement, which is the most widely used and acceptable technique for the characterization of crystalline materials, is often used to identify the potential site preference of dopant in the host crystal matrix, but all observed characteristics mentioned above are in accordance with the limitation of Rietveld refinement. Therefore, Rietveld analysis cannot be used to demonstrate the value of cell parameter or even to identify site preference of dopants in host crystal matrix of ZnO-TiO_2 composite UC phosphor system. For this reason, when Rietveld analysis cannot be applied, the indirect analysis method to predict the site preference of dopant in host crystal matrix should be inspected because this result is one of the important outcomes that might be used to develop the properties of this UC phosphor system or even other phosphors. To find out the most possible indirect method, the consideration on luminescence spectra together with lattice constant, lattice volume, and crystal structure of target host material is the easiest way to predict the site preference of dopants in host crystal matrix of this UC phosphor system.

Regarding the details and the strategies to solve the problems mentioned above, the basic knowledge about UC phosphor is crucial in order to understand them clearly. Therefore, a brief and general background of phosphors, focusing mainly on fundamental knowledge of UC phosphor, mechanism models of the generation of UCL, and the methods of preparation of UC phosphors including supportive information and ideas for the present work are given in the following sections.

1.2 Luminescence and phosphors terminology

Basic concept of luminescence and phosphor is started with the familiar word, "*Light"*. Light is a form of energy and can be categorized into two common ways, *Incandescence* and *Luminescence*. Incandescence is the emission of light by a material that is heated at high enough temperature and then begins to glow. This phenomenon occurs because atoms of heated material release their thermal vibrations as electromagnetic radiation in the form of light. Hence, incandescence is the light that is emitted by heat energy and usually called "hot light" [39]. In general, this is the most common type of light in daily life obtained from, for example a burning of charcoal during cooking, the brightness of the sun and stars, and the light of ordinary light bulbs.

Luminescence is the light from the source of energy where the substance emits light without hotness. The word "*luminescence*" was first used in 1888 by a German physicist, Eilhardt Wiedemann [40]. It comes from the Latin root, "*Lumin*", which means "*Light"*. Educationally, luminescence is a study that focuses mainly on the laws of absorption and emission produced by matter. In the case of emission called luminescence, it is an emission generated by the movement of electrons within the substance from more energetic state to less energetic state which may be caused by various processes through the substance such as absorption of photons, motion of subatomic particles, and chemical reactions. So, the term "*luminescence*" is frequently used to define a process that gives rise to the light at normal or lower temperatures, not resulting from heat [41]. Furthermore, luminescence is an interdisciplinary issue, involving in various fields of study, for instance physics, chemistry, biological science, medical science, material science, and engineering technology. These lead to many contemporary researches of different areas in the field of luminescence, especially the development of organic and inorganic luminescent materials.

Luminescent material is a material that emits light and it can also be called "*phosphor*". The word "*phosphor"* was first invented in the early 17^{th} century by an Italian alchemist, Vincentinus Casciarolo of Bologona. At that time, he found a glossy crystalline stone which was probably barite ($BaSO_4$) at the foot of the volcano. Subsequently, he fired that stone with the purpose to change it into a noble metal. Consequently, he did not obtain any metal, but he discovered that the sintered stone sent out the red light in the dark after exposure to the sunlight.

With present knowledge, his discovery can be expressed as the reaction in which the product obtained is barium sulfide (BaS) which is now known as one of the host materials for producing luminescent material. Later, the green emitting luminescent material was first discovered in 1866 by a French chemist, Théodore Sidot, who demonstrated that the green luminescence can be emitted by zinc sulfide (ZnS) [30]. In 1907, an English engineer, Henry Joseph Round, reported the observation of electroluminescence from a solid-state device. He applied voltage across two contacts on a carborundum (also known as silicon carbide (SiC)) crystal and then the yellow light appeared at low voltages. Besides, various emission colors could be detected when applying higher voltages [42]. His discovery led to the new development of luminescent materials. Further, blue emitting luminescent material was first discovered in 1936 by French physicist, Georges Destriau, who published a report on the occurrence of green and blue light after applying an electrical current through ZnS doped with copper and some chlorine or bromine as a charge compensation (ZnS:Cu,(Cl or Br)). He also proved that luminescence could not occur by using only ZnS compound, but it required the impurities and specific conditions, for example the blue emission from ZnS took place by adding Cu and Cl as impurity and controlling the frequency of applied voltage [43,44]. After the discovery of red, green, and blue emitting luminescent materials, scientific researches on luminescent materials have been developed increasingly due to the interesting in a variety of colors of light that could obtain from the combination of different intensities of emission exhibited by these luminescent materials. The new emission color acquired by this technique is in the scope of RGB color model which contains red (R), green (G), and blue (B) as primary colors.

Typically, the emission of light involves the characteristics time (τ_c) which is used to describe the duration or decay times of emission, therefore, this is one of the parameters that can be used to classify the type of luminescence. Luminescence can be sub-divided into fluorescence and phosphorescence by the basis of duration of emission or decay time. The term "*fluorescence*" denotes as an emission of short decay time less than 10^{-8} seconds ($\tau_c < 10^{-8}$ s). This emission is seen to be happening concurrently with the absorption of radiation and stopping instantaneously when the excitation source is discontinued. On the other hand, the term "*phosphorescence*" signifies as an emission of long decay time more than 10^{-8} seconds ($\tau_c > 10^{-8}$ s). This emission is seen to go on for some time, even if the excitation source has been removed. In addition to the clarification of luminescence by the characteristics time, the study on the effect of

temperature upon the decay of luminescence is one of the obvious ways to differentiate between fluorescence and phosphorescence. The fluorescence is essentially temperature independence, whereas the phosphorescence shows strong dependence on temperature [30,45-47]. In case of the term "*luminescence*" which includes fluorescence and phosphorescence, it is described as a phenomenon in which electronic states of substance are excited by the external energy source and after that, the energy is given off from substance in the form of light at various wavelengths [48].

1.3 Fundamental of luminescence

The phenomena of luminescence can be grouped into various categories, depending on the type of excitation source. For example, cathodoluminescence (CL) is excited by cathode rays or electron beams, thermoluminescence (TL) by the activated thermally after initial irradiation such as α, β, γ, UV or X-rays, photoluminescence (PL) by electromagnetic radiation/photon, and electroluminescence (EL) by electric influences [47,49]. In this dissertation, only PL will be considered and hence the other types of luminescence will not be further discussed.

In theory, the occurrence of luminescence involves two main processes which are the absorption and the release of energy. So, the luminescence mechanism can be described as follows. As shown in Figure 1.1 that represents a basic concept of luminescence mechanism, when a luminescent material absorbs energy (photon) from the excitation source, electrons from its ground state are excited to the excited state, then the relaxation occurs, and some photons may release in the form of heat due to the intermolecular lattice vibrations. In this case, heat is the main possible outcome from non-radiative transition process. Afterwards, electrons in the lower sub-energy level at the same excited state will return to the ground state by the emission of radiation through radiative transition process. Taking into account the two types of energy transition process, one is the radiative transition that gives rise to the light and would be called luminescence, and the other one is non-radiative transition that causes the heat to the molecular lattices during the process and it is the main process that affects the decrease in intensity of luminescence [16]. In general, productive luminescent materials are directly related to radiative transitions which should dominate over non-radiative transitions. Basically, luminescent materials emit a variety of colors of light which the color depends upon the energy gap (ΔE)

between excited state and ground state. In principle, the energy E in each energy state can be calculated using Planck's equation according to equation (1.1).

$$E = h\upsilon = hc / \lambda \tag{1.1}$$

where E is the energy of photon (J), h is Planck's constant (6.63×10^{-34} J.s), c is the speed of light (3×10^{8} m.s^{-1}), λ is wavelength (m), and υ is frequency (s^{-1} or Hz). Normally, light emission that human eyes can detect is called the visible light which consists of wavelengths, ranging from around 380-760 nm. Specific wavelengths within the visible light spectrum correspond to a specific color and the human eyes can perceive different colors for different wavelengths [30]. Considering the relationship between ΔE, λ, and luminescence color detected by the human eyes, according to Figure 1.1 and equation (1.1), if ΔE is 2.95 eV which means that the corresponding radiation wavelength is approximately 420 nm, the human eyes will detect violet color.

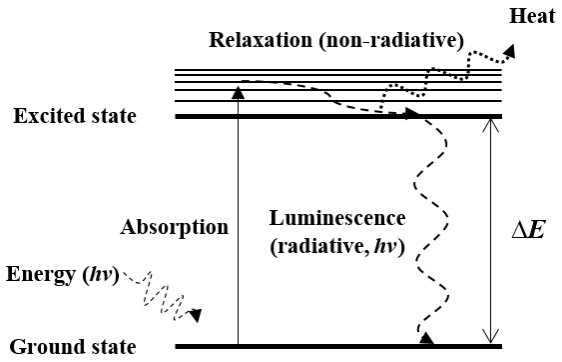

Figure 1.1. Simplified basic luminescence mechanism based on excitation / emission processes.

Luminescent material is a solid that changes certain types of energy into electromagnetic radiation over and above thermal radiation. Most luminescent materials take the advantages of a wide energy gap (ΔE) in their electronic band structure or the presence of defects or impurities which plays a significant role as the localized electronic states. The luminescence emission exhibited by a luminescent material is regularly in the visible range, but it can also occur in ultraviolet (UV) or infrared (IR) regions. In the fields of luminescent material, there are three underlying types of this material which consist of phosphor, upconversion phosphor, and long-persistent phosphor. Herein, only upconversion phosphor will be considered. The following section will initially provide general descriptions of phosphor with the emphasis on its

mechanisms and characteristics. Subsequently, the upconversion phosphor which is the main subject of this dissertation will be discussed in much more detail.

1.4 Phosphor

Generally, materials that generate luminescence are called "phosphor", but in this section, phosphor is a luminescent material type. Phosphor is the simplest form and one of the luminescent materials that can absorb energy from the incident radiation and then emits photons in the form of light after passing through various energy transfer processes. The luminescence emission of phosphor falls into the visible range and can become invisible such as UV or IR radiation. Theoretically, phosphors are classified into organic and inorganic phosphors. Organic phosphors involve specific molecules, while inorganic phosphors involve certain lattice structures. Most luminescent materials are inorganic phosphor which consists of an inert imperfect host crystal lattice to which some impurity ions called dopant, are intentionally added. Typical dopants are transition metals or rare earth elements which are the most common optically active impurity. There are two kinds of dopant used in the fabrication of phosphors. One is employed as luminescent center which emits the radiation and is called an activator. The other one harvests the excited energy efficiently and then transfers that energy to the activator. This dopant is called a sensitizer which would be added to phosphors, if the activator cannot be excited, for example because of the parity forbidden transitions, which take place when there is no change in the parity of one-electron states [30].

1.4.1 Fundamental emission and excitation mechanisms of phosphor

The luminescence of phosphors typically takes place by the absorption of energy at the activator site, followed by energy relaxation, and then the energy returns to the ground state by emission of photons with energy E. In addition, the energy absorption of phosphors can occur via the host lattice or by intentionally doped impurity ions.

Figure 1.2 represents the schematic of how a phosphor emits the light with direct excitation of the activator. The grey circle A is signified as an activator ion which is enclosed by the host lattice (white circle). The luminescence process is a release of energy in the form of emission and some energy loss in the form of heat due to the internal oscillations of material that normally occur through host lattice structure. In the host lattice containing only the activator ion, this ion

will be directly excited by the external energy. After the radiation, activator ion will absorb energy, then this energy raises electrons from its ground state to an excited state and subsequent return to the ground state with the emission of photons

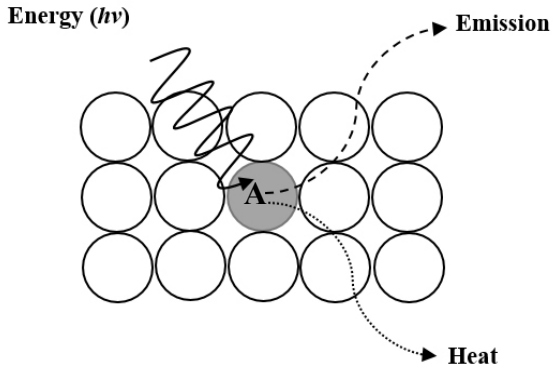

Figure 1.2. Schematic diagram of how a phosphor emits light with direct excitation of the activator.

In Figure 1.3, when the activator ion (grey circle A) can absorb small energy or it means weak energy absorption, second ion will be added which this ion is generally known as the sensitizer ion (grey circle B). Sensitizer ion can absorb more energy and then transfers absorbed energy (dark thick arrow) to activator ion for emitting the emission. In addition, sensitizer ion can exhibit the emission by itself but most cases, the strong emission usually occur via activator ion because of the energy transfer from sensitizer ion to activator ion.

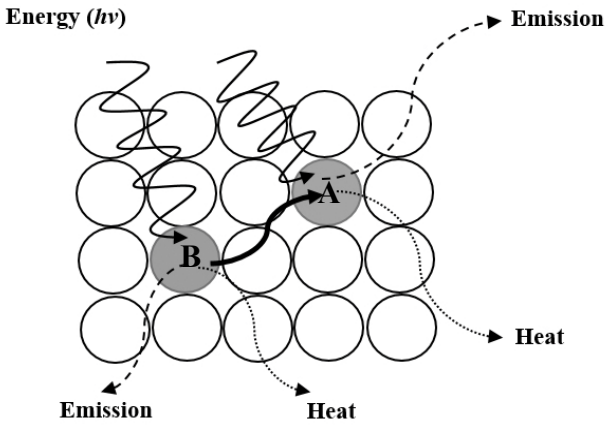

Figure 1.3. Schematic diagram of how a phosphor emits light with indirect excitation of the activator.

1.4.2 Energy transfer processes in phosphor

Energy transfer (ET) is a process in which sensitizer and activator ions show physical interaction. As shown in Figure 1.4, there are four basic mechanisms involved in ET process between sensitizer and activator ions; (1) resonant radiative ET, (2) resonant non-radiative ET, (3) phonon-assisted ET, and (4) cross-relaxation.

In general, an efficient ET process requires a vital spectral overlapping between the emission spectrum of sensitizer and the absorption spectrum of activator because the structure of emission spectrum of sensitizer will change with activator concentration. This is a very significant point of ET process which takes place in a variety of circumstances of phosphors. For resonant radiative ET (Figure 1.4(a)), photons emitted by sensitizer ions are absorbed by activator ions within a photon travel distance and the sensitized emission lifetime does not change with the activator concentration. In contrast to the resonant radiative ET, the resonant non-radiative ET (Figure 1.4(b)) occurs without emission of photons and is often accompanied by an important decrease in the sensitized emission lifetime against activator concentration [50,51].

By concerning the energy level mismatch (expressed as "ε") between sensitizer and activator ions, some ET occurs with emission or absorption of phonons to compensate the energy level mismatch. This mechanism is called phonon-assisted ET (Figure 1.4(c)). Moreover, the ET also involves the distance between sensitizer to sensitizer, activator to activator, or sensitizer to activator. If the distance of two ions is so close and the excited energy of one ion is in higher excited state, the photon which returns to the lower energy level can transfer its energy to neighboring ions. This ET is called cross-relaxation and usually refers to the downconversion (DC) ET (Figure 1.4(d)). With this DC ET model, DC phosphors have been proposed and developed since 1957 as the first type of phosphor [52]. The luminescence mechanism of DC phosphors is described as the process, where one photon with a high energy (short wavelength) is cut to obtain one or more photons with a lower energy (longer wavelength). Nowadays, the DC phosphor is sometimes shortly called as phosphor. In addition, when obtained photons after cutting are more than one, this process is also referred and approached to quantum cutting (QC) or quantum splitting (QS) in many literatures [53].

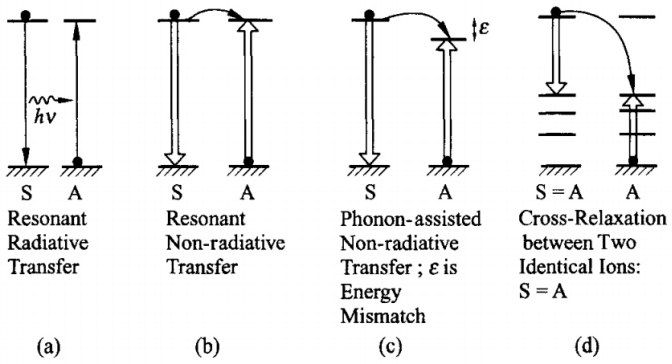

Figure 1.4. Schematic diagram of phosphor with different energy transfer (ET) processes between sensitizer (S) and activator (A) ions, (a) resonant radiative ET, (b) resonant non-radiative ET, (c) phonon-assisted ET, and (d) cross-relaxation. Reproduced with permission from [50]. Copyright (2005) Springer-Verlag Berlin Heidelberg.

DC phosphors have been developed and investigated for two decades for their use in solar cell applications, for example Pr^{3+}/Yb^{3+} co-doped $Y_2Si_2O_7$ [54] or Er^{3+}/Yb^{3+} co-doped $CaMoO_4$ [55]. Moreover, DC process is the essential knowledge for making white light emitting diodes (WLEDs) which have been gained much attention for substituting incandescent and fluorescent light sources, especially general light bulbs and display backlights due to their long lifetime, spectral tunability, small footprint, and, most outstandingly, their high performance in changing electrical to optical power [56,57]. Taking into account the commercial WLEDs, they are phosphor-converted conventional LEDs, consisting of a blue LED (e.g. gallium nitride (GaN)) coated by a yellow phosphor (e.g. yttrium aluminum garnet (YAG)). General luminescence processes of this material for generating white emission are clarified as follows. When a blue LED excited by short wavelength excitation source emits blue emission, a yellow phosphor will absorb that blue emission and then down converts to yellow emission (longer wavelength). So, the combination of blue emission from blue LED and yellow emission from yellow phosphor produces white emission.

1.5 Upconversion phosphor

Upconversion (UC) phosphor is a solid luminescent material in which the process involves the absorption of two or more photons of low energy with subsequent emission of higher energy photons [8]. So, the process of this material is to convert long wavelength radiation into shorter

wavelength radiation. Besides, the UC process is remarked as the reversal process of DC process.

1.5.1 Luminescence mechanisms of upconversion phosphor

UC processes are mainly divided into three classes; excited state absorption (ESA), energy transfer upconversion (ETU), and photon avalanche (PA). These processes involve the population of a highly-excited state by the sequential absorption of two or more photons by metastable long-lived energy states. The history and details of these three UC processes are explained as follows.

In 1959, Bloembergen reported the primary model of UC process that was the ESA which involved the two-step absorption in which a single ion absorbed two subsequent photons. He presented the behavior of IR photons that could be detected and counted through consecutive absorption within the energy levels of a given ion in a solid. This behavior was called "Quantum Counter Action" [50,58]. Nowadays, the identical effect can be simply explained as follows. According to Figure 1.5(a) which shows the ESA model of UC process, at first, photons absorption is started by exciting electrons from the ground state (G) towards an intermediate excited state (E1), this step is called ground state absorption (GSA) process. Later, at E1, the absorption occurs again, provoking electrons into the higher excited state (E2). This subsequent step is called excited state absorption (ESA) process. To provide the efficient ESA process, it should be excited by high excitation source such as a high-power laser light to maintain the energy lifetime in the intermediate excited state. Thereafter, UC luminescence (UCL) takes place through radiative transition from E2 to G [1,8,58]. Besides, it should be noted that the process mentioned above only befalls in UC phosphor doped with single ion or it could occur in UC phosphors with very low dopant concentration.

The role of ET in UC processes was not recognized until 1966. The UC process was first realized by the reports of Auzel [59,60], and Ovsyankin and Feofilov [61] who reported about the UC process by two different neighboring ions and electronic excitations in activated crystals, respectively. From that time until now, by concerning two proposed ideas, one more UC process has been recognized that the ET of two different neighboring ions could take place between them, and the energy should be in the excited state before the beginning of ET steps. Subsequently, there are two possible ways of ET from the excited state of first ion to second

ion. First, the ET is assumed to take place from first ion in its excited state to second ion in its ground state, resulting in the energy in excited state of second ion. Second, under high-power excitation source, the energy in the excited state of first ion could be conveyed to the excited state of second ion, leading to the energy in upper excited state of second ion. With this second ET, it is often called energy transfer upconversion (ETU) process or the APTE effect (French acronym for addition de photons par transfert d' energie = English acronym for addition of photons by transfer of energy) [30,50,62].

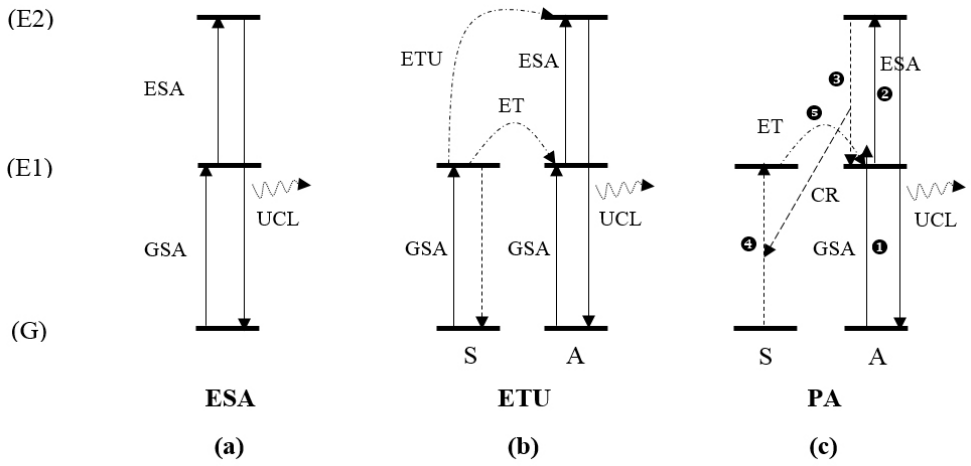

Figure 1.5. Principle energy diagrams of various upconversion (UC) processes for generating UC luminescence (UCL). Adapted with permission from [1]. Copyright (2009) The Royal Society of Chemistry.

Figure 1.5(b) represents the energy diagram of UC process through ETU model. This model is quite different from ESA model because ESA model takes place within a single ion, while ETU model includes two neighboring ions (sensitizer (S) and activator (A)). In the ETU model, each ion absorbs a pump photon of the same excitation energy by GSA process, populating energy to metastable energy level E1. Subsequently, the energy in E1 of S is transferred to A by two ways; ET and ETU, promoting the energy from E1 of A to higher excited state (E2) by ESA process, while the excess energy in E1 of S relaxes back to the ground state G. Afterward, UCL takes place through radiative transition from E2 to G as well as ESA model. Since ETU model consists of two neighboring ions, the most significant point is the average distance between them because it has a highly effect to the efficiency of ET. It is worth noting that the distance between two neighboring ions relies on the dopant concentration.

Back to the history of UC process, in 1979, Chivian *et al*. [63] discovered a phenomenon of photon avalanche (PA) in Pr^{3+}-based infrared quantum counters. The PA-UC features an unusual pump mechanism that requires high pump intensity above the threshold value. According to Figure 1.5(c), the process begins with the population of photons form G of A to E1 of A by non-resonant weak GSA process (❶), followed by a resonant ESA process to populate the higher excited E2 level (❷). Subsequently, photons at E2 relax back to E1 (❸), during this transition, a cross-relaxation energy transfer (CR) (also called ion pair-relaxation) occurs from the E2 → E1 transition of A to ground state G of S (or expressed as ❸ to ❹) and then photons are populated from G of S to E1 of S. After that, the intermediate energy level E1 of S is occupied by that photons, resulting in the ET from E1 of S to E1 of A (❺). Further, E1 of A is populated again to E2 by ESA process to continuously initiate cross-relaxation, producing the looping process or it is called avalanche process. By this looping, the UCL increases dramatically and produces strong UCL.

Considering the UC efficiency of these three UC models. ESA is the least competent UC model. The PA model is the most efficient UC model, but the emission response is delayed due to the CR processes, containing numerous looping processes with a rise time up to a few seconds, weak GSA process, and the high pump power over a certain threshold limit requirement. In contrast, ETU model is prompt and pump power independent, and thus has been extensively used as a reference model for proposing possible UC mechanism of highly efficient UCL of UC phosphors over the past two decades [1,8].

Since the 1960s when the research began in this area, it has been well-known that in the theoretical understanding of UC mechanism, this process can be explained by considering the relationship between UC emission intensity (I) and excitation pump power (P). The intensity I is proportional to the n power of P, which can be expressed as follow:

$$I \propto P^n \tag{1.2}$$

where n is the number of pump photons per one photon emitted. To obtain the n-value, a plotting of log I versus log P yields a straight line with the slope n [8]. Typically, the experimental n-value is in the specific range of values and less than the maximum theoretical n-value for each possible UC mechanism; two-photon process ($1 < n \leq 2$) or three-photon process ($2 < n \leq 3$), because of the saturation effect in the UC emission intensity mainly caused by the

competition between linear decay and UC processes for the depletion of the intermediate excited states [64,65]. In addition, there are other possibilities which would have impact on the reduction of *n*-value such as the ET process to impurity defects, CR, or other complicated processes which can give rise to the depletion of the intermediate excited states of the dopants [64-67].

Focusing on the competition between linear decay and UC processes, the model for explaining this phenomenon was first described by Pollnau *et al*. [64]. They provided the model based on three-level system which is the simplest system in which UCL can be observed. The three-level system contains the ground state (G), intermediate excited state (E1), and UCL state (E2), and the two-photon process is responsible for this system. Also, they mentioned that, for any UC mechanism, even though the two-photon process corresponds to the *n*-value equal to approximately two, but the dependence of UC emission intensity on pump power is also expected to decrease in *n*-value with increasing excitation power. Later, Suyver *et al*. [65] and Agazzi *et al*. [66] proposed additional processes regarding ETU model which were created based on the original model proposed by Pollnau *et al*. [64]. Their models involve the energy migration from sensitizer to sensitizer and subsequent ET from an excited state of sensitizer to its neighboring ion (activator). Besides, they provided a significant point that, in the high-power regime, any emission band will show a slope of one, irrespective of the number of ET steps from the sensitizer to the acceptor ions involved.

Concentrating on the simplest system of UC mechanism together with the relationship between UC emission intensity (I) and pump power (P) ($I \propto P^n$), it was predicted that I was proportional to P^2 (n-value ~ 2) when the linear decay of the E1 was the dominant depletion mechanism, while I was proportional to P^1 (n-value ~ 1) when the UC process of the E1 was the dominant mechanism. Remarkably, these results were proved by presuming that the system was under steady-state excitation. In addition, Lei *et al*. [68] reported steady-state UCL dynamic equations of the UC mechanism that were concerned with the two-step ET between neighboring Er^{3+} and Yb^{3+} and their model was different from the original one [64]. Nevertheless, their result was also similar to that deduced in [64] and the aforementioned discussion. Herein, in the easiest way to sum up the change in *n*-value of UC system, it should be referred to the "saturation effect" for the perception in detail. According to $I \propto P^n$, the plotting of I versus P via log-log

scale yields a straight line with slope *n*. Fundamentally, the slope *n* decreases with increasing *P* because the system moves toward the saturation state of UC emission intensity by the increment of *P*. With this concept, at the intermediate excited state, if the linear decay is the dominant depletion mechanism, UC emission intensity will be released without the influence of saturation effect because the energy is not abundant in the UCL state and the *n*-value for this case should be close to two or equal to two. On the other hand, if the UC process is the dominant depletion mechanism, the energy will be numerous in the UCL state, causing to the saturation effect in UC emission intensity and the *n*-value will decrease to around one. Therefore, the saturation effect caused by the competition of linear decay and UC processes is the considerable reason for the depletion of the intermediate excited state, influencing to the reduction of *n*-value [64,65,69,70].

1.5.2 Structure of upconversion phosphor and the selection criteria

UC phosphors are generally consisted of an inorganic crystalline host and dopants because in most cases at room temperature, any luminescence cannot be emitted by using only host material. Mostly, dopants are lanthanide elements (also known as rare earth (RE) elements) which are commonly in the form of localized luminescent center. Due to the discrete energy states of these elements, RE-doped upconverters exhibit superior IR to visible UC performance. Hence, UCL can be expected in principle from most RE-doped host crystal materials, but the efficient UCL only takes place by using small number of well-designated dopant-host combinations. However, the principle procedure for fabricating UC phosphors encompasses with two steps: the multiformity of host lattice and the variation of dopants within the host lattice structure. Also, varying the host lattice or dopants may cause the different UCL behaviors due to the changes in radiative and non-radiative (e.g. multi-phonon relaxation as well as energy transfer processes) properties [71].

1.5.2.1 Rare earth-based upconverter

Rare earth (RE) elements are a group of seventeen chemical elements in the periodic table, consisting of fifteen lanthanides from La (atomic number 57) to Lu (atomic number 71), of Sc (atomic number 21), and of Y (atomic number 39). The electronic configuration of all trivalent RE (RE^{3+}) ions in the ground state are shown in Table 1.1. As shown in the table, Sc^{3+}, Y^{3+}, La^{3+}, and Lu^{3+} ions do not have electronic energy for inducing excitation and luminescence

processes in or near visible region. On the other hand, other RE^{3+} ions (Ce^{3+} to Yb^{3+}) can induce the excitation and luminescence processes around visible region because of partially filled 4*f* orbitals, leading to a variety of luminescence properties [72].

The RE element is the most desirable option as impurity for the fabrication of UC phosphor due to its radiative transitions which essentially befall between 4*f* electronic energy levels. Theoretically, 4*f* energy levels are placed inside an unfilled inner shell within the cloud of electrons and are shielded from the surrounding by the 5*s* and 5*p* energy levels. So, 4*f* levels are not much affected by the host material because 4*f* electrons are protected from electric fields by outer $5s^2$ and $5p^6$ electrons, leading to the narrow-band excitation and emission lines in the spectra of RE ions in crystals. In addition, according to the parity selection rules [73], it should be taken into account that electric dipole transitions between 4*f* levels are strongly forbidden due to the same parity of 4*f* levels [74,75]. However, the parity forbidden rule can be partially cracked when RE^{3+} ion is introduced into the host lattice due to the mixing of opposite parity into the wave functions of 4*f* levels by non-centrosymmetric crystal field with odd parity [76]. Because of the forbidden character of 4*f*-4*f* transitions, RE^{3+} ions generally exhibit low molar absorption coefficients, causing to small absorption cross-sections, and their excited states are long-lived (typically from microseconds (μs) to milliseconds (ms)), resulting in the large radiative lifetimes [48,77]. For this reason, RE^{3+} ions are appropriate for being luminescent center in UC phosphors.

To comprehend the 4*f* level structure of RE^{3+} ions with the same standard, Dieke [78] and other researchers [79,80] did extensive work to compile the energy level of 4*f* electrons of RE^{3+} ions. According to Dieke's publication [78], he presented the first diagram of 4*f* energy levels of RE^{3+} ions at energy between 0 to 40 x 10^3 cm^{-1} by considering optical spectra of individual ions incorporated into $LaCl_3$ crystals. In his detailed diagram, the width of energy level bars gives the order of magnitude of crystal field splitting which is seen to be very small in comparison to the transition metal ions [48]. Since 4*f* electrons barely interact with the environmental electric field, therefore, Dieke's diagram is applicable to ions in almost any host crystal lattices. However, the highest variation of energy levels of this diagram is still limited. Later, in 1989, Carnall *et al*. [79] did the experiment on spectroscopy of RE^{3+} ions (except Pm^{3+} and Eu^{3+}) doped into single crystal LaF_4. Their observed spectra and energy level calculations resulted in

the extension of Dieke's diagram at higher energies around 40 x 10^3 to 50 x 10^3 cm^{-1}. Due to the lack of information of energy levels of RE^{3+} ions in vacuum ultraviolet (VUV, $\lambda < 200$ nm) and there are many $4f^n$ levels (n is number of energy level) which are in this spectral region, thus, in 2000, Wegh *et al*. [80] did the experiment on spectroscopy of various RE^{3+} ions doped into $LiYF_4$ under VUV excitation and they reported new observed energy levels that provided an extension of Dieke's diagram up to 70 x 10^3 cm^{-1}. However, the interesting UCL is generally in the UV to near-infrared (NIR) regions of electromagnetic spectrum, therefore, the original Dieke's diagram at energy levels around 0 to 35 x 10^3 cm^{-1} (Figure 1.6) is sufficient and it has been widely used to illustrate the possible UC mechanism of RE^{3+} ions doped into the host materials.

Table 1.1. Electronic configuration of all trivalent rare earth (RE^{3+}) ions in the ground state. Adapted with permission from [30]. Copyright (2006) Taylor and Francis Group LLC.

Atomic number	**Name**	**Ion**	**4*f* electron**						
21	Scandium	Sc^{3+}							
39	Yttrium	Y^{3+}							
57	Lanthanum	La^{3+}							
58	Cerium	Ce^{3+}	↑						
59	Praseodymium	Pr^{3+}	↑	↑					
60	Neodymium	Nd^{3+}	↑	↑	↑				
61	Promethium	Pm^{3+}	↑	↑	↑				
62	Samarium	Sm^{3+}	↑	↑	↑	↑			
63	Europium	Eu^{3+}	↑	↑	↑	↑	↑		
64	Gadolinium	Gd^{3+}	↑	↑	↑	↑	↑	↑	
65	Terbium	Tb^{3+}	↑↓	↑	↑	↑	↑	↑	↑
66	Dysprosium	Dy^{3+}	↑↓	↑↓	↑	↑	↑	↑	↑
67	Holmium	Ho^{3+}	↑↓	↑↓	↑↓	↑	↑	↑	↑
68	Erbium	Er^{3+}	↑↓	↑↓	↑↓	↑↓	↑	↑	↑
69	Thulium	Tm^{3+}	↑↓	↑↓	↑↓	↑↓	↑↓	↑	↑
70	Ytterbium	Yb^{3+}	↑↓	↑↓	↑↓	↑↓	↑↓	↑↓	↑
71	Lutetium	Lu^{3+}	↑↓	↑↓	↑↓	↑↓	↑↓	↑↓	↑↓

In general, RE-based upconverters involve at least two significant factors: (1) highly steady host material as the shield and (2) competent dopant as the luminescent center. Typically, the emission emitted by UC phosphors is in the term of sensitized luminescence because there are

two working types of RE^{3+} dopants added into the host material. One is employed as luminescent center which emits the radiation and is called an "*activator*", and the other one harvests the excited energy efficiently and then transfers that energy to the activator and is called a "*sensitizer*". Therefore, the well-organized UCL can be fundamentally observed in RE^{3+} activator-sensitizer combination-based UC phosphor. Besides, efficient UCL can be expected from most RE^{3+} ions [1].

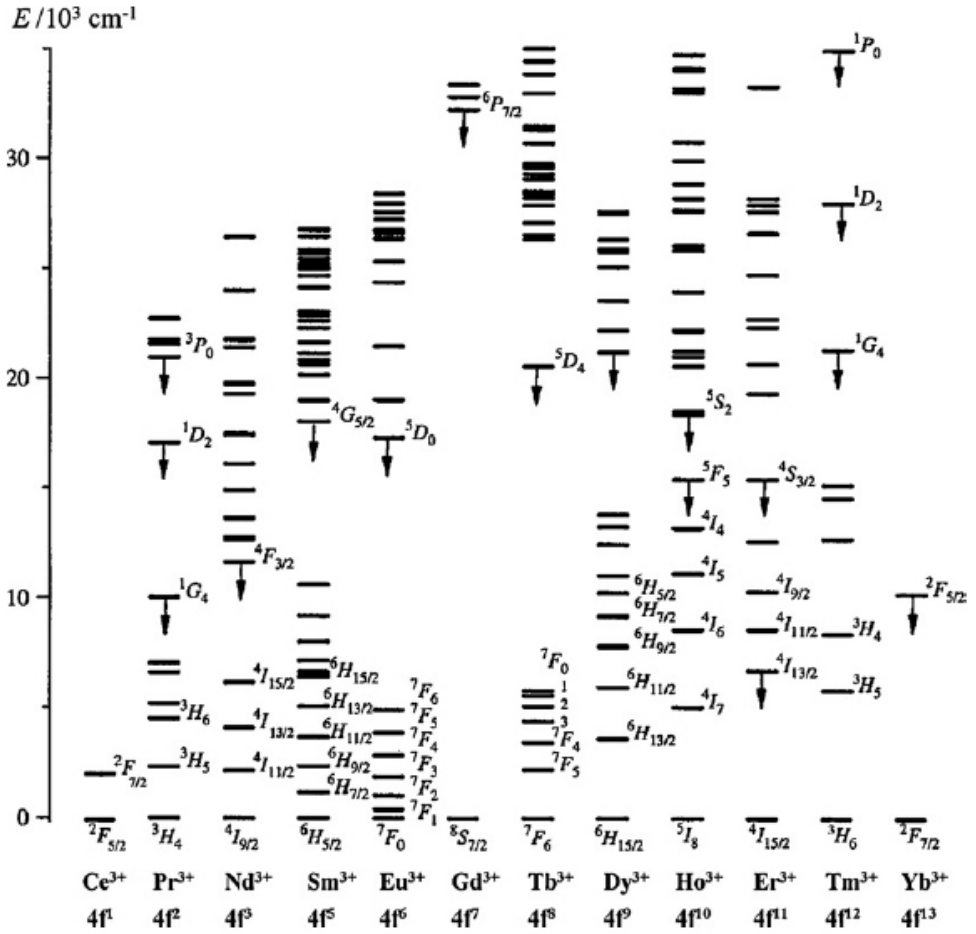

Figure 1.6. Partial energy level diagram of non-radioactive open shell RE^{3+} ions according to Dieke's diagram. Downward arrows indicate standard emission levels. Reproduced with permission from [81]. Copyright (2011) Elsevier B.V.

1.5.2.2 Activator

To generate high performance UCL, the energy difference between excited level and lower-lying intermediate level (ground level) should be close to the excitation energy to facilitate the

photon absorption and ET steps involved in the UC mechanism. Hence, many RE^{3+} ions are not appropriate to work as the activator due to the lack of proper energy level structure. Er^{3+}, Ho^{3+}, and Tm^{3+} are currently the most common activator for the fabrication of UC phosphor due to their plentiful electronic energy levels and ladderlike arranged energy levels to adapt UCL [11-14,71]. Also, these ions are the main activator for producing red, green, and blue emitting UC phosphors. In addition, by the combination of these activator ions (at least two e.g. Er^{3+}/Tm^{3+}), suitable sensitizer ion (e.g. Yb^{3+}), stable inorganic crystal, and eventually tuning dopants concentration ratio, the UC phosphor can provide a variety of UCL colors including white emission [15]. In this section, three most widely used activators for UC phosphors based on activator-sensitizer combination system will be discussed as follows by concerning only Yb^{3+}-based co-dopant; Er^{3+}/Yb^{3+}, Ho^{3+}/Yb^{3+}, and Tm^{3+}/Yb^{3+}.

In the Yb^{3+} sensitized Er^{3+} UCL process (Figure 1.7(a)), the Yb^{3+} is excited from $^2F_{7/2} \rightarrow {}^2F_{5/2}$ energy level by the excitation source which corresponds to the absorption band around 980 nm ($^2F_{7/2} \rightarrow {}^2F_{5/2}$ transition), and at the same time some energy may relax back to the ground state $^2F_{7/2}$ level as radiative or non-radiative transitions. Considering the long lifetime of the excited $^2F_{5/2}$ level (typically one millisecond), Yb^{3+} may well transfer the excitation energy to a neighboring Er^{3+} with higher probability than returning to its ground state [82]. Subsequently, Er^{3+} could be populated to $^4I_{11/2}$, $^4F_{9/2}$, $^4S_{3/2}$, and $^4F_{7/2}$ levels due to the energy absorption and ET from Yb^{3+}. After that, the energy in each energy level of Er^{3+} may relax back to $^2H_{11/2}$, $^4S_{3/2}$ or $^4F_{9/2}$ levels in the form of non-radiative transition. The UCL color is customarily assigned to following transitions: green emission centered at around 520 and 540 nm by $^2H_{11/2} \rightarrow {}^4I_{15/2}$ and $^4S_{3/2} \rightarrow {}^4I_{15/2}$ transitions of Er^{3+}, respectively, and red emission centered around 660 nm by $^4F_{9/2} \rightarrow {}^4I_{15/2}$ transition of Er^{3+}.

In the Yb^{3+} sensitized Tm^{3+} UCL process (Figure 1.7(b)), under 980-nm irradiation, Yb^{3+} is excited from $^2F_{7/2} \rightarrow {}^2F_{5/2}$ energy level. The energy in $^2F_{5/2}$ energy level of Yb^{3+} is transferred to Tm^{3+} as non-radiative transition to excite it up to the corresponding excited energy level. Because of the returning of excited energy to ground state of Tm^{3+} radiatively, emission bands could be centered at around 450, 475, 645, 690, and 800 nm which are attributed to $^1D_2 \rightarrow {}^3H_6$ (ultraviolet), $^1D_2 \rightarrow {}^3F_4$ (violet), $^1G_4 \rightarrow {}^3H_6$ (blue), $^1G_4 \rightarrow {}^3F_4$ (red), and $^3H_4 \rightarrow {}^3H_6$ (NIR) transitions of Tm^{3+}, respectively.

In the Yb^{3+} sensitized Ho^{3+} UCL process (Figure 1.7(c)), by the alike processes as mentioned above, Ho^{3+}/Yb^{3+} co-doped UC phosphors exhibit two main emissions; green and red colors, due to the following transitions: green emission centered at around 550 nm due to the $^5F_4 + {}^5S_2 \rightarrow {}^5I_8$ transition of Ho^{3+}, and red emission centered at around 670 nm due to $^5F_5 \rightarrow {}^5I_8$ transition of Ho^{3+} [1,8,62,83].

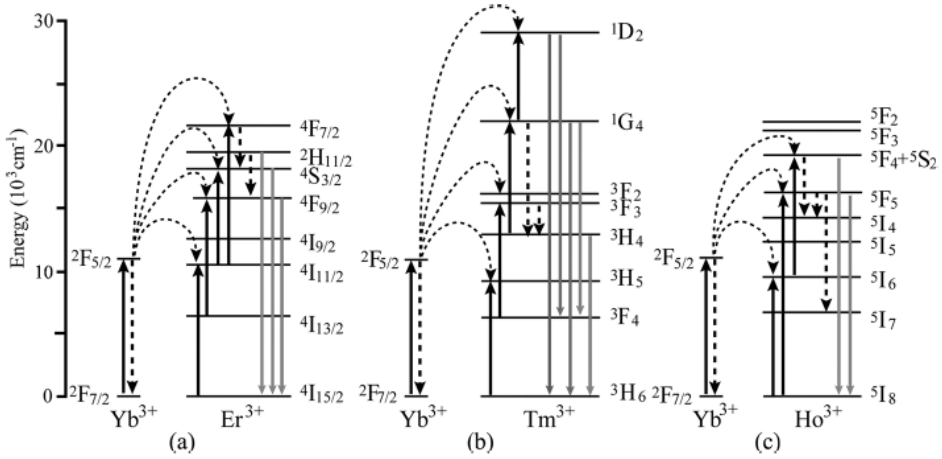

Figure 1.7. UC mechanism of phosphors containing (a) Er^{3+}/Yb^{3+}, (b) Tm^{3+}/Yb^{3+}, and (c) Ho^{3+}/Yb^{3+}. Adapted with permission from [83], Copyright (2015) American Chemical Society.

Examples of various UCL wavelengths based on these three activator-sensitizer combination systems with different host materials, irradiated with the 980-nm continuous waveform laser excitation are shown in Table 1.2.

1.5.2.3 Sensitizer

In UC phosphors containing single RE^{3+} ion, there are two main parameters that affect the UC process which is the distance between two neighboring activator ions and the absorption cross-section of such ion. High doping levels lead to the short distance between active ions, bringing about the CR ET and subsequently resulting in the quenching of excitation energy. This phenomenon is usually called "concentration quenching" which principally causes the reduction of luminescence emission intensity. Hence, the concentration of activator ions should be strictly kept at relatively low concentration (less than 2 mol%) to avoid the quenching effect [1]. However, the most RE^{3+} activator ions exhibit low absorption cross-section, leading to low

pump efficiency, that is why the UC emission intensity of singly doped UC phosphors is relatively low. To enhance UCL efficiency, a sensitizer ion that has the absorption cross-section relating to the used pump wavelength will be added as second dopant into the host crystal [1,8].

Table 1.2. Examples of Er^{3+}/Yb^{3+}, Tm^{3+}/Yb^{3+}, and Ho^{3+}/Yb^{3+} systems co-doped into different host materials and their emission and detected wavelengths results.

Activator/ Sensitizer	Host material	Emission	Detected wavelength (nm)	Reference
Er^{3+}/Yb^{3+}	$CaSc_2O_4$	Red	~ 380, ~ 405, 500-600, **625-725**	84
	α-$NaYF_4$	Red	510-570, **635-700**, 830-860	85
	GdOF	Red	408, 519, 552, **671**	86
	ZnO	Red	410, 525, 555, **665**	87
	TiO_2	Red	520-570, **640-690**	88
	ZnO-TiO_2	Orange	544, 557, **657**, **675**	31
Tm^{3+}/Yb^{3+}	α-$NaYF_4$	Blue	**440-500**, 630-670, 750-850	85
	GdOF	Blue	**446**, 476, 645, **791**	86
	ZrO_2-TiO_2	Blue	**474**, **495**, 644, 693	89
	ZnO	Blue	**478**, 647, 676	90
	TiO_2	Blue	**475**, 647, 685	91
Ho^{3+}/Yb^{3+}	β-$NaYF_4$	Green	**541**, 644, 751	92
	GdOF	Green	**535**, 660, **750**	86
	$ZnNb_2O_6$	Green	**546**, 662	93
	ZnO	Red	545, **660**	94
	TiO_2	Red	540, **650**	95

Remark: 1) **Bold** numbers presented in Table 1.2 are referred to the highest emission intensity peak or the range of detected wavelengths that contains strongest peak. 2) Detected wavelengths are the wavelength related to the general classification of spectral regions (ultraviolet (UV), visible (VIS), and near-infrared (NIR)); ultraviolet (UV, 10-380 nm), violet (VIS, 380-450 nm), blue (VIS, 450-495 nm), green (VIS, 495-570 nm), yellow (VIS, 570-590 nm), orange (VIS, 590-620 nm), red (VIS, 620-750 nm), and near-infrared (NIR, 750-2500 nm) [96].

A sensitizer ion with an adequate absorption cross-section in the NIR region is usually co-doped with activator ion to take the advantages of the competent ETU process between sensitizer and activator ions. The Yb^{3+} possesses an extremely simple energy level scheme with only one excited state $^2F_{5/2}$. Also, the absorption cross-section of Yb^{3+} is located around 980 nm due to

the $^2F_{7/2} \rightarrow {}^2F_{5/2}$ transition and its absorption band has a larger cross-section than other RE^{3+} ions. Moreover, the $^2F_{7/2} \rightarrow {}^2F_{5/2}$ transition of Yb^{3+} is well resonant with many *f-f* transitions of typical UC RE^{3+} activator ions (Er^{3+}, Tm^{3+}, and Ho^{3+}), leading to the well-organized ET from Yb^{3+} to these activator ions.

Up to now, with specific features of energy level diagram of Yb^{3+}, this ion is the most particularly suitable for using as sensitizer in UC phosphor systems. However, the concentration of sensitizer is also limited because of concentration quenching, but its content is rather higher than activator (around 20 mol% in the case of doubly or triply-doped host crystals) [1,8,30]. Additionally, it is found that Dy^{3+} can be used as sensitizer either. In general, Dy^{3+} has an absorption band ($^6H_{9/2}$) around 1300 nm higher than the ground state ($^6H_{15/2}$). So, the excitation source for provoking its electrons from its ground state is different from the system containing Yb^{3+} sensitizer ion. For example, in the Er^{3+}/Dy^{3+} co-doped $BaCl_2$ phosphor [97], Dy^{3+} is excited from $^6H_{15/2} \rightarrow {}^6H_{9/2}$ energy level under 1300-nm laser diode irradiation and further process can be explained as follows. The absorbed energy can be subsequently transferred to the $^4S_{3/2}$ and $^4F_{9/2}$ levels of Er^{3+}, and eventually causes two main emission spectra at around 550 nm (green emission: $^4S_{3/2} \rightarrow {}^4I_{15/2}$ transition of Er^{3+}) and 670 nm (red emission: $^4F_{9/2} \rightarrow {}^4I_{15/2}$ transition of Er^{3+}). Another example is Er^{3+}/Dy^{3+} co-doped YBr_3 phosphor [98]. In this system, with the identical initial process of $^6H_{15/2} \rightarrow {}^6H_{9/2}$ transition of Dy^{3+}, the energy can be subsequently transferred to the $^4F_{9/2}$ level of Er^{3+} and the dominant observed emission spectrum is around 660 nm due to the $^4F_{9/2} \rightarrow {}^4I_{15/2}$ transition of Er^{3+}.

1.5.2.4 Host material

Selection of suitable host materials is underlying to obtain promising optical properties such as high UC efficiency and controllable emission profile. Basically, host materials require close lattice counterparts to dopants and have low phonon energy [1]. Some examples of various compounds that have been investigated as the UC host material are shown in Table 1.3.

According to physical characteristics of RE^{3+} ions that have similar ionic radius and chemical properties, their inorganic compounds are ideal UC phosphor because they may emit the luminescence by themselves or by merely adding one dopant. In addition, general host materials containing alkaline metals ions (Na^+ and Li^+), alkaline earth ions (Ba^{2+}, Ca^{2+}, and Sr^{2+}) or some transition metal ions (Zn^{2+} and Zr^{4+}) are also the good UC host material due to their ionic radii

which are close to that of RE^{3+} dopants, leading to facile substitution or replacement by RE^{3+} sensitizer and activator ions [1]. For this reason, inorganic compounds containing these ions are usually used as UC host material. Additionally, semiconductor materials such as ZnS, ZnO, and TiO_2 have also been proposed as the UC host material, but there are still debatable on "how suitable is this type of materials for being UC host" because, after the incorporation of RE^{3+} ions into these materials, RE^{3+} ions are mainly located in the outermost layer of the host structure due to ionic radii mismatch between ions of host material and dopants, resulting in the low number of active ions for generating UCL [142]. Remarkably, RE^{3+} ions co-doped host material system is usually accompanied by the formation of crystal defects such as vacancies or interstitial sites to keep the charge neutrality. So, to maintain the host crystal structure, the concentration of dopants must be strictly controlled.

Ideal UC host material should have low lattice phonon energy, which is a requirement to decrease non-radiative loss and increase radiative emission. Basically, it seems that heavy halides group (chlorides, bromides, and iodides) is the good UC host material since the materials in this group exhibit very low phonon energy (less than 300 cm^{-1}), but they have many disadvantages such as poor chemical resistance, thermal unsteadiness, and high cost [143]. Therefore, this group is difficult to use in practical applications. Then and now, oxide is one of the most investigated UC phosphor host materials due to its good properties such as chemical stability and intermediate phonon energy (~ 550 cm^{-1}). However, oxide may be not the most appropriate UC host material because its phonon energy is relatively high in comparison with other low phonon energy materials. In addition, the compounds containing RE elements such as RE-oxy-sulfides (e.g. Y_2O_2S, Gd_2O_2S, and La_2O_2S) have been well-known for a long time as the outstanding phosphor host material and widely used in some applications such as cathode ray tubes, displays, and X-ray luminescent screens. However, this type of compound is limited in a wide-range of applications due to the high cost of precursors and time-consuming in the production [144].

Table 1.3. Various types of compounds used as UC host material.

Compound	Material	Reference
Oxides	Y_2O_3	99-101
	Gd_2O_3	102-104
	ZrO_2	105-107
	ZnO	87,90,94
	TiO_2	88,91,95,108,109
Fluorides	$NaYF_4$	85,92,110-112
	$LiYF_4$	113-115
	SrF_2, CaF_2, BaF_2, CdF_2	116,117
	LaF_3	118
Chlorides	$BaCl_2$	119
Oxy-chlorides / bromides	BiOCl, BiOBr	120,121
Oxy-sulfides	Gd_2O_2S	122
	La_2O_2S	123
Garnets	$Y_3Al_5O_{12}$ (YAG)	124,125
	$Gd_3Ga_5O_{12}$ (GGG)	126,127
Phosphates	YPO_4, $LaPO_4$, $GdPO_4$	128
Oxy-fluorides	YOF, $Y_6O_5F_8$	129
	GdOF	86
Others	$CaSc_2O_4$	84
	$LiNbO_3$	130-132
	$CaMoO_4$	133-135
	$BaTiO_3$	136-138
	AlON	139
	$YAlO_3$	140
	$ZnAl_2O_4$, $ZnGa_2O_4$, $ZnIn_2O_4$	141
	ZnO-TiO_2 (Zn_2TiO_4)	31-36

To date, fluoride-based materials are the promising UC host because they show chemical stability, very low phonon energy (~ 350 cm^{-1}), and high optical transparency over a wide wavelength range. Among a large number of fluoride host materials, the crystalline $NaYF_4$ is one of the most efficient host materials for the fabrication of UC phosphor due to its two modification forms; a high temperature cubic phase (alpha-$NaYF_4$ (α-$NaYF_4$)) and a low temperature hexagonal phase (beta-$NaYF_4$ (β-$NaYF_4$)), which means that $NaYF_4$ host-based UC phosphor can provide a variety of physical properties, for example transparent UC phosphor and nanosized UC phosphor [1,16].

It is also known that the crystal structure alignment of each host material can significantly influence on the optical properties. For example, hexagonal $NaYF_4$ (β-$NaYF_4$) doped with Er^{3+} and Yb^{3+} bulk materials exhibit about an order of magnitude enhancement of UC efficiency relative to their cubic phase counterparts (α-$NaYF_4$) that are higher in the site symmetries of RE^{3+} dopant ions [16,145,146]. This phenomenon could be explained by considering the phase dependent optical properties which can be directly attributed to different crystal fields around RE^{3+} ions in matrices of various symmetries. Keeping on symmetry hosts, low symmetry hosts typically exert a crystal field containing more uneven components around dopant ions compared to high symmetry counterparts. In theory, when an ion occupies a crystalline site, there are uneven components of the crystal field. These uneven components enhance the electronic coupling between 4*f* energy levels and higher electronic configurations, and subsequently increase *f-f* transition probabilities of dopant ions. This is the reason why β-$NaYF_4$ (low symmetry host) shows better enhancement of UC efficiency in comparison to α-$NaYF_4$ (higher symmetry host). In addition, the decrease in cation size (or unit cell volume) of the host can cause an increase in the crystal field strength around dopants, leading to the improvement of UC efficiency. For instance, the bulk material of $NaYF_4$ (ionic radius of Y^{3+} = 0.090 nm, 6-fold) containing Er^{3+} and Yb^{3+} shows an UCL two times stronger than Er^{3+}/Yb^{3+} co-doped $NaLaF_4$ (ionic radius of La^{3+} = 0.103 nm, 6-fold) [1,48,147].

Nowadays, many new applications and technologies require a variety of properties of material which traditional materials have limited applicability. Composite materials, which consist of the combination of two phases or more with different physical or chemical properties, have attracted much attention in recent years because this type of material is typically light weight, flexible, high corrosion resistance, and impact strength. Because of these properties, composite materials have been considered as a replacement of classical materials used in aerospace industry, construction, and electrical and electronics [18]. In the field of UC phosphor, the composite material is one of the promising candidates for using as UC host material because it is a multifunctional/hybrid material which has a lot of benefits to improve optical properties and performance of UC phosphor. For example, single-phase nanocrystal UC phosphors may not meet the requirement of high-sensitivity and high-resolution of luminescence temperature sensors, but the composite material, ZnO-$CaTiO_3$:Er^{3+}/Yb^{3+}, which was reported by Tiwari *et al*. [148] can meet the selection criteria of temperature sensors. Additionally, not only the

direct way to use composite material as UC host for the fabrication of UC phosphor, but also the indirect way like the single-phase UC phosphor coated with composite material also increases the performance of UC phosphor and improves optical properties. For instance, Shan *et al*. [149] reported the synthesis and characterizations of $NaYF_4:Er^{3+}/Yb^{3+}@SiO_2$/Dye nano-composite for dual-modality NIR imaging and photo-thermal therapy. Their results showed that optical properties were found to enhance for nano-composite material ($NaYF_4:Er^{3+}/Yb^{3+}@SiO_2$ /Dye) compared to the single-phase material ($NaYF_4:Er^{3+}/Yb^{3+}$). In this dissertation, the ZnO-TiO_2 composite is selected and proposed as a new UC host material for the potential use in the fabrication of UC phosphor. This composite material is chosen due to many reasons which will be explained and discussed below.

The ZnO-TiO_2 composite system obviously consists of two most widely used oxides, zinc oxide (ZnO) and titanium dioxide (TiO_2). ZnO is a very attractive material and important semiconductor, having a wide band gap (3.37 eV at room temperature) and large excitonic binding energy of 60 milli-electron volt (meV) [150,151]. Also, ZnO is one of the most versatile and useful oxides because of its advantages such as high mechanical stability, high thermal conductivity, direct band gap, high electron mobility (~ 100 $cm^2V^{-1}s^{-1}$), high electrochemical stability, transparency in the visible range, non-toxicity, abundance in nature, bio-safety, and bio-compatibility [19,20,152]. Thus, ZnO is a multifunctional material which has been used in many applications, for example photocatalytic, sensors (e.g. gas sensor, chemical and biological sensors), pigment in paint, UC phosphors (as previously presented in Table 1.2 and 1.3) and can be used in semiconductor devices such as thin film transistors and thin film photovoltaic devices [19,150]. Additionally, Jayanti *et al*. [153] reported that doped ZnO or ZnO mixed with other oxides exhibit various properties, different types of morphologies, and have many more potential applications. In the case of TiO_2, it is one of the most extensively used metal oxides in the past several decades and has also received much attention from many researchers because of its excellent properties such as high efficient photoactive ability under UV light because it has a wide band gap ~3.0 eV (rutile phase) and ~3.2 eV (anatase phase) at room temperature [154], relatively high physical and chemical stability, non-toxicity, inexpensive, safety, environmentally benign, and more resistant to photo-corrosion than other commonly studied oxides [21,22,155]. For this reason, TiO_2 is a very significant material and has been widely applied in various fields of applications such as oxide supports, sensors, optoelectronic

materials, UC phosphors (as previously shown in Table 1.2 and 1.3), and especially as photocatalyst (e.g. used as based material for photocatalytic degradation of organic pollutants or decontamination, purification, and deodorization of air and wastewater) [21,22,156]. In addition, when TiO_2 as support is used to pair with other materials to form the composite, such material not only has multifunctional properties, but also apparently enhances some properties [157]. Herein, with these properties of both oxides, the combination of ZnO and TiO_2 semiconductors is considered as a new UC host material and the UC phosphor fabricated using this host might be one of the efficient low-cost UC phosphors with desirable optical properties.

ZnO-TiO_2 composite is considered as a promising UC host material due to its advantages such as low cost, thermal and chemical stability, and environmental friendliness. According to the phase diagram of ZnO-TiO_2 system (Figure 1.8), it has been reported that three main compounds exist in ZnO-TiO_2 system; spinel-type Zn_2TiO_4 (cubic), Ilmenite-type $ZnTiO_3$ (hexagonal), and $Zn_2Ti_3O_8$ (cubic, low temperature form of $ZnTiO_3$). The existence of each compound depends on ZnO/TiO_2 mixing ratio and firing temperature used. Among these compounds, the noteworthy product is Zn_2TiO_4 that is a high thermal stability phase due to its inverse spinel structure. Besides, Zn_2TiO_4 is a steady phase (from room temperature to its melting point (1550 °C [26])) and easily formed by the reaction between ZnO and TiO_2, even if the system has low amount of ZnO.

Focusing on Zn_2TiO_4 phase, it has a faced-centered cubic (FCC) unit cell belonging to space group Fd-3m with a = 0.84608 nm [158] and the atomic arrangement in its crystal structure become more ordered at high temperature by the incorporation of TiO_2 [159]. The Zn_2TiO_4 has an inverse spinel structure (AB_2O_4), where Zn atoms occupy all A-sites (tetrahedral site) and the half of B-sites (octahedral site), and Ti atoms occupy the half of B-sites. The A-site is generally occupied by a larger cation and B-site is occupied by a smaller cation. The crystal structure of inverse spinel Zn_2TiO_4 phase is shown in Figure 1.9 which is created by VESTA (open-source software) [160].

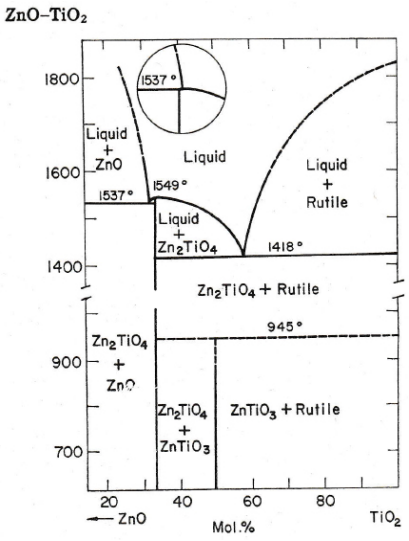

Figure 1.8. Phase diagram of ZnO-TiO_2 system. The inset shows alternative incongruent melting of Zn_2TiO_4. Reproduced with permission from [27]. Copyright (1964) The American Ceramic Society, Inc.

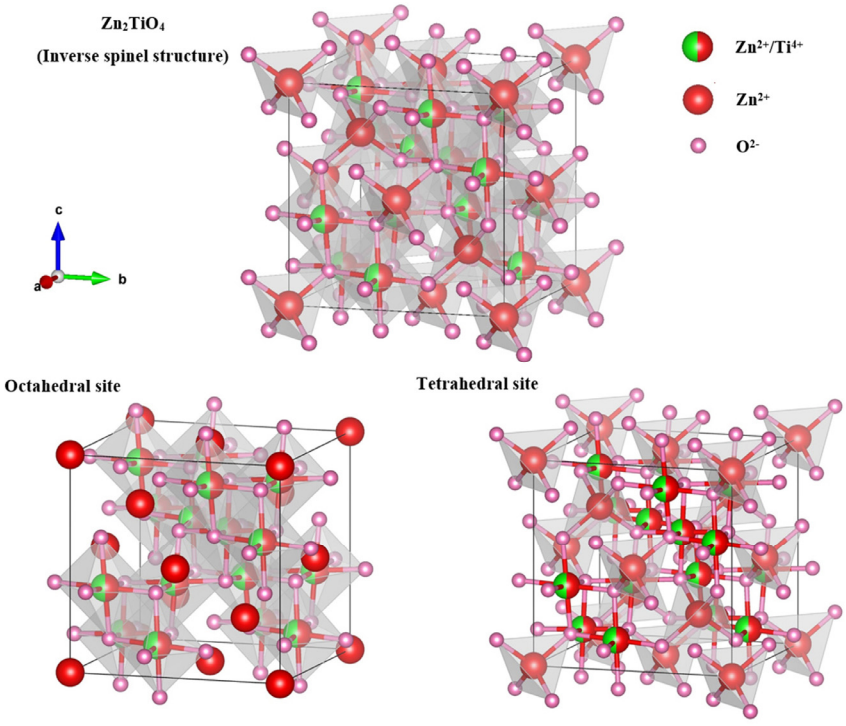

Figure 1.9. The crystal structure of inverse spinel Zn_2TiO_4 phase. Reproduced with permission from [161]. Copyright (2017) Elsevier Ltd and Techna Group S.r.l.

As reported by Kim *et al*. [159], in the system in which Ti^{4+} may remain and due to the bigger size of Zn atoms which has the tendency to occupy tetrahedral sites, therefore, surplus Ti^{4+} with the smaller size should occupy octahedral sites. Since extra Ti^{4+} occupy octahedral site, the vacant Zn site (V''_{Zn}) must appear in tetrahedral site to keep the charge balance [158,159,162]. Based on this feasibility of the appearance of $V''_{Zn(tet)}$ the incorporation of surplus Ti^{4+} into the Zn_2TiO_4 matrix can be manifested by equation (1.3).

$$2TiO_2 \left(\text{in } Zn_{(tet)}(ZnTi)_{(oct)}TiO_4\right) \rightarrow V''_{Zn(tet)} + Ti^{\cdot\cdot}_{Zn(oct)} + Ti_{Ti(oct)} + 4O^{x}_{o} \quad (1.3)$$

According to the properties of $ZnO\text{-}TiO_2$ composite and its products especially Zn_2TiO_4 phase, many researches on $ZnO\text{-}TiO_2$ composite have been conducted and studied for applying in various applications such as nanofiber photocathode [163] and photocatalysis [164]. In addition, Zn_2TiO_4 shows great potential for being the good optical host because it has high value of refractive index n = 2.1 [28] and low phonon energy around 721 cm^{-1} [29], which control part of energy losses in the electron toward phonon energy transfer and other non-radiative processes [30]. Therefore, Zn_2TiO_4 phase could be one of the candidate hosts for UCL applications. Up to now, a series of reports regarding UCL from $ZnO\text{-}TiO_2$ composite phosphors showed only certain results in green and red emission bands which were observed from Er^{3+}/Yb^{3+} co-doped $ZnO\text{-}TiO_2$ composite prepared by various preparation methods. These reports are reviewed and summarized in Table 1.4.

Table 1.4. A review of all published reports concerning $ZnO\text{-}TiO_2$ composite as UC host material (as of May 2018, excluding the reports presented by this study).

Host material	Dopant	Preparation method	Emission	Reference
$ZnO\text{-}TiO_2$	Er^{3+}/Yb^{3+}	Solid-state reaction	Orange	31
			Red	32
		Metal-organic decomposition	Orange	33-35
			Green/Red	36

1.6 Methods of preparation of upconversion phosphor

A variety of methods to synthesize UC phosphors has emerged due to the challenge for obtaining the efficient products with great physical and chemical properties such as monodispersed particles with a narrow size-distribution, uniform shape, phase-purity, and high

aqueous solubility. Various chemical techniques including solid-state reaction method, coprecipitation, thermal decomposition, hydrothermal analysis, sol-gel method, and combustion synthesis, have been employed for fabricating the UC phosphor. Each method has its own advantages and disadvantages which will be shortly summarized in Table 1.5 [1,165]. Even though there are many methods provided by many researchers, but most methods use organic solvent as the medium in the synthesis which it is compulsory to use additional methods for taking it out. Therefore, the surface modification is required for improving photo-stability and rendering the product to be water-soluble for applying the product to various advanced applications such as biological applications [165]. Methods used for surface modification will not be explicated in this dissertation because two main methods presented in this study provide ethanol and deionized water as the medium in the synthesis which they can be eliminated by sintering at high temperature. In this part, the most widely used fundamental methods for preparing general UC phosphors, consisting of solid-state reaction method, combustion synthesis, and sol-gel processing will be explained and discussed in detail.

Table 1.5. A review of some common synthetic methods for the preparation of UC phosphors. A brief description of each process is provided along with the advantages and disadvantages, including the examples of UC phosphor host used in each technique.

Method		**Brief description**
Arrested precipitation	Process	Poorly soluble compounds precipitated within a template under controlled atmosphere.
	Advantages	Simple and fast reaction. Time and cost effective. High temperature or pressure are not required.
	Disadvantages	Requires control of particle shape and size. Post-annealing and calcination step required, resulting in the aggregation of particles.
	Examples (Hosts)	$LaPO_4$ [166], Y_2O_3 [167], $LuPO_4$ and $YbPO_4$ [168]
Coprecipitation	Process	Soluble compounds are collected from the solution during the formation of precipitates under controlled atmosphere.
	Advantages	Simple synthetic procedure. Fast reaction. There is no need for costly equipment and stringent reaction conditions.

Continued…

Method		Brief description
Coprecipitation	Disadvantages	Post-annealing and calcination step required, resulting in the aggregation of particles.
	Examples (Hosts)	LaF_3 [169], $NaYF_4$ [170]
Flame synthesis	Process	Reactants are gas-phase material which is released through the flame source. The crystalline product is formed by controlling amount of heat energy.
	Advantages	High-purity product. Time and cost saving. Readily scalable.
	Disadvantages	Problems about synthesizing multi-component materials. The aggregation of particles is observed.
	Examples (Hosts)	Y_2O_3 [171], La_2O_3 and Ga_2O_3 [172]
Hydro(solvo) thermal synthesis	Process	The solvent which is used to facilitate the interaction between precursors during the synthesis is utilized under moderate to high pressures and temperature above its critical point to increase the solubility of precursors and to speed up the reaction between precursors. (If water is used as solvent, the method is called "Hydrothermal synthesis".)
	Advantages	Cheap raw materials. No post-heat treatment. Highly crystalline phases are produced at much lower temperatures compared to other methods. Excellent control over particle size and shape.
	Disadvantages	Specialized reaction vessels such as autoclaves required.
	Examples (Hosts)	$NaYF_4$ [173], LaF_3 [174]
Microwave assisted synthesis	Process	Heating reaction mixtures by microwave radiation at frequency range around 0.3-300 GHz.
	Advantages	Energy consumption saving. Increased reaction rate. High degree of reproducibility.
	Disadvantages	Specialized microwave source required. The solvent choice is limited because some solvents may be effectively heated by microwave radiation.
	Examples (Hosts)	$NaYF_4$ [175,176], $LiYF_4$ [175]

Continued…

Method		Brief description
Micro-emulsion or reverse micelle method	Process	An isotropic liquid mixture containing oil, water, and surfactant forms as micro-emulsion and then it is controlled until aqueous phase is encapsulated by surfactant (micelles method). Further, the organic solvent which acts as nanoscale reactor is used to de-capsulate for obtaining the product (reverse micelle method).
	Advantages	Homogenous monodisperse products. High degree of reproducibility. Control over particle size and morphology of produced materials.
	Disadvantages	Limited production capacity because the product relies on the amount of aqueous phase that can be solubilized, the encapsulation process, and precursor concentrations. Post treatment required.
	Examples (Hosts)	Y_2O_3 and Gd_2O_3 [177], YVO_4 [178]
Thermal decomposition	Process	Decomposition of a substance at the temperature in which its chemical bonds is broken.
	Advantages	Excellent control over particle size. High quality monodisperse products. Relatively short reaction time.
	Disadvantages	Expensive. Air-sensitive metal precursors. Toxic volatile by-products. Requires the system to be continually purged with an inert gas.
	Examples (Hosts)	$NaYF_4$ [85], LaF_3 [174]

1.6.1 Solid-state reaction method

In general, this is the most extensively used method for synthesizing almost all phosphors. Theoretically, the solid-state reaction method provides a large range of selection of raw materials (solid form) such as oxides and oxy-sulfides. Since solids do not react with another solid at room temperature, therefore, this method is started by the reaction between starting solid materials at high temperature which the reaction takes place at appreciable rate (typically, starting materials are mixed at temperature that is more than two-thirds of the melting point of lowest melting reactant. Hence, considerable aspects that are responsible for this method are thermodynamic and kinetic factors. The fabrication process of UC phosphors via this method can be explained as follows. Firstly, high purity starting solid materials of host material,

sensitizer, and activator are mixed to obtain homogenous mixture by using solvent. Subsequently, there are different processes to produce the product that could be in the form of powder or molded materials (e.g. pellet). For example, in the case of pellet form, the raw mixture should be dried at room temperature or in drying oven at low temperature (< 100 °C) to evaporate the solvent. Further, the dried mixture is passed to the molding process (e.g. pelletization) and then fired at high temperature in a container to get the final product. For the powder form, with the identical drying process, the dried mixture can be fired at high temperature in a container immediately and the final product will be obtained after grounding by coarse crushing machine such as crusher, ball mill, or vibration mill. Considering the used solvent especially organic solvent, phosphors prepared by solid-state reaction method do not show the presence of any residual organic solvent due to the high firing temperature used eliminating all remaining organic solvent components.

Concentrating on reaction processes between a host material and dopant compositions (sensitizer and activator ions), there are two feasible reactions in phosphors synthesized by this method. One is the incorporation of dopants into the completely synthesized host material. Second is when a host material is forming, dopants incorporate simultaneously into the forming host. The simple schematic synthetic process of UC phosphors by solid-state reaction method is shown in Figure 1.10. In most cases, the first mechanism is usually preferable for UC phosphors. For instance, in the preparation of ZnO-TiO_2: Er^{3+}/Yb^{3+} [31], ZnO powder, TiO_2 powder, Er_2O_3, and Yb_2O_3 were mixed together and blended by ethanol to get homogeneous mixture. Subsequently, the mixture was dried at room temperature and followed by making as the pellet. Then, this molded material was fired at optimum temperature 1200 °C for 4 h. During the firing process, Zn_2TiO_4 crystal was formed, and Er^{3+} and Yb^{3+} were incorporated into the formed host crystal matrix by substituting one of the host lattice cations. In the case of second possibility, there is one example that is clearly observed about this phenomenon which is detected by analyzing manganese (Mn) activated Zn_2SiO_4 phosphor. According to the Takagi's report [179], this phosphor was prepared by three staring materials, ZnO, SiO_2, and $MnCO_3$ powders, and the second behavior mentioned above regarding the formation of phosphors was detected by differential thermal analysis (DTA). This analyzed result showed that the raw material, ZnO and SiO_2, initially reacted at 770 °C where the reaction proceeded by the

diffusion of ZnO into the SiO_2 lattice. Subsequently, Mn ions incorporated into the forming lattice concurrently in proportion to the amount of synthesized Zn_2SiO_4.

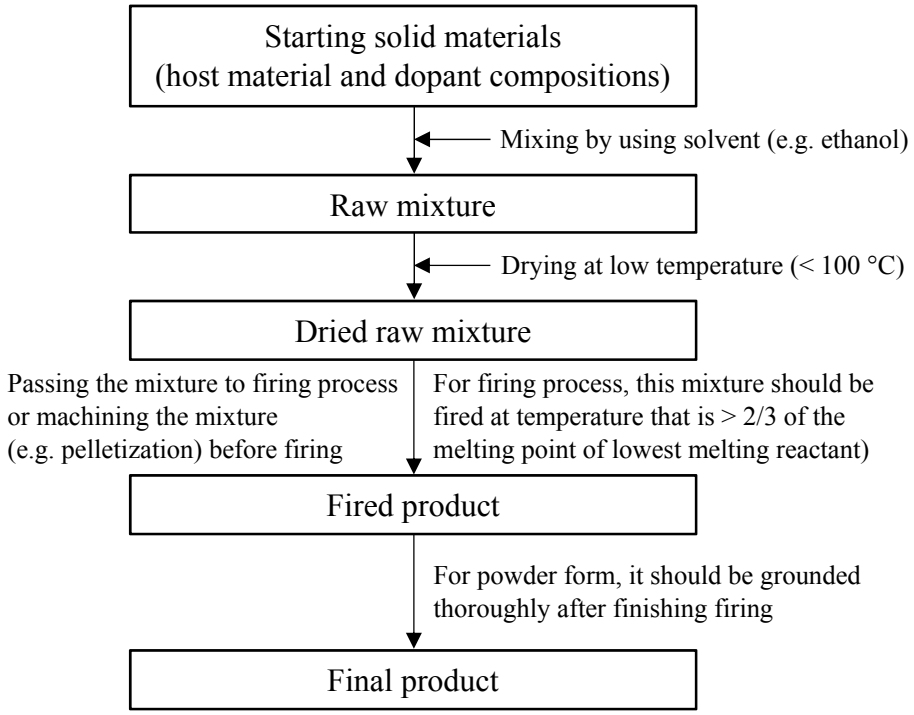

Figure 1.10. Schematic synthetic process of UC phosphors by solid-state reaction method.

Considering the strong point and drawback of solid-state reaction method, this method is simple to accomplish, raw materials are readily available at low cost, and the reaction is clean because there are no any toxic chemical elements involved. Hence, this method is an eco-friendly method because toxic products or undesirable by-products are not produced. Additionally, the product is in the solid form with high thermodynamic stability and structurally pure due to the high firing temperature used. For the disadvantage, due to the high operating temperature, this method could be an expensive method, even if raw materials are readily available at low cost. In theory, the formation of the products prepared by this method is diffusion limited, leading to incomplete reaction, some loss of reactants, and compositionally inhomogeneous products [16]. Also, the agglomeration of particles is observed due to high firing temperature used and if the powder form is the final target product, this method requires the crushing machine to separate the agglomerated particles. Because of the agglomeration of particles, the final product will be in the form of polycrystalline structure, thus, large single crystals are not obtained by this

method, and desired microstructure is not achieved either. It should be noted that the average particle size of UC phosphors prepared by this method is larger than 5 μm. Nowadays, the solid-state reaction method is still widely used for preparing various UC phosphors such as ZnO-TiO_2: Er^{3+}/Yb^{3+} [31], Gd_2O_3: Er^{3+}/Yb^{3+} [180], and $Ba_3Lu_4O_9$: Er^{3+}/Yb^{3+} [181].

1.6.2 Combustion synthesis

Combustion synthesis is a rapid technique for producing UC phosphors through the controlled incineration. Products prepared by this method are normally chemically homogeneous, have less impurities, and have higher surface areas compared to solid-state reaction method. In general, this method is one of the liquid phase synthesis methods which means that main components (host material and dopant compositions) can be precisely controlled and mixed to acquire the homogeneous mixture. However, this method involves the burning of reactant solutions, thus, such solutions not only contain host material and dopants but also include a fuel for completing the mechanism in the initial stage. For this reason, starting materials of this method are usually salts (e.g. dissolved metal nitrates or acetates for both host material and dopants) as oxidant and a fuel (e.g. urea, glycine, and ethylene glycol) as reductant.

The formation process of the products prepared by this method is explained as follows. Firstly, all oxidants are mixed using deionized water and followed by the addition of proper amount of fuel. Further, this mixture is stirred and heated at low temperature (< 100 °C) to free the water until the solution changes to viscous sol. In this step, bubbles and heat occur because of the exothermic redox reaction between oxidants and fuel. After that, the viscous sol is inserted into the furnace for pre-heating at around 300-500 °C and the combustion reaction between oxidants and fuel takes place energetically and gives rise to some gaseous by-products such as CO_2 and N_2. When the combustion is complete, and the sample is cooled down to room temperature, the resultant sample is crushed and then fired at high temperature (> 800 °C) depending on various conditions planned, and the reaction time is usually less than 10 minutes. The simple schematic synthetic process of UC phosphors by combustion synthesis is shown in Figure 1.11.

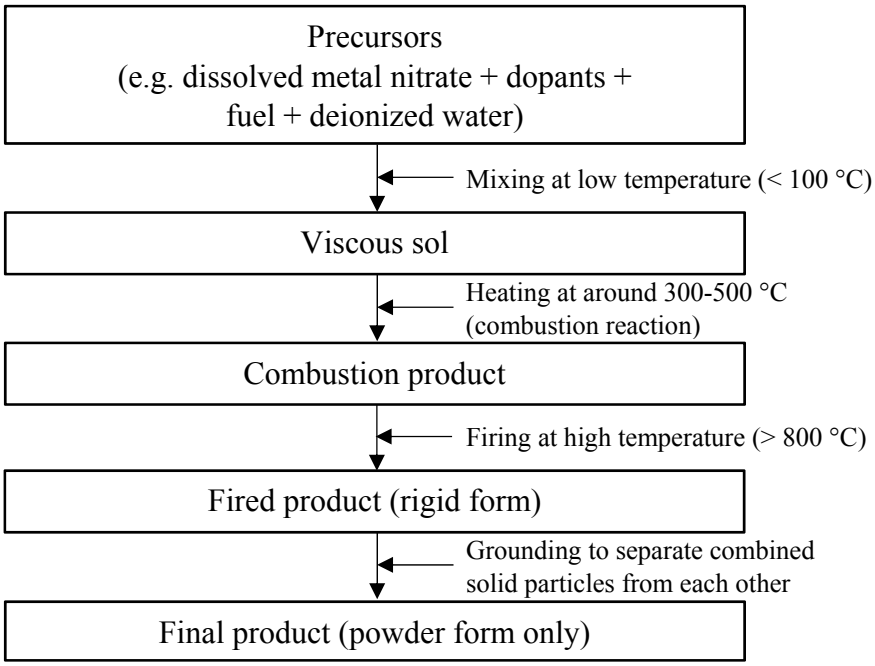

Figure 1.11. Schematic synthetic process of UC phosphors by combustion synthesis.

Taking into account the strong point and drawback of combustion synthesis, this method is very rapid synthesis, cost effective, and low energy cost because it requires low firing temperature to start the reaction and high temperature with short reaction time to obtain the final product. Besides, due to the short reaction time used at high temperature, the nanosized product can be obtained. In the case of disadvantage, the particle shape, size, and purity are difficult to control, and the product fired at high temperature is usually transformed to rigid agglomerates which are not easily separated. Nowadays, the combustion synthesis is still extensively used for preparing various UC phosphors such as Gd_2O_3: Er^{3+}/Yb^{3+} [180], $CaZr_4O_9$: Er^{3+}/Yb^{3+} [182], and $LaAlO_3$: Er^{3+}/Yb^{3+} [183].

1.6.3 Sol-gel processing

Sol-gel processing is a solution-based chemical process which is widely used in the production of oxides and fluorides nanoparticles. Also, this method is a considerable based process for various methods of preparation of UC thin film materials, for example ZnO-TiO_2: Er^{3+}/Yb^{3+} prepared by metal-organic decomposition (MOD) [33-36] and YF_3: Er^{3+}/Yb^{3+} prepared by pulsed liquid injection metal-organic chemical vapor deposition (PLI-MOCVD) [184]. For the basic process of sol-gel processing, it begins with a liquid solution of metal alkoxide precursors

that forms a sol phase via hydrolysis when it is mixed with deionized water or alcohol under acidic condition (the reaction rate is faster than basic condition), showing the colloidal of solid particles suspended in liquid and giving rise to by-products in the form of hydroxide compounds. During the process, dopants are also added and mixed together. Further, agglomerates of all precursor particles are formed by the gelation process, creating a larger macromolecule network which is called gel phase. Subsequently, the gel is fired at low temperature around 500-800 °C to evaporate the water and remove organics (thermal treatment process), resulting in the organic-free mixture in powder form. After that, this powder is fired at appropriate temperature to get final product. The simple schematic synthetic process of UC phosphors by sol-gel processing is shown in Figure 1.12.

To clearly understand the complex precursors of this method, starting materials and mixing processes of a UC phosphor prepared via this method will be provided as follows. According to a report of Vega *et al*. [185], $BaTiO_3$: Er^{3+}/Yb^{3+} phosphor was synthesized using tetrabutyl titanate (TBT), barium acetate, erbium nitrate, ytterbium nitrate, acetic acid, acetylacetone, and deionized water. At first, barium acetate was mixed with acetic acid at suitable stoichiometric ratio and then this solution was added drop-wise to the solution of TBT diluted by acetylacetone. Subsequently, this liquid mixture was heated at 50 °C for 2 h under continuous stirring to form titania sol. Later, erbium nitrate and ytterbium nitrate were added to titania sol and heated at 100 °C for 24 h to form gel phase and powder of dried barium erbium-ytterbium titanate, respectively. Eventually, the final product was obtained by following steps, the dried powder was grounded in an agate mortar, placed in a combustion boat, and fired at 1000 °C for 2 h in a muffle furnace.

Considering the advantage and disadvantage of sol-gel processing in comparison to solid-state reaction method and combustion synthesis, this method produces the product with better physical and chemical properties than those two methods, for example the homogenous particle growth, having small particle size (particularly nanosized particles), and high uniformity of dopants distribution in the host material. Additionally, it is also very easy to handle and set up, cost effective, and effortless control processing over the stoichiometry of resultant product. Therefore, this method has been using broadly in the UC phosphor research. However, some drawbacks of this method also exist, for instance little control over particle size and shape, the

treatment process (high temperature annealing or calcination) required due to the use of organic reagents which may cause the product contamination (e.g. carbon), and by using high temperature, undesirable properties of the product may occur (e.g. particle aggregation).

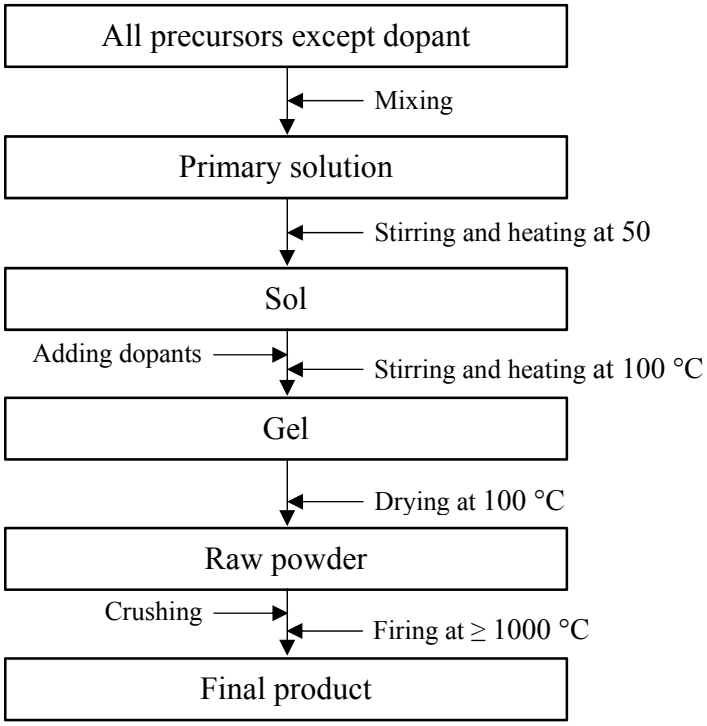

Figure 1.12. Schematic synthetic process of UC phosphors by sol-gel processing.

According to the ZnO-TiO_2 composite as a host material for UC phosphor, there are only six reports involved and in two of them, ZnO-TiO_2 UC phosphor is prepared by solid-state reaction method [31,32]. As discussed in these two reports, the authors suggest that ZnO-TiO_2 composite is a potential material for being the UC host. However, the existed reports demonstrate only the UCL properties of Er^{3+}/Yb^{3+} co-doped ZnO-TiO_2 composite. Therefore, the initial stage of this dissertation will provide the following research regarding ZnO-TiO_2 composite doped with Ho^{3+} and Yb^{3+} prepared by the solid-state reaction method to confirm the possibility of using ZnO-TiO_2 composite not only as UC host but also its performance when it is doped by other dopants. Later, by considering the disadvantages of solid-state reaction method such as diffusion limited, incomplete reaction, some loss of reactants, and compositionally inhomogeneous products, including taking into account pros and cons of combustion synthesis and sol-gel processing, the new and easy preparation method, namely powder-solution mixing

method, has been designed and proposed to increase the strong points of the product and overcome the drawbacks of these three most widely used preparation methods. This method contains both solid phase and liquid phase of inorganic reactants as precursor and deionized water as solvent to produce the compositionally homogeneous products without any contamination that may come from organic precursors and solvents. This new synthetic method will be explained in detail in the experimental section of Chapter III.

1.7 Applications of upconversion phosphor

Over the past decade, the research on UC phosphors has made gigantic progresses in many applications such as solar cells [16,186-189], displays [16,189,190], and photocatalysis [16,189,191]. However, most interesting applications of UC phosphors are in the field of biomedical such as imaging, sensing, and cancer therapy, because of their outstanding merits, for example multi-color emission capability under single-wavelength excitation, high signal to noise ratio, low cytotoxicity, and high chemical- and photo- stability [83]. Hence, in this part, two most popular types of biomedical technology, *in vivo* detection and *in vivo* imaging, including some examples of the UC phosphor used in these applications will be discussed as follows.

In the *in vivo* detection applications, UC phosphors have been used as luminescent reporter in a variety of *in vivo* assays including immunoassays, bio-affinity assays, and DNA hybridization assays, which offers dramatically enhanced signal-to-noise ratio and thus improved detection limits compared to conventional reporters [1,83]. For example, Hampl *et al*. [192] reported a detection limit of 10 picogram human chorionic gonadotropin in a 100-microliter (μL) sample by using submicron-sized Y_2O_2S:Yb/Er particles in immunochromatographic assays. Simultaneous detection of multiple analyses using multicolor UC nanocrystals was demonstrated by Niedbala *et al*. [193]. In a lateral flow based competitive inhibition assay, a selection of drugs containing low concentrations of amphetamine, methamphetamine, phencyclidine (PCP), and opiates was detected in a single multiplexed assay strip. To achieve the multiplexed detection, antibodies for PCP and amphetamine were conjugated to green-emitting particles, while methamphetamine and morphine were conjugated to blue-emitting particles. Similarly, Ukonaho *et al*. [194] demonstrated a detection limit of 0.53 ng/L free prostate-specific antigens by using Y_2O_2S:Yb/Er particles in two-site immunoassay.

For the *in vivo* imaging, the non-toxic UC phosphor is a very promising material for bio-imaging applications. In principle, UC phosphors generally contain less toxic elements. With their photo-stable luminescence and minimized background auto-luminescence by NIR excitation, UC phosphors show great potential as alternatives to organic fluorophores and quantum dots for *in vivo* bio-imaging [1,83]. For example, an intriguing recent development was demonstrated by Chatterjee *et al*. [195] for *in vivo* imaging in anesthetized Wistar rats by using 50-nm $NaYF_4$:Yb/Er nanoparticles. These rats were injected with the nanoparticles under the skin in the groin and upper leg regions. Using a combination of simple optical techniques and a 980-nm NIR laser, these UC nanoparticles can be detected up to 10 mm beneath the skin, far deeper than depths managed using conventional equipment based on quantum dots. This method holds the promise of providing a new technique for imaging tissue structures at different depths and for performing minimally invasive detection.

1.8 Research objective

The research described in the present work is based on the determination of introducing and developing novel UC phosphors, highlighting the fabrication of new efficient UC phosphors with good physical and optical properties from low-cost precursors, proposing a new and easy synthetic route which is able to increase the strong points of the product, and overcome the drawbacks of conventional preparation methods like solid-state reaction, and targeting to produce the homogeneous phase of UC phosphors because this characteristic can give rise to the high regularity of the distribution of UCL intensity. In this study, the ZnO-TiO_2 composite is selected as a UC host material due to the reasons mentioned earlier and one of the obvious reasons is that there are a few reports on the systematic study of the ZnO-TiO_2 composite UC phosphor. The detailed objectives of this study are:

1. To explore the scope of phosphors, especially UC phosphor.
2. To propose the use of ZnO-TiO_2 composite as a new host material for the fabrication of UC phosphor.
3. To explore a novel simple preparation method for generation of homogenous phase of UC phosphor.
4. To prepare and characterize ZnO-TiO_2 composite UC phosphor containing different sensitizer-activator pairs of ions.

5. To find out the effect of various parameters; firing temperature, ZnO/TiO_2 mixing ratio, and dopant concentration ranges, on the structural and UCL properties.
6. To study the UCL characteristics under a 980-nm laser excitation and examine the dependent UCL intensity on the change in laser pump power for the suggestion of possible UC mechanism.
7. To investigate the potential site preference of dopants in target UC host crystal matrix.
8. To synthesize the $ZnO\text{-}TiO_2$ composite UC phosphor by solid-state reaction method and a new proposed method and compare its UCL characteristics to find out the suitable method of preparation that provides the product with high regularity of the distribution of UCL intensity.

1.9 Dissertation outline

This dissertation is divided into six chapters. First chapter provides general introduction and basic theories involved in research background and research objective.

In Chapter II, $ZnO\text{-}TiO_2$ composite doped with Ho^{3+} and Yb^{3+} is examined by preparing via solid-state reaction method to confirm the possibility of using $ZnO\text{-}TiO_2$ composite not only as UC host material but also its performance when it is doped by other dopants. Effects of ZnO/TiO_2 mixing ratio, Ho^{3+} and Yb^{3+} doping concentrations, and their ratios on the crystal phase and UCL properties are methodically investigated. To understand the UC mechanism of Ho^{3+}/Yb^{3+} co-doped $ZnO\text{-}TiO_2$ composite prepared by solid-state reaction method, the dependence of UC emission intensity on different excitation powers is calculated and discussed in detail. Also, the UC mechanism that might be responsible for this system is proposed and described based on pumping power dependence of UC emission intensity.

In Chapter III, $ZnO\text{-}TiO_2$ composite doped with Er^{3+} and Yb^{3+} is studied by the new simple method, namely powder-solution mixing method, to produce the UC phosphor with homogeneous phase in the form of powder. At first, raw materials and raw mixtures are analyzed by TG-DTA measurement to demonstrate the thermal process. Subsequently, the effects of firing temperature, ZnO/TiO_2 mixing ratio, Er^{3+} and Yb^{3+} doping concentrations and their ratios on the crystal phase, crystal morphology, and UCL properties are systematically investigated. Further, the XRF analysis is performed to confirm the actual mixing ratio of the

final products. Later, the study on the analysis of possible site preference of Er^{3+} and Yb^{3+} in the host crystal matrix is explained and discussed in detail. In addition, the simple chemical formula equations of Er^{3+} and Yb^{3+} site preferences are developed for the rendition of the experimental results. Also, the UC mechanism that might be responsible for this system is proposed and designated based on pumping power dependence of UC emission intensity. Eventually, the comparison between ZnO-TiO_2: Er^{3+}/Yb^{3+} prepared by solid-state reaction and powder-solution mixing methods is studied and the results are discussed in detail.

In Chapter IV, the following research, ZnO-TiO_2 composite doped with Ho^{3+} and Yb^{3+} prepared by powder-solution mixing method is investigated. Holmium (III) nitrate pentahydrate and raw mixtures are analyzed by TG-DTA measurement to demonstrate the thermal process. The effects of firing temperature, ZnO/TiO_2 mixing ratio, Ho^{3+} and Yb^{3+} doping concentrations and their ratios on the crystal phase, crystal morphology, and UCL properties are methodically examined. XRF analysis is performed to confirm the actual mixing ratio of the final products. The study on the analysis of possible site preference of Ho^{3+} and Yb^{3+} in the host crystal matrix is described and discussed in detail. Additionally, the simple chemical formula equations of Ho^{3+} and Yb^{3+} site preferences are proposed for the interpretation of the experimental results. The UC mechanism that might be accountable for this system is proposed and designated based on pumping power dependence of UC emission intensity. Finally, the comparison between ZnO-TiO_2: Ho^{3+}/Yb^{3+} prepared by solid-state reaction and powder-solution mixing methods is considered and the results are discussed in detail.

In Chapter V, the following research, ZnO-TiO_2 composite doped with Tm^{3+} and Yb^{3+} prepared by powder-solution mixing method is considered. The effects of ZnO/TiO_2 mixing ratio, Tm^{3+} and Yb^{3+} doping concentrations and their ratios on the crystal phase, crystal morphology, and UCL properties are methodically examined. The study on the analysis of possible site preference of Tm^{3+} and Yb^{3+} in the host crystal matrix is interpreted and discussed in detail. Additionally, the simple chemical formula equations of Tm^{3+} and Yb^{3+} site preferences are proposed for the rendition of the experimental results. Lastly, the comparison of ZnO-TiO_2 composite UC phosphors prepared by various methods is summarized and discussed in detail.

The summary of all significant results and recommendations for future work are given in the final chapter (Chapter VI).

References

[1] F. Wang, X. Liu, *Chem. Soc. Rev.*, **38** (2009) 976-989.

[2] A. Stepuk, G. Casola, C.M. Schumacher, K.W. Krämer, W.J. Stark, *Chem. Mater.*, **26** (2014) 2015-2020.

[3] T. Sun, F. Ai, G. Zhu, F. Wang, *Chem-Asian J.*, **13** (2018) 373-385.

[4] M. Lin, Y. Zhao, S. Wang, M. Liu, Z. Duan, Y. Chen, F. Li, F. Xu, T. Lu, *Biotechnol. Adv.*, **30** (2012) 1551-1561.

[5] W. Zheng, P. Huang, D. Tu, E. Ma, H. Zhu, X. Chen, *Chem. Soc. Rev.*, **44** (2015) 1379-1415.

[6] R. Deng, F. Qin, R. Chen, W. Huang, M. Hong, X. Liu, *Nat. Nanotechnol.*, **10** (2015) 237-242.

[7] G. Chen, H. Ågren, T.Y. Ohulchanskyy, P.N. Prasad, *Chem. Soc. Rev.*, **44** (2015) 1680-1713.

[8] F. Auzel, *Chem. Rev.*, **104** (2004) 139-174.

[9] L. Liang, Y. Yulin, Z. Mi, F. Ruiqing, Q. Lele, W. Xin, Z. Lingyun, Z. Xuesong, H. Jianglong, *J. Solid State Chem.*, **198** (2013) 459-465.

[10] L. Wang, M. Lan, Z. Liu, G. Qin, C. Wu, X. Wang, W. Qin, W. Huang, L. Huang, *J. Mater. Chem. C*, **1** (2013) 2485-2490.

[11] K. Yamamoto, M. Fujii, S. Sowa, K. Imakita, K. Aoki, *J. Phys. Chem. C*, **119** (2015) 1175-1179.

[12] H. Lin, G. Meredith, S. Jiang, X. Peng, T. Luo, N. Peyghambarian, E.Y.B. Pun, *J. Appl. Phys.*, **93** (2003) 186-191.

[13] G.-S. Yi, G.-M. Chow, *Chem. Mater.*, **19** (2007) 341-343.

[14] X. Wang, S. Xiao, Y. Bu, J.W. Ding, *J. Alloy. Compd.*, **477** (2009) 941-945.

[15] Z. Wang, J. Feng, M. Pang, S. Pan, H. Zhang, *Dalton T.*, **42** (2013) 12101-12108.

[16] R.-S. Liu, Phosphors, Up conversion Nano Particles, Quantum Dots and Their Applications (Volume 2), Springer Science+Business Media Singapore, Singapore (2016).

[17] H. Huang, H. Zhou, J. Zhou, T. Wang, D. Huang, Y. Wu, L. Sun, G. Zhou, J. Zhan, J. Hu, *RSC Adv.*, **7** (2017) 16777-16786.

[18] K.K. Kar, Composite Materials: Processing, Applications, Characterizations, Springer-Verlag Berlin Heidelberg (2017).

[19] D. Ramírez-Ortega, A.M. Meléndez, P. Acevedo-Peña, I. González, R. Arroyo, *Electrochim. Acta*, **140** (2014) 541-549.
[20] M.M. Rahman, A.J.S. Ahammad, J.-H. Jin, S.J. Ahn, J.-J. Lee, *Sensors*, **10** (2010) 4855-4886.
[21] Y. Liu, X. Wang, F. Yang, X. Yang, *Micropor. Mesopor. Mat.*, **114** (2008) 431-439.
[22] J. Gao, X. Luan, J. Wang, B. Wang, K. Li, Y. Li, P. Kang, G. Han, *Desalination*, **268** (2011) 68-75.
[23] G. Marci, V. Augugliaro, M.J. López-Muñoz, C. Martín, L. Palmisano, V. Rives, M. Schiavello, R.J.D. Tilley, A.M. Venezia, *J. Phys. Chem B*, **105** (2001) 1033-1040.
[24] B. Jiao, M. Li, X. Zhang, X. Wang, *Adv. Mater. Res.*, **652-654** (2013) 622-627.
[25] B.L. Zhu, C.S. Xie, W.Y. Wang, K.J. Huang, J.H. Hu, *Mater. Lett.*, **58** (2004) 624-629.
[26] E.Y. Tonkov, High Pressure Phase Transformations: A Handbook, CRC Press, Boca Raton, Florida (1992).
[27] E.M. Levin, C.R. Robbins, H.F. McMurdie, Phase Diagram for Chemists Volume I (Figures 1-2066), The American Ceramic Society, Inc., Columbus, Ohio (1964).
[28] L. Li, Y. Fan, D. Wang, G. Feng, D. Xu, *Cryst. Res. Technol.*, **46** (2011) 475-479.
[29] L. Li, F. Li, T. Cui, Q. Zhou, D. Xu, *Phys. Status Solidi A*, **209** (2012) 2596-2599.
[30] W.M. Yen, S. Shionoya, H. Yamamoto, Phosphor Handbook, Second Edition, CRC Press, Boca Raton, Florida (2006).
[31] H.N. Luitel, K. Ikeue, R. Okuda, R. Chand, T. Torikai, M. Yada, T. Watari, *Opt. Mater.*, **36** (2014) 591-595.
[32] K. Ohyama, T. Nonaka, T. Kanamori, S.-I. Yamamoto, 22nd International Workshop on Active-Matrix Flatpanel Displays and Devices (AM-FPD) (2015) 89-90.
[33] S.-I. Yamamoto, K. Ohyama, T. Nonaka, T. Kanamori, 21st International Workshop on Active-Matrix Flatpanel Displays and Devices (AM-FPD) (2014) 271-272.
[34] T. Nonaka, T. Kanamori, K. Ohyama, S.-I. Yamamoto, *Jpn. J. Appl. Phys.*, **54** (2015) 03CA02.
[35] T. Nonaka, S.-I. Yamamoto, *T. MRS Jap.*, **42** (2017) 57-60.
[36] T. Nonaka, T. Ban, S.-I. Yamamoto, *T. MRS Jap.*, **42** (2017) 139-143.
[37] M. Serényi, T. Lohner, G. Sáfrán, J. Szívós, *Vacuum*, **128** (2016) 213-218.

[38] Y. Ando, D. Kindole, Y. Noda, R.N. Mbiu, B.K. Kosgey, S.M. Maranga, A. Kobayashi, *Vacuum*, **136** (2017) 203-208.
[39] D. Lardner, Treatise on Heat, Printed for Longman, Rees, Orme, Brown, Green & Longman, London (1833).
[40] E. Wiedemann, *Ann. Phys.-Leipzig*, **34** (1888) 446-463.
[41] N.T. Kalyani, H. Swart, S.J. Dhoble, Principles and Applications of Organic Light Emitting Diodes (OLEDs), Woodhead Publishing, Cambridge (2017).
[42] H.J. Round, *Electr. World*, **49** (1907) 308.
[43] G. Destriau, *J. Chem. Phys.*, **33** (1936) 587-625.
[44] R. Withnall, J. Silver, P.G. Harris, T.G. Ireland, P.J. Marsh, *J. Soc. Inf. Display*, **19** (2011) 798-810.
[45] S.W.S. Mckeever, Thermoluminescence of Solids, Cambridge University, Cambridge (1985).
[46] R.C. Ropp, Luminescent and the Solid State 2nd Edition, Elsevier (2004).
[47] K.V.R. Murthy, H.S. Virk, *Mater. Sci. Forum*, **347** (2014) 1-34.
[48] G. Blasse, B.C. Grabmaier, Luminescent Materials, Springer-Verlag Berlin Heidelberg (1994).
[49] D.R. Vij, Luminescence of Solids, Plenum Press, New York (1998).
[50] G. Liu, B. Jacquier, Spectroscopic Properties of Rare Earths in Optical Materials, Springer-Verlag Berlin Heidelberg (2005).
[51] X. Huang, S. Han, W. Huang, X. Liu, *Chem. Soc. Rev.*, **42** (2013) 173-201.
[52] D.L. Dexter, *Phys. Rev.*, **108** (1957) 630.
[53] Q.Y. Zhang, X.Y. Huang, *Prog. Mater. Sci.*, **55** (2010) 353-427.
[54] K. Grzeszkiewicz, L. Marciniak, W. Stręk, D. Hreniak, *J. Lumin.*, **177** (2016) 172-177.
[55] A. Verma, S.K. Sharma, *Ceram. Int.*, **43** (2017) 8879-8885.
[56] S. Abe, J.J. Joos, L.I.D.S. Martin, Z. Hens, P.F. Smet, *Light Sci. Appl.*, **6** (2017) e16271.
[57] P.F. Smet, J.J. Joos, *Nat. Mater.*, **16** (2017) 500-501.
[58] N. Bloembergen, *Phys. Rev. Lett.*, **2** (1959) 84-85.
[59] F. Auzel, *Cr. Acad. Sci. B Phys.*, **262** (1966) 1016-1019.
[60] F. Auzel, *Cr. Acad. Sci. B Phys.*, **263** (1966) 819-821.
[61] V. Ovsyankin, P.P. Feofilov, *J. Exp. Theor. Phys. Lett.*, **3** (1966) 322-323.

[62] H. Lian, Z. Hou, M. Shang, D. Geng, Y. Zhang, J. Lin, *Energy*, **57** (2013) 270-282.
[63] J.S. Chivian, W.E. Case, D.D. Eden, *Appl. Phys. Lett.*, **35** (1979) 124-125.
[64] M. Pollnau, D.R. Gamelin, S.R. Lüthi, H.U. Güdel, M.P. Hehlen, *Phys. Rev. B*, **61** (2000) 3337-3346.
[65] J.F. Suyver, A. Aebischer, S. García-Revilla, P. Gerner, H.U. Güdel, *Phys. Rev. B*, **71** (2005) 125123.
[66] L. Agazzi, K. Wörhoff, M. Pollnau, *J. Phys. Chem. C*, **117** (2013) 6759-6776.
[67] G.C. Righini, M. Ferrari, *Riv. Nuovo Cimento*, **28** (2005) 1-50.
[68] Y. Lei, H. Song, L. Yang, L. Yu, Z. Liu, G. Pan, X. Bai, L. Fan, *J. Chem. Phys.*, **123** (2005) 174710.
[69] L. Tian, Z. Xu, S. Zhao, Y. Cui, Z. Liang, J. Zhang, X. Xu, *Materials*, **7** (2014) 7289-7303.
[70] A.J.M. Sales, D.G. Sousa, H.O. Rodrigues, M.M. Costa, A.S.B. Sombra, F.N.A. Freire, M.J. Soares, M.P.F. Graça, J.S. Kumar, *Ceram. Int.*, **42** (2016) 6899-6905.
[71] F. Zhang, Photon Upconversion Nanomaterials, Springer-Verlag Berlin Heidelberg (2015).
[72] G. Blasse, Chapter 34 Chemistry and physics of R-activated phosphors, Handbook on the Physics and Chemistry of Rare Earths, **4** (1979) 237-274.
[73] O. Laporte, W.F. Meggers, *J. Opt. Soc. Am.*, **11** (1925) 459-463.
[74] D.V. Rosse, Focus on Materials Science Research, Nova Science Publishers, New York (2007).
[75] P.W. Atkins, R.S. Friedman, Molecular Quantum Mechanics 5th Edition, Oxford University Press, Oxford (2010).
[76] P. Hänninen, H. Härmä, Lanthanide Luminescence: Photophysical, Analytical and Biological Aspects, Springer-Verlag Berlin Heidelberg (2011).
[77] C. Altavilla, Upconverting Nanomaterials: Perspectives, Synthesis, and Applications, CRC Press, Boca Raton, Florida (2016).
[78] G.H. Dieke, Spectra and Energy Levels of Rare Earth Ions in Crystals, John Wiley, New York (1968).
[79] W.T. Carnall, G.L. Goodman, K. Rajnak, R.S. Rana, *J. Chem. Phys.*, **90** (1989) 3443-3457.
[80] R.T. Wegh, A. Meijerink, R.-J. Lamminmäki, J. Hölsä, *J. Lumin.*, **87-89** (2000) 1002-1004.

[81] L. Aboshyan-Sorgho, M. Cantuel, S. Petoud, A. Hauser, C. Piguet, *Coordin. Chem. Rev.*, **256** (2012) 1644-1663.

[82] I. Hyppänen, J. Hölsä, J. Kankare, M. Lastusaari, L. Pihlgren, *J. Nanomater.*, **Article ID 16391** (2007) 1-8.

[83] J. Zhou, Q. Liu, W. Feng, Y. Sun, F. Li, *Chem. Rev.*, **115** (2015) 395-465.

[84] A. Ştefan, O. Toma, Ş. Georgescu, *J. Lumin.*, **180** (2016) 376-383.

[85] J.-C. Boyer, L.A. Cuccia, J.A. Capobianco, *Nano Lett.*, **7** (2007) 847-852.

[86] T. Grzyb, A. Tymiński, *J. Alloy. Compd.*, **660** (2016) 235-243.

[87] R. Elleuch, R. Salhi, J.-L. Deschanvres, R. Maalej, *RSC Adv.*, **5** (2015) 60246-60253.

[88] Q. Shang, H. Yu, X. Kong, H. Wang, X. Wang, Y. Sun, Y. Zhang, Q. Zeng, *J. Lumin.*, **128** (2008) 1211-1216.

[89] J. Lu, D. Wang, H. Wang, *J. Alloy. Compd.*, **509** (2011) 9946-9950.

[90] Y. Liu, C. Xu, Q. Yang, *J. Appl. Phys.*, **105** (2009) 084701.

[91] G. Xie, Y. Wei, L. Fan, J. Wu, *J. Phys. Conf. Ser.*, **339** (2012) 012010.

[92] D. Patel, A. Lewis, D. Wright III, M. Velentine, D. Lewis, R. Valentine, S. Sarkisov, *Proc. SPIE*, **8982** (2014) 898221.

[93] R. Wang, W. Zhang, Y. Xu, L. Xing, *Opt. Laser Technol.*, **58** (2014) 52-55.

[94] X. Yu, S. Liang, Z. Sun, Y. Duan, Y. Qin, L. Duan, H. Xia, P. Zhao, D. Li, *Opt. Commun.*, **313** (2014) 90-93.

[95] M. Pedroni, F. Piccinelli, S. Polizzi, A. Speghini, M. Bettinelli, P. Haro-González, *Mater. Lett.*, **80** (2012) 81-83.

[96] T.J. Bruno, P.D.N. Svoronos, CRC Handbook of Fundamental Spectroscopic Correlation Charts, CRC Press, Boca Raton, Florida (2005).

[97] J. Ohwaki, Y. Wang, *Appl. Phys. Lett.*, **65** (1994) 129-131.

[98] J. Ohwaki, M. Otsuka, *Electron. Lett.*, **31** (1995) 752-753.

[99] V. Singh, P. Haritha, V. Venkatramu, S.H. Kim, *Spectrochim. Acta A*, **126** (2014) 306-311.

[100] H. Wang, T. Jiang, M. Xing, Y. Fu, Y. Peng, X. Luo, *Ceram. Int.*, **41** (2015) 259-263.

[101] Y. Guo, D. Wang, X. Wu, Q. Wang, Y. He, *J. Alloy. Compd.*, **688** (2016) 816-819.

[102] Ž. Antić, V. Lojpor, M.G. Nikolić, V. Đorđevi, P.S. Ahrenkiel, M.D. Dramićanin, *J. Lumin.*, **145** (2014) 466-472.

[103] R.K. Tamrakar, D.P. Bisen, K. Upadhyay, I.P. Sahu, *J. Alloy. Compd.*, **655** (2016) 423-432.

[104] D. Li, W. Qin, T. Aidilibike, P. Zhang, S. Liu, L. Wang, S. Li, *J. Alloy. Compd.*, **675** (2016) 31-36.

[105] I. Hyppänen, J. Hölsä, J. Kankare, M. Lastusaari, M. Malkamäki, L. Pihlgren, *J. Lumin.*, **129** (2009) 1739-1743.

[106] L. Pihlgren, T. Laihinen, L.C.V. Rodrigues, S. Carlson, K.O. Eskola, A. Kotlov, M. Lastusaari, T. Soukka, H.F. Brito, J. Hölsä, *Opt. Mater.*, **36** (2014) 1698-1704.

[107] J. Liao, Q. Wang, L. Nie, W. You, J. Chen, *Opt. Mater.*, **62** (2016) 479-484.

[108] X. Mao, B. Yan, J. Wang, J. Shen, *Vacuum*, **102** (2014) 38-42.

[109] R. Salhi, J.-L. Deschanvres, *J. Lumin.*, **176** (2016) 250-259.

[110] A. de Pablos-Martín, J. Méndez-Ramos, J. del-Castillo, A. Durán, V.D. Rodríguez, M.J. Pascual, *J. Eur. Ceram. Soc.*, **35** (2015) 1831-1840.

[111] M. Tuomisto, E. Palo, T. Laihinen, I. Hyppänen, M. Lastusaari, H.C. Swart, J. Hölsä, *Opt. Mater.*, **59** (2016) 115-119.

[112] I.Z. Dinic, M.E. Rabanal, K. Yamamoto, Z. Tan, S. Ohara, L.T. Mancic, O.B. Milosevic, *Adv. Powder Technol.*, **27** (2016) 845-853.

[113] W. Gao, H. Zheng, E. He, Y. Lu, F. Gao, *J. Lumin.*, **152** (2014) 44-48.

[114] L. Fu, H. Xia, Y. Dong, S. Li, X. Gu, J. Zhang, D. Wang, H. Jiang, B. Chen, *J. Alloy. Compd.*, **617** (2014) 584-587.

[115] M. Secu, C.E. Secu, *J. Non-Cryst. Solids*, **426** (2015) 78-82.

[116] J.P. Jouart, M. Bouffard, G. Klein, G. Mary, *J. Lumin*., **60-61** (1994) 93-96.

[117] M. Bouffard, J.P. Jouart, M.-F. Joubert, *Opt. Mater.*, **14** (2000) 73-79.

[118] X. Cheng, X. Ma, H. Zhang, Y. Ren, K. Zhu, *Physica B*, **521** (2017) 270-274.

[119] M. Secu, C.E. Secu, *J. Eur. Ceram. Soc.*, **36** (2016) 1699-1703.

[120] P. Du, J.S. Yu, *Mater. Lett.*, **169** (2016) 135-139.

[121] W. Wu, D. Chen, Y. Zhou, Z. Wan, Z. Ji, *J. Alloy. Compd.*, **682** (2016) 275-283.

[122] F. Wang, B. Yang, X. Chen, W. Ma, B. Xu, *Mater. Chem. Phys.*, **169** (2016) 113-119.

[123] N. Hakmeh, C. Chlique, O. Merdrignac-Conanec, B. Fan, F. Cheviré, X. Zhang, X. Fan, X. Qiao, *J. Solid State Chem.*, **226** (2015) 255-261.

[124] S. Li, Y. Guo, L. Zhang, J. Wang, Y. Li, Y. Li, B. Wang, *J. Power Sources*, **252** (2014) 21-27.

[125] Y. Li, Y. Guo, S. Li, Y. Li, J. Wang, *Int. J. Hydrogen Energ.*, **40** (2015) 2132-2140.

[126] X. Chen, T. Nguyen, Q. Luu, B.D. Bartolo, *J. Lumin.*, **85** (2000) 295-299.

[127] C. Sun, W. Lü, F. Yang, C. Tu, *J. Alloy. Compd.*, **512** (2012) 160-164.

[128] T. Grzyb, A. Gruszeczka, S. Lis, *J. Lumin.*, **175** (2016) 21-27.

[129] S. Park, W. Yang, C.-Y. Park, M. Noh, S. Choi, D. Park, H.S. Jang, S.H. Cho, *Mater. Res. Bull.*, **71** (2015) 25-29.

[130] H. Liu, Y. Jia, Y. Ren, S. Akhmadaliev, S. Zhou, F. Chen, *Nucl. Instrum. Meth. B*, **320** (2014) 22-25.

[131] L. Dai, Z. Yan, S. Jiao, C. Xu, Y. Xu, *J. Alloy. Compd.*, **644** (2015) 502-505.

[132] M. Stoffel, H. Rinnert, E. Kokanyan, G. Demirkhanyan, H. Demirkhanyan, M. Aillerie, *Opt. Mater.*, **57** (2016) 79-84.

[133] H.N. Luitel, R. Chand, T. Watari, *Displays*, **42** (2016) 1-8.

[134] R. Dey, V.K. Rai, K. Kumar, *Solid State Sci.*, **61** (2016) 185-194.

[135] J. Li, T. Zhang, G. Zhu, H. Zheng, *J. Rare Earth.*, **35** (2017) 645-651.

[136] A.G.A. Darwish, Y. Badr, M. El Shaarawy, N.M.H. Shash, I.K. Battisha, *J. Alloy. Compd.*, **489** (2010) 451-455.

[137] X. Chen, Z. Liu, Q. Sun, M. Ye, F. Wang, *Opt. Commun.*, **284** (2011) 2046-2049.

[138] L. Chen, X-H. Wei, X. Fu, *T. Nonferr. Metal. Soc.*, **22** (2012) 1156-1160.

[139] M. Su, Y. Zhou, K. Wang, D. Huang, W. Xu, Y. Cao, *J. Rare Earth.*, **33** (2015) 227-230.

[140] M. Malinowski, M. Kaczkan, S. Turczyński, *Opt. Mater.*, **63** (2017) 128-133.

[141] R.J. Wiglusz, A. Watras, M. Malecka, P.J. Deren, R. Pazik, *Eur. J. Inorg. Chem.*, **6** (2014) 1090-1101.

[142] A.A. Bol, R. van Beek, A. Meijerink, *Chem. Mater.*, **14** (2002) 1121-1126.

[143] L.C. Ong, M.K. Gnanasammandhan, S. Nagarajan, Y. Zhang, *Luminescence*, **25** (2010) 290-293.

[144] H. Lin, Q. Luo, W.-Y. Tong, C. Jiang, R. Huang, H. Peng, L.-C. Zhang, J. Travas-Sejdic, C.-G. Duan, *RSC Adv.*, **5** (2015) 86885-86890.

[145] S. Heer, K. Kömpe, H.-U. Güdel, M. Haase, *Adv. Mater.*, **16** (2004) 2102-2105.

[146] K.W. Krämer, D. Biner, G. Frei, H.U. Güdel, M.P. Hehlen, S.R. Lüthi, *Chem. Mater.*, **16** (2004) 1244-1251.
[147] Y.-M. Chiang, D.P. Birnie, W.D. Kingery, Physical Ceramics: Principle for Ceramic Science and Engineering, John Wiley & Sons, New York (1997).
[148] S.P. Tiwari, M.K. Mahata, K. Kumar, V.K. Rai, *Spectrochim. Acta A*, **150** (2015) 623-630.
[149] G. Shan, R. Weissleder, S.A. Hilderbrand, *Theranostics*, **3** (2013) 267-274.
[150] H.A. Wahab, A.A. Salama, A.A. El-Saeid, O. Nur, M. Willander, I.K. Battisha, *Results Phys.*, **3** (2013) 46-51.
[151] B.C. Yadav, R. Srivastava, C.D. Dwivedi, *Philos. Mag.*, **88** (2008) 1113-1124.
[152] N.K. Pandey, K. Tiwari, A. Roy, *B. Mater. Sci.*, **35** (2012) 347-352.
[153] K. Jayanthi, S. Chawla, K.N. Sood, M. Chhibara, S. Singh, *Appl. Surf. Sci.*, **255** (2009) 5869-5875.
[154] S. Dong, S. Dong, D. Zhou, X. Zhou, D. Ma, Y. Du, *J. Mol. Catal. A-Chem.*, **407** (2015) 38-46.
[155] S. Yildirim, M. Yurddaskal, T. Dikici, I. Aritman, K. Ertekin, E. Celik, *Ceram. Int.*, **42** (2016) 10579-10586.
[156] C. Tang, W. Hou, E. Liu, X. Hu, J. Fan, *J. Lumin.*, **154** (2014) 305-309.
[157] T. Ji, F. Yang, H. Du, H. Guo, J. Yang, *J. Rare Earth.*, **28** (2010) 529-533.
[158] R.L. Millard, R.C. Peterson, B.K. Hunter, *Am. Mineral.*, **80** (1995) 885-896.
[159] H.T. Kim, Y. Kim, M. Valant, D. Suvorov, *J. Am. Ceram. Soc.*, **84** (2001) 1081-1086.
[160] K. Momma, F. Izumi, *J. Appl. Crystallogr.*, **44** (2011) 1272-1276.
[161] K. Kobwittaya, Y. Oishi, T. Torikai, M. Yada, T. Watari, H.N. Luitel, *Ceram. Int.*, **43** (2017) 13505-13515.
[162] Y.-S. Chang, Y.-H. Chang, I.-G. Chen, G.-J. Chen, Y.-L. Chai, S. Wu, T.-H. Fang, *J. Alloy. Compd.*, **354** (2003) 303-309.
[163] M.-W. Kim, H. Yoon, T.Y. Ohm, H.S. Jo, S. An, S.K. Choi, H. Park, S.S. Al-Deyab, B.K. Min, M.T. Swihart, S.S. Yoon, *Appl. Catal. B-Environ.*, **201** (2017) 479-485.
[164] H.-S. Lim, J. Lee, S. Lee, Y.S. Kang, Y.-K. Sun, K.-D. Suh, *Acta Mater.*, **122** (2017) 287-297.
[165] M.V. DaCosta, S. Doughan, Y. Han, U.J. Krull, *Anal. Chim. Acta*, **832** (2014) 1-33.

[166] P. Ghosh, J. Oliva, E. de la Rosa, K.K. Haldar, D. Solis, A. Patra, *J. Phys. Chem. C*, **112** (2008) 9650-9658.

[167] F. Vetrone, J.C. Boyer, J.A. Capobianco, A. Speghini, M. Bettinelli, *J. Phys. Chem. B*, **107** (2003) 1107-1112.

[168] S. Heer, O. Lehmann, M. Haase, H.-U. Güdel, *Angew. Chem. Int. Edit.*, **42** (2003) 3179-3182.

[169] H. Shen, F. Wang, X. Fan, M. Wang, *J. Exp. Nanosci.*, **2** (2007) 303-311.

[170] G. Yi, H. Lu, S. Zhao, Y. Ge, W. Yang, D. Chen, L.-H. Guo, *Nano Lett.*, **4** (2011) 2191-2196.

[171] X. Qin, T. Yokomori, Y. Ju, *Appl. Phys. Lett.*, **90** (2007) 073104.

[172] W. Kong, J. Shan, Y. Ju, *Mater. Lett.*, **64** (2010) 688-691.

[173] J.-H. Zeng, J. Su, Z.-H. Li, R.-X. Yan, Y.-D. Li, *Adv. Mater.*, **17** (2005) 2119-2123.

[174] C. Liu, D. Chen, *J. Mater. Chem.*, **17** (2007) 3875-3880.

[175] H.-Q. Wang, R.D. Tilley, T. Nann, *CrystEngComm*, **12** (2010) 1993-1996.

[176] C. Mi, Z. Tian, C. Cao, Z. Wang, C. Mao, S. Xu, *Langmuir*, **27** (2011) 14632-14637.

[177] T. Wang, Y. Wang, S. Shi, B. Li, J. Zhou, *Key Eng. Mater.*, **336-338** (2007) 101-104.

[178] J. Zhang, Wulantuya, X.-W. Di, Z.-L. Liu, G. Xu, S.-M. Xu, *T. Nonferr. Metal. Soc.*, **20** (2010) s231-s235.

[179] K. Takagi, *J. Chem. Soc. Jpn., Ind. Chem. Sec.*, **65** (1962) 847.

[180] R.K. Tamrakar, D.P. Bisen, K. Upadhyay, I.P. Sahu, *J. Phys. Chem. C*, **119** (2015) 21072-21086.

[181] S. Liu, S. Liu, M. Zhou, X. Ye, D. Hou, W. You, *RSC Adv.*, **7** (2017) 36935-36948.

[182] M.S. Pathak, M. Seshadri, N. Singh, V. Singh, J.-K. Lee, *Opt. Mater.*, **62** (2016) 717-722.

[183] V. Singh, V.K. Rai, N. Singh, M.S. Pathak, M. Rathaiah, V. Venkatramu, R.V. Patel, P.K. Singh, S.J. Dhoble, *Spectrochim. Acta A*, **171** (2017) 229-235.

[184] E.L. Payrer, A.L. Joudrier, P. Aschehoug, R.M. Almeida, J.L. Deschanvres, *J. Lumin.*, **187** (2017) 247-254.

[185] M. Vega, P. Alemany, I.R. Martin, J. Llanos, *RSC Adv.*, **7** (2017) 10529-10538.

[186] P. Ramasamy, P. Manivasakan, J. Kim, *RSC Adv.*, **4** (2014) 34873-34895.

[187] J.C. Goldschmidt, S. Fischer, *Adv. Opt. Mater.*, **3** (2015) 510-535.

[188] G. Arnaoutakis, J. Marques-Hueso, A. Ivaturi, S. Fischer, J.C. Goldschmidt, K.W. Krämer, B.S. Richards, *Sol. Energ. Mat. Sol. C.*, **140** (2015) 217-223.

[189] B. Zhou, B. Shi, D. Jin, X. Liu, *Nat. Nanotechnol.*, **10** (2015) 924-936.

[190] A. Rapaport, J. Milliez, M. Bass, A. Cassanho, H. Jenssen, *J. Disp. Technol.*, **2** (2006) 68-78.

[191] X. Liu, H. Chu, J. Li, L. Niu, C. Li, H. Li, L. Pan, C.Q. Sun, *Catal. Sci. Technol.*, **5** (2015) 4727-4740.

[192] J. Hampl, M. Hall, N.A. Mufti, Y.M. Yao, D.B. MacQueen, W.H. Wright, D.E. Cooper, *Anal. Biochem.*, **288** (2001) 176-187.

[193] R.S. Niedbala, H. Feindt, K. Kardos, T. Vail, J. Burton, B. Bielska, S. Li, D. Milunic, P. Bourdelle, R.Vallejo, *Anal. Biochem.*, **293** (2001) 22-30.

[194] T. Ukonaho, T. Rantanen, L. Jämsen, K. Kuningas, H. Päkkilä, T. Lövgren, T. Soukka, *Anal. Chim. Acta*, **596** (2007) 106-115.

[195] D.K. Chatterjee, A.J. Rufaihah, Y. Zhang, *Biomaterials*, **29** (2008) 937-943.

Chapter II

Synthesis and upconversion luminescence properties of $ZnO\text{-}TiO_2$ containing Ho^{3+} and Yb^{3+}

2.1 Introduction

Photon upconversion (UC) involves the absorption of two or more photons of low energy with subsequent emission of higher energy photon. Due to the discrete energy states of rare earth (RE) ions, RE doped upconverters exhibit superior infrared to visible UC performance [1,2]. Since its discovery in the 1960s, RE-based UC phosphors have been researched by many researchers for the advancement in new applications and technologies such as in the fabrication of electronic and optical communication devices (e.g. displays and lasers) [3-5], ultraviolet C (UVC) light emitting antimicrobial surface [6], and medical diagnostic [7].

There are two working types of RE ions doped into UC phosphors. One is employed as the luminescent center which emits the radiation and is called an activator, and the other ion harvests the excited energy efficiently and then transfers that energy to the activator and is called a sensitizer. For the activator, Er^{3+}, Ho^{3+}, and Tm^{3+} are the most widely used due to their plentiful electronic energy levels to adapt UC luminescence (UCL) [4,8-10]. Also, these ions are the main activator for fabricating red, green, and blue emitting UC phosphors. In addition, by the combination of these activator ions (at least two e.g. Er^{3+}/Tm^{3+}), suitable sensitizer ion (e.g. Yb^{3+}), stable inorganic crystal, and eventually tuning dopants concentration ratio, the UC phosphor can provide a variety of UCL colors including white emission [11].

Trivalent ytterbium (Yb^{3+}) ion is generally a co-dopant because it has large absorption cross-section around 980 nm [12]. The Yb^{3+} plays a significant role to pump excited photons, transfers the energy to adjacent activator ions through multiple photon processes into the excited state productively [13,14]. The holmium (Ho^{3+}) ion as an activator is a good candidate dopant to generate short wavelength luminescence, green light (495-550 nm) and red light (620-750 nm) [15,16]. With these possible emission colors, Ho^{3+}/Yb^{3+} co-doped host materials have been

investigated by many researchers for employing in various applications such as full-color range display [17], biomedical [18], and optical temperature sensing [19].

Host material is also important for the fabrication of UC phosphor. Theoretically, the most significant point for selecting the efficient UC host material to obtain high performance UCL is phonon energy. It is well established that UC host material should have low phonon energy because phonons (related to lattice vibrations) provide non-radiative decay ways to suppress radiative emission, leading to low UCL intensity [17]. Even though some host materials such as halides and sulfides exhibit low phonon energy, but they have many disadvantages such as poor chemical resistance, thermal unsteadiness, and high cost, therefore, difficult to use in practical applications [17,20-22]. So far, the most investigated UC host materials are oxides and fluorides because they show low phonon energy and high chemical stability [23,24].

Nowadays, many new applications and technologies require a variety of properties of material which traditional materials have limited applicability. Composite materials, which consist of the combination of two phases or more with different physical and chemical properties, have attracted much attention in recent years because this type of material is typically light weight, flexible, high corrosion resistance, and impact strength. Because of these properties, composite materials have been considered as a replacement of classical materials used in aerospace industry, construction, and electrical and electronics [25]. The ZnO-TiO_2 composite is considered as a promising UC host material due to its good properties such as low cost, thermal and chemical stability, and environmental friendliness [17]. Additionally, the noteworthy product of ZnO-TiO_2 composite is Zn_2TiO_4 phase that is a high thermal stability phase due to its inverse spinel structure. With these properties, many researches regarding ZnO-TiO_2 composite have been conducted and studied for applying in various applications such as nanofiber photocathode [26] and photocatalysis [27]. In addition, Zn_2TiO_4 shows great potential for being the good optical host because it has high value of refractive index n = 2.1 [28] and low phonon energy around 721 cm^{-1} [29].

Recently, strong UCL and color tenability in ZnO-TiO_2 composite doped with Er^{3+} and Yb^{3+} prepared by solid-state reaction method was reported [30]. As discussed in this report, ZnO-TiO_2 as host material in the form of Zn_2TiO_4 is suitable for using in the field of UC phosphor when the system consists of mixed phases of Zn_2TiO_4, TiO_2, and $RE_2Ti_2O_7$ (RE = Er^{3+} and/or

Yb^{3+}). Besides, excess Ti^{4+} in the system affect vacancies generation, leading to higher solubility of RE^{3+} ion into host material. In this chapter, the following research, ZnO-TiO_2 composite doped with Ho^{3+} and Yb^{3+} was examined by preparing via solid-state reaction method to confirm the possibility of using ZnO-TiO_2 composite not only as UC host material but also its performance when it was doped by other dopants. Effects of ZnO/TiO_2 mixing ratio, Ho^{3+} and Yb^{3+} doping concentrations, and their ratios on the crystal phase and UCL properties were methodically investigated. To understand the UC mechanism of Ho^{3+}/Yb^{3+} co-doped ZnO-TiO_2 composite prepared by solid-state reaction method, the dependence of UC emission intensity on different excitation powers was calculated and discussed in detail. Also, the UC mechanism that might be responsible for this system was proposed and described based on pumping power dependence of UC emission intensity.

2.2 Experimental

ZnO-TiO_2 composite doped with Ho^{3+} and Yb^{3+} was prepared by solid-state reaction method using zinc oxide (ZnO; Aldrich, AR purity), titanium dioxide (TiO_2; Aldrich, AR purity), holmium oxide (Ho_2O_3; Aldrich, 99.99+%), and ytterbium oxide (Yb_2O_3; Aldrich, 99.99+%). All raw powders were thoroughly mixed together by mortar and pestle using ethanol. Various ZnO-TiO_2 composite samples with different ZnO/TiO_2 mixing ratios were made by changing ZnO moles, while keeping constant TiO_2 (1 mole). ZnO/TiO_2 mixing ratios changed from 0.5-2 and named as Z*x*T1. Ho^{3+} and Yb^{3+} concentrations varied from 0.005-2 and 3-12 mol% based on TiO_2 content, respectively. The mixed powder was molded to the pellet (Φ 13 mm x 3 mm) by two axial press and fired in an air atmosphere at 1200 °C for 4 h. Then, the resultant pellets were finely grounded in vibration mill before characterization and UCL analysis. The complete preparation scheme is shown in Figure 2.1.

The crystalline phase of the products was carried out using X-ray diffraction (XRD), a Shimadzu XRD-6300 instrument with CuKα radiation in the range of 2θ = 10-80°. To explain the crystallization process, the relative phase content by pseudo-quantitative analysis of a specific phase was estimated from the XRD results by using equation (2.1):

$$\text{Relative phase content} = I_{(\text{phase})} / I_{(\text{total})} \quad (2.1)$$

where $I_{(phase)}$ is the intensity of selected peak from a main peak position that consists of only one phase; $I_{(311)}$ for Zn_2TiO_4, $I_{(110)}$ for TiO_2, $I_{(004)}$ for $RE_2Ti_2O_7$, and $I_{(102)}$ for RE_2TiO_5; and $I_{(total)}$ is the intensity summation of all selected peaks.

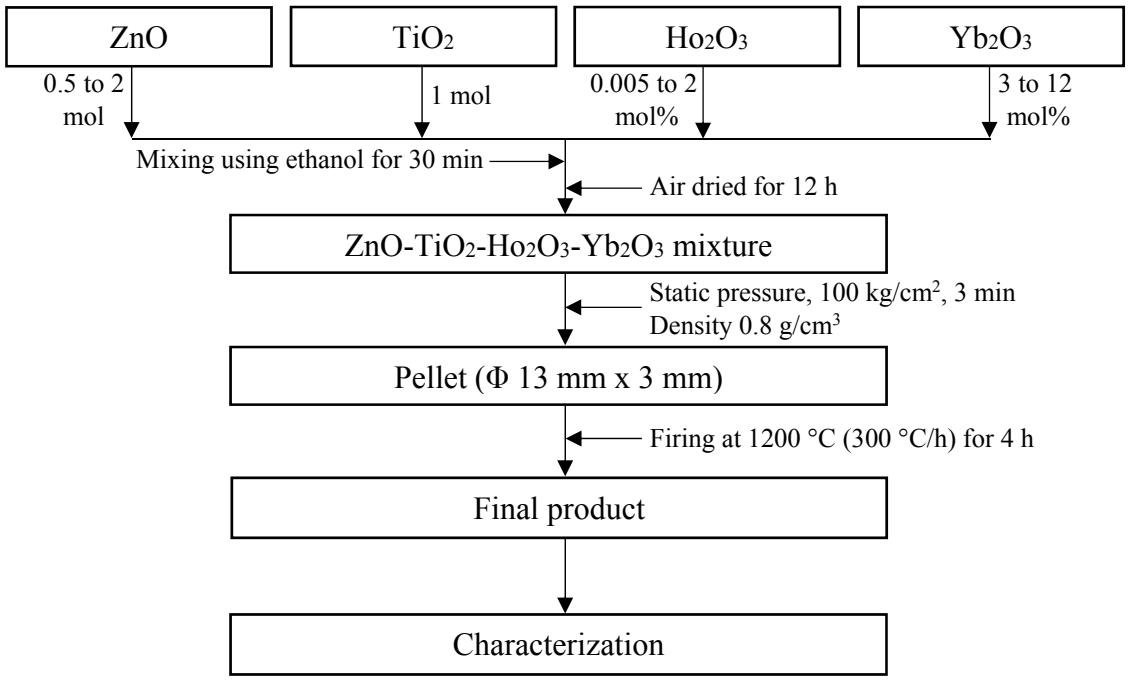

Figure 2.1. Flow chart for the preparation of ZnO-TiO_2:Ho^{3+}/Yb^{3+} phosphor by solid-state reaction method.

The UC emission behavior excited by a 980-nm continuous waveform laser was recorded from 250-800 nm spectral range using USB 4000 UV-VIS-NIR miniature fiber optic spectrometer (Ocean optics), having spectral resolution 1.34 nm (full width at half maximum, FWHM) and slit width 25 μm. The change in the maximum UC emission intensity on the laser power (0-200 mW) was used for considering the UC mechanism. All samples were measured at room temperature.

2.3 Results and discussion

XRD patterns of the Z*x*T1 samples with different *x*-values are shown in Figure 2.2. In the case of the lowest amount of ZnO (x = 0.5), Zn_2TiO_4 (JCPDS: 25-1164), rutile TiO_2 (JCPDS: 21-1276), $RE_2Ti_2O_7$ ($Ho_2Ti_2O_7$, JCPDS: 23-0283 and/or $Yb_2Ti_2O_7$, JCPDS: 17-0454) and RE_2TiO_5 (Ho_2TiO_5 and/or Yb_2TiO_5) phases were observed [31].

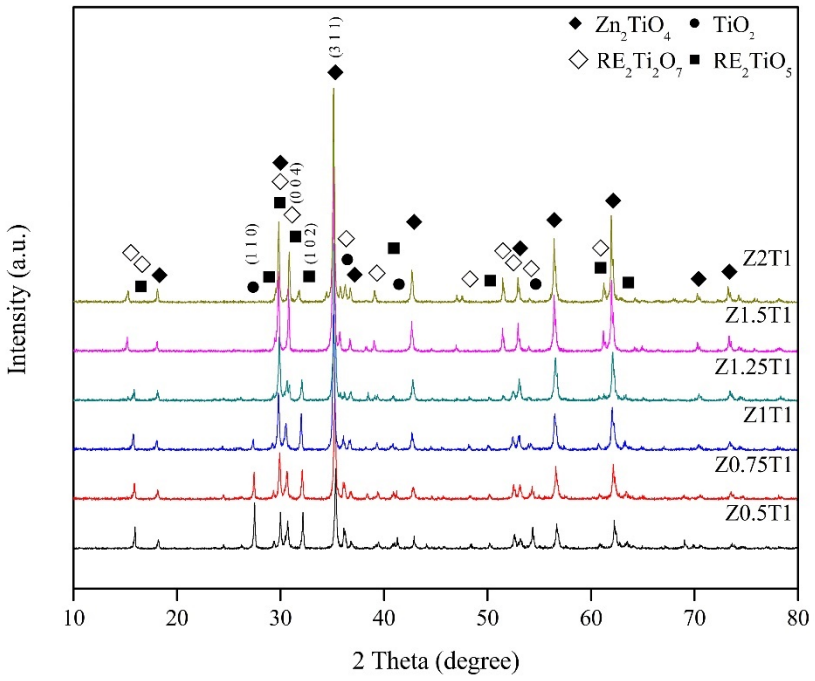

Figure 2.2. XRD patterns of various ZnO/TiO_2 mixing ratios doped with 0.05 mol% $Ho^{3+}$and 9 mol% Yb^{3+}. Reproduced with permission from Kobwittaya *et al.*, *J. Ceram. Soc. Jpn.*, **125** (2017) 559-564. Copyright (2017) The Ceramic Society of Japan. (License: CC BY-ND 4.0)

According to the phase diagram of ZnO-TiO_2 system [32], Zn_2TiO_4 is a stable phase and easily formed by the reaction between ZnO and TiO_2, even if the system has lower amount of ZnO than ZnO/TiO_2 = 2. The effect of ZnO/TiO_2 mixing ratio on relative phase content of the products is shown in Figure 2.3. With the increase of ZnO amount up to x = 1.25, Zn_2TiO_4 content increased and at the same time, TiO_2, $RE_2Ti_2O_7$, and RE_2TiO_5 contents gradually decreased. Subsequently, at x = 1.25, TiO_2 phase disappeared. And, at above x = 1.25, Zn_2TiO_4 phase remained unchanged and was still the dominant phase. $RE_2Ti_2O_7$ content primarily increased, but RE_2TiO_5 phase disappeared when increasing ZnO amount above x = 1.25. These phase changes can be explained as follows. Zn_2TiO_4 phase is formed by the reaction between 2 moles of ZnO and 1 mole of TiO_2. Therefore, as increasing ZnO amount from 0.5-2 (stoichiometric composition of Zn_2TiO_4 phase (2ZnO:1TiO_2)), Zn_2TiO_4 content increases absolutely. Further, remaining TiO_2 reacts with RE_2O_3 and then $RE_2Ti_2O_7$ and RE_2TiO_5 phases are formed owing to the negative formation energy of $RE_2Ti_2O_7$ (-3.8 eV) and RE_2TiO_5 (-3.79 eV) phases compared to Zn_2TiO_4 phase (-2.88 eV) [33]. These reactions are competitive ones. In general, RE^{3+} ions can get into the host crystal matrix (resulting in the varying in RE_2O_3

content), therefore, for the changes in $RE_2Ti_2O_7$ and RE_2TiO_5 contents for all conditions of ZnO concentration, the amount of RE^{3+} ions in Zn_2TiO_4 crystal including the content of Zn_2TiO_4 phase may directly cause these behaviors.

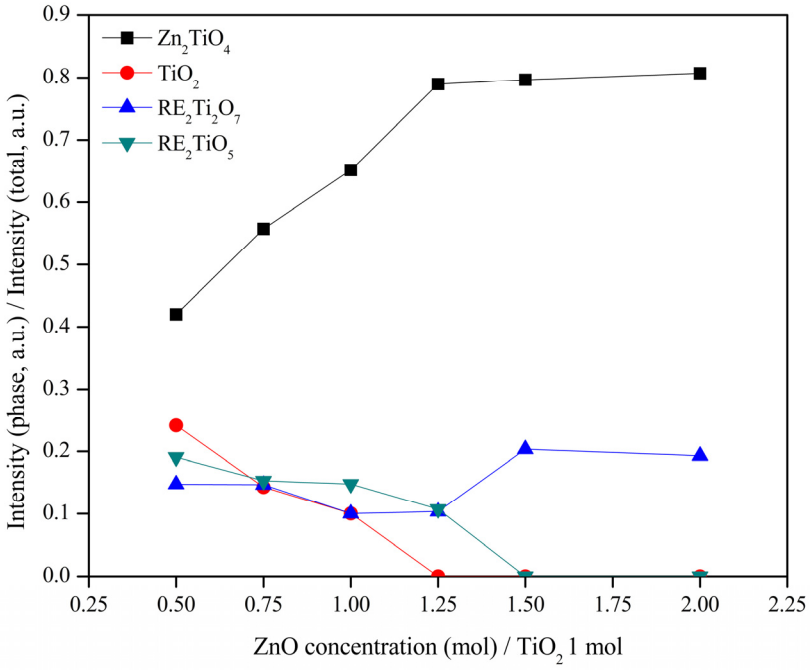

Figure 2.3. Calculated relative phase contents of Zn_2TiO_4, TiO_2, $RE_2Ti_2O_7$, and RE_2TiO_5 phases according to the compositions in Figure 2.2. Reproduced with permission from Kobwittaya *et al.*, *J. Ceram. Soc. Jpn.*, **125** (2017) 559-564. Copyright (2017) The Ceramic Society of Japan. (License: CC BY-ND 4.0)

UCL spectra of various ZnO/TiO_2 mixing ratios doped with 0.05 mol% Ho^{3+} and 9 mol% Yb^{3+} are shown in Figure 2.4. These emission spectra consisted of two strong emission bands, a green emission band from 537-557 nm (maximum at 542 nm) and a red emission band from 639-675 nm (maximum at 670 nm). Corresponding emission photographs are shown in Figure 2.5. These photographs showed that UCL color changed from green to reddish with increasing ZnO amount.

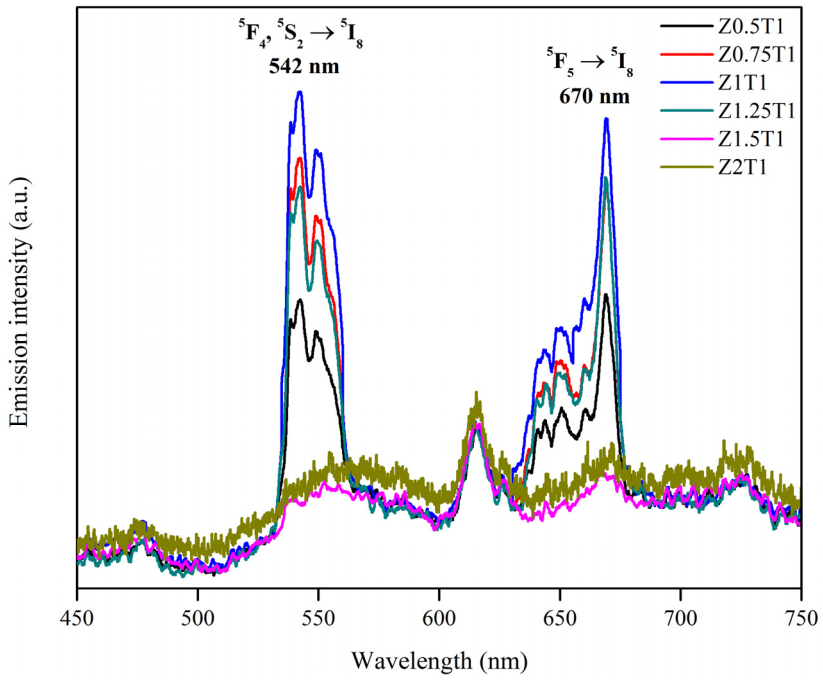

Figure 2.4. UC emission spectra of various ZnO/TiO_2 mixing ratios doped with 0.05 mol% Ho^{3+} and 9 mol% Yb^{3+}, and irradiated with a 980-nm 125 mW laser. Adapted with permission from Kobwittaya *et al.*, *J. Ceram. Soc. Jpn.*, **125** (2017) 559-564. Copyright (2017) The Ceramic Society of Japan. (License: CC BY-ND 4.0)

The luminescence emission color of the samples; Z0.5T1, Z0.75T1, Z1T1, and Z1.25T1, was green because the emission intensity of green emission band was equal or higher than red emission band. Further, the emission color of the samples; Z1.5T1 and Z2T1, became reddish because the emission intensity of red emission band was higher than green emission band. The central area of the samples; Z0.5T1, Z0.75T1, Z1T1, and Z1.25T1, seems to be white, which this observed emission is typically caused by the strong emission. In general, the emission occurs by the incorporation of RE^{3+} ions into the host material at high temperature. As discussed by Luitel *et al*. in ZnO-TiO_2 composite doped with Er^{3+} and Yb^{3+} [30], Zn_2TiO_4 has an AB_2O_4 type inverse spinel structure, where Zn atoms occupy all A-sites (tetrahedral), and B-sites (octahedral) are occupied by randomly arranged Zn and Ti atoms. For this occupant behavior, Zn^{2+} site is 4-fold (ionic radius = 0.060 nm) and 6-fold (ionic radius = 0.074 nm), and Ti^{4+} site is 6-fold (ionic radius = 0.061 nm). In addition, when the system has excess Ti^{4+} which have tendency to occupy octahedral site, vacancies are created (presumably in tetrahedral sites) to compensate the charge. Therefore, Ho^{3+} (ionic radius = 0.090 nm, 6-fold) and Yb^{3+} (ionic radius

= 0.087 nm, 6-fold) should get into tetrahedral vacancy site in Zn_2TiO_4 crystal more easily than direct occupying Zn^{2+} and Ti^{4+} because ionic radii of RE^{3+} ions are much larger than Zn^{2+} and Ti^{4+}, including the valence mismatch of these three ions.

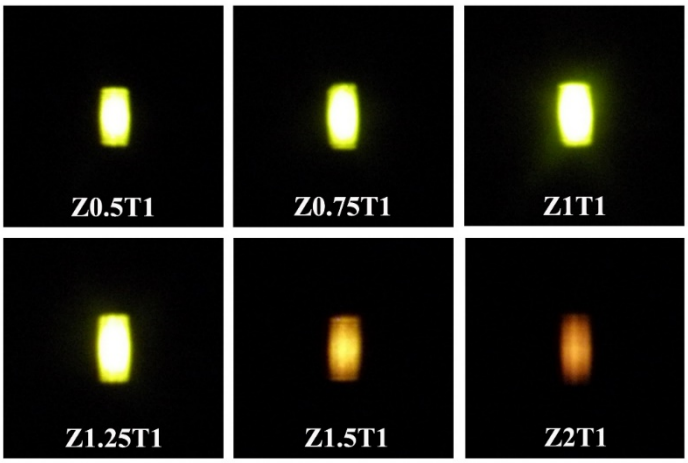

Figure 2.5. UC emission color of various ZnO/TiO_2 mixing ratios doped with 0.05 mol% Ho^{3+} and 9 mol% Yb^{3+}, and irradiated with a 980-nm 125 mW laser. Adapted with permission from Kobwittaya *et al*., *J. Ceram. Soc. Jpn.*, **125** (2017) 559-564. Copyright (2017) The Ceramic Society of Japan. (License: CC BY-ND 4.0)

The maximum emission intensity (at 542 nm) of various ZnO/TiO_2 mixing ratios doped with 0.05 mol% Ho^{3+} and 9 mol% Yb^{3+} is shown in Figure 2.6. In the case of lower x-value ($x < 1$), the emission intensity increased as the increase of ZnO amount. In the case of $x > 1$, with increasing ZnO amount, the emission intensity decreased. These behaviors can be explained by considering relative phase contents of the products as presented in Figure 2.3. When emission intensity increased ($x = 0.5$, 0.75, and 1), there were four phases; Zn_2TiO_4, TiO_2, $RE_2Ti_2O_7$, and RE_2TiO_5. Further, when emission intensity initially decreased (x = 1.25), there were three phases; Zn_2TiO_4, $RE_2Ti_2O_7$, and RE_2TiO_5 without TiO_2 phase. At x = 1.5 and 2, the emission intensity decreased continuously and there were only two phases; Zn_2TiO_4 and $RE_2Ti_2O_7$. Therefore, the difference between these three conditions of ZnO amount x is the existence of TiO_2 phase, whose solubility in Zn_2TiO_4 may affect the UCL intensity. In addition, by considering the effect of ZnO/TiO_2 mixing ratio on crystalline phase presented in this study ($ZnO\text{-}TiO_2$: Ho^{3+}/Yb^{3+} system) and the study reported by Luitel *et al*. ($ZnO\text{-}TiO_2$:Er^{3+}/Yb^{3+} system) [30], some identical results are observed. For both systems, the brightest UCL on green

and red bands is detected at optimum mixing ratio $ZnO:TiO_2$ = 1:1 (in mole) and under the situation that the system contains multiple phases of Zn_2TiO_4, TiO_2, and rare earth titanates.

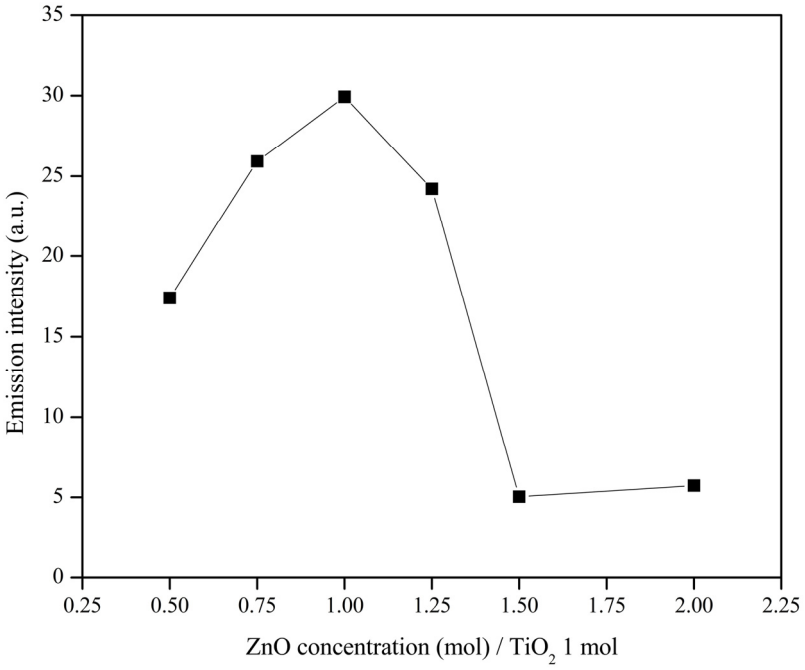

Figure 2.6. The green emission intensities at 542 nm versus various ZnO/TiO_2 mixing ratios doped with 0.05 mol% Ho^{3+} and 9 mol% Yb^{3+}. Reproduced with permission from Kobwittaya *et al*., *J. Ceram. Soc. Jpn.*, **125** (2017) 559-564. Copyright (2017) The Ceramic Society of Japan. (License: CC BY-ND 4.0)

The green (542 nm) and red (670 nm) emission intensities versus various Ho^{3+} concentrations (keeping 9 mol% Yb^{3+} concentration) of Z1T1 composite are shown in Figure 2.7. Here too, the UCL behavior can be separated into three parts. In the initial part, with the increase of Ho^{3+} concentration from 0.005-0.05 mol%, the emission intensity increased because Ho^{3+} activator concentration in Zn_2TiO_4 phase increased. In the second part, with increasing Ho^{3+} concentration up to 0.3 mol%, the emission intensity sharply decreased because of concentration quenching. In the third part, with Ho^{3+} concentration more than 0.3 mol%, slow and continuous decrease in emission intensity was observed. At higher Ho^{3+} concentration (0.3-2 mol%), the emission intensity was very low. This must be due to the saturation of Ho^{3+} solid solution in Zn_2TiO_4 phase.

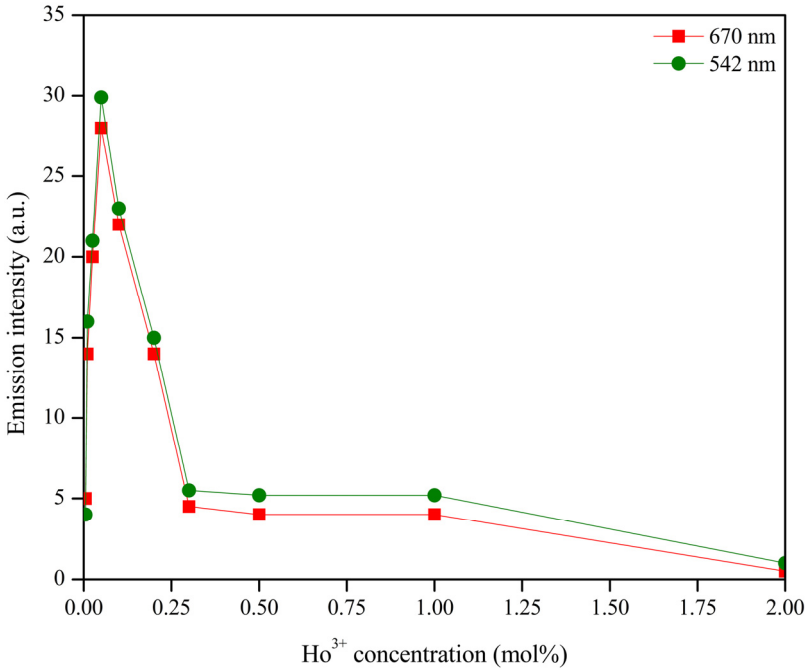

Figure 2.7. The green (542 nm) and red (670 nm) emission intensities of $ZnO:TiO_2$ = 1:1 (in mole) (Z1T1) doped with various mol% Ho^{3+} and 9 mol% Yb^{3+}. Reproduced with permission from Kobwittaya *et al.*, *J. Ceram. Soc. Jpn.*, **125** (2017) 559-564. Copyright (2017) The Ceramic Society of Japan. (License: CC BY-ND 4.0)

Figure 2.8 shows the dependent Yb^{3+} concentration on the emission intensity of the products, while keeping Ho^{3+} concentration at 0.05 mol%. With the increase of Yb^{3+} concentration from 3-9 mol%, the emission intensity increased, reached maximum at 9 mol% Yb^{3+} doping concentration, and then decreased in higher concentration. The increased emission intensity is due to the higher concentration of dissolved Yb^{3+} into the Zn_2TiO_4 phase, which increases the photon absorption and hence the excited Ho^{3+}. The decreased emission intensity at higher Yb^{3+} concentration agrees with concentration quenching. Thus, the optimum Ho^{3+} and Yb^{3+} concentrations for obtaining the brightest UC emission in this system are 0.05 and 9 mol%, respectively.

As a result of very low optimum Ho^{3+} concentration, the incorporation of Ho^{3+} including Yb^{3+} into Zn_2TiO_4 phase is the significant point which can be simply explained by considering XRD patterns of controlled variables based on the best condition for emitting brightest UC emission of this system, consisting of undoped Z1T1, 0.05 mol% Ho^{3+} doped Z1T1, 9 mol% Yb^{3+} doped

Z1T1, and 0.05 mol% Ho^{3+}/9 mol% Yb^{3+} co-doped Z1T1. As shown in Figure 2.9(a), the result showed that when the system consisted of single dopant, $RE_2Ti_2O_7$ and RE_2TiO_5 phases appeared. Hence, Ho^{3+} and Yb^{3+} exist in the form of RE titanate compounds, even if the system has very low amount of RE^{3+} ions. Further, the XRD peaks were found to shift to higher angle with increasing RE^{3+} ion compositions. As shown in Figure 2.9(b), the magnified XRD patterns of Figure 2.9(a) around $2\theta = 35.2°$ (main peak position of Zn_2TiO_4 phase) showed the single peak with a shift toward higher angles. The shift in the position of diffraction peak confirms the substitution effects and designates a structural modification due to the lattice distortion caused by the incorporation of RE^{3+} ions into Zn_2TiO_4 crystal lattice. Thus, Ho^{3+} and Yb^{3+} also get into the lattice of Zn_2TiO_4 phase.

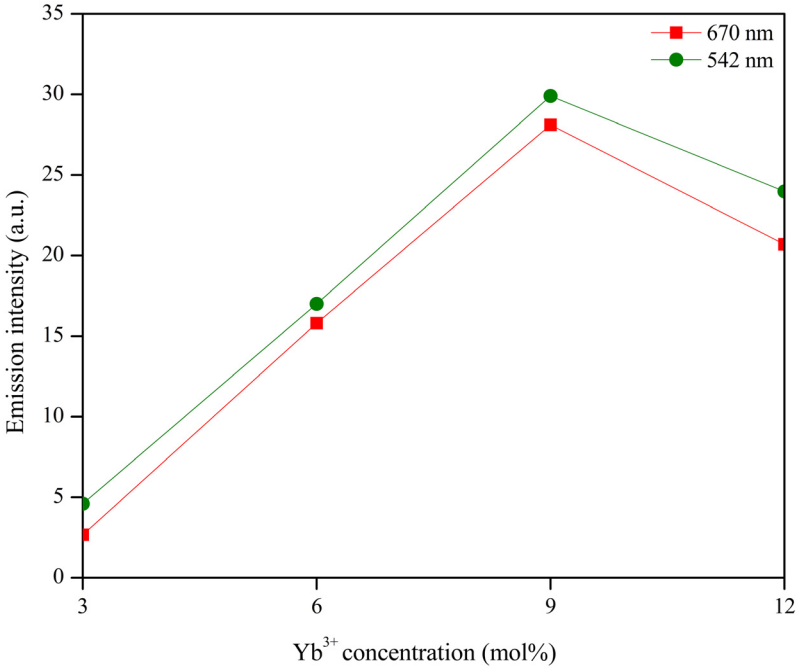

Figure 2.8. The green (542 nm) and red (670 nm) emission intensities of ZnO:TiO_2 = 1:1 (in mole) (Z1T1) doped with 0.05 mol% Ho^{3+} and various mol% Yb^{3+}. Reproduced with permission from Kobwittaya *et al.*, *J. Ceram. Soc. Jpn.*, **125** (2017) 559-564. Copyright (2017) The Ceramic Society of Japan. (License: CC BY-ND 4.0)

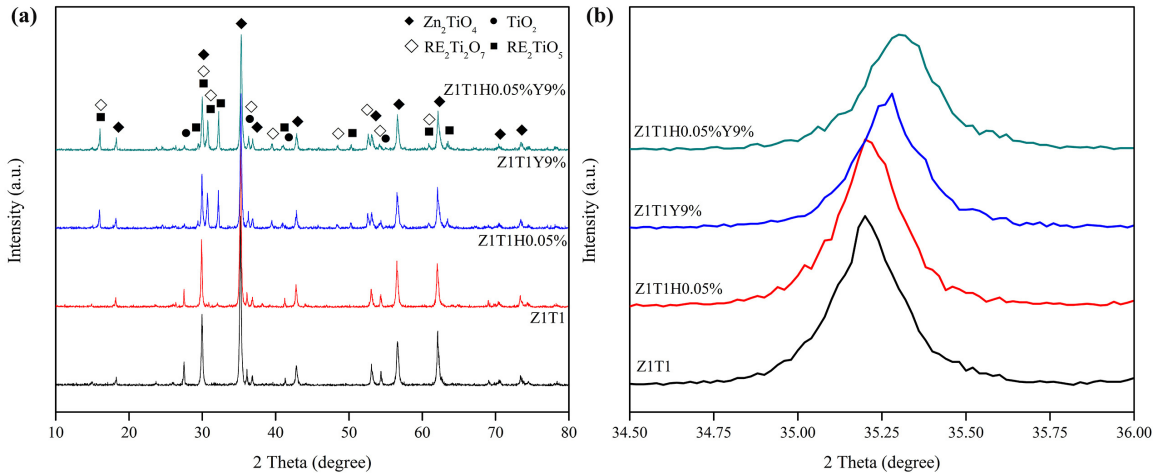

Figure 2.9. (a) XRD patterns of various controlled variables, and (b) the magnified XRD patterns of (a) around 2θ = 35.2°. Reproduced with permission from Kobwittaya *et al.*, *J. Ceram. Soc. Jpn.*, **125** (2017) 559-564. Copyright (2017) The Ceramic Society of Japan. (License: CC BY-ND 4.0)

To comprehend the UC mechanism of ZnO-TiO_2 composite doped with 0.05 mol% Ho^{3+} and 9 mol% Yb^{3+}, the UC emission intensity I was measured as a function of the pump power P. In the UC mechanism, I is proportional to the n power of P, $I \propto P^n$, where n is the number of the pumped photons per the emitted photon [34]. As shown in Figure 2.10, the plotting of log (I) versus log (P) yielded a straight line, resulting the n-value of 1.29 and 1.16 (under between P = 15-196 mW) for the green and red emissions, respectively. Typically, the experimental n-value is in the specific range of values and less than the maximum theoretical n-value for each possible UC mechanism; two-photon process ($1 < n \leq 2$) or three-photon process ($2 < n \leq 3$), because of the saturation effect in the UC emission intensity mainly caused by the competition between linear decay and UC processes for the depletion of the intermediate excited states [35]. By this consideration, therefore, the two-photon process is responsible for the UC mechanism of this UC phosphor system. Taking into account the obtained n-values, they are relatively much lower than two owing to the following reasons. In the UC phosphor system, not only the competition between linear decay and UC processes is a main cause of the decrease in n-value, but some processes like energy transfer to impurity defects, multi-phonon relaxation, and cross-relaxation also influence on the diminution of n-value because these

processes result in the lack of energy in the intermediate excited states of Ho^{3+} and Yb^{3+} which directly affects the change in slope value.

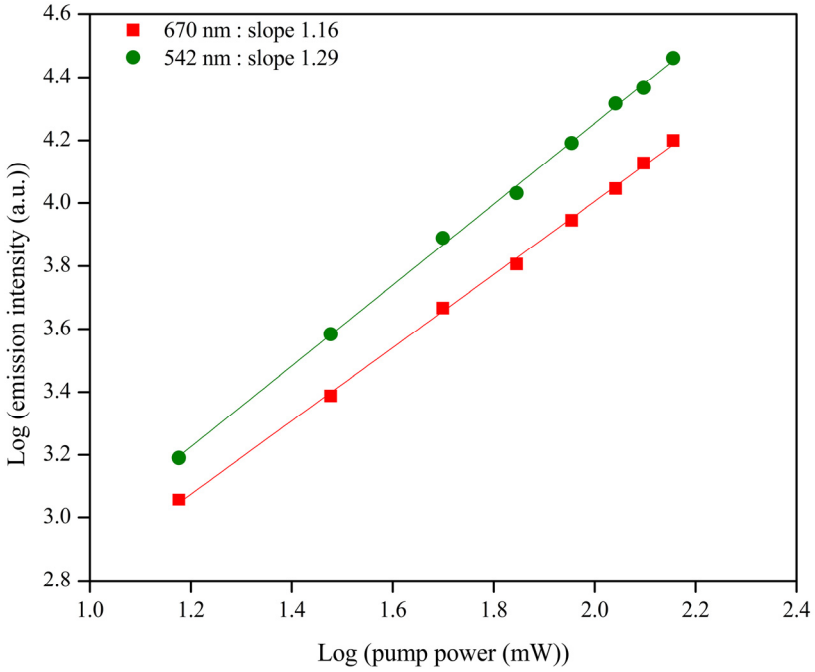

Figure 2.10. Pump power dependent UC of $ZnO:TiO_2$ = 1:1 (in mole) (Z1T1) doped with 0.05 mol% Ho^{3+} and 9 mol% Yb^{3+}. Reproduced with permission from Kobwittaya *et al.*, *J. Ceram. Soc. Jpn.*, **125** (2017) 559-564. Copyright (2017) The Ceramic Society of Japan. (License: CC BY-ND 4.0)

Figure 2.11 shows the simplified energy level diagram of Ho^{3+} and Yb^{3+}, and the possible mechanism of energy transfer (ET) under a 980-nm laser excitation. First, Yb^{3+} is excited from $^2F_{7/2} \rightarrow {}^2F_{5/2}$ energy level. Further, Yb^{3+} transfers its energy to adjacent Ho^{3+} by three ETs. The first ET is $^2F_{5/2}$ (Yb^{3+}) + $^5I_8$ (Ho^{3+}) → $^2F_{7/2}$ (Yb^{3+}) + $^5I_6$ (Ho^{3+}) (probably straight to the same level as $^2F_{5/2}$ (Yb^{3+}), named virtual $^2F_{5/2,}$ Dashed line). Subsequently, the non-radiative (NR) transition of virtual $^2F_{5/2} \rightarrow {}^5I_6$ takes place and then the second ET is $^2F_{5/2}$ (Yb^{3+}) + $^5I_6$ (Ho^{3+}) → $^2F_{7/2}$ (Yb^{3+}) + $^5F_{4,}$ $^5S_2$ (Ho^{3+}). The green emission centered maximum at 542 nm is observed by radiative transition of $^5F_{4,}$ $^5S_2$ → $^5I_8$. The red emission centered maximum at 670 nm in accordance with $^5F_5 \rightarrow {}^5I_8$ transition is possibly due to the two possible processes. One is the NR transition of Ho^{3+} related to $^5F_{4,}$ $^5S_2 \rightarrow {}^5F_5$ transition. The second is the NR transition of Ho^{3+} related to $^5I_6 \rightarrow {}^5I_7$ transition and subsequent process of populating energy to $^5F_5$ energy

level by $^5I_7 \rightarrow {}^5F_5$ transition. This second possibility is related to the third ET that can be written as the ET process in the term of $^2F_{5/2}(Yb^{3+}) + {}^5I_7(Ho^{3+}) \rightarrow {}^2F_{7/2}(Yb^{3+}) + {}^5F_5(Ho^{3+})$. Considering the observed *n*-values and this proposed energy level diagram, it is obvious that the two-photon process is liable for the green and red UCL in ZnO-TiO_2 composite containing Ho^{3+} and Yb^{3+}, with the contemplation of NR between ETs of each energy level.

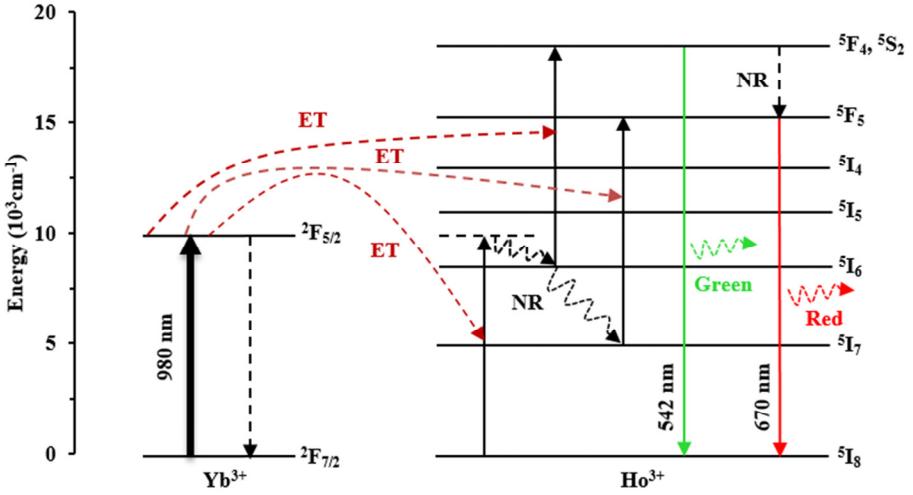

Figure 2.11. Energy level diagram illustrating the proposed energy transfers mechanism of ZnO-TiO_2 composite doped with 0.05 mol% Ho^{3+} and 9 mol% Yb^{3+} under a 980-nm laser excitation. Reproduced with permission from Kobwittaya *et al.*, *J. Ceram. Soc. Jpn.*, **125** (2017) 559-564. Copyright (2017) The Ceramic Society of Japan. (License: CC BY-ND 4.0)

2.4 Conclusion

ZnO-TiO_2 composite system containing Ho^{3+} and Yb^{3+} was successfully synthesized by solid-state reaction method. The UC emission intensity centered at 542 and 670 nm wavelengths was observed at room temperature. The green and red emission intensities reached a maximum value in the sample containing 0.05 mol% Ho^{3+} and 9 mol% Yb^{3+}. The optimum ZnO/TiO_2 mixing ratio was ZnO:TiO_2 = 1:1 (in mole). Brightest UCL emitted by ZnO-TiO_2: Ho^{3+}/Yb^{3+} phosphor occurred when the system consisted of mixed phases; Zn_2TiO_4, TiO_2, $RE_2Ti_2O_7$, and RE_2TiO_5 (RE = Ho^{3+} and/or Yb^{3+}). In addition, when using solid-state reaction method, it is possible that Ho^{3+} dissolve into Zn_2TiO_4 matrix more difficult than Er^{3+} due to the existence of RE_2TiO_5 phase that occurs only in Ho^{3+}/Yb^{3+} system.

2.5 Acknowledgements

This chapter contains contributions from co-authors and was published in: K. Kobwittaya, Y. Oishi, T. Torikai, M. Yada, T. Watari, H.N. Luitel, Synthesis and upconversion luminescence properties of ZnO-TiO_2 containing Ho^{3+} and Yb^{3+}, *Journal of the Ceramic Society of Japan*, **125** (2017) 559-564.

2.6 Copyright permission

References

[1] L. Wang, M. Lan, Z. Liu, G. Qin, C. Wu, X. Wang, W. Qin, W. Huang, L. Huang, *J. Mater. Chem. C*, **1** (2013) 2485-2490.

[2] K. Yamamoto, M. Fujii, S. Sowa, K. Imakita, K. Aoki, *J. Phys. Chem. C*, **119** (2015) 1175-1179.

[3] E. Downing, L. Hesselink, J. Ralston, R. Macfarlane, *Science*, **273** (1996) 1185-1189.

[4] H. Lin, G. Meredith, S. Jiang, X. Peng, T. Luo, N. Peyghambarian, E.Y.B. Pun, *J. Appl. Phys.*, **93** (2003) 186-191.

[5] G.-S. Yi, G.-M. Chow, *Chem. Mater.*, **19** (2007) 341-343.

[6] E.L. Cates, M. Cho, J.-H. Kim, *Environ. Sci. Technol.*, **45** (2011) 3680-3686.

[7] S. Heer, O. Lehmann, M. Haase, H.-U. Güdel, *Angew. Chem. Int. Edit.*, **42** (2003) 3179-3182.

[8] X. Wang, S. Xiao, Y. Bu, J.W. Ding, *J. Alloy. Compd.*, **477** (2009) 941-945.

[9] Y. Li, B. Chen, X. Zhao, Z. Wang, H. Lin, *J. Alloy. Compd.*, **536** (2012) 198-203.

[10] Z. Li, S. Xiao, X. Yang, J.W. Ding, G.Y. Tan, X.H. Yan, *Physica B*, **407** (2012) 2584-2587.

[11] Z. Wang, J. Feng, M. Pang, S. Pan, H. Zhang, *Dalton T.*, **42** (2013) 12101-12108.
[12] H.X. Yang, H. Lin, L. Lin, Y.Y. Zhang, B. Zhai, E.Y.B. Pun, *J. Alloy. Compd.*, **453** (2008) 493-498.
[13] J. Shan, X. Qin, N. Yao, Y. Ju, *Nanotechnology*, **18** (2007) 445607-445614.
[14] N. Niu, P. Yang, Y. Liu, C. Li, D. Wang, S. Gai, F. He, *J. Colloid Interf. Sci.*, **362** (2011) 389-396.
[15] W.M. Yen, S. Shionoya, H. Yamamoto, Phosphor Handbook, Second Edition, CRC Press, Boca Raton, Florida (2006).
[16] T.J. Bruno, P.D.N. Svoronos, CRC Handbook of Fundamental Spectroscopic Correlation Charts, CRC Press, Boca Raton, Florida (2005).
[17] R.-S. Liu, Phosphors, Up conversion Nano Particles, Quantum Dots and Their Applications (Volume 2), Springer Science+Business Media Singapore, Singapore (2016).
[18] X. Li, J. Zhu, Z. Man, Y. Ao, H. Chen, *Sci. Rep.*, **4** (2014) 4446.
[19] R. Dey, A. Kumari, A.K. Soni, V.K. Rai, *Sensor. Actuat. B-Chem.*, **210** (2015) 581-588.
[20] J. Ohwaki, Y. Wang, *Jpn. J. Appl. Phys.*, **33** (1994) L334-L337.
[21] X.-X. Luo, W.-H. Cao, *Mater. Lett.*, **61** (2007) 3696-3700.
[22] X.P. Chen, W.J. Zhang, Q.Y. Zhang, *Physica B*, **406** (2011) 1248-1252.
[23] M. Haase, H. Schäfer, *Angew. Chem. Int. Edit.*, **50** (2011) 5808-5829.
[24] F. Wang, X. Liu, *Chem. Soc. Rev.*, **38** (2009) 976-989.
[25] K.K. Kar, Composite Materials: Processing, Applications, Characterizations, Springer-Verlag Berlin Heidelberg (2017).
[26] M.-W. Kim, H. Yoon, T.Y. Ohm, H.S. Jo, S. An, S.K. Choi, H. Park, S.S. Al-Deyab, B.K. Min, M.T. Swihart, S.S. Yoon, *Appl. Catal. B-Environ.*, **201** (2017) 479-485.
[27] H.-S. Lim, J. Lee, S. Lee, Y.S. Kang, Y.-K. Sun, K.-D. Suh, *Acta Mater.*, **122** (2017) 287-297.
[28] L. Li, Y. Fan, D. Wang, G. Feng, D. Xu, *Cryst. Res. Technol.*, **46** (2011) 475-479.
[29] L. Li, F. Li, T. Cui, Q. Zhou, D. Xu, *Phys. Status Solidi A*, **209** (2012) 2596-2599.
[30] H.N. Luitel, K. Ikeue, R. Okuda, R. Chand, T. Torikai, M. Yada, T. Watari, *Opt. Mater.*, **36** (2014) 591-595.
[31] Y. Xu, M. Yamazaki, P. Villars, *Jpn. J. Appl. Phys.*, **50** (2011) 11RH02.

[32] E.M. Levin, C.R. Robbins, H.F. McMurdie, Phase Diagram for Chemists Volume I (Figures 1-2066), The American Ceramic Society, Inc., Columbus, Ohio (1964).
[33] A. Jain, G. Hautier, S.P. Ong, C.J. Moore, C.C. Fischer, K.A. Persson, G. Ceder, *Phys. Rev. B*, **84** (2011) 045115.
[34] F. Auzel, *Chem. Rev.*, **104** (2004) 139-174.
[35] M. Pollnau, D.R. Gamelin, S.R. Lüthi, H.U. Güdel, M.P. Hehlen, *Phys. Rev. B*, **61** (2000) 3337-3346.

Chapter III

Bright red upconversion luminescence from Er^{3+} and Yb^{3+} co-doped $ZnO\text{-}TiO_2$ composite phosphor powder

3.1 Introduction

Upconversion luminescence (UCL) can be simply described as the light conversion which converts near infrared (NIR) light into visible (VIS) or ultraviolet (UV) light. In consequent of the absorption of at least two photons, a higher energy photon is emitted [1]. Since the UCL was discovered in the 1960s until nowadays, trivalent rare earth (RE^{3+}) ions are employed as UCL center because of their energy levels structure [2-4]. The luminescence emission from RE^{3+} ions mainly occurs due to its particular 4*f* transitions, leading to sharp emissions and narrow emission bands [5,6]. In recent decades, RE^{3+} ions doped UC phosphors have been extensively investigated for the advancement in new applications and technologies such as latent fingerprint identification [7], and electronic and optical communication devices [8,9].

The RE^{3+} ions in the host crystal matrix play an important role as the activator and the sensitizer for generating UCL. The activator is employed as luminescent center which emits high energy light, and the sensitizer is an ion that harvests the excited energy efficiently and then transfers that energy to the activator. In general, Er^{3+}, Ho^{3+}, and Tm^{3+} are the most widely used activator due to their plentiful electronic energy levels to adapt UCL [8,10,11], and Yb^{3+} is generally a co-dopant which plays a significant role as sensitizer because it has large absorption cross-section around 980 nm [12]. According to the energy level and the role of each RE^{3+} ion, Er^{3+}/Yb^{3+} co-doped host materials have been widely studied because of good energy level matching between these two ions, offering the efficient energy transfer from $Yb^{3+} \rightarrow Er^{3+}$ which advocates the NIR to visible UC process [1,13].

Host material is also significant for generating efficient UCL. In theory, the most considerable point for choosing productive UC host materials to obtain high performance UCL is phonon

energy. It is well established that the UC host material should have low phonon energy because phonons provide non-radiative decay ways to suppress radiative emission, causing to the low UCL intensity [13]. Even though some host materials such as halides and fluorides exhibit low phonon energy around 300 cm^{-1} and 350 cm^{-1}, respectively, but the practical applications are still limited due to their instability and hygroscopic. In comparison, oxides exhibit higher thermal and chemical stability, therefore, suitable oxides with low phonon energy may have more promising applications [14].

Nowadays, many new applications and technologies require a variety of properties of material which traditional materials have limited applicability. Composite materials, which consist of the combination of two phases or more with different physical and chemical properties, have gained much attention, study, and investigation in recent years since this type of material is typically light weight, flexible, high corrosion resistance, and impact strength. Because of these properties, composite materials have been considered as an alternative material for supplanting classical materials used in aerospace industry, construction, and electrical and electronics [15]. The ZnO-TiO_2 composite is considered as a promising UC host material due to its low cost, thermal and chemical stability, and environmental friendliness. Additionally, the noteworthy product of ZnO-TiO_2 composite is Zn_2TiO_4 that is a high thermal stability phase due to its inverse spinel structure. With these properties, many researches on ZnO-TiO_2 composite have been conducted and studied for applying in various applications such as nanofiber photocathode [16] and photocatalysis [17]. In addition, Zn_2TiO_4 shows great potential for being the good optical host because it has high value of refractive index n = 2.1 [18] and low phonon energy around 721 cm^{-1} [19], which control part of energy losses in the electron toward phonon energy transfer and other non-radiative processes [20]. Therefore, Zn_2TiO_4 phase could be one of the candidate hosts for UCL applications. However, now there are a few reports regarding UCL on ZnO-TiO_2 composite. For example, the intense visible UCL was observed in ZnO-TiO_2 composite doped with Er^{3+} and Yb^{3+} prepared by solid-state reaction method [21,22] and metal-organic decomposition method [23,24].

According to the report presented by Luitel *et al.* [21], ZnO-TiO_2: Er^{3+},Yb^{3+} prepared by solid-state reaction method showed bright orange emission and the suitable condition for emitting the brightest emission was ZnO:TiO_2 = 1:1 (in mole): 2 mol% Er^{3+}, 6 mol% Yb^{3+} fired at 1200 °C

for 4 h and the product consisted of Zn_2TiO_4, TiO_2, and $RE_2Ti_2O_7$ phases. Theoretically, the formation of the product prepared by solid-state reaction method is diffusion limited, leading to incomplete reaction, some loss of reactants, and compositionally inhomogeneous products [13]. Therefore, in this chapter, ZnO-TiO_2 composite doped with Er^{3+} and Yb^{3+} was examined by the new simple method, namely powder-solution mixing method, to produce the UC phosphor with homogeneous phase in the form of powder. The effect of firing temperature, ZnO/TiO_2 mixing ratio, Er^{3+} and Yb^{3+} doping concentrations and their ratios on the crystal phase, and UCL properties were systematically investigated. To our best knowledge, ZnO-TiO_2:Er^{3+},Yb^{3+} phosphor system shows the complex product in the form of multiphase coexistence, causing to uncertain investigation on finding out actual position of RE^{3+} ions in host crystal matrix. So, this is the first study on the analysis of possible site preference of RE^{3+} ions in the host material, when the system contains the final product with multiple phases. This analysis was attentively considered by focusing on luminescence spectra together with lattice constant, lattice volume, and crystal structure of target host material. In addition, the simple chemical formula equations of RE^{3+} ions site preference are developed for the rendition of the experimental results.

3.2 Experimental

3.2.1 Sample preparation

ZnO-TiO_2 composite doped with Er^{3+} and Yb^{3+} was prepared by powder-solution mixing method using zinc oxide powder (ZnO; NanoTek, ~ 34 nm, 99%), titanium dioxide sol solution (TiO_2; Ishihara Sangyo Kaisha, 39.5 wt%), erbium (III) nitrate pentahydrate ($Er(NO_3)_3 \cdot 5H_2O$; Aldrich, 99.9%), and ytterbium (III) nitrate pentahydrate ($Yb(NO_3)_3 \cdot 5H_2O$; Aldrich, 99.9%). All raw materials were completely mixed together by a high-power mixer using deionized water. Various ZnO-TiO_2 samples with different ZnO/TiO_2 mixing ratios were made by changing ZnO amounts, while keeping constant TiO_2 (1 mole). The ZnO/TiO_2 mixing ratio (x) varied from x = 0.25-1.75 mole and the sample was named as ZxT1. Er^{3+} and Yb^{3+} concentrations changed from 0-5 mol% and 0-12 mol% based on TiO_2 content, respectively. After thoroughly mixing, the sample was dried at 90 °C in drying oven for 12 h and then fired in an air atmosphere with various temperatures of 800-1400 °C for 1 h. To obtain the final

product, the fired sample was grounded by using Vibrating Sample Mill (HEIKO, TI-100). The complete preparation scheme is shown in Figure 3.1.

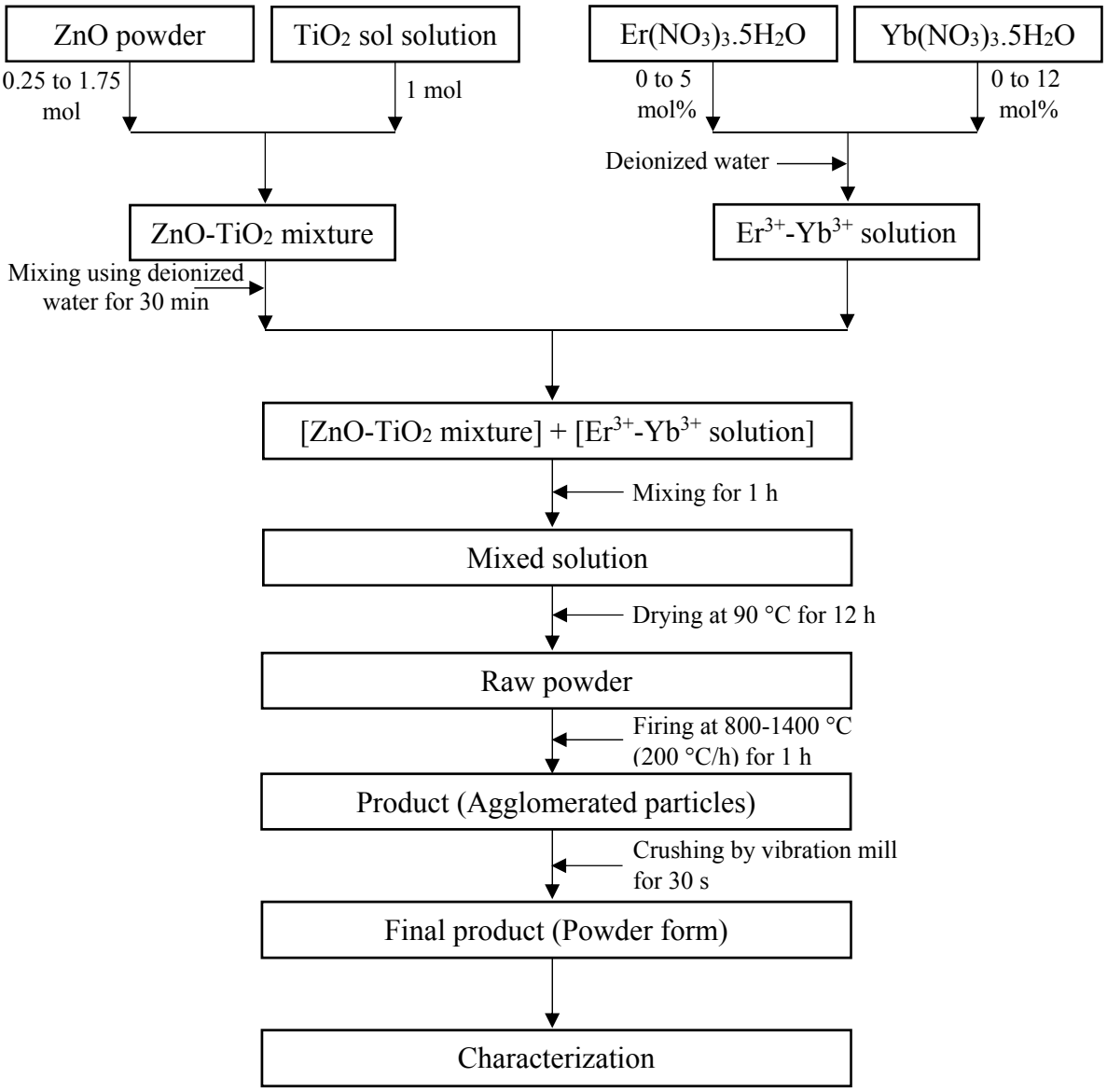

Figure 3.1. Flow chart for the preparation of ZnO-TiO_2:Er^{3+}/Yb^{3+} phosphor by powder-solution mixing method.

3.2.2 Characterizations

Thermogravimetric and differential thermal analysis (TG-DTA) of raw material and raw mixture was carried out using a SEIKO EXSTAR6000 TG/DTA6300 instrument. About 10 mg

of each sample were heated from room temperature to target temperature at heating rate of 10 °C/min. Fourier transform infrared spectroscopy analysis (FTIR) of TiO_2 sol solution was performed using a JASCO FT/IR-460 Plus Fourier transform infrared (FTIR) spectrometer. The disc was prepared by mixing 1 mg of powdered TiO_2 (dried and/or fired TiO_2 sol solution) with 100 mg of potassium bromide (KBr). The FTIR spectra were recorded in the wavenumber range of 4000-399 cm^{-1}.

The crystallinity was evaluated using X-Ray diffraction (XRD), a Shimadzu XRD-6300 instrument with CuKα radiation in the range of 2θ = 10-80°. In this study, there were two types of XRD analysis that was operated. First, continuous scan type, the instruction set was fixed at step size = 0.02°, time per point = 0.6 s, and scan speed = 2° min^{-1}. Second, to obtain the high accuracy and precision XRD results, the step scan type was used by fixing the maximum count = 8000, step size = 0.02°, and the time per point for analyzing was calculated using equations (3.1) and (3.2):

count per sec (cps) = [maximum count from continuous scan data] / [0.6 s] (3.1)

time per point (s) = [8000 counts] / [count per sec (cps)] (3.2)

Typically, the XRD result with step scan type is suitable for determining the variation of host material composition and site preference of dopants via Rietveld refinement. In this study, Rietveld analysis cannot be used to demonstrate the value of cell parameter or even to identify site preference of dopants in host crystal matrix because the final product was in the state of multiple phases and its XRD result showed many overlapping peaks in which some peaks were nebulous and hard to define the phase of such peak position. The result of Rietveld analysis of the products according to the mentioned details will be provided and discussed in more detail later. Herein, to explain the crystallization process of the final product with multiple phases, the relative phase content by pseudo-quantitative analysis of a specific phase was estimated from the XRD results (continuous scan type) and calculated using equation (3.3):

$$\text{Relative phase content} = I_{(\text{phase})} / I_{(\text{total})} \quad (3.3)$$

where $I_{(\text{phase})}$ is the intensity of selected peak from a main peak position that consists of only one phase; $I_{(311)}$ for Zn_2TiO_4, $I_{(110)}$ for TiO_2, $I_{(004)}$ for $RE_2Ti_2O_7$, and $I_{(102)}$ for RE_2TiO_5; and $I_{(\text{total})}$ is the intensity summation of all selected peaks.

The microstructure of the samples was characterized by scanning electron microscopy (SEM), a Hitachi S-3000N instrument. Before SEM measurement, the sample was mounted securely by means of conductive carbon tape. Subsequently, the sample was coated with a thin layer of Pt-Pd (coating time of 90 s, around 5 nm thickness) under vacuum condition (vacuum-argon gas flushing) by ion sputter (Hitachi, E-1030).

The surface structure measurement was carried out using digital microscope Keyence VHX-5000. The elemental composition analysis was carried out using X-ray fluorescence spectroscopy (XRF), a Shimadzu Energy Dispersive X-ray Fluorescence Spectrometer (Rayny EDX-800HS) instrument. The UC emission excited by a 980-nm continuous waveform laser was recorded from 250-800 nm spectral range using USB 4000 UV-VIS-NIR fiber optic spectrometer (Ocean optics), having spectral resolution 1.34 nm (full width at half maximum, FWHM) and slit width 25 μm. The change in maximum luminescence emission intensity on the laser power range of 0-200 mW was used for considering the UC mechanism. All samples were measured at room temperature.

3.3 Results and discussion

3.3.1 Thermogravimetric and differential thermal analysis (TG-DTA) of raw material

To understand the formation of the final product, it is compulsory to observe the thermal behavior of the raw mixture. As shown in Figure 3.2, TG-DTA measurement was carried out in the temperature range from room temperature (20 °C) to 1300 °C for a representative sample (raw powder mixture of the most efficient product), and it was obvious that no thermal effect and no further weight loss were observed after 600 °C. So that, to explain this result in detail, the TG-DTA of each precursor was studied by considering the thermal process of each precursor in the temperature range from room temperature to 600 °C.

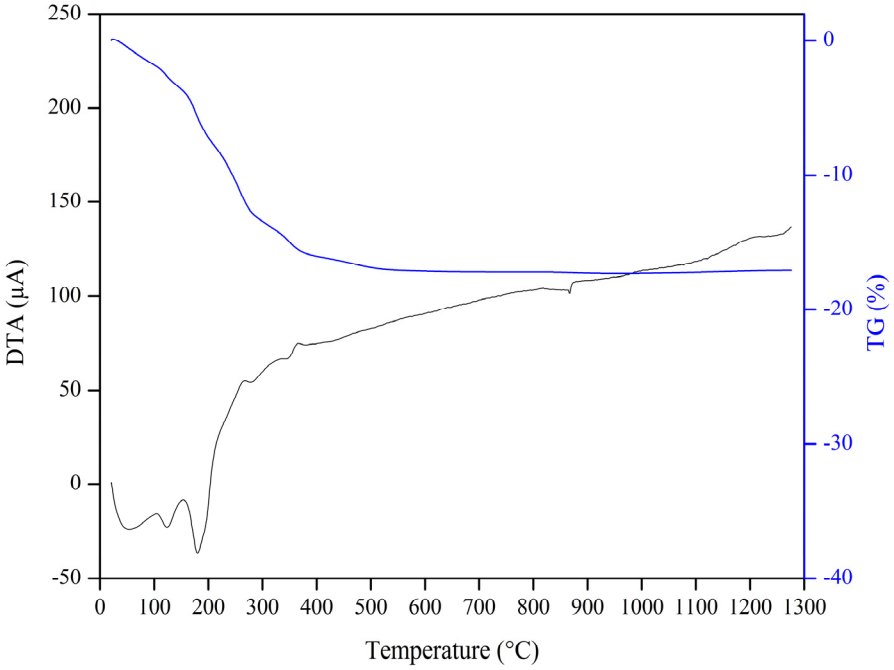

Figure 3.2. TG-DTA curves in the temperature range from room temperature (20 °C) to 1300 °C for ZnO:TiO_2 = 1:1 (in mole) doped with 3 mol% Er^{3+} and 9 mol% Yb^{3+} dried at 90 °C.

3.3.1.1 ZnO

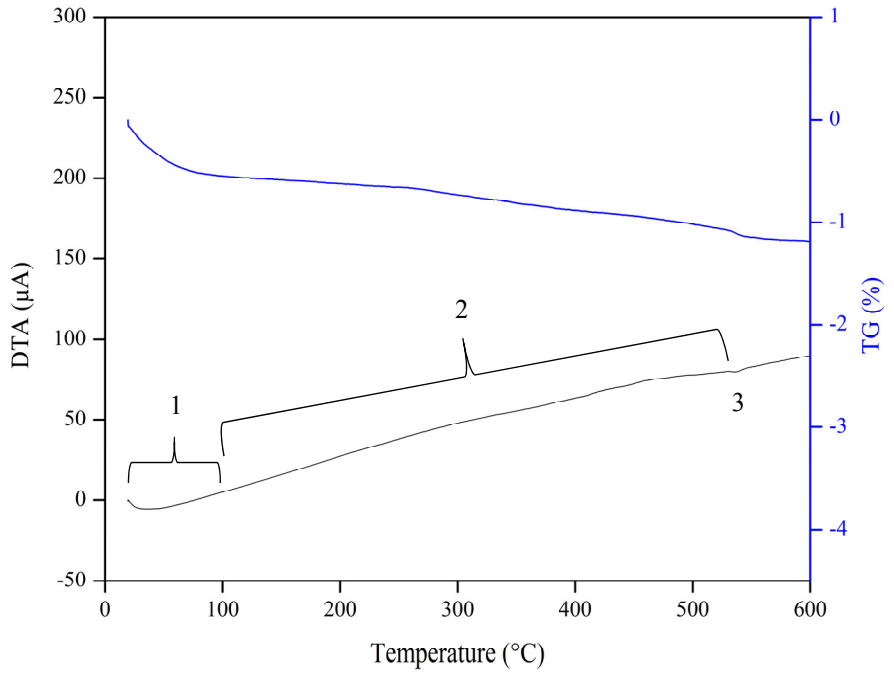

Figure 3.3. TG-DTA curves in the temperature range from room temperature (20 °C) to 600 °C for ZnO powder dried at 90 °C.

As shown in Figure 3.3, it was clearly seen that the dried ZnO powder showed small weight loss about 1.2% in the temperature range from room temperature (20 °C) to 600 °C. At the initial stage, the TG curve decreased about 0.6% due to the endothermic process which corresponded to the DTA curve in the temperature range from 20-100 °C (No.1). This weight loss was due to the dehydration of surface-absorbed water [25]. Subsequently, the DTA curve did not exhibit obvious endothermic or exothermic peaks in the temperature range from 100-530 °C (No. 2), but the weight loss was detected in the TG curve about 0.4%. Further, there was an endothermic process that occurred at around 540 °C (No.3) and the weight loss was observed about 0.2%. The second and third weight losses were related to the evaporation of water and the decomposition of ZnO powder. Therefore, it can be summarized that most weight losses observed come from the evaporation process and this precursor is relatively stable above 540 °C. In addition, similar results were reported by Raoufi [26,27]. He reported the TG-DTA curves of ZnO nanoparticles and his results proved that the decomposition of ZnO nanoparticles is mainly complete at temperature below 600 °C.

3.3.1.2 TiO_2 sol solution

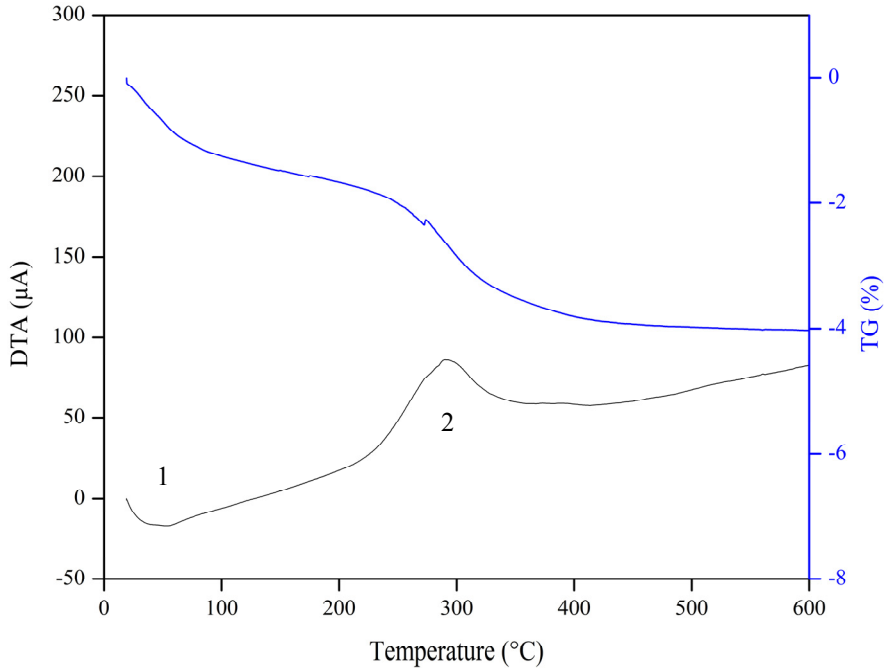

Figure 3.4. TG-DTA curves in the temperature range from room temperature (20 °C) to 600 °C for TiO_2 sol solution dried at 90 °C.

As shown in Figure 3.4, the TG curve represented small weight loss which was in accordance with DTA curve in the temperature range from room temperature (20 °C) to 250 °C. The total weight loss in this temperature range was caused by the endothermic process and corresponded to about 2%. It could contribute to the removals of adsorbed water, consisting of the dehydration of surface-absorbed water (around 20-100 °C, No.1) and the evaporation of water (around 90-250 °C). Later, there was one peak corresponding to the exothermic process and the weight loss about 2% located around 250-400 °C (No.2). This exothermic process might come from the burning out of the surfactant which it was added to the TiO_2 sol solution for the dispersion stabilization of TiO_2 particles and it cannot be removed with drying at low temperature. Generally, the surfactant is organic compound which can be analyzed using FTIR to confirm the existence of this compound by finding out fundamental structure of carbon bonds. The FTIR result of TiO_2 sol solution will be discussed later. Under between 400-600 °C, a very small change in the weight loss was observed, indicating that the decomposition of TiO_2 is almost complete at this stage.

3.3.1.3 $Yb(NO_3)_3{\cdot}5H_2O$

The TG-DTA curves of $Yb(NO_3)_3{\cdot}5H_2O$ are shown in Figure 3.5. There were eleven endothermic processes, covering total weight loss about 60% which was in accordance with the temperature range from room temperature (20 °C) to 498 °C. The initial process started by the melting of material because the physical change took place during raising temperature [28-30]. Subsequently, $Yb(NO_3)_3{\cdot}5H_2O$ changed to $Yb(NO_3)_3{\cdot}4H_2O$ through dehydration process according to process No.1. Further, process No.2 to No.5 were the dehydration and evaporation processes that agreed with the transformation of $Yb(NO_3)_3{\cdot}4H_2O$ to $Yb(NO_3)_3$. Also, it could be considered that process No.2 to No.5 were the overlapping endothermic mass loss process. And, the dehydration and evaporation processes were confirmed by the calculation of the change in observed weight loss for each process which were close to theoretically calculated weight loss for releasing 4 moles of water (Table 3.1). Process No.6 to No.11 were the decomposition process which decayed $Yb(NO_3)_3$ to $YbO_{0.5}NO_3$. Taking into account process No.8 and No.10 that showed strong endothermic process, peaking at around 339 °C and 470 °C, respectively, these two peaks were related to NO_x by-product formation during the decomposition process [28]. In the last process (No. 12), the final product was Yb_2O_3 that came

from the decomposition process of $YbO_{0.5}NO_3$. Eventually, there was only one remaining product, Yb_2O_3, and no thermal effect and no further weight loss were observed. The summarized data from TG-DTA result of $Yb(NO_3)_3{\cdot}5H_2O$ is shown in Table 3.1 and it should be noted that all compositions (except Yb_2O_3) presented in Table 3.1 are predicted based on the calculation of the change in theoretical weight loss of each compound that mainly concerns the observed weight loss at specific temperature. Atomic weights used for calculating theoretical weight loss are Yb = 173.045, N = 14.007, H = 1.008, and O = 15.999. Additionally, similar results were obtained by Balboul [28] in the study of the decomposition of $Yb(NO_3)_3{\cdot}6H_2O$ that showed Yb_2O_3 as a final product at 510 °C. With this report, the comparison of TG-DTA result of $Yb(NO_3)_3{\cdot}5H_2O$ and Balboul's work [28] is concluded and shown in Table 3.2.

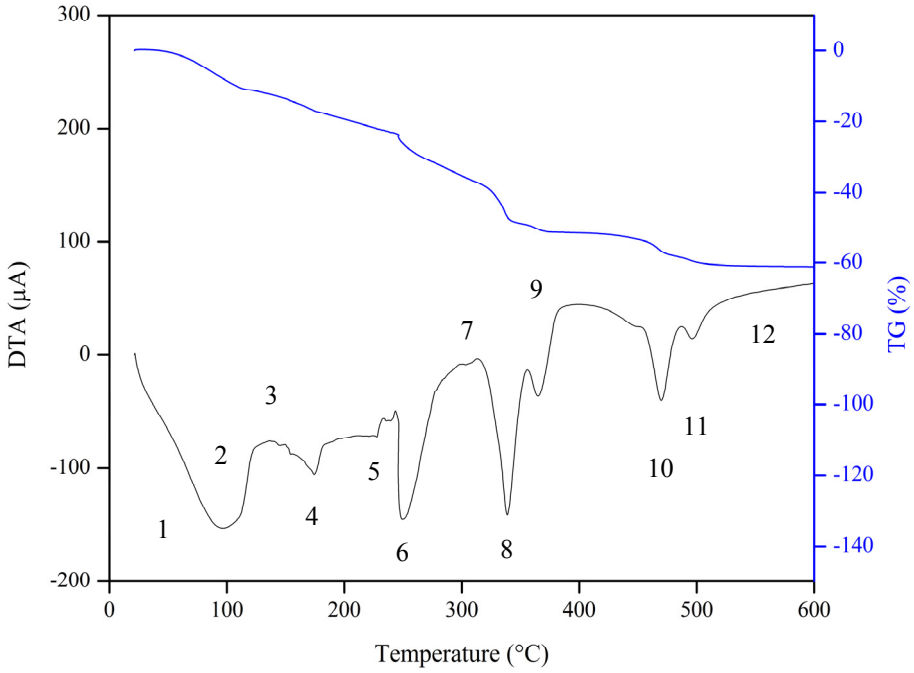

Figure 3.5. TG-DTA curves in the temperature range from room temperature (20 °C) to 600 °C for $Yb(NO_3)_3{\cdot}5H_2O$.

Table 3.1. Thermal processes of $Yb(NO_3)_3{\cdot}5H_2O$; experimental and theoretical weight losses, corresponding temperature point, and composition proposed in each process.

Process	Accumulated weight losses (%) [observed]	Accumulated weight losses (%) [theoretical]	Temperature (°C)	Composition
Start	-	Melting	-	$Yb(NO_3)_3{\cdot}5H_2O$
1	4.0	4.01	78	$Yb(NO_3)_3{\cdot}4H_2O$
2	7.5	8.19	95	$Yb(NO_3)_3{\cdot}3H_2O$
3	12.1	12.55	145	$Yb(NO_3)_3{\cdot}2H_2O$
4	16.9	17.11	174	$Yb(NO_3)_3{\cdot}H_2O$
5	22.0	21.89	227	$Yb(NO_3)_3$
6	26.3	26.34	250	$YbNO_2(NO_3)_2$
7	37.0	37.42	320	$YbO_{0.5}(NO_3)_2$
8	46.9	46.27	339	$YbO_{0.75}(NO_3)_{1.5}$
9	50.5	50.59	366	$Yb(NO_3)_{1.5}$
10	56.8	56.23	470	$YbO(NO_3)$
11	59.7	59.42	498	$YbO_{0.5}(NO_3)$
12	> 59.7	> 59.42	> 498	Yb_2O_3

Table 3.2. Comparison of thermal processes of $Yb(NO_3)_3{\cdot}5H_2O$ and of $Yb(NO_3)_3{\cdot}6H_2O$; experimental and theoretical weight losses, and composition proposed in each process.

Process	In this work			Balboul [28]		
	Accumulated weight losses (%)		Composition	Accumulated weight losses (%)		Composition
	observed	theoretical		observed	theoretical	
Start	-	Melting	$Yb(NO_3)_3{\cdot}5H_2O$	-	Melting	$Yb(NO_3)_3{\cdot}6H_2O$
				3.85	6.85	$Yb(NO_3)_3{\cdot}5H_2O$
1	4.0	4.01	$Yb(NO_3)_3{\cdot}4H_2O$	7.50	7.50	$Yb(NO_3)_3{\cdot}4H_2O$
2	7.5	8.19	$Yb(NO_3)_3{\cdot}3H_2O$	11.56	11.56	$Yb(NO_3)_3{\cdot}3H_2O$
3	12.1	12.55	$Yb(NO_3)_3{\cdot}2H_2O$	-	-	-
4	16.9	17.11	$Yb(NO_3)_3{\cdot}H_2O$	19.27	19.27	$Yb(NO_3)_3{\cdot}H_2O$
5	22.0	21.89	$Yb(NO_3)_3$	23.40	23.12	$Yb(NO_3)_3$
6	26.3	26.34	$YbNO_2(NO_3)_2$	-	-	-
7	37.0	37.42	$YbO_{0.5}(NO_3)_2$	34.30	34.68	$YbO_{0.5}(NO_3)_2$
8	46.9	46.27	$YbO_{0.75}(NO_3)_{1.5}$	40.80	40.47	$YbO_{0.75}(NO_3)_{1.5}$
9	50.5	50.59	$Yb(NO_3)_{1.5}$	-	-	-
10	56.8	56.23	$YbO(NO_3)$	46.20	46.25	$YbO(NO_3)$
11	59.7	59.42	$YbO_{0.5}(NO_3)$	52.10	52.03	$YbO_{1.25}(NO_3)_{0.5}$
12	> 59.7	> 59.42	Yb_2O_3	57.70	57.80	Yb_2O_3

3.3.1.4 $Er(NO_3)_3{\cdot}5H_2O$

The TG-DTA curves of $Er(NO_3)_3{\cdot}5H_2O$ are shown in Figure 3.6. There were ten endothermic processes, covering total weight loss about 53% which was in accordance with the temperature range from room temperature (20 °C) to 533 °C. The first process (No.1) was due to the melting of material because the physical change took place during raising temperature [28-30]. Further, process No.2 to No.7 were the dehydration and evaporation processes that were in accordance with the change in compositions from $Er(NO_3)_3{\cdot}5H_2O$ to $Er(NO_3)_3{\cdot}0.5H_2O$. Also, it could be considered that these processes were overlapping endothermic mass loss process. The dehydration and evaporation processes were confirmed by the calculation of the change in observed weight loss for each process which were close to theoretically calculated weight loss for releasing 5 moles of water Table 3.3. Later, process No.8 to No.10 were the decomposition process which decayed $Er(NO_3)_3{\cdot}0.5H_2O$ to $ErO_{0.5}(NO_3)_{1.25}$. Considering process No.8 and No.9 that showed strong endothermic process, peaking at around 343 °C and 479 °C, respectively, these two peaks were related to NO_x by-product formation during the decomposition process [28]. In the last process (No. 11), the final product was Er_2O_3 that came from the decomposition process of $ErO_{0.5}(NO_3)_{1.25}$. Finally, there was only one remaining product, Er_2O_3, and no thermal effect and no further weight loss were observed.

Up to now, there is no proof of the decomposition of erbium nitrate, but according to Balboul's reports [28-30], Yb_2O_3, Ho_2O_3, and Er_2O_3 were the final decomposition product of the reactants that contained rare earth element. Thus, all nitrate molecules could be totally decomposed at high temperature especially over 500 °C. The summarized data from TG-DTA result of $Er(NO_3)_3{\cdot}5H_2O$ is shown in Table 3.3 and it should be noted that all compositions (except Er_2O_3) presented in Table Table 3.3 are predicted based on the calculation of the change in theoretical weight loss of each compound that mainly concerns the observed weight loss at specific temperature. Atomic weights used for calculating theoretical weight loss are Er = 167.259, N = 14.007, H = 1.008, and O = 15.999.

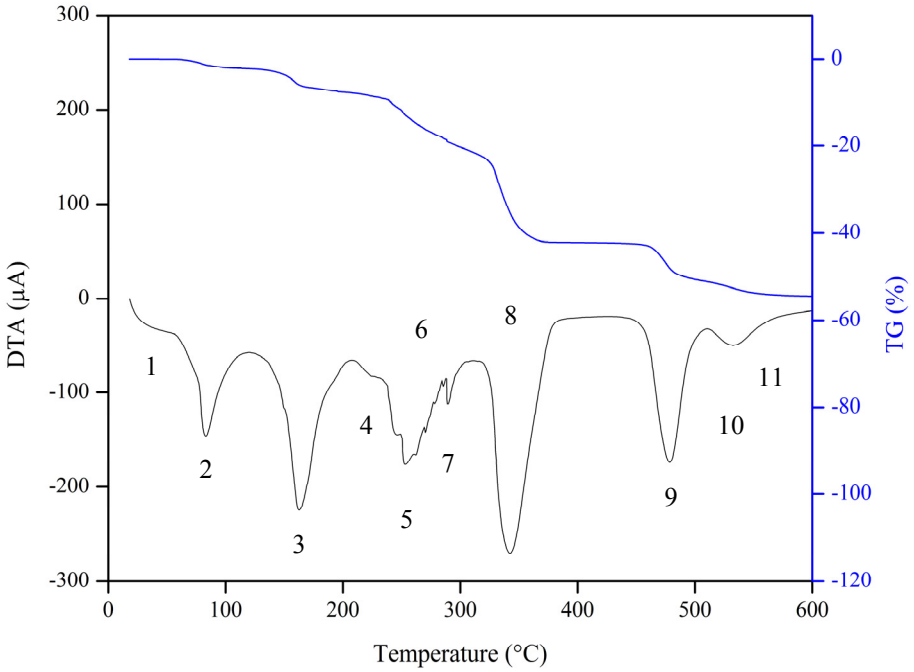

Figure 3.6. TG-DTA curves in the temperature range from room temperature (20 °C) to 600 °C for $Er(NO_3)_3{\cdot}5H_2O$.

Table 3.3. Thermal processes of $Er(NO_3)_3{\cdot}5H_2O$; experimental and theoretical weight losses, corresponding temperature point, and composition proposed in each process.

Process	Accumulated weight losses (%) [observed]	Accumulated weight losses (%) [theoretical]	Temperature (°C)	Composition
Start	-	-	-	$Er(NO_3)_3{\cdot}5H_2O$
1	-	Melting	50	$Er(NO_3)_3{\cdot}5H_2O$
2	1.2	4.06	82	$Er(NO_3)_3{\cdot}4H_2O$
3	5.9	6.18	163	$Er(NO_3)_3{\cdot}3.5H_2O$
4	8.5	8.35	224	$Er(NO_3)_3{\cdot}3H_2O$
5	12.8	12.77	253	$Er(NO_3)_3{\cdot}2H_2O$
6	17.4	17.40	275	$Er(NO_3)_3{\cdot}H_2O$
7	19.2	19.82	290	$Er(NO_3)_3{\cdot}0.5H_2O$
8	35.4	35.01	343	$ErO(NO_3)_2$
9	48.2	47.70	479	$ErO_{0.5}(NO_3)_{1.5}$
10	52.6	53.48	533	$ErO_{0.5}(NO_3)_{1.25}$
11	> 52.6	> 53.48	> 533	Er_2O_3

3.3.2 Thermogravimetric and differential thermal analysis (TG-DTA) of ZnO:TiO_2 = 1:1 (in mole) doped with 3 mol% Er^{3+} and 9 mol% Yb^{3+} dried at 90 °C

To verify the thermal stability of ZnO-TiO_2 doped with $Er^{3+}$and Yb^{3+}, TG-DTA was conducted using the mixture dried at 90 °C. As shown in Figure 3.7, there were three endothermic peaks at 47.5 °C, 125 °C, and 179.3 °C (No.1 to 3) in the DTA curve, and corresponding weight loss was about 0.41%, 2.71%, and 5.62%, respectively, which it could be inferred that the surface-absorbed water of this dried mixture was evaporated. This phenomenon agreed with the TG-DTA result of all precursors mentioned previously. Further, according to process No.4 to No.6, there were overlapping and complicated processes which might be classified as two endothermic peaks (No.4 and No.6) and one exothermic peak (No.5), and corresponding weight loss was 12.84%, 14.93%, and 15.73% for process No.4, No.5, and No.6, respectively. However, in comparison to the TG-DTA result of raw materials, the process that was responsible for these weight losses was the dehydration and decomposition processes that, in this analysis, it would take place simultaneously. For exothermic peak, it might come from the surfactant decomposition process that was mentioned in the case of TG-DTA result of TiO_2 sol solution since it showed similar weight loss (about 2%) at the similar temperature (around 300 °C). Focusing on TG-DTA result of $Yb(NO_3)_3{\cdot}5H_2O$ and $Er(NO_3)_3{\cdot}5H_2O$, there were at least two peaks related to the NO_x by-product formation during the thermal process in the temperature range from 250-480 °C, but this analysis did not show the obvious peak of that process because of the low content of nitrate. Under between 480-600 °C, a very small change in the weight loss was observed, indicating that the decomposition of this mixture almost completed at this stage. From all TG-DTA results, it can be concluded that the significant point is the total weight loss of ZnO and TiO_2 in the temperature range from room temperature to 600 °C about 1.2% and 4%, respectively. These weight losses may have the influences on the formation of target host material and a little change in stoichiometric of ZnO/TiO_2 mixing ratio.

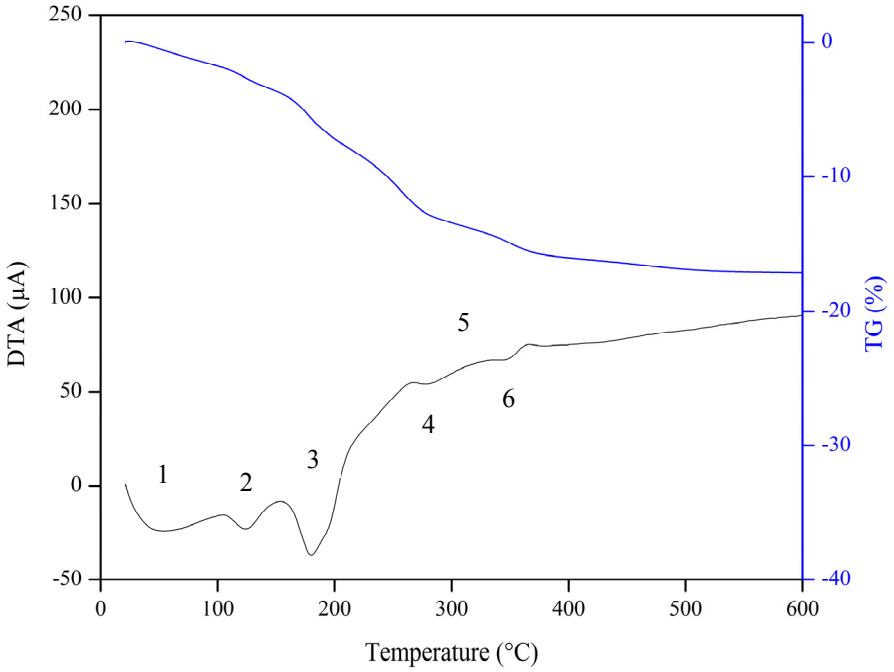

Figure 3.7. TG-DTA curves in the temperature range from room temperature (20 °C) to 600 °C for $ZnO:TiO_2$ = 1:1 (in mole) doped with 3 mol% Er^{3+} and 9 mol% Yb^{3+} dried at 90 °C.

3.3.3 Fourier Transform Infrared Spectroscopy (FTIR) of TiO_2 sol solution

According to the TG-DTA result of TiO_2 sol solution that one detected exothermic process might come from the burning out of surfactant which it was added to the TiO_2 sol solution for the dispersion stabilization of TiO_2 particles, in this section, the existence of this surfactant will be proved by using FTIR analysis because the surfactant-based structures are usually organic compounds. Typically, organic compounds are categorized according to the functional groups (e.g. alcohols and carboxylic acids) and each functional group has its own specific molecular vibrational frequency, giving rise to various bond vibrations which can be classified by considering the wavenumber. Nevertheless, the main objective of this section is only the confirmation of the presence of surfactant. So, the result will be explained regarding the type of carbon bond vibrations only.

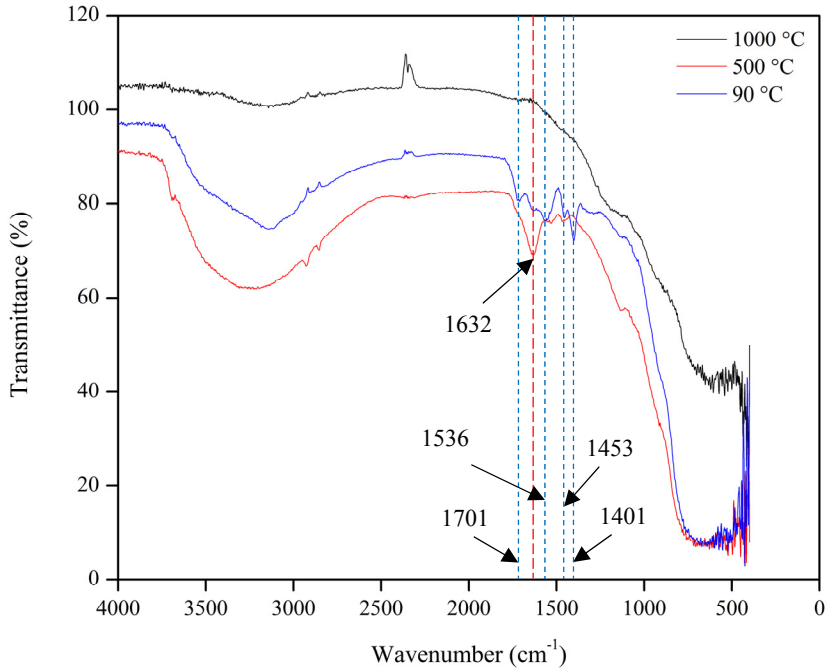

Figure 3.8. FTIR spectra of TiO_2 sol solution dried and fired at various temperatures with the labeled wavenumber.

FTIR spectra of TiO_2 sol solution dried and fired at different temperatures (Figure 3.8) were recorded in the wavenumber range of 4000-399 cm^{-1}. The result showed that, on heating the sample up to 90 °C, the peaks that corresponded to the wavenumber of 1401, 1453, 1536, 1632, and 1701 cm^{-1} appeared. These wavenumbers were related to the characteristic of C-H bend (1400-1500 cm^{-1}), C=C asymmetric stretch (1500-1650 cm^{-1}), and C=O stretch (1600-1750 cm^{-1}) [31]. Further, on heating the sample up to 500 °C, the peaks at 1401, 1453, 1536, and 1701 cm^{-1} disappeared, remaining only the peak at 1632 cm^{-1} which this peak was related to the characteristic of C=C asymmetric stretch and C=O stretch. Later, at the firing temperature of 1000 °C, all peaks disappeared which means that this organic compound was completely removed. By considering these results, it can be summarized that TiO_2 sol precursor solution contains the surfactant which is added to the solution for the dispersion stabilization of TiO_2 particles. And, the possible chemical structure of this surfactant conforms to the functional group that contains three vibrations: C-H bend, C=C asymmetric stretch, and C=O stretch.

3.3.4 Effect of firing temperature on crystalline phase

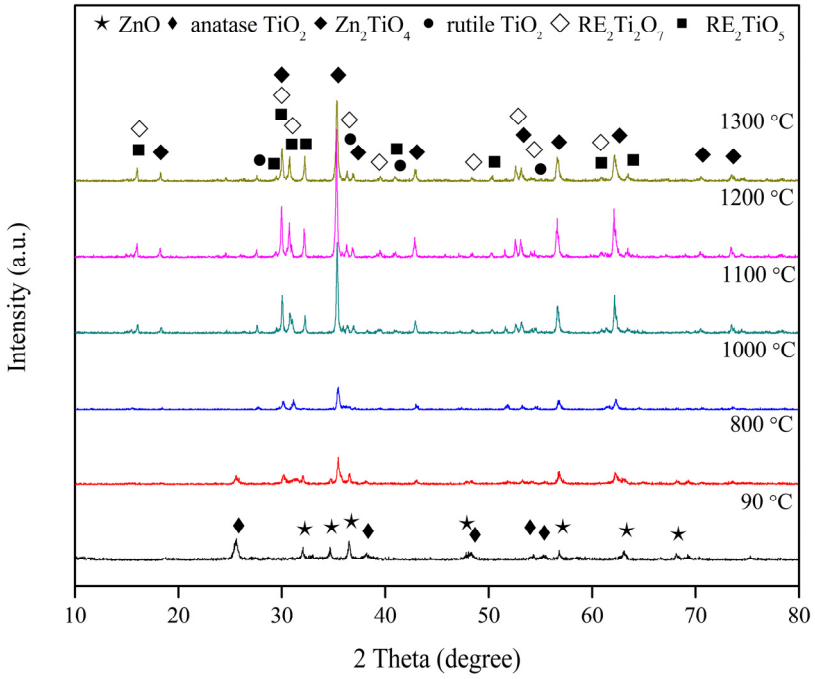

Figure 3.9. XRD patterns of ZnO:TiO_2 = 1:1 (in mole) doped with 3 mol% Er^{3+} and 9 mol% Yb^{3+} dried and fired at various temperatures (90-1300 °C). Reproduced with permission from Kobwittaya *et al.*, *Ceram. Int.*, **43** (2017) 13505-13515. Copyright (2017) Elsevier Ltd and Techna Group S.r.l.

The crystalline phase of the samples, ZnO:TiO_2 = 1:1 (in mole) doped with 3 mol% Er^{3+} and 9 mol% Yb^{3+} dried and fired at various temperatures (90-1400 °C), was identified using XRD analysis. XRD patterns of the products prepared at the temperature of 90 °C (raw mixture powder) to 1300 °C are described in Figure 3.9. The raw mixture contained two phases, ZnO (JCPDS: 36-1451) and anatase TiO_2 (JCPDS: 21-1272). At 800 °C, Zn_2TiO_4 phase (JCPDS: 25-1164) appeared as the dominant peak along with the decrease in ZnO and anatase TiO_2 phase contents. According to the phase diagram of ZnO-TiO_2 system [32], Zn_2TiO_4 is a stable phase and easily formed by the reaction between ZnO and TiO_2, even if the system has low amount of ZnO. At 1000 °C, Zn_2TiO_4 was still the dominant phase, but ZnO and anatase TiO_2 phases disappeared. Theoretically, Zn_2TiO_4 is formed by 2 moles of ZnO and 1 mole of TiO_2, therefore, it is possible that all ZnO amounts are used, resulting in the disappearance of ZnO phase. At the same time, rutile TiO_2 phase (JCPDS: 21-1276) appeared due to the phase transformation

of TiO_2 by the phase change in all remaining anatase TiO_2 [33]. At higher firing temperature (1100-1300 °C), Zn_2TiO_4, rutile TiO_2, $RE_2Ti_2O_7$ ($Er_2Ti_2O_7$, JCPDS: 18-0499 and/or $Yb_2Ti_2O_7$, JCPDS: 17-0454), and RE_2TiO_5 (Er_2TiO_5 and/or Yb_2TiO_5) phases were observed [34]. However, it is worth noting that at further increasing firing temperature (1350 °C and 1400 °C), the sample partially melts and reacts with the combustion boat (mullite ($3Al_2O_3{\cdot}2SiO_2$) boat), forming Al_2O_3 [34] and Al_2TiO_5 (JCPDS: 26-0040) phases. The detailed XRD patterns and further characterizations of these two samples will be discussed later.

The microstructure of these six processed powders is shown in Figure 3.10. It was observed that all samples had different morphological structures, depending on each temperature used. At 90 °C, the particle bonding bonds between powder particles were loosely formed because atomic diffusion between particles did not take place at this temperature. Further increasing temperature, it seemed that the powder particles were bonded more tightly. This might be due to the growth of particles caused by the atomic diffusion between particles. In addition, the agglomeration of particles occurred as the firing temperature increased. Taking into account the sample fired at 1300 °C, the agglomerated and fractured grain morphologies were observed together because of the high firing temperature and milling process. It should be noted that, in this study, the physical characteristics like irregular shapes and different sizes are caused by the milling process.

As shown in Figure 3.11, at 1350 °C, there were dominant Zn_2TiO_4 phase and small amount of rutile TiO_2, $RE_2Ti_2O_7$, and RE_2TiO_5 phases. Besides, two additional phases, Al_2O_3 [34] and Al_2TiO_5 (JCPDS: 26-0040), were observed. Further increasing firing temperature (1400 °C), Zn_2TiO_4, rutile TiO_2, $RE_2Ti_2O_7$, RE_2TiO_5, and Al_2TiO_5 phase contents decreased and Al_2O_3 phase became dominant.

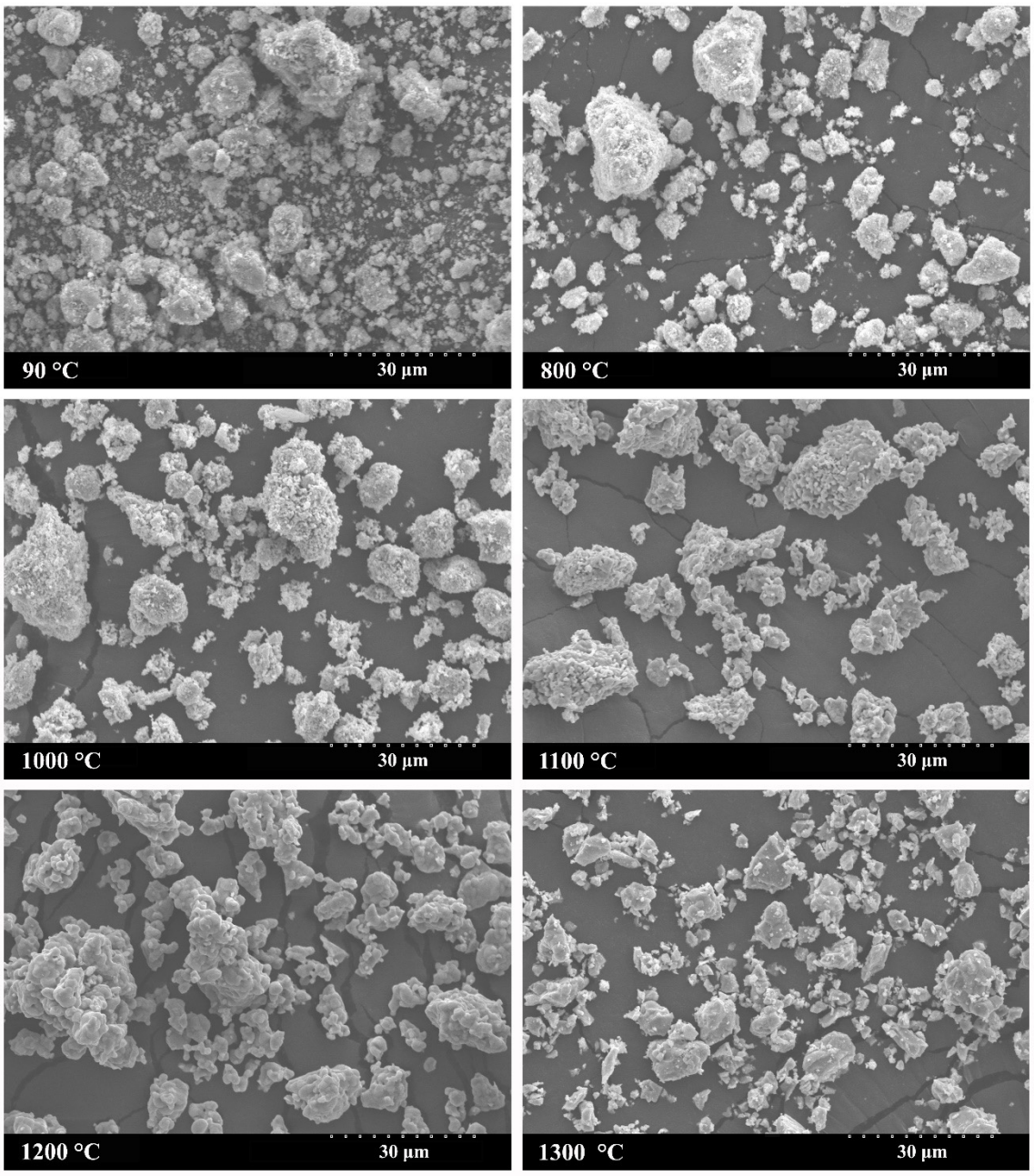

Figure 3.10. SEM images of $ZnO:TiO_2$ = 1:1 (in mole) doped with 3 mol% Er^{3+} and 9 mol% Yb^{3+} dried and fired at various temperatures (90-1300 °C).

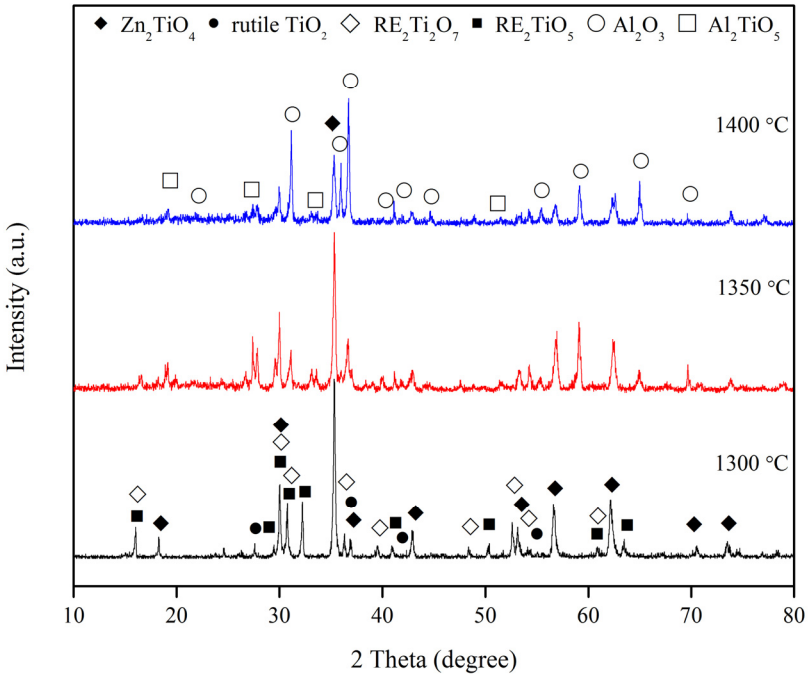

Figure 3.11. XRD patterns of ZnO:TiO_2 = 1:1 (in mole) doped with 3 mol% Er^{3+} and 9 mol% Yb^{3+} fired at various temperatures (1300-1400 °C). Reproduced with permission from Kobwittaya *et al*., *Ceram. Int.*, **43** (2017) 13505-13515. Copyright (2017) Elsevier Ltd and Techna Group S.r.l.

Corresponding photograph of the samples fired at 1300-1400 °C is shown in Figure 3.12. Firstly, in this study, it should be noted that the samples fired at 1300 °C and below keep the powder state and are easily removed from the combustion boat. So, the sample fired at 1300 °C is a representative sample to compare with the physical characteristics of the samples fired at 1350 °C and 1400 °C. As shown in Figure 3.12, it was clear that the color of the samples was dissimilar. Observed colors were soft pink, dark purple, and purple related to firing temperature at 1300 °C, 1350 °C and 1400 °C, respectively. Moreover, at 1350 °C and 1400 °C, both samples became bulky state and could not be removed from the combustion boat. The bulky state occurs because they are in the form of liquid phase at high temperature, then phase transformation takes place, resulting in the change in liquid phase to bulky state during cooling down. According to the phase diagram of ZnO-TiO_2 system [32], it is clear that the Zn_2TiO_4 and rutile TiO_2 phases remain in the temperature range from 1300-1418 °C. At higher temperature (1419-1537 °C), there are only two phases; ZnO-TiO_2 liquid and Zn_2TiO_4 that appeared. With these circumstances, it is possible that the temperature at contact area between

combustion boat and the sample would be higher than operating temperature, leading to the formation of liquid phase at firing temperature below 1419 °C.

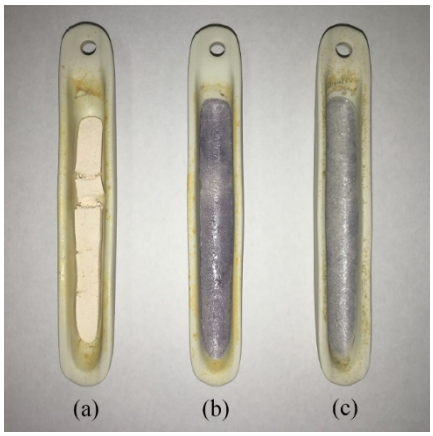

Figure 3.12. Photograph of ZnO:TiO_2 = 1:1 (in mole) doped with 3 mol% Er^{3+} and 9 mol% Yb^{3+} fired at (a) 1300 °C, (b) 1350 °C, and (c) 1400 °C. Reproduced with permission from Kobwittaya *et al*., *Ceram. Int.*, **43** (2017) 13505-13515. Copyright (2017) Elsevier Ltd and Techna Group S.r.l.

To comprehend the existence of Al_2O_3 and Al_2TiO_5 phases that occurred at 1350 °C and 1400 °C, at first, the combustion boat was analyzed using XRD analysis and the result showed that there was only $Al_6Si_2O_{13}$ phase (JCPDS: 15-0776) that appeared (Figure 3.13). The $Al_6Si_2O_{13}$ phase is well-known in the name of mullite ($3Al_2O_3{\cdot}2SiO_2$). Subsequently, the phase diagram of ZnO-TiO_2 and SiO_2-Al_2O_3 systems [32] (Figure 3.14) is considered simultaneously. At 1350 °C, the combustion boat and the sample at the contact area might melt and then the mixed liquid phase was formed which it consisted of Zn_2TiO_4, Al_2O_3, and SiO_2 phases. Further, the reactions between these compositions in the mixed liquid phase were probably started with following steps. The SiO_2 initially reacted with Zn_2TiO_4 and then appeared as glassy phase and at the same time, Al_2TiO_5 phase was produced by the reaction between Al_2O_3 and rutile TiO_2. Further increase of temperature (1400 °C), the combustion boat and the sample melted increasingly. Therefore, Zn_2TiO_4 content decreased due to the increase of glassy phase formation, and Al_2O_3 phase increased and became the dominant phase. Additionally, the decrease in Al_2TiO_5 phase content was mainly caused by the disappearance of rutile TiO_2 phase. With processes mentioned

above, all formations are in accordance with these following reaction equations (equations (3.4) to (3.6)).

$$3Al_2O_3{\cdot}2SiO_2 \rightarrow 3Al_2O_3 + 2SiO_2 \quad (3.4)$$

$$SiO_2 + Zn_2TiO_4\ (liquid) \rightarrow \text{glassy phase} \quad (3.5)$$

$$Al_2O_3 + TiO_2 \rightarrow Al_2TiO_5 \quad (3.6)$$

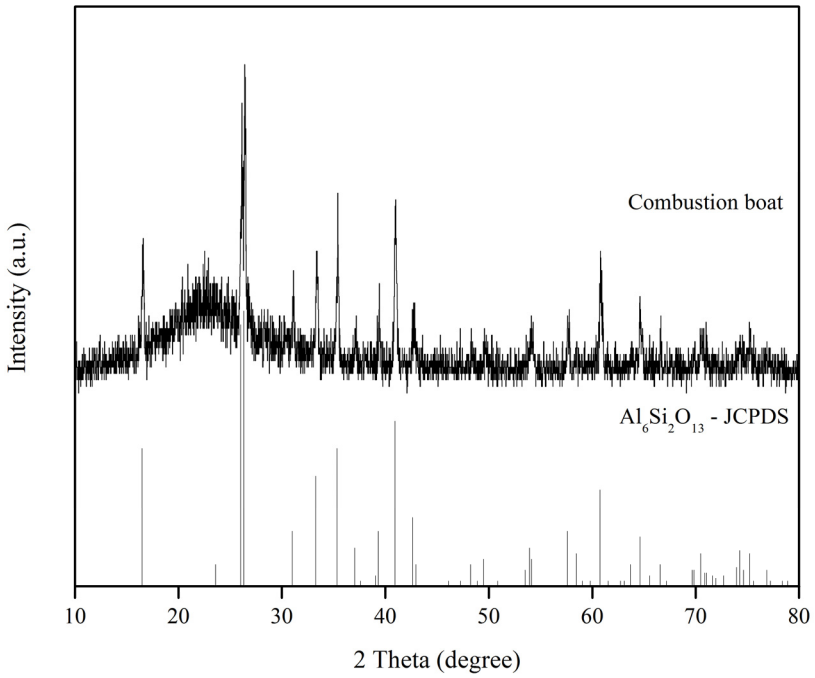

Figure 3.13. XRD pattern of combustion boat with the $Al_6Si_2O_{13}$-JCPDS card values. Reproduced with permission from Kobwittaya *et al*., *Ceram. Int.*, **43** (2017) 13505-13515. Copyright (2017) Elsevier Ltd and Techna Group S.r.l.

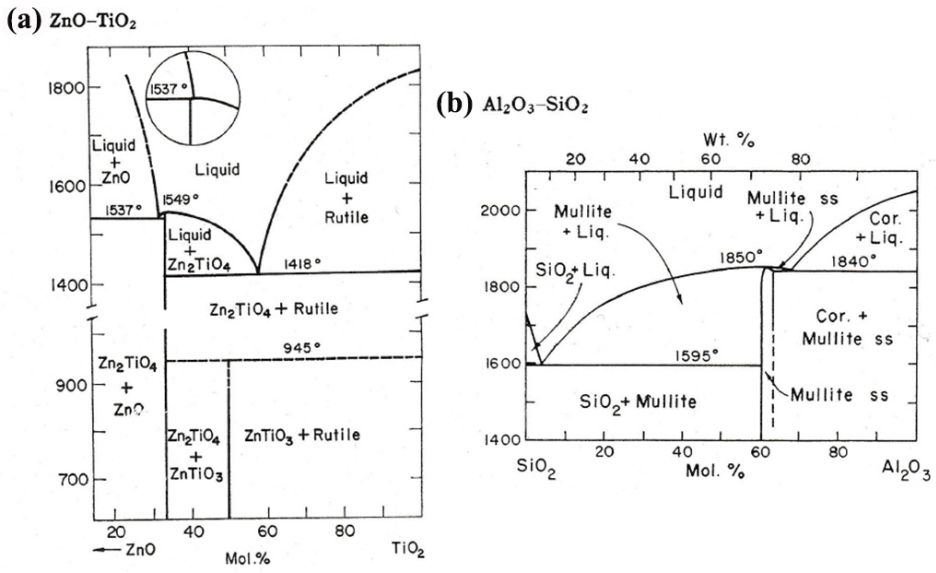

Figure 3.14. (a) phase diagram of ZnO-TiO_2 system (the inset shows alternative incongruent melting of Zn_2TiO_4), and (b) phase diagram of SiO_2-Al_2O_3 system (Cor. = corundum, ss = solid solution). Reproduced with permission from [32]. Copyright (1964) The American Ceramic Society, Inc.

Figure 3.15 shows digital microscopes (200x magnification) of the products fired at 1300 °C, 1350 °C, and 1400 °C. Photograph (a), (c), and (e) showed the crystal formation at the contact area between the combustion boat and the sample, demonstrating holes that would take place during the melting of sample at high temperature. Further, photograph (b), (d), and (e) showed many crystal growth lines (red arrow) at the center of surface area of the sample located in the combustion boat. In the case of firing temperature at 1300 °C, there were small particles of crystals that attached together and were easily separated. At 1350 °C and 1400 °C, the characteristic of sample structure was seemingly glassy, strongly attached, and hardly separated. With these physical properties, it is indicated that the glassy phase may occur at firing temperature 1350 °C and 1400 °C, causing to the decrease in Zn_2TiO_4 phase content and direct influencing to UCL properties.

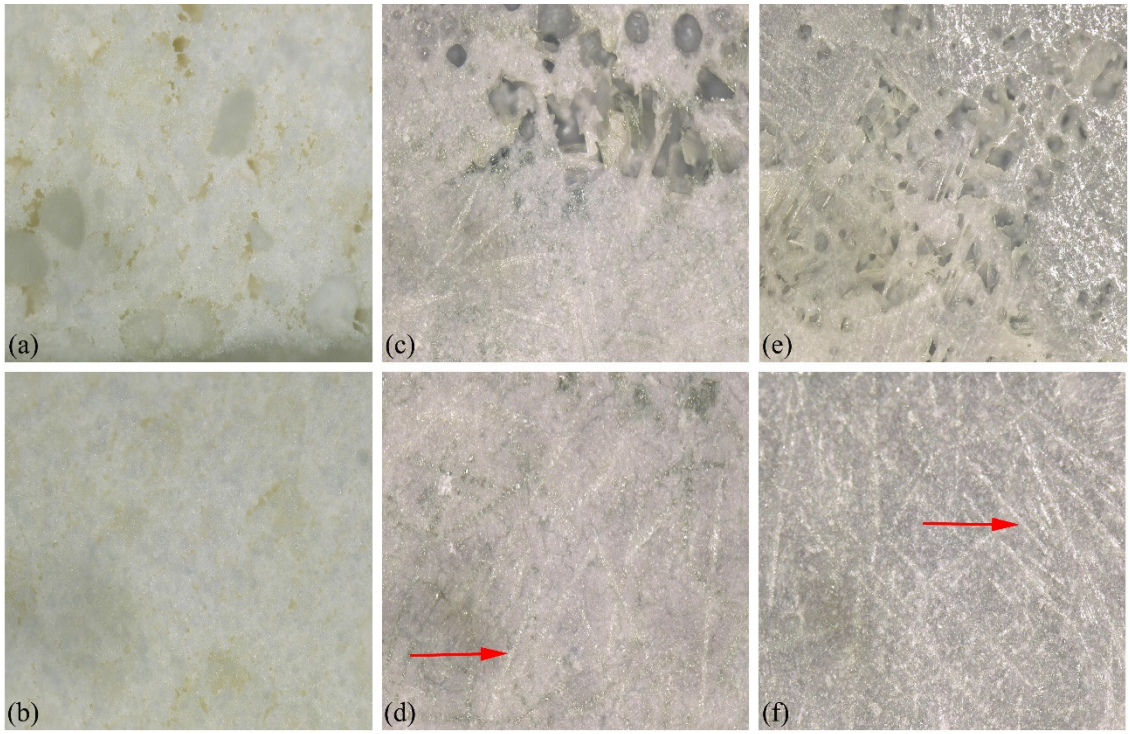

Figure 3.15. Digital microscopes (200x magnification) of ZnO:TiO_2 = 1:1 (in mole) doped with 3 mol% Er^{3+} and 9 mol% Yb^{3+} fired at 1300 °C ((a) and (b)), 1350 °C ((c) and (d)), and 1400 °C ((e) and (f)). Photograph (a), (c), and (e) are related to the contact area between the combustion boat and the sample. Photograph (b), (d), and (f) are related to the center of surface area of the sample located in the combustion boat. Reproduced with permission from Kobwittaya *et al*., *Ceram. Int.*, **43** (2017) 13505-13515. Copyright (2017) Elsevier Ltd and Techna Group S.r.l.

3.3.5 Effect of ZnO/TiO_2 mixing ratio on crystalline phase

XRD patterns of the Z*x*T1 samples with different *x*-values are shown in Figure 3.16. At *x* = 0.25, there were four phases; Zn_2TiO_4, rutile TiO_2, $RE_2Ti_2O_7$, and RE_2TiO_5. The effect of ZnO/TiO_2 mixing ratios on the relative phase content of the products is shown in Figure 3.17. With increasing ZnO amount up to *x* = 1.25, Zn_2TiO_4 content increased and, in the meantime, TiO_2, $RE_2Ti_2O_7$, and RE_2TiO_5 contents gradually decreased. Subsequently, at *x* = 1.25, TiO_2 phase disappeared. Nevertheless, with further increase of ZnO amount *x* > 1.25, Zn_2TiO_4 content slowly increased and still was the major phase. As increasing ZnO amount up to *x* = 1.75, $RE_2Ti_2O_7$ content initially increased, but RE_2TiO_5 content sharply decreased and then

almost disappeared. However, under $1.25 < x \leq 1.5$, it is possible that there were indistinct and complex reactions for the formation of RE titanate phases, causing to the sharp decrease in RE_2TiO_5 content and the increase in $RE_2Ti_2O_7$ content.

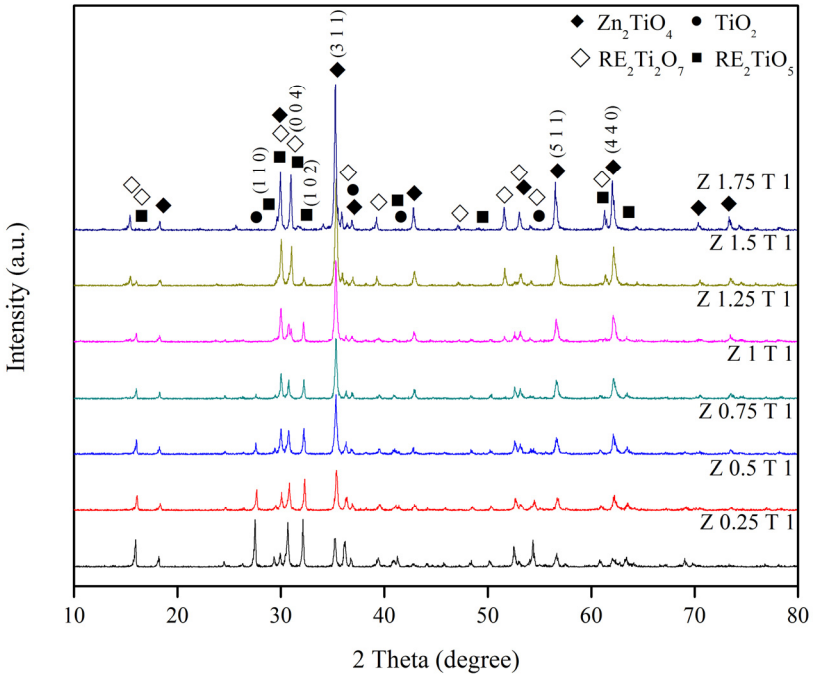

Figure 3.16. XRD patterns of various ZnO/TiO_2 mixing ratios doped with 3 mol% Er^{3+} and 9 mol% Yb^{3+} fired at 1300 °C. Adapted with permission from Kobwittaya *et al.*, *Ceram. Int.*, **43** (2017) 13505-13515. Copyright (2017) Elsevier Ltd and Techna Group S.r.l.

These phase changes can be explained as follows. Firstly, Zn_2TiO_4 phase is formed by the reaction between 2 moles of ZnO and 1 mole of TiO_2. Therefore, as increasing ZnO amount x from 0.25-1.75, Zn_2TiO_4 content increases absolutely. Subsequently, TiO_2 reacts with RE_2O_3 (final product of hydrated rare earth nitrate decomposition under high temperature [28-30]), and then RE_2TiO_5 and $RE_2Ti_2O_7$ phases are formed. This formation is put in order based on the theoretical formation energy value of each phase from most positive to most negative value; Zn_2TiO_4 (-2.88 eV), RE_2TiO_5 (-3.79 eV), and $RE_2Ti_2O_7$ (-3.8 eV). It is worth noting that all formation energies are computed at 0 K and 0 atm and neglect zero-point effects because heat capacity and density differences between solid phases are normally rather small, leading to only slight effects of temperature and pressure [35]. Besides, it is clear that $RE_2Ti_2O_7$ and RE_2TiO_5 formations are the competitive reaction. Herein, Zn_2TiO_4 content and the amount of RE^{3+} ions

in the host crystal matrix directly affect the phase content. On this basis, as increasing ZnO amount up to x = 1.25 and when Zn_2TiO_4 content increases, it means that the amount of RE^{3+} ions in the host crystal matrix also increases, resulting in the decrease in $RE_2Ti_2O_7$ and RE_2TiO_5 contents. In the case of TiO_2 content, its abatement is not only from the reaction with ZnO and RE_2O_3, but also from solid solubility of TiO_2 into Zn_2TiO_4 crystal structure (maximum at 0.33 mole over stoichiometry) [36]. The SEM analysis of these seven processed powders is shown in Figure 3.18. It was observed that all samples had the same physical characteristics; micron-scale particles in irregular shapes and different sizes which they were caused by milling process. Besides, this kind of morphology was obviously due to the agglomeration of particles that corresponded with the high firing temperature used in the final stage of preparation.

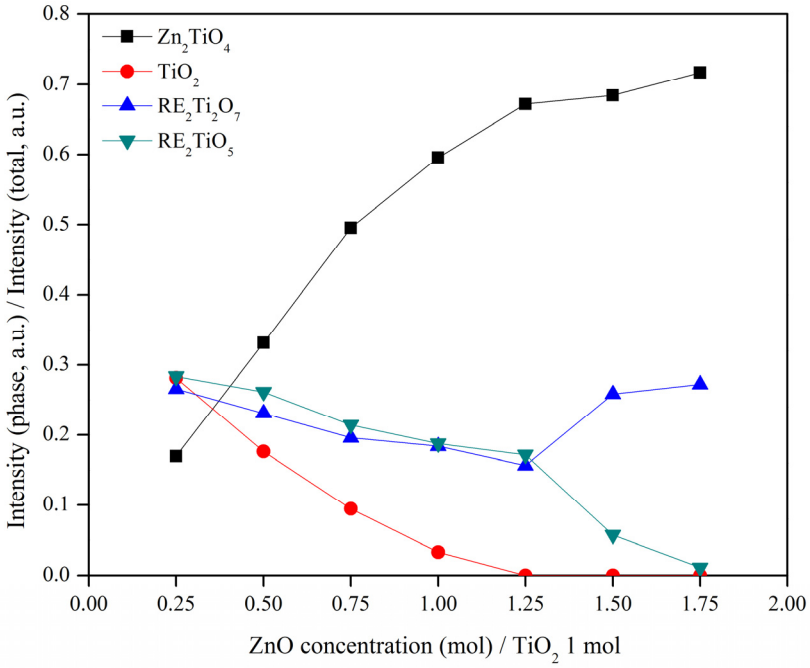

Figure 3.17. Calculated relative phase contents of Zn_2TiO_4, TiO_2, $RE_2Ti_2O_7$, and RE_2TiO_5 phases according to the compositions in Figure 3.16. Reproduced with permission from Kobwittaya *et al*., *Ceram. Int.*, **43** (2017) 13505-13515. Copyright (2017) Elsevier Ltd and Techna Group S.r.l.

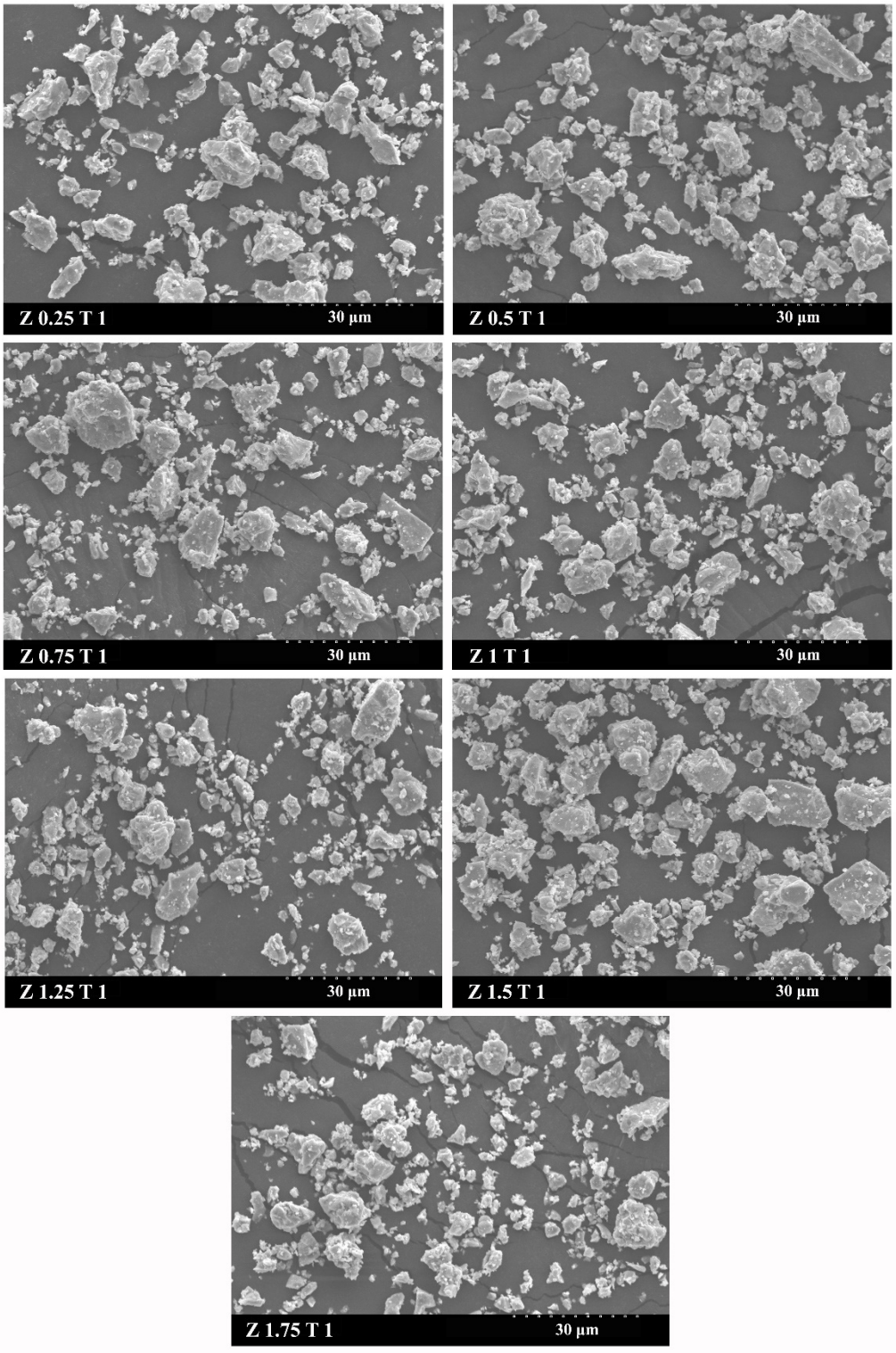

Figure 3.18. SEM images of various ZnO/TiO_2 mixing ratios doped with 3 mol% Er^{3+} and 9 mol% Yb^{3+} fired at 1300 °C.

3.3.6 Effect of firing temperature on upconversion luminescence (UCL)

UC emission photographs of $ZnO:TiO_2$ = 1:1 (in mole) doped with 3 mol% Er^{3+} and 9 mol% Yb^{3+} samples fired at different temperatures are shown in Figure 3.19. These showed that the color of the UC emission was red and changed from weak to strong red with increasing firing temperature up to 1300 °C. Additionally, the central area of the samples fired at 1100-1300 °C seems to be white, which this observed emission is typically caused by the strong emission. Further increase of temperature (1350 °C and 1400 °C), the sample showed very weak or no emission. According to UCL spectra in Figure 3.20, the sample heated below 1100 °C and above 1300 °C exhibited weak emission intensity or no emission spectra, but the samples fired at 1100-1300 °C exhibited strong emission intensity. These emission spectra comprised of two emission bands. The weak green spectral situated in the range of 540-568 nm which was attributed to $^2H_{11/2} \rightarrow {}^4I_{15/2}$ and $^4S_{3/2} \rightarrow {}^4I_{15/2}$ transitions of Er^{3+} with two maxima at 544 and 559 nm, respectively. The strong red spectral located in the range of 642-695 nm which was ascribed to $^4F_{9/2} \rightarrow {}^4I_{15/2}$ transition of Er^{3+} with two maxima at 657 and 675 nm. As shown in Figure 3.19, only red color is obviously observed because the red emission has higher emission intensity than the green one.

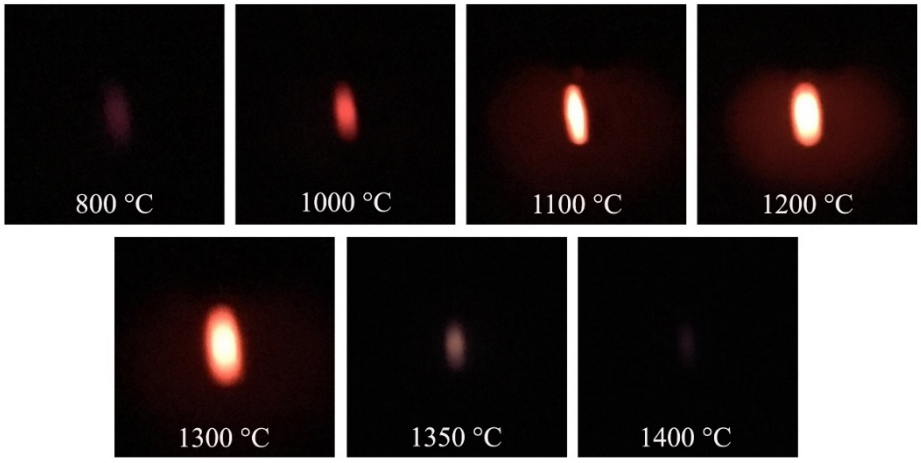

Figure 3.19. UC emission color of $ZnO:TiO_2$ = 1:1 (in mole) doped with 3 mol% Er^{3+} and 9 mol% Yb^{3+} fired at various temperatures (800-1400 °C), and irradiated with a 980-nm 125 mW laser. Reproduced with permission from Kobwittaya *et al*., *Ceram. Int.*, **43** (2017) 13505-13515. Copyright (2017) Elsevier Ltd and Techna Group S.r.l.

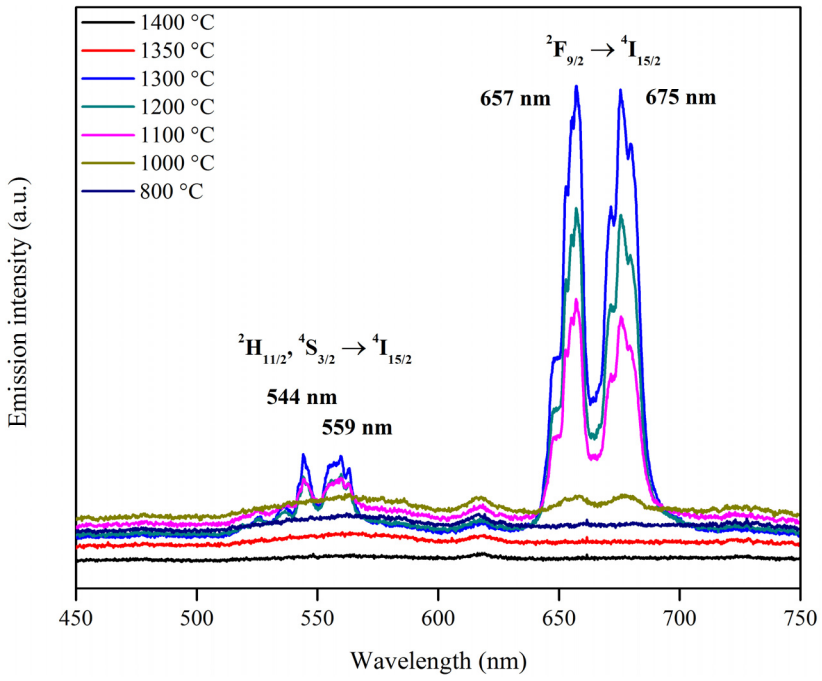

Figure 3.20. UC emission spectra of ZnO:TiO_2 = 1:1 (in mole) doped with 3 mol% Er^{3+} and 9 mol% Yb^{3+} fired at various temperatures (800-1400 °C), and irradiated with a 980-nm 125 mW laser. Reproduced with permission from Kobwittaya *et al*., *Ceram. Int.*, **43** (2017) 13505-13515. Copyright (2017) Elsevier Ltd and Techna Group S.r.l.

As discussed by Luitel *et al*. in ZnO-TiO_2 composite doped with Er^{3+} and Yb^{3+} prepared by solid-state reaction method [21], Zn^{2+} sites in Zn_2TiO_4 crystal are occupied by RE^{3+} ions. Hence, the increase in the amount of RE^{3+} ions at Zn site affects the changes in red (657 nm and 675 nm) and green (544 nm and 559 nm) emission intensities as a function of various firing temperatures (Figure 3.21). This kind of phenomenon can be explained by considering the result in Figure 3.21 together with relative phase contents in Figure 3.17.

The samples fired at 800 °C and 1000 °C showed very low emission intensity because there was small Zn_2TiO_4 content and the total amount of RE^{3+} ions in Zn_2TiO_4 crystal was small either. Further increase of firing temperature up to 1300 °C, the emission intensity sharply increased because of the increment of total RE^{3+} ions in the Zn_2TiO_4 crystal when Zn_2TiO_4 content augmented. With further increasing firing temperature (1350 °C and 1400 °C), the emission intensity dramatically decreased because Zn_2TiO_4 content extremely decreased, causing to the decrease in the amount of RE^{3+} ions incorporated into Zn_2TiO_4 crystal.

As discussed, it could be summarized that the samples fired at 1300 °C and below might be categorized as solid state and above 1300 °C might be classified as partially liquid state. Thus, at 1300 °C, the product exhibited the brightest red emission and this behavior will be discussed in the next section.

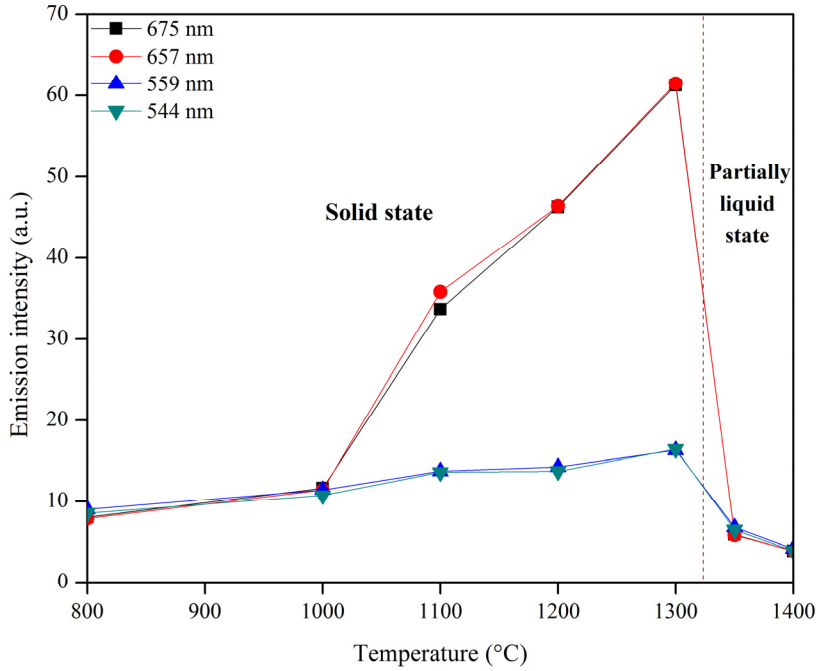

Figure 3.21. The red (657 nm and 675 nm) and green (544 nm and 559 nm) emission intensities versus various firing temperatures according to the details in Figure 3.20. Reproduced with permission from Kobwittaya *et al.*, *Ceram. Int.*, **43** (2017) 13505-13515. Copyright (2017) Elsevier Ltd and Techna Group S.r.l.

3.3.7 Effect of ZnO/TiO_2 mixing ratio on upconversion luminescence (UCL)

The UC emission color of various ZnO/TiO_2 mixing ratios doped with 3 mol% Er^{3+} and 9 mol% Yb^{3+} sample fired at 1300 °C was red (Figure 3.22) and corresponding UCL spectra of these products are shown in Figure 3.23.

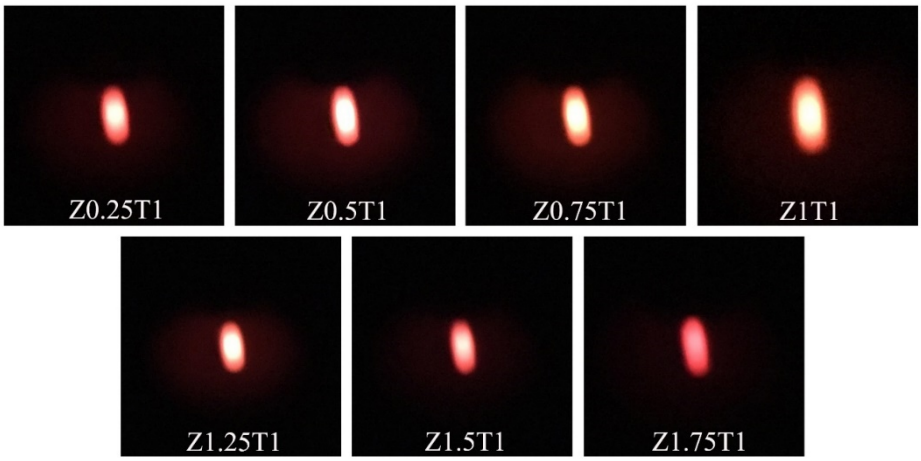

Figure 3.22. UC emission color of various ZnO/TiO_2 mixing ratios doped with 3 mol% Er^{3+} and 9 mol% Yb^{3+} fired at 1300 °C, and irradiated with a 980-nm 125 mW laser. Adapted with permission from Kobwittaya *et al*., *Ceram. Int.*, **43** (2017) 13505-13515. Copyright (2017) Elsevier Ltd and Techna Group S.r.l.

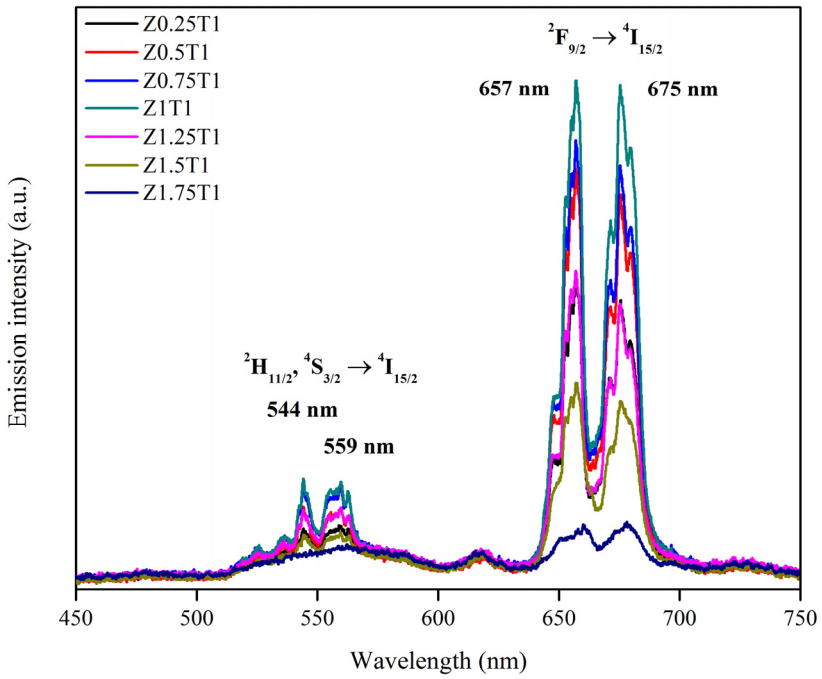

Figure 3.23. UC emission spectra of various ZnO/TiO_2 mixing ratios doped with 3 mol% Er^{3+} and 9 mol% Yb^{3+} fired at 1300 °C, and irradiated with a 980-nm 125 mW laser. Reproduced with permission from Kobwittaya *et al*., *Ceram. Int.*, **43** (2017) 13505-13515. Copyright (2017) Elsevier Ltd and Techna Group S.r.l.

The emission color brightness and emission intensity augmented with increasing ZnO amount up to x = 1. Further increase of ZnO amount (x = 1.25, 1.5, and 1.75), the brightness and emission intensity decreased. Hence, it is clear that the emission intensity changes for both green and red emission bands with varying ZnO amounts and the brightest emission is observed for the sample Z1T1. The effect of x-value on the maximum emission intensity of red (657 nm and 675 nm) and green (544 nm and 559 nm) bands of various ZnO/TiO_2 mixing ratios doped with 3 mol% Er^{3+} and 9 mol% Yb^{3+} is shown in Figure 3.24. Here too, the UC behavior can be divided into two parts. In the lower x-value (x < 1), the increment of ZnO amount up to x = 1, the emission intensity of both bands increased. In the case of higher x-value (x > 1), further increasing amount of ZnO, the emission intensity of both bands decreased. However, there were different line patterns of emission intensity between green and red emission bands. These observed patterns can be explained by considering the solubility of RE^{3+} ions into Zn_2TiO_4 crystal and it is indicated that the amount of soluble Er^{3+} and Yb^{3+} (in the term of Er^{3+}/Yb^{3+} ratio) in Zn_2TiO_4 crystal of each condition is different. When ZnO:TiO_2 = 1:1 (in mole), the brightest emission was observed on both green and red emission bands. This behavior can be described by focusing on the relative phase contents of final products and the details are showed in Figure 3.17. When emission intensity increased (ZnO amount x = 0.25-1), Zn_2TiO_4, TiO_2, $RE_2Ti_2O_7$, and RE_2TiO_5 phases were observed. Further, when emission intensity primarily decreased (x = 1.25), Zn_2TiO_4, $RE_2Ti_2O_7$, and RE_2TiO_5 phases were observed without TiO_2 phase. With higher ZnO amount (x = 1.5 and 1.75), the emission intensity uninterruptedly decreased and there were only two observed phases, Zn_2TiO_4 and $RE_2Ti_2O_7$. In these three sections of ZnO amount, the dissimilarity is the existence of TiO_2 phase, whose solubility in Zn_2TiO_4 may affect the UCL intensity. Hence, the brightest UC emission is obtained by Er^{3+} transitions in the mixed phases system that comprises of Zn_2TiO_4, TiO_2, $RE_2Ti_2O_7$, and RE_2TiO_5 phases.

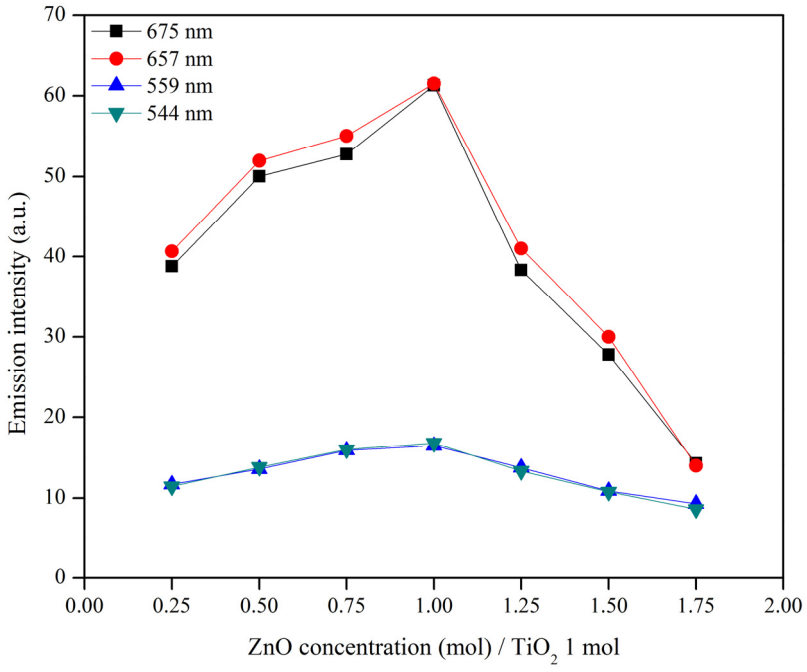

Figure 3.24. The red (657 nm and 675 nm) and green (544 nm and 559 nm) emission intensities versus various ZnO/TiO_2 mixing ratios according to the details in Figure 3.23. Reproduced with permission from Kobwittaya *et al*., *Ceram. Int.*, **43** (2017) 13505-13515. Copyright (2017) Elsevier Ltd and Techna Group S.r.l.

3.3.8 Site preference of Er^{3+} and Yb^{3+} in Zn_2TiO_4 crystal structure

According to the phase diagram of ZnO-TiO_2 system [32], it has been reported that three compounds exist in ZnO-TiO_2 system; spinel type Zn_2TiO_4 (cubic), Ilmenite type $ZnTiO_3$ (hexagonal), and $Zn_2Ti_3O_8$ (cubic, low temperature form of $ZnTiO_3$). Among these compounds, the spinel-type Zn_2TiO_4 has a faced-centered cubic (FCC) unit cell belonging to space group Fd-3m with a = 0.84608 nm [37] and is stable from room temperature to its melting point. According to Kim *et al*. [36], the atomic arrangement in the crystal become more ordered at high temperature by the incorporation of TiO_2 into the Zn_2TiO_4 structure. The Zn_2TiO_4 has an inverse spinel structure (AB_2O_4), where Zn atoms occupy all A-sites and the half of B-sites, and Ti atoms occupy the half of B-sites. Basically, in this crystal structure, A-site is generally occupied by a larger cation and B-site is occupied by a smaller cation. The crystal structure of inverse spinel Zn_2TiO_4 phase is shown in Figure 3.25 and created by VESTA (open-source software) [38].

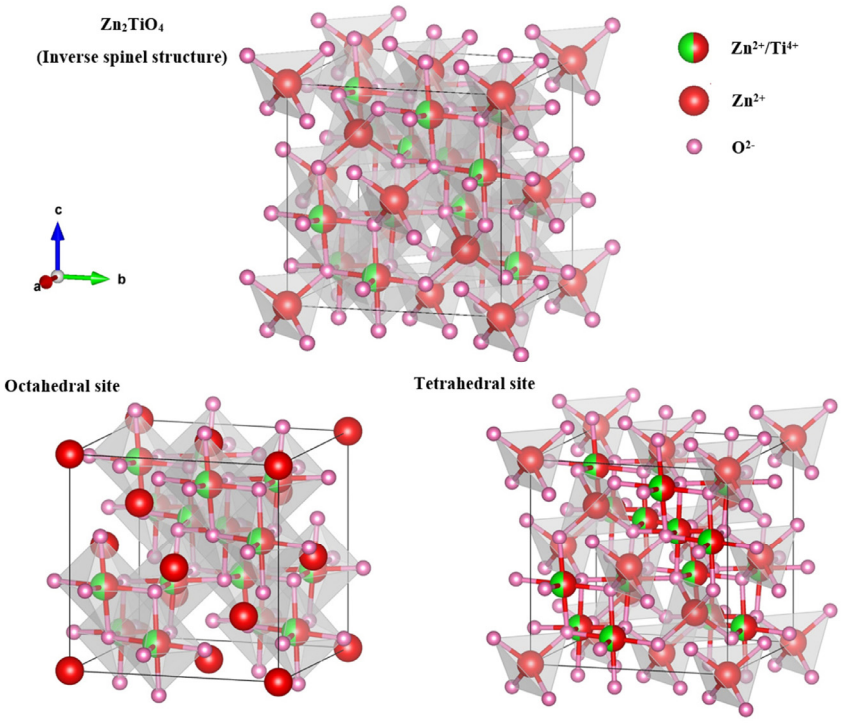

Figure 3.25. The crystal structure of inverse spinel Zn_2TiO_4 phase. Reproduced with permission from Kobwittaya *et al*., *Ceram. Int.*, **43** (2017) 13505-13515. Copyright (2017) Elsevier Ltd and Techna Group S.r.l.

Due to the bigger size of Zn, which has the tendency to occupy tetrahedral sites, surplus Ti^{4+} with the smaller size should occupy octahedral sites. Since the extra Ti^{4+} occupy octahedral site, the vacant Zn site (V''_{Zn}) must be appeared in tetrahedral site to keep the charge balance [36,37,39]. Based on this feasibility of the appearance of $V''_{Zn(tet)}$, the incorporation of surplus Ti^{4+} into the Zn_2TiO_4 matrix can be manifested by equation (3.7). It should be noted that only $V''_{Zn(tet)}$ is generated when the system has remaining Ti^{4+} [36].

$$2TiO_2\left(\text{in } Zn_{(tet)}(ZnTi)_{(oct)}TiO_4\right) \rightarrow V''_{Zn(tet)} + Ti^{\cdot\cdot}_{Zn(oct)} + Ti_{Ti(oct)} + 4O^{x}_{o} \quad (3.7)$$

Generally, to determine the crystal structure and to calculate the cell parameter of synthesized products, including consideration of site preference of dopants in the host crystal matrix, Rietveld refinement is the most widely used method to investigate these physical characteristics and this method is usually performed with the accurate and precise XRD results in order to easily evaluate a very complex curve since powder diffraction patterns are a set of peaks and

some overlapped. The Rietveld analysis is used to adjust various parameters (e.g. peak-shape and profile points) via statistical analysis, "least squares method", to minimize the difference between the observed value and calculated value. The minimization (*M*) by fitting two data sources at various points (*i*) can be calculated using the expression of equation (3.8).

$$M = \sum_i w_i[(y_{i(obs)} - y_{i(cal)})^2] \tag{3.8}$$

where w_i = weight function of profile point *i*

= the reciprocal of variance (σ^2) of $y_{i(obs)}$ = $1 / [\sigma^2(y_{i(obs)})]$

$y_{i(obs)}$ = the observed data of profile point *i*

$y_{i(cal)}$ = the calculated data of profile point *i*

The quality of least squares refinement relies on two main agreement indices which are called "Residual" (also known as R factor). The first is the weighted-profile residual (R_{wp}) which is directly related to equation (3.8) and can be expressed as equations (3.9) and (3.10).

$$R_{wp} = \sqrt{\sum_i w_i[(y_{i(obs)} - y_{i(cal)})^2] / \sum_i w_i y_{i(obs)}^2} \tag{3.9}$$

$$R_{wp} = \sqrt{M / \sum_i w_i y_{i(obs)}^2} \tag{3.10}$$

Even though this function is the essential equation and much widespread to all Rietveld software, but there is one problem that the summation is only applied to all points (*i*) in the profile without taking into account specific points where considerable diffraction density is present, causing to the lack of precision and accuracy in profile fittings. Therefore, by considering only R_{wp}, it may be inadequate to obtain the believable result. For this reason, the second R factor that does not involve the peak-shape function is proposed and used by focusing on various significant diffraction points (hkl planes; Miller indices) in the profile. This R factor is called profile residual (R_p) and is expressed as equation (3.11).

$$R_p = \sum_{hkl} |y_{hkl(obs)} - y_{hkl(cal)}| / \sum_{hkl} y_{hkl(obs)} \tag{3.11}$$

These Rietveld refinement explanations, details, and equations are adapted from the book of Dinnebier *et al*. [40] and the report of Yamazaki *et al*. [41] in order to easily comprehend the fundamental theory of Rietveld analysis.

Nowadays, the Rietveld refinement is operated by various software such as FullProf Suite, General Structure Analysis System (GSAS), X'pert Highscore Plus, and Material Analysis Using Diffraction (MAUD) because manual calculation lacks precision and accuracy of result due to the error from various circumstances. These software are mainly created based on two R factors mentioned above and the other controlled factors to acquire the highest performance of profile fitting.

According to the XRD results of the products represented in Figure 3.9 and Figure 3.16, there were four phases, Zn_2TiO_4, TiO_2, $RE_2Ti_2O_7$, and RE_2TiO_5 (RE = Er^{3+} and/or Yb^{3+}) that appeared in the final product at optimum firing temperature. With observed multiphase and patterns of XRD results with step scan type, it was detected that there were many overlapping peaks in which one peak position was related to two or more phases. Besides, in the case of RE_2TiO_5, this phase is ambiguous due to the lack of information of crystal structure, reference pattern (e.g. JCPDS, NIMS databases), and actual properties. Therefore, in this study, crystallographic parameters were obtained via Rietveld analysis of XRD patterns using Materials Analysis Using Diffraction (Maud) software [42] and concerning only three phases; Zn_2TiO_4, TiO_2, $RE_2Ti_2O_7$. This software was selected to provide the example of Rietveld analysis and to confirm how it is impossible to use Rietveld analysis in this study. It is worth noting that other software may show similar result in the case of graph fitting due to the same crystallographic information databases used, but the R factors may be different because of dissimilar algorithms of each software.

Figure. 3.26 shows the profile fitting by Rietveld refinement without adding predicted site preference of RE^{3+} ions (red line is a calculated profile). The result showed very high R factors, R_{wp} = 45.586% and R_p = 34.798%, resulting in unsuitable fitting model. Normally, good R factor is usually less than 10% which demonstrates high performance of profile fitting, leading to the proper model and high reliability of information. Therefore, with this result, Rietveld refinement could not be applied and did not show the good performance of profile fitting. Taking into account RE^{3+} ions that should occupy some site of Zn_2TiO_4 crystal structure, thus,

it is indicated that Zn_2TiO_4 is the most important phase. Therefore, the calculated profile (red line) of some examples (Z0.25T1, Z1T1, and Z1.25T1) analyzed by Rietveld analysis and matched with only Zn_2TiO_4 phase is shown in Figure 3.27 to 3.29.

Rietveld refinement results in Figure 3.27 to 3.29 also showed very high R factors. So, it would imply that various ZnO/TiO_2 mixing ratios doped with 3 mol% Er^{3+} and 9 mol% Yb^{3+} fired at 1300 °C demonstrate the similar result, showing very high R factors. Even though very high R factors were observed but these values could be used as the based R factor for comparison with the case of adding predicted site preference of RE^{3+} ions. Hereafter, the Z1T1 which showed the brightest UCL was selected to investigate the comparative relation of R factors between profile fitting without (Figure 3.28) and with adding predicted site preference of RE^{3+} ions. The predicted site preferences of RE^{3+} ions in Zn_2TiO_4 crystal structure with various site occupancies and various fractions of crystallographic parameters are separated into four parts as follows:

1. RE^{3+} ions occupy Zn^{2+} position in tetrahedral site
   (Appendix A: Figure A1 to A4, Table A2 to A5)
2. RE^{3+} ions occupy Zn^{2+} position in octahedral site
   (Appendix A: Figure A5 to A8, Table A6 to A9)
3. RE^{3+} ions occupy Ti^{4+} position in octahedral site
   (Appendix A: Figure A9 to A12, Table A10 to A13)
4. RE^{3+} ions occupy both Zn^{2+} and Ti^{4+} positions in octahedral site
   (Appendix A: Figure A13 to A16, Table A14 to A17)

The results of Rietveld refinement of these four categories analyzed by MAUD software are summarized in Table 3.4.

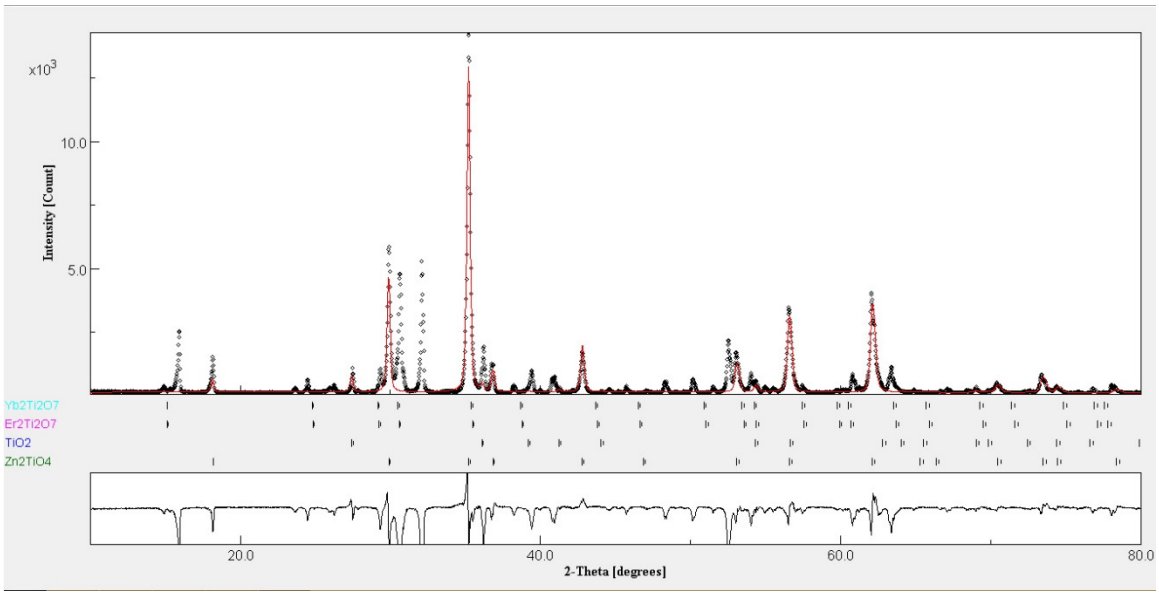

Figure 3.26. Rietveld plot of ZnO:TiO_2 = 1:1 (in mole) doped with 3 mol% Er^{3+} and 9 mol% Yb^{3+} fired at 1300 °C (R_{wp} = 45.586%, R_p = 34.798%).

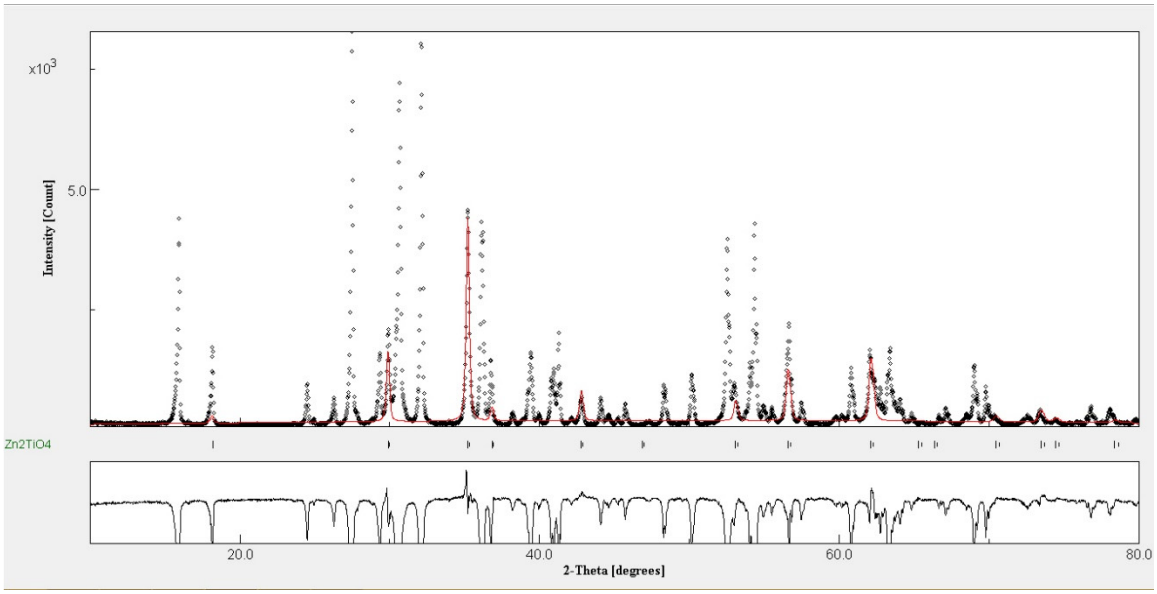

Figure 3.27. Rietveld plot of ZnO:TiO_2 = 0.25:1 (in mole) doped with 3 mol% Er^{3+} and 9 mol% Yb^{3+} fired at 1300 °C (R_{wp} = 65.625%, R_p = 56.521%).

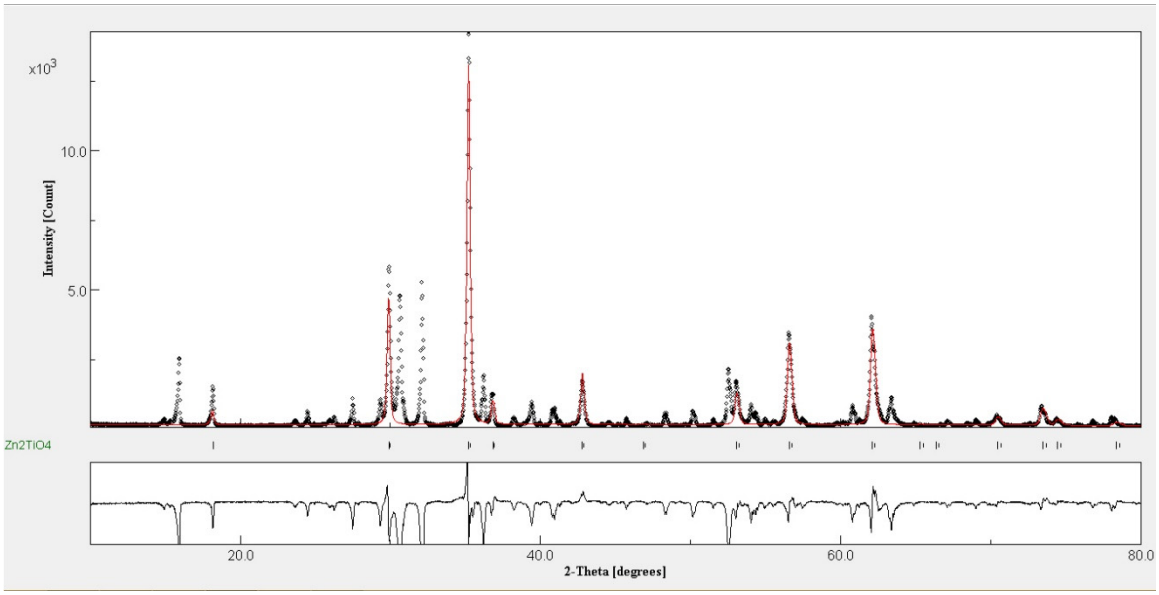

Figure 3.28. Rietveld plot of ZnO:TiO_2 = 1:1 (in mole) doped with 3 mol% Er^{3+} and 9 mol% Yb^{3+} fired at 1300 °C (R_{wp} = 46.533%, R_p = 35.679%).

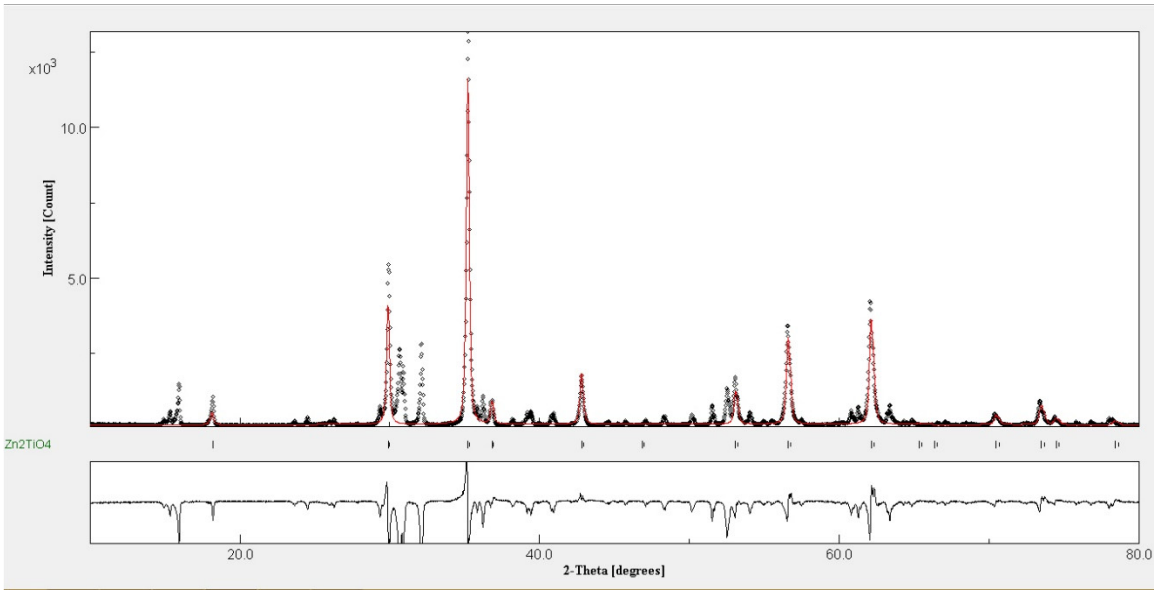

Figure 3.29. Rietveld plot of ZnO:TiO_2 = 1.25:1 (in mole) doped with 3 mol% Er^{3+} and 9 mol% Yb^{3+} fired at 1300 °C (R_{wp} = 40.489%, R_p = 30.367%).

Table 3.4. The R factors from Rietveld analysis via MAUD software with various possibilities of site preferences of RE^{3+} ions in Zn_2TiO_4 crystal matrix.

Figure	Table	Predicted molecular formula	R_{wp} (%)	R_p (%)
3.28	A1	$Zn_{(tet)}(ZnTi)_{(oct)}O_4$ (*reference*)	46.533	35.679
A1	A2	$(Zn_{0.999}RES_{0.001})_{(tet)}(ZnTi)_{(oct)}O_4$	46.530	35.675
A2	A3	$(Zn_{0.99}RES_{0.01})_{(tet)}(ZnTi)_{(oct)}O_4$	46.502	35.607
A3	A4	$(Zn_{0.95}RES_{0.01})_{(tet)}(ZnTi)_{(oct)}O_4$	46.462	35.369
A4	A5	$(Zn_{0.9}RES_{0.1})_{(tet)}(ZnTi)_{(oct)}O_4$	46.514	35.279
A5	A6	$Zn_{(tet)}(Zn_{0.499}RES_{0.001}Ti_{0.5})_{(oct)}O_4$	46.516	35.637
A6	A7	$Zn_{(tet)}(Zn_{0.49}RES_{0.01}Ti_{0.5})_{(oct)}O_4$	46.468	35.503
A7	A8	$Zn_{(tet)}(Zn_{0.45}RES_{0.05}Ti_{0.5})_{(oct)}O_4$	46.657	35.427
A8	A9	$Zn_{(tet)}(Zn_{0.4}RES_{0.1}Ti_{0.5})_{(oct)}O_4$	47.293	36.371
A9	A10	$Zn_{(tet)}(Zn_{0.5}Ti_{0.499}RES_{0.001})_{(oct)}O_4$	46.561	35.726
A10	A11	$Zn_{(tet)}(Zn_{0.5}Ti_{0.49}RES_{0.01})_{(oct)}O_4$	46.476	35.523
A11	A12	$Zn_{(tet)}(Zn_{0.5}Ti_{0.45}RES_{0.05})_{(oct)}O_4$	46.612	35.379
A12	A13	$Zn_{(tet)}(Zn_{0.5}Ti_{0.4}RES_{0.1})_{(oct)}O_4$	47.120	36.141
A13	A14	$Zn_{(tet)}(Zn_{0.4995}Ti_{0.4995}RES_{0.001})_{(oct)}O_4$	46.537	35.698
A14	A15	$Zn_{(tet)}(Zn_{0.495}Ti_{0.495}RES_{0.01})_{(oct)}O_4$	46.485	35.537
A15	A16	$Zn_{(tet)}(Zn_{0.475}Ti_{0.475}RES_{0.05})_{(oct)}O_4$	46.601	35.428
A16	A17	$Zn_{(tet)}(Zn_{0.45}Ti_{0.45}RES_{0.1})_{(oct)}O_4$	47.204	36.240

Remark: REs is Er^{3+} and/or Yb^{3+}.

According to Figure 3.28 and Figure A1 to A16, including the crystal structure parameters in Table A1 to A17, the results which were related to various possibilities of site preferences of RE^{3+} ions in Zn_2TiO_4 crystal matrix showed very high R factors more than 46% and 35% for R_{wp} and R_p, respectively. Besides, there was no any significant involvement or obvious tendency between profile fitting without (Figure 3.28) and with adding predicted site preferences of RE^{3+} ions (Figure A1 to A16). Therefore, the Rietveld refinement is not able to be applied to the XRD results of these synthesized products which means that their actual crystal structure and lattice parameters cannot be determined and calculated. For this reason, in this study, the indirect method to identify site preference of RE^{3+} ions in Zn_2TiO_4 crystal was suggested by considering the changes in its crystal structure and lattice parameters.

In theory, the fundamental crystal structure is considered by concentrating on close-packed planes of anions. Typically, the close-packed planes consist of large anions, these planes stack top each other, small interstitial sites are created between them in which cations may reside.

Hence, the possible ionic radius of occupying cation in Zn_2TiO_4 crystal can be calculated based on the close-packed of oxygen ions [43]. Since the ionic radius of oxygen ion is 0.138 nm, calculated ionic radius of cation in a tetrahedral site (coordination number (CN) = 4) should be in the range of 0.032-0.058 nm to maintain the tetrahedral structure. In the case of an octahedral site (CN = 6), the ionic radius of oxygen ion is 0.140 nm. Thus, calculated ionic radius of cation should be in the range of 0.059-0.102 nm to keep the octahedral structure. With these calculations, Er^{3+} and Yb^{3+} could not directly occupy cation in tetrahedral site (Zn^{2+}), octahedral site (Zn^{2+}/Ti^{4+}), or even get into the $V''_{Zn(tet)}$ because the ionic radii of Er^{3+} (0.089 nm, CN 6) and Yb^{3+} (0.087 nm, CN 6) are much larger than that of Zn^{2+} (0.060 nm, CN 4, and 0.074 nm, CN 6), Ti^{4+} (0.061 nm, CN 6), and $V''_{Zn(tet)}$ (0.032-0.058 nm), including the mismatch of valence between Zn^{2+}, Ti^{4+} and RE^{3+} ions. According to the calculated possible ionic radius of cation in octahedral site that should be in the range of 0.059-0.102 nm, therefore, RE^{3+} ions should go in the vacant sites, that may be created in octahedral site, more easily than direct occupying the Zn^{2+} and Ti^{4+} or entering the $V''_{Zn(tet)}$. One possibility that vacant site is created in octahedral site is the change in position of Zn^{2+}, moving from octahedral site to $V''_{Zn(tet)}$, because of bigger ionic radii of RE^{3+} ions forcing them. Herein, site preference of RE^{3+} ions in Zn_2TiO_4 crystal can be expressed as follows;

Firstly, according to equation (3.7), by the incorporation of RE^{3+} ions into Zn_2TiO_4 crystal, the term "$V''_{Zn(tet)}$" is eliminated due to the change in position of Zn^{2+} from octahedral site to $V''_{Zn(tet)}$ and then vacant Zn site in octahedral ($V''_{Zn(oct)}$) takes place as shown in equation (3.12).

$$2TiO_2\left(\text{in } Zn_{(tet)}(ZnTi)_{(oct)}TiO_4\right) \rightarrow V''_{Zn(oct)} + Ti^{\cdot\cdot}_{Zn(oct)} + Ti_{Ti(oct)} + 4O^{x}_{o} \quad (3.12)$$

Secondly, equation (3.12) is multiplied by two because at least two RE^{3+} ions from RE_2O_3 enter two $V''_{Zn(oct)}$ and then express as equation (3.13);

$$4TiO_2\left(\text{in } Zn_{(tet)}(ZnTi)_{(oct)}TiO_4\right) \rightarrow 2V''_{Zn(oct)} + 2Ti^{\cdot\cdot}_{Zn(oct)} + 2Ti_{Ti(oct)} + 8O^{x}_{o} \quad (3.13)$$

Later, two RE^{3+} ions from RE_2O_3 enter two $V''_{Zn(oct)}$ which is expressed as equation (3.14);

$$RE_2O_3 + 2V''_{Zn(oct)} \rightarrow 2RE^{\cdot}_{Zn(oct)} + \frac{3}{2}O_{2(g)} + 6e' \quad (3.14)$$

By adding equations (3.13) and (3.14), and then express as equation (3.15);

$RE_2O_3 + 2V''_{Zn(oct)} + 4TiO_2$ (all in $Zn_{(tet)}(ZnTi)_{(oct)}TiO_4$)

$$\rightarrow 2RE^{\cdot}_{Zn(oct)} + \frac{3}{2}O_{2(g)} + 6e' + 2V''_{Zn(oct)} + 2Ti^{\cdot\cdot}_{Zn(oct)} + 2Ti_{Ti(oct)} + 8O^{x}_{o} \quad (3.15)$$

Remove duplicate terms from equation (3.15) and then express as equation (3.16);

$$RE_2O_3 + 4TiO_2 \rightarrow 2RE^{\cdot}_{Zn(oct)} + \frac{3}{2}O_{2(g)} + 6e' + 2Ti^{\cdot\cdot}_{Zn(oct)} + 2Ti_{Ti(oct)} + 8O^{x}_{o} \quad (3.16)$$

Hence, when RE is Er^{3+} and/or Yb^{3+}, two final equations are expressed as equations (3.17) and (3.18);

$$Er_2O_3 + 4TiO_2 \rightarrow 2Er^{\cdot}_{Zn(oct)} + \frac{3}{2}O_{2(g)} + 6e' + 2Ti^{\cdot\cdot}_{Zn(oct)} + 2Ti_{Ti(oct)} + 8O^{x}_{o} \quad (3.17)$$

$$Yb_2O_3 + 4TiO_2 \rightarrow 2Yb^{\cdot}_{Zn(oct)} + \frac{3}{2}O_{2(g)} + 6e' + 2Ti^{\cdot\cdot}_{Zn(oct)} + 2Ti_{Ti(oct)} + 8O^{x}_{o} \quad (3.18)$$

To certify these possible reactions, electrical charge balance of equations (3.14) and (3.16) which they are the fundamental reaction to explain site preference of RE^{3+} ions in Zn_2TiO_4 crystal are checked and proved. The electrical charge for the left and right sides of each equation is equal; minus four (-4) for equation (3.14) and neutral (0) for equation (3.16). Additionally, this proposed site preference is also verified by considering A and B-sites of Zn_2TiO_4 crystal structure. The tetrahedral (A-site) corresponds to $2Zn_{Zn}$ due to the $2Zn^{2+}$ from the occurrence of $2V''_{Zn(oct)}$ and octahedral (B-site) conforms to $(2RE^{\cdot}_{Zn} + 2Ti^{\cdot\cdot}_{Zn}) + 2Ti_{Ti}$. Thus, the possible site preference of RE^{3+} ions in this crystal system is $(Zn_{Zn})_{2(tet)}((RE^{\cdot}_{Zn} + Ti^{\cdot\cdot}_{Zn}) + Ti_{Ti})_{4(oct)}(O^{x}_{o})_8$ that equals to theoretical site AB_2O_4 type of Zn_2TiO_4 crystal structure. Furthermore, it was observed that the occupancy of RE^{3+} ions in $V''_{Zn(oct)}$ directly affected the lattice volume of Zn_2TiO_4, leading to the variation on UC emission intensity. This behavior will be explained below by considering following information.

In accordance with the cubic Zn_2TiO_4 crystal structure, the lattice constant is calculated using equation (3.19):

$$\text{lattice constant (Å)} = \sqrt{d^2(h^2+k^2+l^2)} \quad (3.19)$$

where d is the distance between adjacent planes (d-spacing). The *h*, *k*, and *l* are Miller indices. These two values are selected from main peak position of Zn_2TiO_4 phase that consists of only one phase; (3 1 1) at 2θ = 35.14°, (5 1 1) at 2θ = 56.52°, and (4 4 0) at 2θ = 61.99°. So, there are three calculated values of lattice constant that obtained from each position and then the average lattice constant is used to calculate lattice volume as expressed in equation (3.20).

$$\text{lattice volume } \left(\text{Å}^3\right) = \left(\frac{\text{lattice constant}_{(311)} + \text{lattice constant}_{(511)} + \text{lattice constant}_{(440)}}{3}\right)^3 \quad (3.20)$$

The crystallographic data of Zn_2TiO_4; lattice constant and lattice volume, according to various ZnO/TiO_2 mixing ratios doped with 3 mol% Er^{3+} and 9 mol% Yb^{3+} fired at 1300 °C are shown in Table 3.5. Taking into account Zn_2TiO_4 unit cell volume in Table 3.5 and the dependent lattice volumes of Zn_2TiO_4 crystal on various ZnO/TiO_2 mixing ratios in Figure 3.30, the calculated lattice volumes of all samples were lower than calculated lattice volume from JCPDS card values. These results also showed the change in lattice volume, depending on ZnO amount. With the increase of ZnO amount up to $x = 1$, the lattice volume of Zn_2TiO_4 decreased. Further increase of ZnO amount $x > 1$, the lattice volume of Zn_2TiO_4 increased. This behavior corresponds to the positive charge that occurs when excess Ti^{4+} occupy Zn^{2+} in octahedral and further RE^{3+} ions substitute $V''_{Zn(oct)}$, respectively. The positive charge in all cation positions is much more than the negative charge of oxygen. So, according to Coulomb force, the positive charge would attract the negative charge, leading to the abatement of Zn_2TiO_4 lattice volume. Figure. 3.31 shows the effect of lattice volume on emission intensity. The emission intensity decreased when the lattice volume increased for both green and red bands. By considering these results, it is possible that the amount of RE^{3+} ions that incorporates into Zn_2TiO_4 crystal is not equal in each sample, influencing to the variation of luminescence emission intensity, and resulting in the changes in lattice volume of host material.

Table 3.5. The crystallographic data of Zn_2TiO_4; lattice constant and lattice volume of various ZnO/TiO_2 mixing ratios doped with 3 mol% Er^{3+} and 9 mol% Yb^{3+} fired at 1300 °C. Reproduced with permission from Kobwittaya *et al*., *Ceram. Int.*, **43** (2017) 13505-13515. Copyright (2017) Elsevier Ltd and Techna Group S.r.l.

Sample	Lattice constant (Å)	Lattice volume (Å^3)
Zn_2TiO_4 (JCPDS 25-1164)	8.4602	605.54
Z 0.25 T 1	8.4376	600.70
Z 0.5 T 1	8.4191	596.76
Z 0.75 T 1	8.4128	595.42
Z 1 T 1	8.4053	593.83
Z 1.25 T 1	8.4229	597.56
Z 1.5 T 1	8.4282	598.69
Z 1.75 T 1	8.4407	601.36

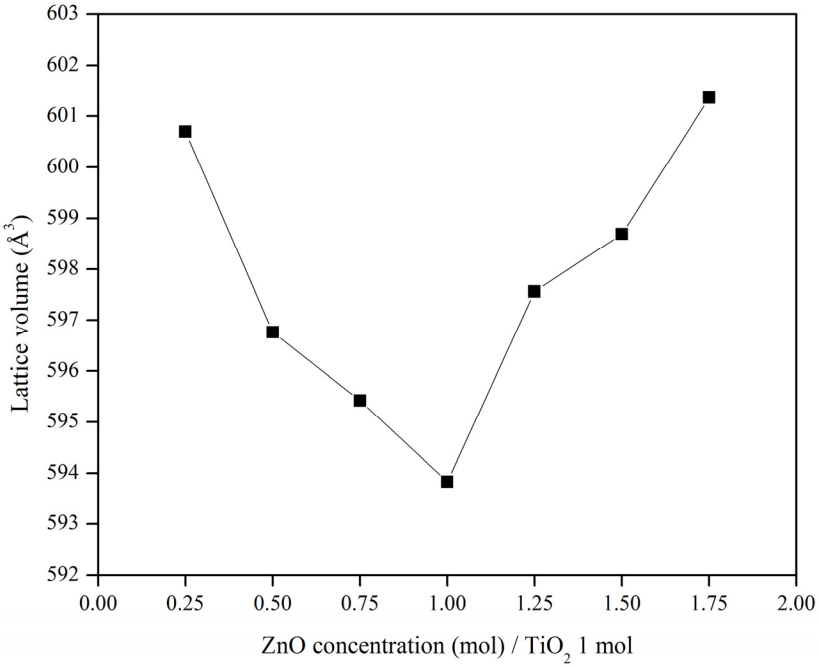

Figure 3.30. The dependent lattice volumes of Zn_2TiO_4 crystal on various ZnO/TiO_2 mixing ratios doped with 3 mol% Er^{3+} and 9 mol% Yb^{3+} fired at 1300 °C. Reproduced with permission from Kobwittaya *et al*., *Ceram. Int.*, **43** (2017) 13505-13515. Copyright (2017) Elsevier Ltd and Techna Group S.r.l.

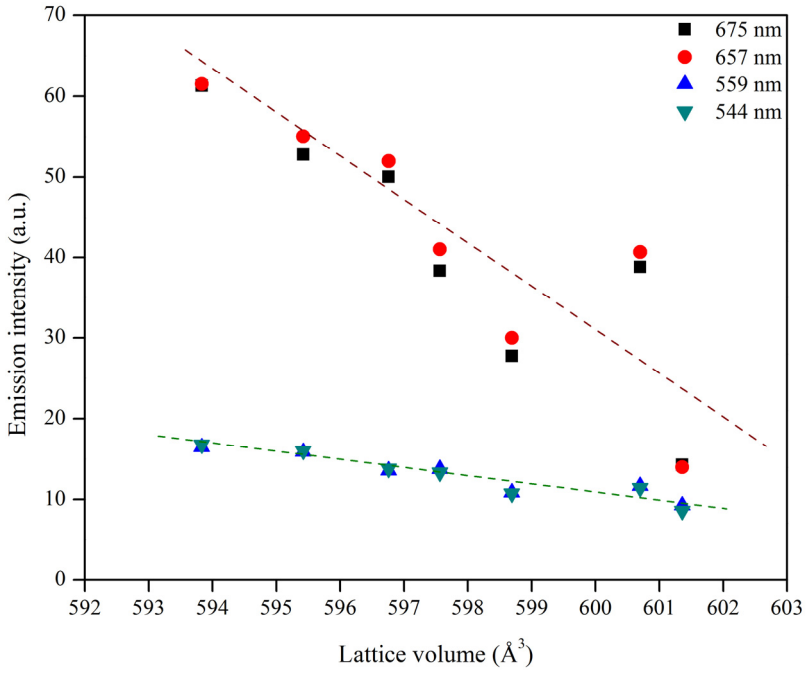

Figure 3.31. The red (657 nm and 675 nm) and green (544 nm and 559 nm) emission intensities of various ZnO/TiO_2 mixing ratios doped with 3 mol% Er^{3+} and 9 mol% Yb^{3+} fired at 1300 °C versus various lattice volumes of Zn_2TiO_4 crystal according to the details in Figure 3.24 and Table 3.5. Reproduced with permission from Kobwittaya *et al*., *Ceram. Int.*, **43** (2017) 13505-13515. Copyright (2017) Elsevier Ltd and Techna Group S.r.l.

3.3.9 Effect of Er^{3+} and Yb^{3+} concentrations on upconversion luminescence (UCL)

UCL spectra were investigated as a function of Er^{3+} and Yb^{3+} concentrations. The effect of various Er^{3+} concentrations, while keeping 9 mol% Yb^{3+} concentration is shown in Figure 3.32, which the red (657 and 675 nm) and green (544 and 559 nm) emission intensities are plotted versus various Er^{3+} concentrations. These UCL behaviors can be separated into two parts. In the initial part, as increasing Er^{3+} concentration from 0-3 mol%, the emission intensity augmented because the Er^{3+} activator concentration in the Zn_2TiO_4 crystal increased. Further increase of Er^{3+} concentration up to 5 mol%, the emission intensity decreased because of concentration quenching. Taking into account the UC emission color, the luminescence was red and changed from weak to strong red with increasing Er^{3+} concentration from 1-3 mol%. Further increase of Er^{3+} concentration more than 3 mol%, the brightness of red emission decreased. In addition, when the system did not have Er^{3+}, no emission color was observed.

Hence, the maximum emission intensity is detected on red emission band for Er^{3+} concentration at 3 mol%.

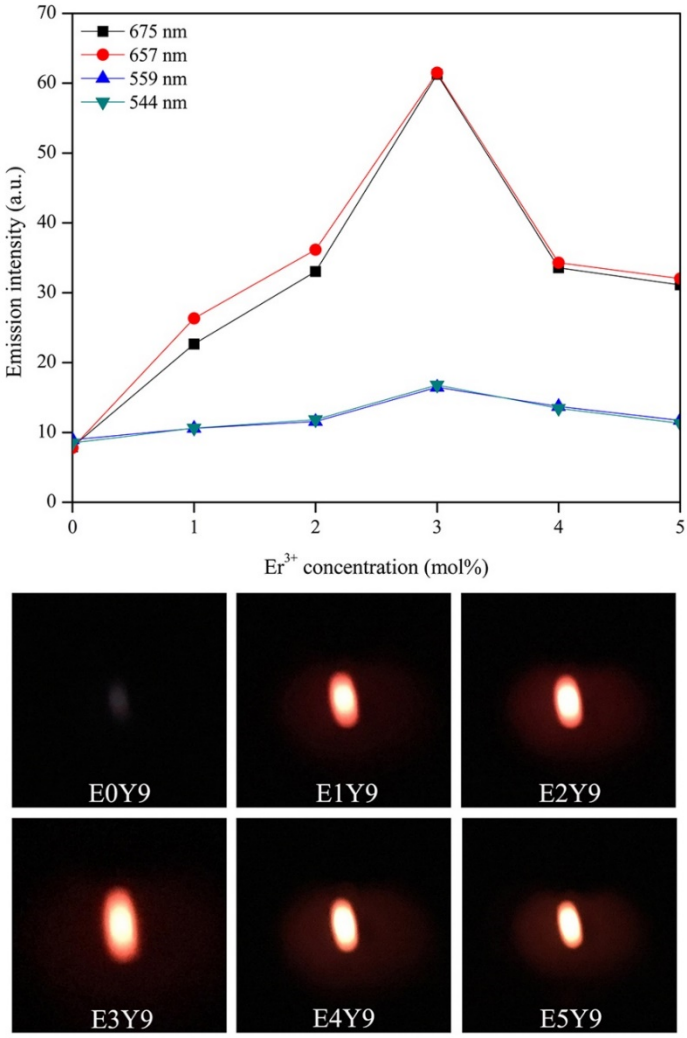

Figure 3.32. The red (657 nm and 675 nm) and green (544 nm and 559 nm) emission intensities versus ZnO:TiO_2 = 1:1 (in mole) doped with various mol% Er^{3+} and 9 mol% Yb^{3+} fired at 1300 °C, and corresponding photographs of UC emission color irradiated with a 980-nm 125 mW laser. Reproduced with permission from Kobwittaya *et al.*, *Ceram. Int.*, **43** (2017) 13505-13515. Copyright (2017) Elsevier Ltd and Techna Group S.r.l.

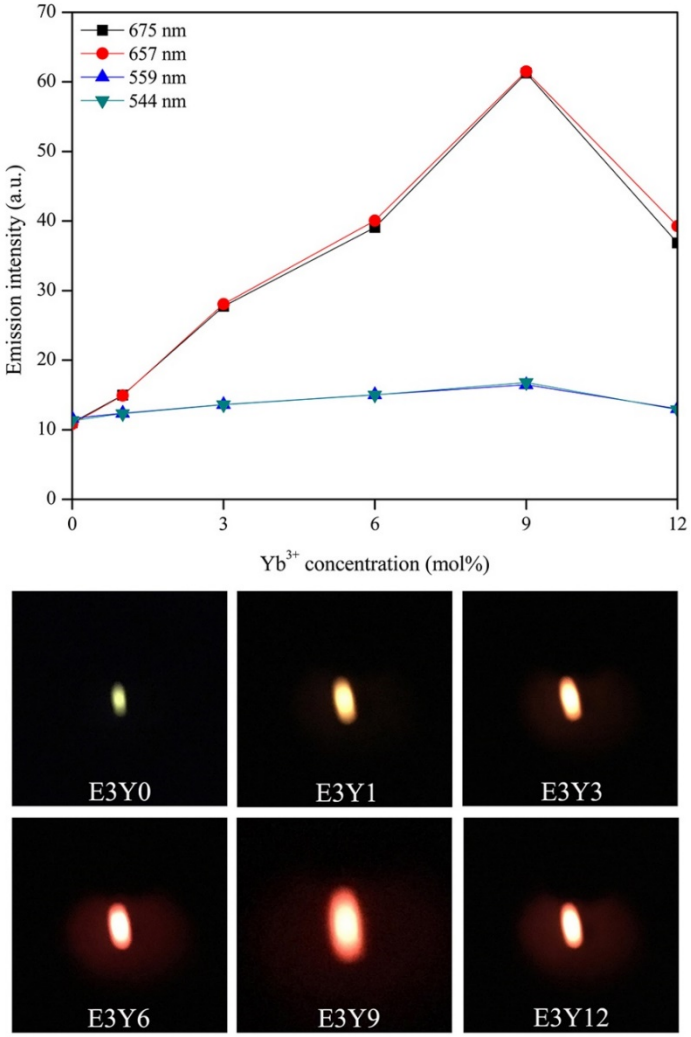

Figure 3.33. The red (657 nm and 675 nm) and green (544 nm and 559 nm) emission intensities versus ZnO:TiO_2 = 1:1 (in mole) doped with 3 mol% Er^{3+} and various mol% Yb^{3+} fired at 1300 °C, and corresponding photographs of UC emission color irradiated with a 980-nm 125 mW laser. Reproduced with permission from Kobwittaya *et al.*, *Ceram. Int.*, **43** (2017) 13505-13515. Copyright (2017) Elsevier Ltd and Techna Group S.r.l.

The effect of various Yb^{3+} concentrations, while keeping 3 mol% Er^{3+} concentration is shown in Figure 3.33, which the red (657 and 675 nm) and green (544 and 559 nm) emission intensities are plotted versus various Yb^{3+} concentrations. By keeping Er^{3+} concentration at 3 mol%, the Yb^{3+} concentration influences on the emission intensity of the products. With increasing Yb^{3+} concentration from 0-12 mol%, the emission intensity increased, reached maximum at 9 mol% Yb^{3+} doping concentration, and then decreased on further increasing it. The increased emission

intensity is viable owing to higher concentration of dissolved Yb^{3+} concentration into the Zn_2TiO_4 phase which augments the number of pump photons and the excited Er^{3+}. The decreased emission intensity at higher Yb^{3+} concentration corresponds to concentration quenching. Considering the UC emission color, the color changed from green to red with increasing Yb^{3+} concentration. The green emission occurred when the system did not have Yb^{3+}. Further increase of Yb^{3+} concentration from 1-9 mol%, the emission color started with yellow/orange at 1 mol% and initially changed to red at 3 mol% Yb^{3+}. Then, the brightness of red emission increased and reached maximum brightness at 9 mol%. Subsequently, increasing Yb^{3+} concentration up to 12 mol%, brightness of red emission decreased. With these two results, varying Er^{3+} and Yb^{3+} concentrations, while keeping the other, it can be concluded that the red emission depends mainly on the amount of Yb^{3+} in the host material, while the green emission relies on the amount of Er^{3+}. Thus, optimum Er^{3+} and Yb^{3+} concentrations for the brightest UC emission are 3 and 9 mol%, respectively.

3.3.10 Elemental composition analysis

3.3.10.1 Standard calibration curve of various ZnO/TiO_2 mixing ratios

According to TG-DTA results, the weight loss of raw material and raw mixture was observed due to the thermal process, therefore, the elemental composition of the product should be considered in order to confirm the actual ZnO/TiO_2 mixing ratio. Typically, the chemical composition is contemplated using XRF measurement which uses X-ray fluorescence technology to determine the product composition by comparing the target product with standard calibration curve based on its components. Hence, the best way to obtain the result with high accuracy and precision is the preparation of standard calibration curve by using standard sample of various ZnO/TiO_2 mixing ratios. This standard sample was in the form of raw powder mixture (no further thermal process) and produced by the mixing of ZnO powder (NanoTek, ~ 34 nm, 99%) and TiO_2 powder (Katayama Chemical) via solid-state reaction method. The calibration curve was made by the XRF technique and consisted of two graphs. First was the graph of Zn intensity versus weight% of Zn (Figure 3.34) and second was the graph of Ti intensity versus weight% of Ti (Figure 3.35).

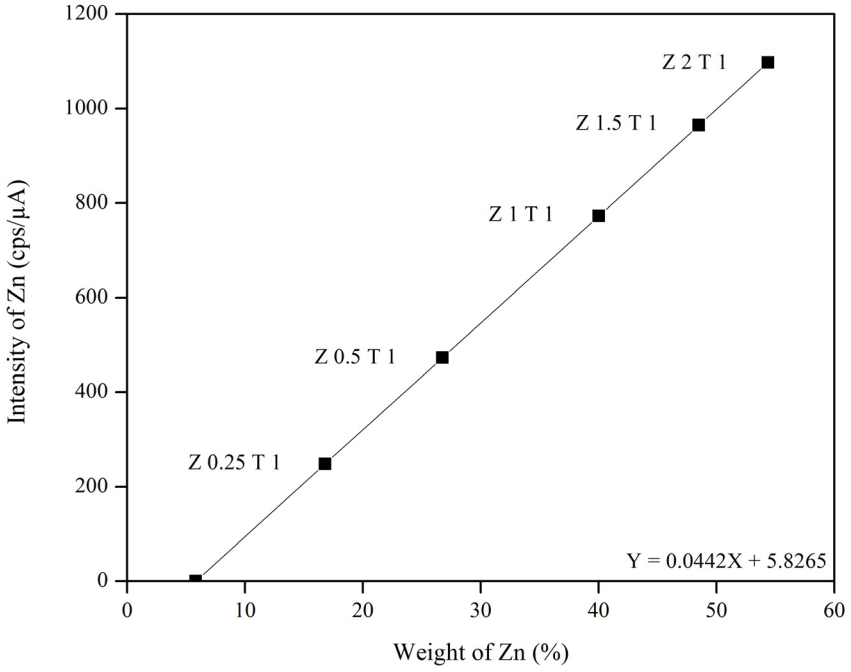

Figure 3.34. The calibration curve of Zn contents for different ZnO/TiO_2 mixing ratios.

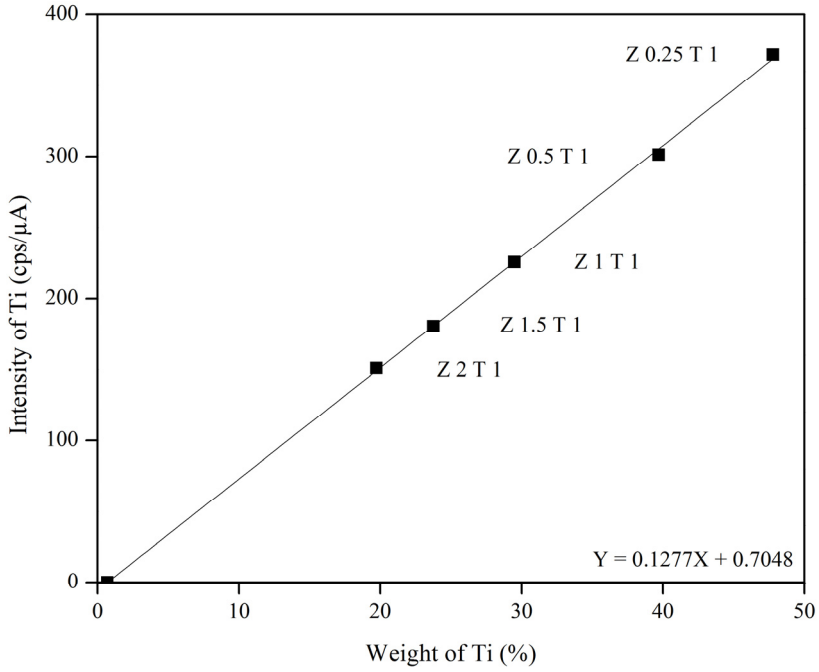

Figure 3.35. The calibration curve of Ti contents for different ZnO/TiO_2 mixing ratios.

As shown in Figure 3.34 and Figure 3.35, the linear equation of both graphs was Y = 0.0442X + 5.8265 and Y = 0.1277X + 0.7048 for Zn and Ti contents, respectively. It is obvious that the linear line does not cross the zero at origin point because the error of measurement inherent to the analyzer could cause the difference between expected and measured content values. However, these calibration curves can be used to analyze Zn and Ti contents of the target sample since, after reverse checking the composition of standard samples, observed values were not much different from calculated value of each condition (Table 3.6).

Table 3.6. The comparison between the observed and calculated values of Zn and Ti contents (in weight% and mole) for each sample.

Mixing ratio	Zn content (weight%)		Ti content (weight%)	
	Calculated	Observed	Calculated	Observed
Zn 0.25 Ti 1	16.3109	16.7942	47.7657	48.1862
Zn 0.5 Ti 1	27.1164	26.7459	39.7047	39.1711
Zn 1 Ti 1	40.5473	40.0300	29.6852	29.4984
Zn 1.5 Ti 1	48.5655	48.5021	23.7037	23.7624
Zn 2 Ti 1	53.8943	54.3684	19.7284	19.9719

Converting weight% to mole and followed by keeping 1 mole of Ti;

Mixing ratio	Zn content (mole)		Ti content (mole)	
	Calculated	Observed	Calculated	Observed
Zn 0.25 Ti 1	0.2500	0.2552	1.0000	1.0000
Zn 0.5 Ti 1	0.5000	0.4999	1.0000	1.0000
Zn 1 Ti 1	1.0000	0.9935	1.0000	1.0000
Zn 1.5 Ti 1	1.5000	1.4943	1.0000	1.0000
Zn 2 Ti 1	2.0000	1.9930	1.0000	1.0000

Remark: For preparing these calibration curves and acquiring observed and calculated values of Zn and Ti contents, all calculations are based on ZnO and TiO_2 compounds, and atomic weights used to calculate these results are Zn = 65.382, Ti = 47.867, and O = 15.999.

3.3.10.2 X-ray fluorescence (XRF) of ZnO:TiO_2 = 1:1 (in mole) doped with 3 mol% Er^{3+} and 9 mol% Yb^{3+} dried and fired at various temperatures

In this XRF analysis, Zn and Ti contents of the samples were analyzed by comparing with Zn and Ti standard calibration curves that were mentioned in section 3.3.10.1. For Er and Yb contents, their standard calibration curve cannot be created due to the uncertainty of standard sample caused by very low content of both elements. Herein, to analyze Er and Yb contents, the fundamental parameter (FP) method was used to examine the content of them. An overview of XRF analysis of synthesized powder samples, ZnO:TiO_2 = 1:1 (in mole) doped with 3 mol% Er^{3+} and 9 mol% Yb^{3+} dried and fired at various temperatures, is given in Table 3.7.

Table 3.7. An overview of XRF analysis of ZnO:TiO_2 = 1:1 (in mole) doped with 3 mol% Er^{3+} and 9 mol% Yb^{3+} powder samples dried and fired at various temperatures, their expected mixing ratio values and XRF elemental analysis results (each sample was measured five times at different positions and data were averaged).

Temperature	Zn (mole)		Ti (mole)		Er (mole)		Yb (mole)	
(°C)	Expected	XRF	Expected	XRF	Expected	XRF	Expected	XRF
90	1.0000	0.9745	1.0000	1.0000	0.0300	0.0265	0.0900	0.0825
800	1.0000	0.9638	1.0000	1.0000	0.0300	0.0255	0.0900	0.0761
1000	1.0000	0.9642	1.0000	1.0000	0.0300	0.0257	0.0900	0.0735
1100	1.0000	0.9618	1.0000	1.0000	0.0300	0.0252	0.0900	0.0757
1200	1.0000	0.9619	1.0000	1.0000	0.0300	0.0254	0.0900	0.0729
1300	1.0000	0.9622	1.0000	1.0000	0.0300	0.0251	0.0900	0.0736

Remark:

1. Atomic weights used to calculate these results are Zn = 65.382, Ti = 47.867, Er = 167.259, and Yb = 173.045.
2. These results are converted from weight% to mole and followed by keeping 1 mole of Ti.

As shown in Table 3.7, the results showed that all observed values were lower than the expected content. These could be due to many situations, for example the errors during sample preparation and the weight loss of raw material and raw mixture during the thermal process. However, the XRF is only a semi-quantitative technique except a calibration curve is used. So, it should be noted that Er and Yb contents are too low to detect with precision. With these results, it could be concluded that the temperature used has little effect on the change in mixing

ratio and the final mixing ratio of these samples after adjustment based on 1 mole of Ti is still acceptable as Zn:Ti:Er:Yb = 1:1:0.03:0.09 (in mole).

3.3.10.3 X-ray fluorescence (XRF) of various ZnO/TiO_2 mixing ratios doped with 3 mol% Er^{3+} and 9 mol% Yb^{3+} fired at 1300 °C

According to the procedures used for XRF analysis in section 3.3.10.2, the analyzed results of synthesized powder samples, various ZnO/TiO_2 mixing ratios doped with 3 mol% Er^{3+} and 9 mol% Yb^{3+} fired at 1300 °C, is given in Table 3.8.

Table 3.8. An overview of XRF analysis of various ZnO/TiO_2 mixing ratios doped with 3 mol% Er^{3+} and 9 mol% Yb^{3+} powder samples fired at 1300 °C, their expected mixing ratio values and XRF elemental analysis results (each sample was measured five times at different positions and data were averaged).

Mixing ratio	Zn (mole)		Ti (mole)		Er (mole)		Yb (mole)	
	Expected	XRF	Expected	XRF	Expected	XRF	Expected	XRF
Z 0.25 T 1	0.2500	0.2195	1.0000	1.0000	0.0300	0.0241	0.0900	0.0774
Z 0.5 T 1	0.5000	0.4485	1.0000	1.0000	0.0300	0.0253	0.0900	0.0781
Z 0.75 T 1	0.7500	0.7075	1.0000	1.0000	0.0300	0.0256	0.0900	0.0791
Z 1 T 1	1.0000	0.9622	1.0000	1.0000	0.0300	0.0251	0.0900	0.0736
Z 1.25 T 1	1.2500	1.2031	1.0000	1.0000	0.0300	0.0257	0.0900	0.0757
Z 1.5 T 1	1.5000	1.3441	1.0000	1.0000	0.0300	0.0260	0.0900	0.0777
Z 1.75 T 1	1.7500	1.6142	1.0000	1.0000	0.0300	0.0260	0.0900	0.0757

Remark:

1. Atomic weights used to calculate these results are Zn = 65.382, Ti = 47.867, Er = 167.259, and Yb = 173.045.
2. These results are converted from weight% to mole and followed by keeping 1 mole of Ti.

As shown in Table 3.8, the results showed that all observed values were lower than the expected content. These could be due to many situations as mentioned in section 3.3.10.2. With these results, it could be summarized that the final mixing ratio of these samples after adjustment based on 1 mole of Ti is in accordance with the expected mixing ratio.

3.3.11 Upconversion (UC) mechanism

The UC mechanism can be interpreted with the emission spectra as a function of pump power of the excitation source. The UC emission intensity I was measured as a function of the pump power P. In the UC mechanism, I is proportional to the n power of P, $I \propto P^n$, where n is the

number of the pumped photons per the emitted photon [1]. As shown in Figure 3.36, a plotting of log (I) versus log (P) of the sample, ZnO:TiO_2 = 1:1 (in mole) doped with 3 mol% Er^{3+} and 9 mol% Yb^{3+} fired at 1300 °C, which it emitted the brightest emission, yielded a straight line, resulting in the n-value of 0.94 and 0.97 for green emission, and n-value of 1.32 and 1.34 for red emission, under between P = 15-196 mW. Principally, under steady-state excitation, the experimental n-value is in the specific range of values and less than the maximum theoretical n-value for each possible UC mechanism; two-photon process ($1 < n \leq 2$) or three-photon process ($2 < n \leq 3$), because of the saturation effect in the UCL intensity caused by the competition between a few processes, for instance the nonradiative energy transfer and UC processes between dopant ions for the depletion of the intermediate excited states [44,45]. Herein, the observed n-values for green and red emissions could be estimated that they are related to the condition of $1 < n \leq 2$. Therefore, it may suggest that the two-photon process is responsible for the green and red UC emissions mechanism of this phosphor system. To better understand the decrease in n-value and the saturation effect, these phenomena will be discussed in detail in the next section.

As shown in Figure 3.37, to clearly explain about n-value, the n-value of various ZnO/TiO_2 mixing ratios doped with 3 mol% Er^{3+} and 9 mol% Yb^{3+} fired at 1300 °C was calculated and then the relationship between them was plotted based on red (657 nm and 675 nm) and green (544 nm and 559 nm) emission bands. With increase of ZnO amount up to x = 1, the increase in n-value was observed on both green and red bands, and the slope of two lines seemed to be parallel. In general, the n-value is related to UC mechanism and directly involves with the ratio of activator/sensitizer in host crystal matrix. Hence, at this condition ($x \leq 1$), the amount of Er^{3+} and Yb^{3+} in the host crystal matrix may increase equally from the beginning until at x = 1 with the same ratio. Besides, it is possible that the Er^{3+}/Yb^{3+} pairs of ions are possibly formed in the host crystal. Further increase of ZnO amount $x > 1$, the n-value for the green band gradually decreased, but n-value for the red band sharply decreased. At this condition ($x > 1$), it is obvious that the amount of Er^{3+} and Yb^{3+} in the host crystal matrix decreases. In this phosphor system, the increase and decrease of the amount of RE^{3+} ions in host crystal matrix depend mainly on the number of vacant sites including the performance of the incorporation of RE^{3+} ions into the host material. With overall result in Figure 3.37, it can be summarized that, under the constant number of vacant site, the performance in the substitution of Er^{3+} in host crystal matrix is higher

than Yb^{3+} because of the constant change in tendency line of green band and inconstant change in tendency line of red band (green and red bands are directly related to Er^{3+} and Yb^{3+}, respectively, as described in section 3.3.9). Besides, by considering the changes in tendency line, it could be implied that the prior ion for the substitution in host crystal matrix should be Er^{3+} and further Yb^{3+} would enter some part of vacant site.

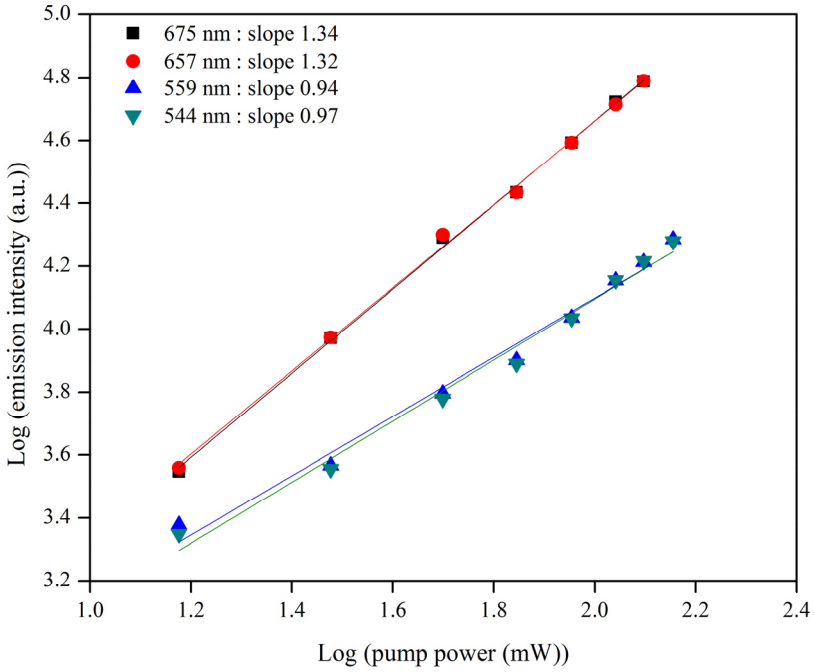

Figure 3.36. Pump power dependent UC of $ZnO:TiO_2$ = 1:1 (in mole) doped with 3 mol% Er^{3+} and 9 mol% Yb^{3+} fired at 1300 °C, and irradiated with a 980-nm, 15-196 mW laser. Reproduced with permission from Kobwittaya *et al*., *Ceram. Int.*, **43** (2017) 13505-13515. Copyright (2017) Elsevier Ltd and Techna Group S.r.l.

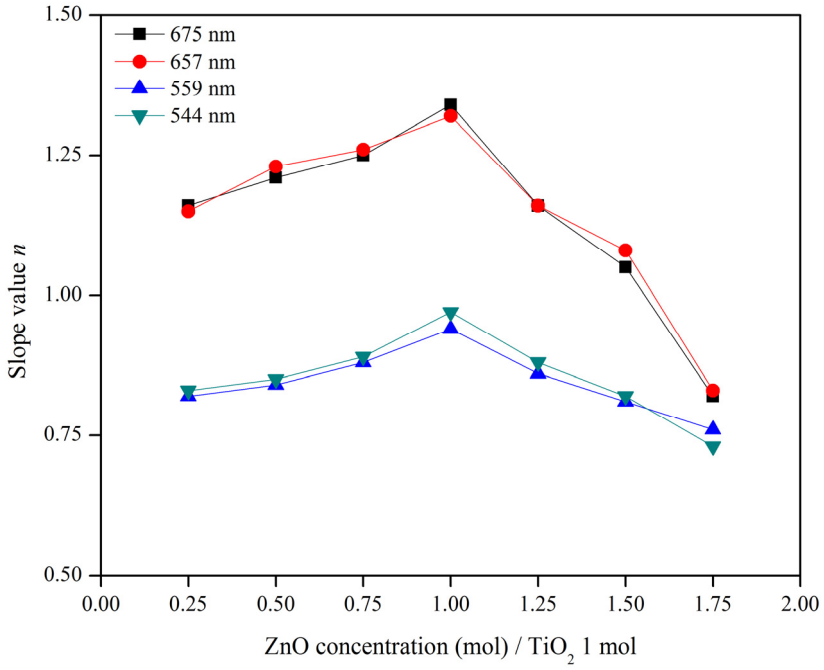

Figure 3.37. The *n*-values of red (657 nm and 675 nm) and green (544 nm and 559 nm) emission bands versus various ZnO/TiO_2 mixing ratios doped with 3 mol% Er^{3+} and 9 mol% Yb^{3+} fired at 1300 °C. Reproduced with permission from Kobwittaya *et al*., *Ceram. Int.*, **43** (2017) 13505-13515. Copyright (2017) Elsevier Ltd and Techna Group S.r.l.

The schematic energy level diagram of Er^{3+} and Yb^{3+}, and proposed UC mechanism in ZnO-TiO_2 composite containing Er^{3+} and Yb^{3+} under a 980-nm laser excitation is depicted in Figure 3.38. The 980-nm laser excites the $^2F_{7/2}$ state of Yb^{3+} and $^4I_{15/2}$ state of Er^{3+} to the $^2F_{5/2}$ and $^4I_{11/2}$ states, respectively, by the ground state absorption (GSA) process. Besides, the energy in $^2F_{5/2}$ state of Yb^{3+} drops back in the form of nonradiative transition to the ground state $^2F_{7/2}$ due to excess energy which is associated with lattice vibrations of host material. Taking into account the long lifetime of the excited $^2F_{5/2}$ level of Yb^{3+} (typically one millisecond), Yb^{3+} may well transfer the excitation energy (as expressed as ET) to Er^{3+} with higher probability than decaying the excited energy to its ground state [46]. Thus, the energy is transferred to the neighboring Er^{3+}, resulting in the population of $^4I_{11/2}$ state. Further, the multi-phonon relaxation (MPR) process occurs, the energy in $^4I_{11/2}$ state decays to $^4I_{13/2}$ state and then the energy is populated to $^4F_{9/2}$ state by excited state absorption process 1 (ESA1). Meanwhile, Yb^{3+} repeatedly absorbs the photon energy from excitation source, leading to more energy transfer to the adjacent Er^{3+}, and the $^4F_{9/2}$ and $^4F_{7/2}$ states are populated by ESA2. Subsequently, the electrons relax to the

$^2H_{11/2}$, $^4S_{3/2}$, and $^4F_{9/2}$ states as non-radiative (NR) process. According to the results that the products show higher red emission intensity than green emission one, they are related to the energy relaxation from $^4F_{9/2}$ state to $^4I_{9/2}$ state that leads to the increase of energy in the range of red emission. Thus, the bright red UC emission is observed due to the $^4F_{9/2} \rightarrow {}^4I_{15/2}$ transition of Er^{3+}.

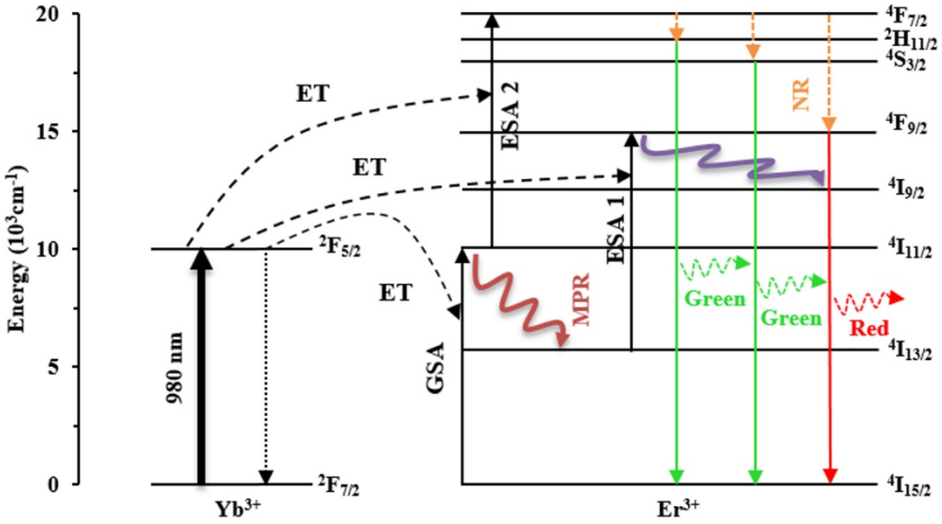

Figure 3.38. Energy level diagram illustrating the proposed energy transfer mechanisms of ZnO-TiO_2 doped with 3 mol% Er^{3+} and 9 mol% Yb^{3+} under a 980-nm laser excitation. Reproduced with permission from Kobwittaya *et al*., *Ceram. Int.*, **43** (2017) 13505-13515. Copyright (2017) Elsevier Ltd and Techna Group S.r.l.

3.3.12 The saturation effect in the upconversion luminescence (UCL) intensity and its influence on the change in *n*-value

For UC mechanism, even though the two-photon process corresponds to the *n*-value equal to approximately two but the dependence of UCL intensity on pump power is also expected to decrease in *n*-value with increasing excitation power. This experimentally observed behavior is theoretically proven by Pollnan *et al*. [44] who reported that this phenomenon was attributed to the saturation process of UCL intensity. According to their report, the saturation effect in the UCL intensity was mostly caused by the competition between linear decay and UC processes for the depletion of the intermediate excited states. This behavior can be conceived by considering the significant models suggested by Pollnan *et al*. [44], Suyver *et al*. [45], and

Agazzi *et al*. [47]. Their models were based on the same underlying UC mechanism which was the simplest UCL system (related to two-photon process), consisting of ground state (G), intermediate excited state (E1), and UCL state (E2). Keeping on the simplest system together with the relationship between UC emission intensity I and pump power P ($I \propto P^n$), it was anticipated that I was proportional to P^2 (n-value ~ 2) when the linear decay of the E1 was the dominant depletion mechanism, while I was proportional to P^1 (n-value ~ 1) when the UC process of the E1 was the dominant mechanism. Notably, these results were proved by presuming that the system was under steady-state excitation. In addition, Lei *et al*. [48] reported the steady-state UCL dynamic equations of the UC process that were concerned with the two step ET between neighboring Er^{3+} and Yb^{3+}, and their model was different from the original one [44]. Nevertheless, their result was also similar to that deduced in [44] and the discussion mentioned above. Hence, in the easiest way to conclude the change in n-value in UCL system, it should be referred to the "saturation effect" for the perception in detail. According to the $I \propto P^n$, the plotting of I versus P via log-log scale yields a straight line with slope n. Basically, the slope n decreases with increasing P because the system is moved toward the saturation state of UCL intensity by the increment of P. With this concept, at the intermediate excited state, if the linear decay is the dominant depletion mechanism, UCL intensity will be released without the influence of saturation effect because the energy is not abundant in the UCL state and the n-value for this case should be close to two or equal two. On the other hand, if the UC process is the dominant depletion mechanism, the energy will be numerous in the UCL state, causing to the saturation effect in UCL intensity and the n-value will be decreased to around one. Therefore, the saturation effect caused by the competition of linear decay and UC processes is the considerable reason for the depletion of the intermediate excited state, influencing to the reduction of n-value [44,45,49,50].

In this study, the n-value for green emission was around 0.95, while n-value for the red emission was around 1.33. This could be ascribed to the difference of the intermediate excited state between the green and red emissions. For the green emission, the intermediate excited state is $^4I_{11/2}$ of Er^{3+}, and the UC process and linear decay at this excited state are ESA2 from the $^4I_{11/2} \rightarrow {}^4F_{7/2}$ and MPR from $^4I_{11/2} \rightarrow {}^4I_{13/2}$, respectively. Because of the n-value that is approximately one for the green emission, therefore, the UC process (ESA2) is the dominant depletion mechanism which causes the saturation effect in UCL intensity and the decrease in n-value.

In the case of red emission, the intermediate excited state is $^4I_{13/2}$ of Er^{3+} and the reduced *n*-value is related to the competition between UC process (ESA1: $^4I_{13/2} \rightarrow {}^4F_{9/2}$) and linear decay ($^4I_{13/2} \rightarrow {}^4I_{15/2}$). However, the *n*-values for red emission tended towards one, therefore, the UC process is dominant mechanism for the depletion of the intermediate state $^4I_{13/2}$ of Er^{3+}, leading to the diminution of *n*-value and the saturation effect in UCL intensity. Also, there are minor possibilities which would have influence on the decrease in *n*-value such as the ET processes to impurity defects, cross-relaxation, or other complicated processes, which can also give rise to the depletion of the intermediate excited states of Er^{3+} and Yb^{3+} [44,45,47,51].

3.3.13 Comparison of upconversion (UC) emission intensity of phosphors prepared by solid-state reaction and powder-solution mixing methods

The solid-state reaction (SSR) and powder-solution mixing (PSM) methods are the similar technique, and the raw mixture of both procedures is in the powder form. Hence, by using these two methods to fabricate UC phosphors, they can only be obtained in the form of powder (by sintering raw mixture directly) or pellet (compaction of raw mixture before sintering). Nevertheless, as mentioned in the process of SSR, the main problems of this preparation method are the inhomogeneity of phosphor for both pellet and powder forms, and low luminescence emission intensity of phosphor powder even irradiated by high power laser output. For the phosphor pellet and powder, the inhomogeneity will lead to the change in luminescence emission intensity with different positions over the whole surface of the product. For the phosphor powder, it normally shows lower emission intensity than phosphor pellet because the contact distance of reactants is not adequate to provide efficient diffusion process, causing to the lower number of dopants within the host material. With these disadvantages of SSR method, therefore, the PSM method is proposed as the optional technique to produce the UC phosphor with homogenous phase and high luminescence emission intensity for both powder and pellet forms.

In this section, the UC phosphors prepared by SSR and PSM methods will be compared by considering the products with the same physical characteristic (pellet (SSR) / pellet (PSM) and powder (SSR) / powder (PSM)) and their UC emission intensity. The phosphor pellets were prepared with the optimum condition presented by Luitel *et. al.* [21], $ZnO:TiO_2$ = 1:1 (in mole) doped with 2 mol% Er^{3+} and 6 mol% Yb^{3+} fired at 1200 °C for 4 h, for both SSR and PSM

methods. The phosphor powders were prepared with the optimum condition presented in this chapter; $ZnO:TiO_2$ = 1:1 (in mole) doped with 3 mol% Er^{3+} and 9 mol% Yb^{3+} fired at 1300 °C for 1 h, for both SSR and PSM methods. Besides, to acquire the reliable result, the UC emission intensity of each sample was measured at different positions of its surface. The results of these comparisons will be discussed below.

In the case of phosphor pellet, according to the photograph in Figure 3.39, the physical characteristics of the samples prepared by SSR and PSM were different. After firing at 1200 °C for 4 h, the SSR sample showed small decrease in the size of the pellet, while the PSM sample showed larger decrease. Also, each sample demonstrated dissimilar colors, pink and orange, for SSR and PSM samples, respectively. These miscellaneous changes are caused by the complex and dissimilar reaction mechanisms between raw precursors of each preparation method. For example, taking into account the thermal reaction of the sample, the SSR raw mixture mainly contains the oxide reactants and organic solvent, therefore, only decomposition and burning processes take place during the phosphor formation. On the other hand, the PSM raw mixture chiefly comprises of oxide reactants, nitrate reactants, and moisture. So, there are more than two processes to finalize the phosphor pellet. This difference is one of the possibilities that leads to the changes in physical characteristics of both SSR and PSM phosphor pellets.

The UC emission spectra of both fired samples are measured at different positions of its surface and the results are shown in Figure 3.40 and Figure 3.41. The inset shows the photograph of the measured positions. The results showed that both samples exhibited the same peak emission wavelengths which were at 544 and 559 nm for green region, and 657 and 675 nm for red region. Also, the maximum emission intensity of both samples was almost at the same level. However, in the red region, the maximum emission intensity of SSM sample was at 657 nm but PSM sample was at 675 nm. The different formation processes may cause this behavior.

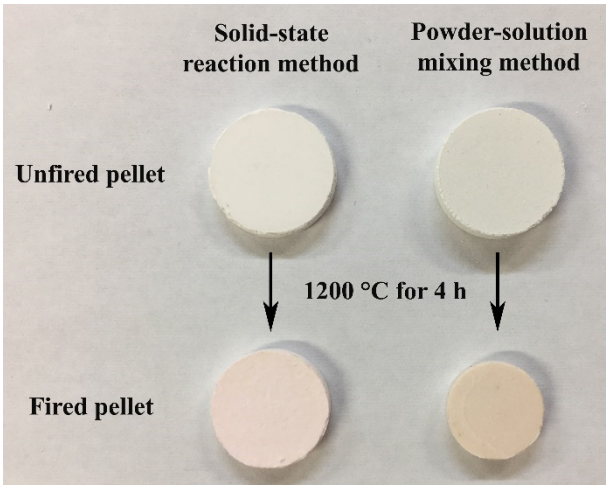

Figure 3.39. Photograph of ZnO:TiO_2 = 1:1 (in mole) doped with 2 mol% Er^{3+} and 6 mol% Yb^{3+} phosphor pellets (before and after firing) prepared by solid-state reaction and powder-solution mixing methods.

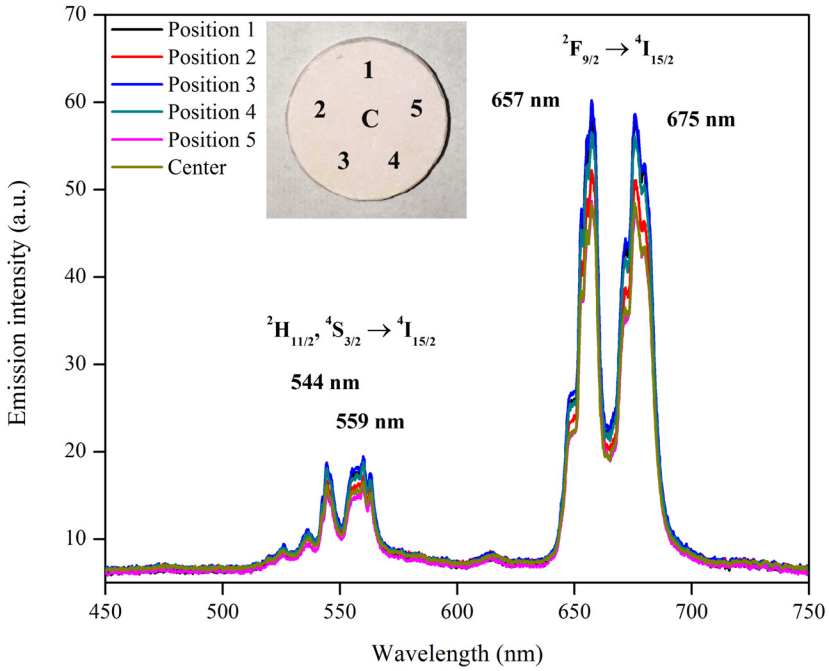

Figure 3.40. UC emission spectra at different positions of pellet surface of the phosphor (ZnO:TiO_2 = 1:1 (in mole) doped with 2 mol% Er^{3+} and 6 mol% Yb^{3+} fired at 1200 °C for 4 h) prepared by solid-state reaction method, and irradiated with a 980-nm 70 mW laser. The inset shows the photograph of the corresponding measured positions as labeled.

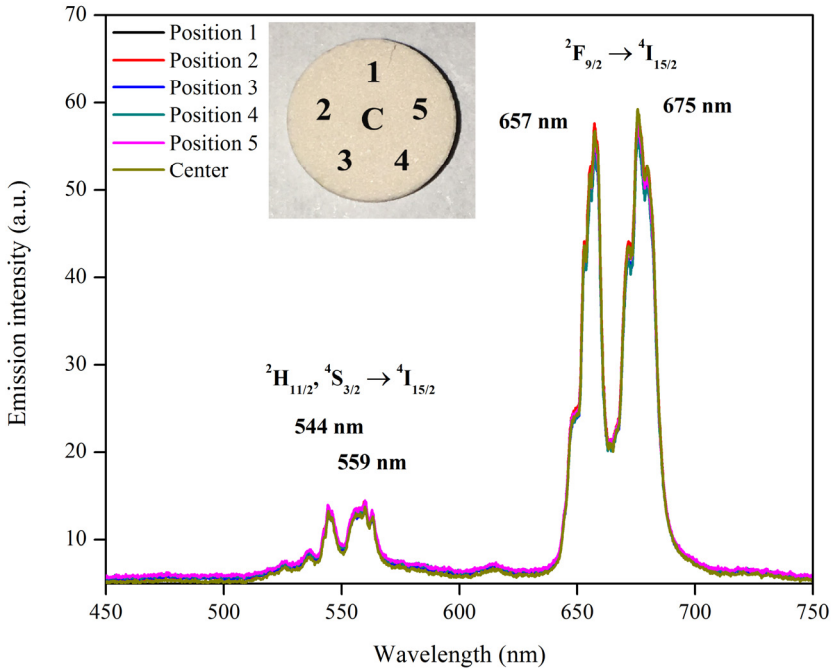

Figure 3.41. UC emission spectra at different positions of pellet surface of the phosphor ($ZnO:TiO_2$ = 1:1 (in mole) doped with 2 mol% Er^{3+} and 6 mol% Yb^{3+} fired at 1200 °C for 4 h) prepared by powder-solution mixing method, and irradiated with a 980-nm 70 mW laser. The inset shows the photograph of the corresponding measured positions as labeled.

Focusing on the UC emission intensity at various measured positions of each phosphor pellet, it was obvious that the emission intensity of PSM sample was more well-distributed over the whole surface than that of SSR sample. This can be explained as follows. The SSR method provides the direct reaction between the reactants (solid-solid reaction) at high temperature via diffusion process, therefore, the inhomogeneity of the product may take place due to the incomplete mixing of raw materials and the formation process. On the other hand, the PSM method involves various blending steps based on the mixing of nitrate-based compounds, sol solution, and solid particles in deionized water. Due to the use of dopants in the form of solution and the preparation via liquid-phase mixing, the PSM method results in the complete mixing of raw materials and the homogeneity of raw mixture. For this reason, in the case of PSM sample, the dopants are well-distributed over the raw mixture and they easily get into the host material more than in the case of SSR sample. Hence, higher homogeneity of the product can be obtained.

For the phosphor powder, the UC emission spectra of both fired samples are also measured at different positions of its surface and the results are shown in Figure 3.42 and Figure 3.43. The inset shows the photograph of the measured positions. The results showed that both samples showed the same peak emission wavelengths as observed in phosphor pellet which were at 544 and 559 nm for green region, and 657 and 675 nm for red region. So, it can be concluded that ZnO-TiO_2 composite doped with Er^{3+} and Yb^{3+} exhibits the particular emission wavelength for green and red bands, even if the preparation method and physical characteristics are dissimilar. In addition, it is clear that the emission intensity of PSM sample is more well-distributed than that of SSR sample either. This must be due to the same reason as mentioned above about phosphor pellet. However, the emission intensity of phosphor powder is usually lower than that of phosphor pellet because the bulk density of powder mixture, which relies on how intimately individual particles pack together, directly affects the formation process of phosphor powder.

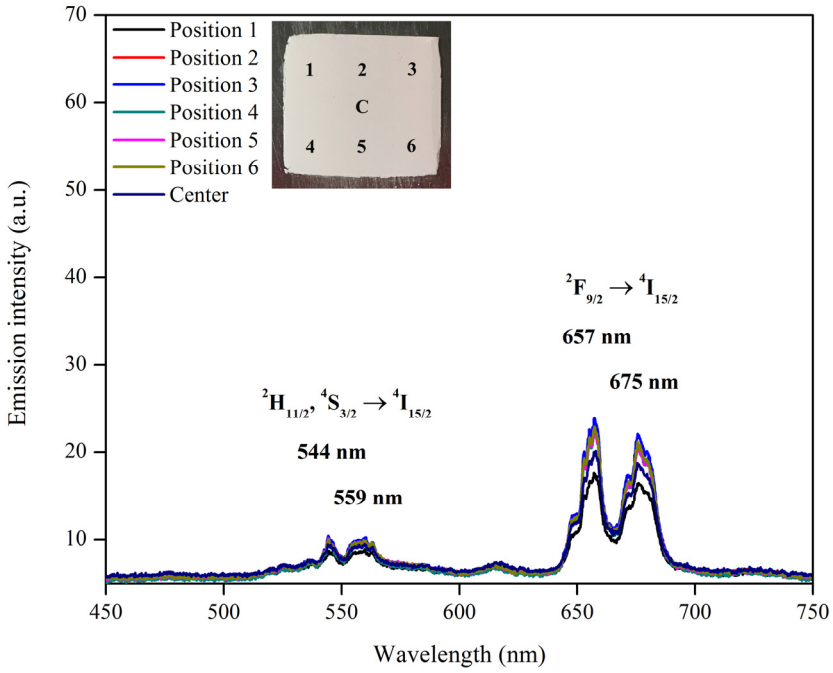

Figure 3.42. UC emission spectra at different positions of powder surface of the phosphor (ZnO:TiO_2 = 1:1 (in mole) doped with 3 mol% Er^{3+} and 9 mol% Yb^{3+} fired at 1300 °C for 1 h) prepared by solid-state reaction method, and irradiated with a 980-nm 110 mW laser. The inset shows the photograph of the corresponding measured positions as labeled.

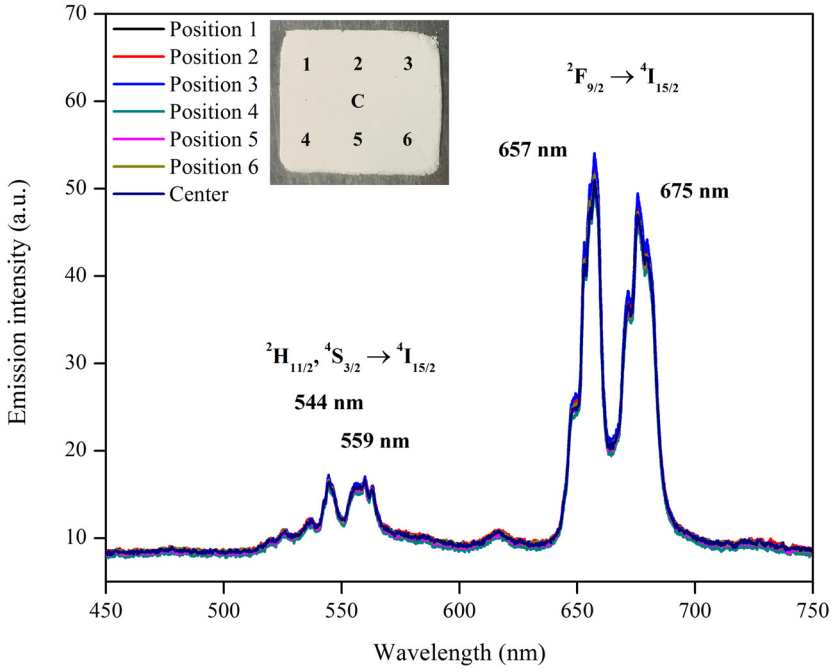

Figure 3.43. UC emission spectra at different positions of powder surface of the phosphor ($ZnO:TiO_2$ = 1:1 (in mole) doped with 3 mol% Er^{3+} and 9 mol% Yb^{3+} fired at 1300 °C for 1 h) prepared by powder-solution mixing method, and irradiated with a 980-nm 110 mW laser. The inset shows the photograph of the corresponding measured positions as labeled.

Basically, raw powder mixture prepared by SSR and PSM methods demonstrates dissimilar bulk density due to the difference of physical appearances of reactants, the type of solvent used, and the mixing process. Herein, the PSM powder sample shows higher bulk density than SSR powder sample because the PSM method provides very short contact distance of reactants due to the solution processing and dissolution process which result in the dense powder. In comparison, the powder sample prepared by SSR method provides longer contact distance of reactants because the mixing of solid reactants is hard to obtain the dense powder due to their morphology, shape, and size of particles, and these are the main reason that gives rise to inefficient diffusion process, leading to the low emission intensity of SSR phosphor powder.

It is worth noting that these comparisons focus only on the homogeneity of the phosphor by considering the UC emission intensity of the sample under the same physical characteristic and condition. However, the conditions used for PSM phosphor pellet and SSR phosphor powder are not the optimum condition for them to emit the strongest emission intensity. Additionally,

it should be noted that the phosphor powder produced by grounding phosphor pellet demonstrates lower emission intensity than directly preparing phosphor powder and phosphor pellet due to the change in their bulk density. For the phosphor pellet fabricated by compacting phosphor powder, it shows the instability of the product because the phosphor powder cannot attach to form stable phosphor pellet. So, this means is not appropriate for making phosphor pellet.

Eventually, it can be summarized that, for the Er^{3+}/Yb^{3+} co-doped ZnO-TiO_2 composite phosphor, these two methods show the same optimum ZnO/TiO_2 mixing ratio = 1:1 (in mole), even if the optimum firing temperature, preparation time, and dopant concentration are different; 1200 °C for 4 h (SSR) and 1300 °C for 1 h (PSM), 2 mol% Er^{3+}/6 mol% Yb^{3+} (SSR) and 3 mol% Er^{3+}/9 mol% Yb^{3+} (PSM). The dissimilar formation processes of the products and the process of incorporation of RE^{3+} ions into the host material may cause these differences. In general, Er^{3+} and Yb^{3+} get into the host material by diffusion-based and dissolution/diffusion-based processes for SSR and PSM methods, respectively. In addition, it is obvious that, for ZnO-TiO_2:Er^{3+}/Yb^{3+} phosphor, the product prepared by PSM method presents great potential for enhancing the UC phosphor to be more homogenous phase than SSR method, becoming the leading cause of the increase in the amount of dopant ions (concentration used increases either) inside the host material.

3.4 Conclusion

Er^{3+} and Yb^{3+} co-doped ZnO-TiO_2 composite UC phosphors were successfully synthesized by powder-solution mixing method. When the product was excited by a 980-nm laser, two UC emission bands were observed in the emission spectra, green band centered at 544 and 559 nm, and red band centered at 657 and 675 nm which were in accordance with $^2H_{11/2}$, $^4S_{3/2} \rightarrow {}^4I_{15/2}$ and $^4F_{9/2} \rightarrow {}^4I_{15/2}$ transitions of Er^{3+}, respectively. The green and red emission intensities reached a maximum value in the sample containing 3 mol% Er^{3+} and 9 mol% Yb^{3+}. The optimum mixing ratio of ZnO/TiO_2 was ZnO:TiO_2 = 1:1 (in mole). Brightest UCL of ZnO-TiO_2 composite doped with Er^{3+} and Yb^{3+} occurred when the system consisted of mixed phases; Zn_2TiO_4, TiO_2, $RE_2Ti_2O_7$, and RE_2TiO_5 (RE = Er^{3+} and/or Yb^{3+}).

The site preference of Er^{3+} and Yb^{3+} in Zn_2TiO_4 host crystal matrix was discussed in detail. The most possibility of this site preference should be at the vacant Zn site in octahedral ($V''_{Zn(oct)}$) that would appear when there were excess TiO_2 in the system and followed by the incorporation of RE^{3+} ions into Zn_2TiO_4 crystal structure. The Er^{3+} and Yb^{3+} went to ($V''_{Zn(oct)}$) easier than occupied Zn^{2+} or Ti^{4+} sites, and vacant Zn site in tetrahedral ($V''_{Zn(tet)}$) due to the mismatch ionic radii and different electronic charges of Er^{3+} and Yb^{3+}, and Zn^{2+} or Ti^{4+}, including inappropriate radius of ($V''_{Zn(tet)}$), So, the possible site preference of RE^{3+} ions in Zn_2TiO_4 crystal matrix is $(Zn_{Zn})_{2(tet)}((RE'_{Zn} + Ti''_{Zn}) + Ti_{Ti})_{4(oct)}(O^x_o)_8$ that equals to theoretical site AB_2O_4 type of Zn_2TiO_4 crystal structure. Besides, this phenomenon is mostly expressed in the changes in unit cell parameter of Zn_2TiO_4 crystal, which lead to the decrease in its lattice constant and lattice volume.

In addition, the comparison of the optimum mixing ratio and dopant concentration of ZnO-TiO_2:Er^{3+}/Yb^{3+} phosphors prepared by solid-state reaction and powder-solution mixing methods was discussed in detail. Even though the optimum firing temperature and preparation time were different, 1200 °C for 4 h (solid-state reaction method) and 1300 °C for 1 h (powder-solution mixing method), but these two methods showed the same optimum ZnO/TiO_2 mixing ratio = 1:1 (in mole). The most effective product that was synthesized by solid-state reaction method showed the optimum dopant concentrations at 2 mol% Er^{3+} and 6 mol% Yb^{3+}, while using powder-solution mixing method, the optimum dopant concentrations were 3 mol% Er^{3+} and 9 mol% Yb^{3+}. The dissimilar formation processes of the products and the process of incorporation of RE^{3+} ions into the host material may cause these differences. In general, Er^{3+} and Yb^{3+} get into the host material by diffusion-based and dissolution/diffusion-based processes for SSR and PSM methods, respectively. In addition, it is obvious that, for ZnO-TiO_2:Er^{3+}/Yb^{3+} phosphor, the product prepared by PSM method presents great potential for enhancing the UC phosphor to be more homogenous phase than SSR method, becoming the leading cause of the increase in the amount of dopant ions (concentration used increases either) inside the host material.

3.5 Acknowledgements

This chapter contains contributions from co-authors and some portions were published in: K. Kobwittaya, Y. Oishi, T. Torikai, M. Yada, T. Watari, H.N. Luitel, Bright red upconversion luminescence from Er^{3+} and Yb^{3+} co-doped ZnO-TiO_2 composite phosphor powder, *Ceramics International*, **43** (2017) 13505-13515.

3.6 Copyright permission

References

[1] F. Auzel, *Chem. Rev.*, **104** (2004) 139-174.

[2] L. Liang, Y. Yulin, Z. Mi, F. Ruiqing, Q. Lele, W. Xin, Z. Lingyun, Z. Xuesong, H. Jianglong, *J. Solid State Chem.*, **198** (2013) 459-465.

[3] L. Wang, M. Lan, Z. Liu, G. Qin, C. Wu, X. Wang, W. Qin, W. Huang, L. Huang, *J. Mater. Chem. C*, **1** (2013) 2485-2490.

[4] K. Yamamoto, M. Fujii, S. Sowa, K. Imakita, K. Aoki, *J. Phys. Chem. C*, **119** (2015) 1175-1179.

[5] W. Chen, J.-O. Malm, V. Zwiller, Y. Huang, S. Liu, R. Wallenberg, J.-O. Bovin, L. Samuelson, *Phys. Rev. B*, **61** (2000) 11021-11024.

[6] D. Li, W. Qin, S. Liu, W. Pei, Z. Wang, P. Zhang, L. Wang, L. Huang, *J. Alloy. Compd.*, **653** (2015) 304-309.

[7] H.-H. Xie, Q. Wen, H. Huang, T.-Y. Sun, P. Li, Y. Li, X.-F. Yu, Q.-Q. Wang, *RSC Adv.*, **5** (2015) 79525-79531.

[8] H. Lin, G. Meredith, S. Jiang, X. Peng, T. Luo, N. Peyghambarian, E.Y.B. Pun, *J. Appl. Phys.*, **93** (2003) 186-191.

[9] G.-S. Yi, G.-M. Chow, *Chem. Mater.*, **19** (2007) 341-343.

[10] X. Wang, S. Xiao, Y. Bu, J.W. Ding, *J. Alloy. Compd.*, **477** (2009) 941-945.

[11] Y. Li, B. Chen, X. Zhao, Z. Wang, H. Lin, *J. Alloy. Compd.*, **536** (2012) 198-203.
[12] G. Liu, B. Jacquier, Spectroscopic Properties of Rare Earths in Optical Materials, Springer-Verlag, Berlin Heidelberg (2005).
[13] R.-S. Liu, Phosphors, Up conversion Nano Particles, Quantum Dots and Their Applications (Volume 2), Springer Science+Business Media Singapore, Singapore (2016).
[14] H. Huang, H. Zhou, J. Zhou, T. Wang, D. Huang, Y. Wu, L. Sun, G. Zhou, J. Zhan, J. Hu, *RSC Adv.*, **7** (2017) 16777-16786.
[15] K.K. Kar, Composite Materials: Processing, Applications, Characterizations, Springer-Verlag Berlin Heidelberg (2017).
[16] M.-W. Kim, H. Yoon, T.Y. Ohm, H.S. Jo, S. An, S.K. Choi, H. Park, S.S. Al-Deyab, B.K. Min, M.T. Swihart, S.S. Yoon, *Appl. Catal. B-Environ.*, **201** (2017) 479-485.
[17] H.-S. Lim, J. Lee, S. Lee, Y.S. Kang, Y.-K. Sun, K.-D. Suh, *Acta Mater.*, **122** (2017) 287-297.
[18] L. Li, Y. Fan, D. Wang, G. Feng, D. Xu, *Cryst. Res. Technol.*, **46** (2011) 475-479.
[19] L. Li, F. Li, T. Cui, Q. Zhou, D. Xu, *Phys. Status Solidi A*, **209** (2012) 2596-2599.
[20] W.M. Yen, S. Shionoya, H. Yamamoto, Phosphor Handbook, Second Edition, CRC Press, Boca Raton, Florida (2006).
[21] H.N. Luitel, K. Ikeue, R. Okuda, R. Chand, T. Torikai, M. Yada, T. Watari, *Opt. Mater.*, **36** (2014) 591-595.
[22] K. Ohyama, T. Nonaka, T. Kanamori, S.-I. Yamamoto, 22nd International Workshop on Active-Matrix Flatpanel Displays and Devices (AM-FPD) (2015) 89-90.
[23] S.-I. Yamamoto, K. Ohyama, T. Nonaka, T. Kanamori, 21st International Workshop on Active-Matrix Flatpanel Displays and Devices (AM-FPD) (2014) 271-272.
[24] T. Nonaka, T. Kanamori, K. Ohyama, S.-I. Yamamoto, *Jpn. J. Appl. Phys.*, **54** (2015) 03CA02.
[25] F. Hassan, M.S. Miran, H.A. Simol, M.A.B.H. Susan, M.Y.A. Mollah, *Bangladesh J. Sci. Ind. Res.*, **50** (2015) 21-28
[26] D. Raoufi, *Appl. Surf. Sci.*, **255** (2009) 5812-5817.
[27] D. Raoufi, *J. Lumin.*, **134** (2013) 213-219.
[28] B.A.A. Balboul, *Thermochim. Acta*, **419** (2004) 173-179.
[29] B.A.A.A. Balboul, *Powder Technol.*, **107** (2000) 168-174.

[30] B.A.A. Balboul, *Thermochim. Acta*, **351** (2000) 55-60.

[31] B. Faust, Modern Chemical Techniques: An Essential Reference for Students and Teachers, Infrared Spectroscopy, The Royal Society of Chemistry (1997) 62-91.

[32] E.M. Levin, C.R. Robbins, H.F. McMurdie, Phase Diagram for Chemists Volume I (Figures 1-2066), The American Ceramic Society, Inc., Columbus, Ohio (1964).

[33] D.A.H. Hanaor, C.C. Sorrell, *J. Mater. Sci.*, **46** (2011) 855-874.

[34] Y. Xu, M. Yamazaki, P. Villars, *Jpn. J. Appl. Phys.*, **50** (2011) 11RH02.

[35] A. Jain, G. Hautier, S.P. Ong, C.J. Moore, C.C. Fischer, K.A. Persson, G. Ceder, *Phys. Rev. B*, **84** (2011) 045115.

[36] H.T. Kim, Y. Kim, M. Valant, D. Suvorov, *J. Am. Ceram. Soc.*, **84** (2001) 1081-1086.

[37] R.L. Millard, R.C. Peterson, B.K. Hunter, *Am. Mineral.*, **80** (1995) 885-896.

[38] K. Momma, F. Izumi, *J. Appl. Crystallogr.*, **44** (2011) 1272-1276.

[39] Y.-S. Chang, Y.-H. Chang, I.-G. Chen, G.-J. Chen, Y.-L. Chai, S. Wu, T.-H. Fang, *J. Alloy. Compd.*, **354** (2003) 303-309.

[40] R.E. Dinnebier, S.J.L. Billinge, Powder Diffraction: Theory and Practice, RSC Publishing, Cambridge (2008).

[41] S. Yamazaki, H. Toraya, *J. Appl. Cryst.*, **32** (1999) 51-59.

[42] L. Lutterotti, M. Bortolotti, G. Ischia, I. Lonardelli, H.-R. Wenk, *Z. Kristallogr. Suppl.*, **26** (2007) 125-130.

[43] Y.-M. Chiang, D.P. Birnie, W.D. Kingery, Physical Ceramics: Principle for Ceramic Science and Engineering, John Wiley & Sons, New York (1997).

[44] M. Pollnau, D.R. Gamelin, S.R. Lüthi, H.U. Güdel, M.P. Hehlen, *Phys. Rev. B*, **61** (2000) 3337-3346.

[45] J.F. Suyver, A. Aebischer, S. García-Revilla, P. Gerner, H.U. Güdel, *Phys. Rev. B*, **71** (2005) 125123.

[46] I. Hyppänen, J. Hölsä, J. Kankare, M. Lastusaari, L. Pihlgren, *J. Nanomater.*, **Article ID 16391** (2007) 1-8.

[47] L. Agazzi, K. Wörhoff, M. Pollnau, *J. Phys. Chem. C*, **117** (2013) 6759-6776.

[48] Y. Lei, H. Song, L. Yang, L. Yu, Z. Liu, G. Pan, X. Bai, L. Fan, *J. Chem. Phys.*, **123** (2005) 174710.

[49] L. Tian, Z. Xu, S. Zhao, Y. Cui, Z. Liang, J. Zhang, X. Xu, *Materials*, **7** (2014) 7289-7303.

[50] A.J.M. Sales, D.G. Sousa, H.O. Rodrigues, M.M. Costa, A.S.B. Sombra, F.N.A. Freire, M.J. Soares, M.P.F. Graça, J.S. Kumar, *Ceram. Int.*, **42** (2016) 6899-6905.
[51] G.C. Righini, M. Ferrari, *Riv. Nuovo Cimento*, **28** (2005) 1-50.

Chapter IV

Upconversion luminescence of ZnO-TiO_2: Ho^{3+}/Yb^{3+} phosphor powder

4.1 Introduction

Photon upconversion (UC) is a nonlinear optical process that involves the absorption of two or more low energy photons by way of intermediate long-lived energy states, leading to the emission of higher energy photon. Due to the distinct energy states of the trivalent rare earth (RE^{3+}) ions which are appropriate for UC process, the upconverters containing RE^{3+} ions exhibit the superior UC infrared to visible performance [1-3]. The RE^{3+} ions used in UCL materials have the intra-4*f* electronic orbitals which are shielded by the outer 5*s* and 5*p* orbits, resulting in the excellent luminescence characteristics [3]. Theoretically, there are two functions of RE^{3+} ions after doped into a host material. One is employed as the luminescent center which mainly exhibits the radiation and is called an activator, and the other ion absorbs the excited energy efficiently and then transfers that energy to the activator. Among various RE^{3+} ions, Yb^{3+} is often selected as sensitizer because of its large absorption cross-section around 980 nm, leading to efficient absorption of pump energy [4]. In the case of activator, Er^{3+} and Ho^{3+} are the most commonly used ions for the fabrication of UC phosphor because of their plentiful electronic energy levels [5,6].

Host material is also important to produce efficient UC phosphor. According to many researches in the field of UC phosphor, the most efficient host is fluoride-based material because fluorides usually exhibit low phonon energy about 350 cm^{-1} and high chemical stability [7]. Nevertheless, they are hygroscopic and are of limited use. In comparison, oxide-based materials demonstrate higher chemical and thermal durability, hence, oxides with low phonon energy may have more promising applications [8]. Among various oxide-based materials, ZnO-TiO_2 composite is considered as potential UC host material because of its stable product, Zn_2TiO_4, that shows great potentials for being a good optical host, for example high thermal

stability due to its inverse spinel structure, high value of refractive index n = 2.1 [9], and low phonon energy around 721 cm^{-1} [10].

In a series of reports regarding UCL from ZnO-TiO_2 composite phosphors, the reports showed the results of only one system, Er^{3+}/Yb^{3+} co-doped ZnO-TiO_2 composite prepared by solid state reaction method and metal-organic decomposition (MOD), and their products exhibited only the intense visible UC emission in the range of red emission band [11-14]. To obtain a variety of luminescence emission colors, the Ho^{3+}/Yb^{3+} system has gained much attention due to its two possible UC emissions, green light (495-550 nm) and red light (620-750 nm) [15,16]. With these conceivable colors, therefore, host materials containing Ho^{3+}/Yb^{3+} system have been studied for applying in many applications such as $Ca_5(PO_4)_3F$: Ho^{3+}/Yb^{3+} for biomedical [17] and Gd_2O_3: Ho^{3+}/Yb^{3+} for fingermark detection [18].

In this chapter, the details are provided based on the final product in the form of powder, therefore, only solid-state reaction method is considered to compare with the new proposed method, powder-solution mixing method, presented in this study because of the similarity of formation process and of the characteristic of the final product. Concerning the mechanism of solid-state reaction method, RE^{3+} ions diffuse into a host material at high temperature, obtaining low homogenous phase of the product. Hence, in this study, a systematic preparation of Ho^{3+}/Yb^{3+} co-doped ZnO-TiO_2 composite phosphor prepared by powder-solution mixing method was performed. With this method, the product was formed by the reaction between mixed RE^{3+} ions solution, fine TiO_2, and ZnO powders, resulting in more homogenous phase of the product. Additionally, the effect of ZnO/TiO_2 mixing ratio, Ho^{3+} and Yb^{3+} doping concentrations, and their ratios on the crystal phase and UCL properties were investigated. To understand the UC mechanism of Ho^{3+}/Yb^{3+} co-doped ZnO-TiO_2 composite phosphor, the dependence of UC emission intensity on the excitation power was calculated and discussed in detail.

4.2 Experimental

4.2.1 Chemicals

The starting materials in this study were: zinc oxide (ZnO; NanoTek, ~34 nm, 99%), titanium dioxide sol solution (TiO_2; Ishihara Sangyo Kaisha, 39.5 wt.%), holmium (III) nitrate pentahydrate ($Ho(NO_3)_3 \cdot 5H_2O$; Aldrich, 99.9%), and ytterbium (III) nitrate pentahydrate ($Yb(NO_3)_3 \cdot 5H_2O$; Aldrich, 99.9%).

4.2.2 Sample preparation

Ho^{3+} and Yb^{3+} co-doped ZnO-TiO_2 composite system was synthesized via powder-solution mixing method. The starting materials were thoroughly mixed by a high power-mixer using deionized water. Various ZnO-TiO_2 composite samples containing different ZnO/TiO_2 mixing ratios were prepared by varying ZnO contents (expressed as *x* mole), while keeping constant TiO_2 (1 mole). The *x*-value changed from x = 0.5-1.5 and the sample was named as Z*x*T1. In the case of dopants, Ho^{3+} and Yb^{3+} concentrations varied from 0-0.05 mol% and 0-12 mol%, which were calculated based on TiO_2 content, respectively. After thoroughly mixing, the sample was dried at 90 °C in drying oven for 12 h and then fired in an air atmosphere with various temperatures 800-1400 °C for 1 h. To obtain the final product, the fired sample was grounded using Vibrating Sample Mill (HEIKO, TI-100). The complete preparation scheme is shown in Figure 4.1.

4.2.3 Characterizations

Thermogravimetric and differential thermal analysis (TG-DTA) of raw material and raw mixture was carried out using a SEIKO EXSTAR6000 TG/DTA6300 instrument. About 10 mg of each sample were heated from room temperature to target temperature at heating rate of 10 °C/min. The crystal phase identification was analyzed using X-ray diffraction (XRD), a Shimadzu XRD-6300 instrument with CuKα radiation in the range of 2θ = 10-80°. In this study, the phase composition was approximated by calculating as relative phase content via pseudo-quantitative analysis related to equation (4.1).

$$\text{Relative phase content} = I_{(\text{phase})} / I_{(\text{total})} \quad (4.1)$$

where $I_{(phase)}$ is the intensity of selected peak from a main peak position that consists of only one phase; $I_{(311)}$ for Zn_2TiO_4, $I_{(110)}$ for TiO_2, $I_{(004)}$ for $RE_2Ti_2O_7$, and $I_{(102)}$ for RE_2TiO_5; and $I_{(total)}$ is the intensity summation of all selected peaks.

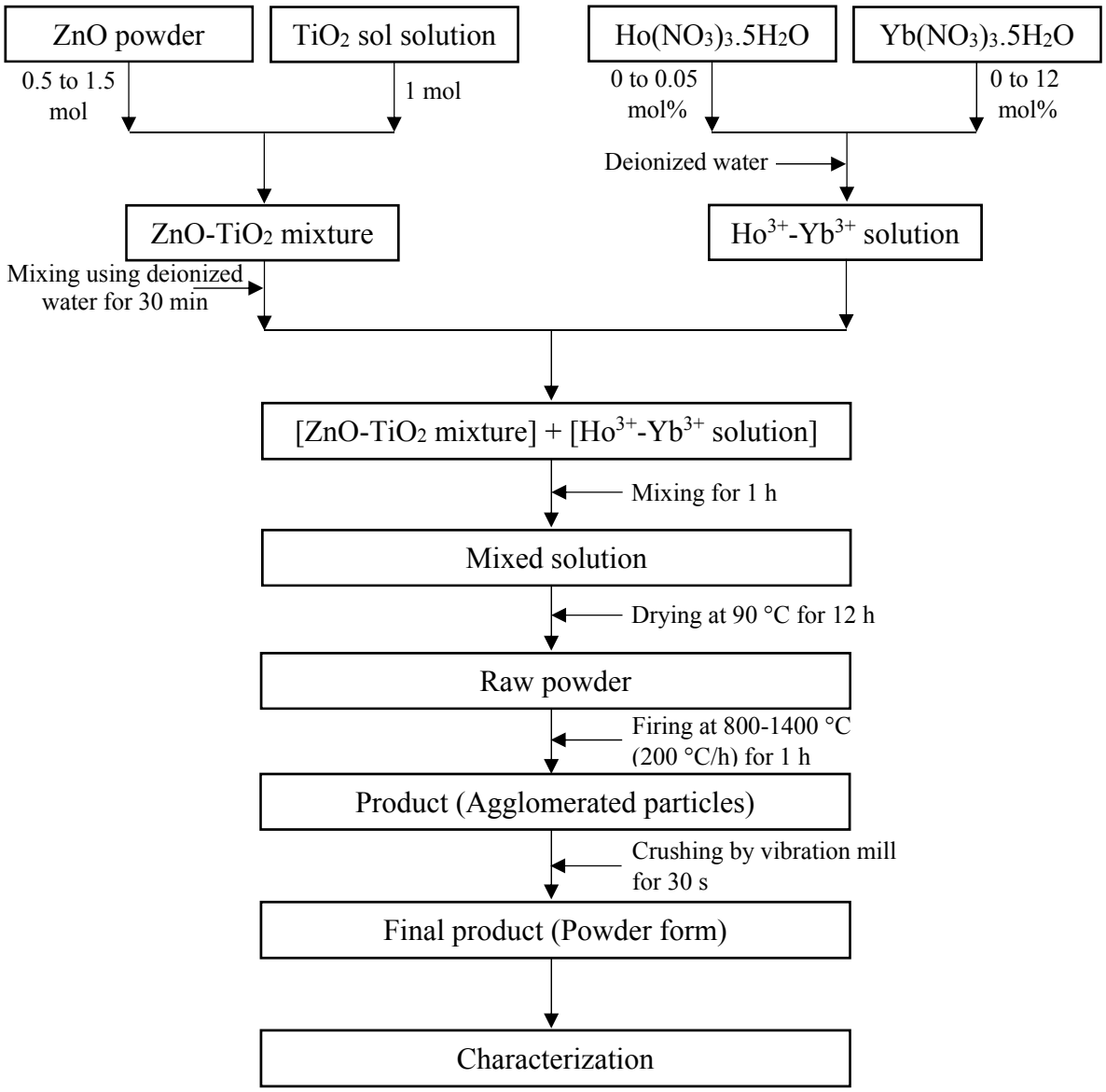

Figure 4.1. Flow chart for the preparation of $ZnO\text{-}TiO_2:Ho^{3+}/Yb^{3+}$ phosphor by powder-solution mixing method.

The microstructure of the samples was characterized by scanning electron microscopy (SEM), a Hitachi S-3000N instrument. Before SEM measurement, the sample was mounted securely by means of conductive carbon tape. Subsequently, the sample was coated with a thin layer of Pt-Pd (coating time of 90 s, around 5 nm thickness) under vacuum condition (vacuum-argon gas flushing) by ion sputter (Hitachi, E-1030).

The elemental composition analysis was carried out using X-ray fluorescence spectroscopy (XRF), a Shimadzu Energy Dispersive X-ray Fluorescence Spectrometer (Rayny EDX-800HS) instrument. The UC emission behavior excited by a 980-nm continuous waveform laser was recorded from 250-800 nm spectral range using USB 4000 UV-VIS-NIR miniature fiber optic spectrometer (Ocean optics), having spectral resolution 1.34 nm (full width at half maximum, FWHM) and slit width 25 μm. A continuous waveform laser equipped with variable power output (0-200 mW) was used as a pumping source to stimulate electrons in RE^{3+} ions to consider the change in luminescence emission intensity for explaining the UC mechanism. All samples were measured at room temperature.

4.3 Results and discussion

4.3.1 Thermogravimetric and differential thermal analysis (TG-DTA) of raw material

To comprehend the formation of the final product, it is necessary to observe the thermal behavior of the raw mixture. As shown in Figure 4.2, the TG-DTA measurement was carried out in the temperature range from room temperature (25 °C) to 1300 °C for a representative sample (raw mixture of the most efficient product), and it was obvious that no thermal effect and no further weight loss were observed after 600 °C. So that, to explain this result in detail, the TG-DTA of each raw material was investigated by considering the thermal processes of each raw material in the temperature range from room temperature to 600 °C. The TG-DTA curves of ZnO powder, TiO_2 sol solution, and $Yb(NO_3)_3{\cdot}5H_2O$ will not be provided in this chapter because they can be referred to as mentioned earlier in Chapter III, section 3.3.1.

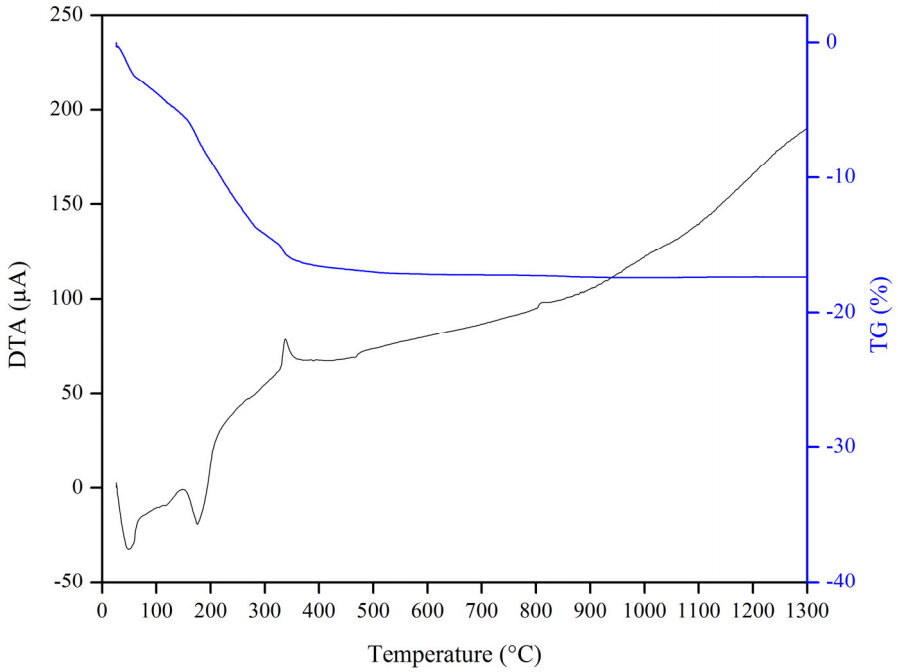

Figure 4.2. TG-DTA curves in the temperature range from room temperature (25 °C) to 1300 °C for ZnO:TiO_2 = 1:1 (in mole) doped with 0.03 mol% Ho^{3+} and 9 mol% Yb^{3+} dried at 90 °C.

4.3.1.1 $Ho(NO_3)_3{\cdot}5H_2O$

The TG-DTA curves of $Ho(NO_3)_3{\cdot}5H_2O$ are shown in Figure 4.3. There were nine endothermic processes, covering total weight loss about 60% which was in accordance with the temperature range from room temperature (25 °C) to 535 °C. The first process (No.1) was due to the melting of material because the physical change occurred during the increase of temperature [19-21]. Further, the process No.2 to No.6 were the dehydration and evaporation processes that agreed with the change in compositions from $Ho(NO_3)_3.5H_2O$ to $Ho(NO_3)_3$. Also, it could be well thought-out that the process No.2 to No.6 were the overlapping endothermic mass loss process. The dehydration and evaporation processes were confirmed by the calculation of the change in observed weight losses for each process which were close to theoretically calculated for releasing 5 moles of water (Table 4.1). Later, the process No.7 to No.9 were the decomposition process which decayed $Ho(NO_3)$ to $HoO_{0.5}(NO_3)$. Considering the process No.7 and No.8 that showed strong endothermic process, peaking at around 353 °C and 479 °C, respectively, these two peaks were related to NOx by-product formation during the decomposition process [19]. In the last process (No. 10), the final product was Ho_2O_3 that came from the decomposition

process of $HoO_{0.5}(NO_3)$. Eventually, there was only one remaining product, Ho_2O_3, and no thermal effect and no further weight loss were observed. Until now, there is no proof of the decomposition of holmium nitrate, but according to Balboul's reports [19-21], Yb_2O_3, Ho_2O_3, and Er_2O_3 were the final decomposition product of the reactants that contained rare earth element. Hence, all nitrate molecules could be totally decomposed at high temperature especially over 500 °C. The summarized data from TG-DTA result of $Ho(NO_3)_3.5H_2O$ is shown in Table 4.1 and it is worth noting that all compositions (except Ho_2O_3) presented in Table 4.1 are anticipated based on the calculation of the change in theoretical weight loss of each compound that mainly concerns the observed weight loss at specific temperature. Atomic weights used for calculating theoretical weight loss are Ho = 164.930, N = 14.007, H = 1.008, and O = 15.999.

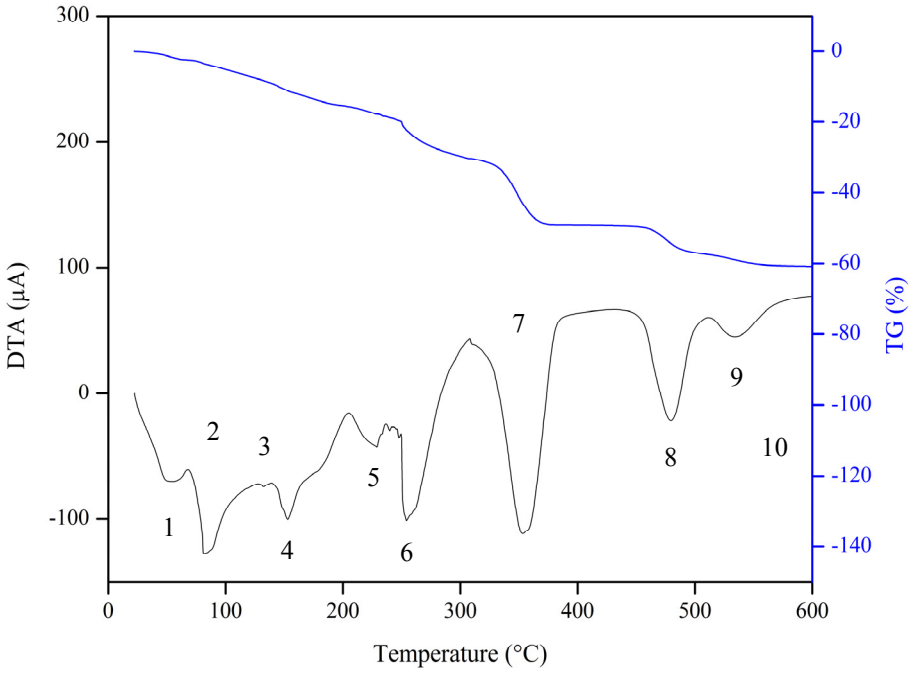

Figure 4.3. TG-DTA curves in the temperature range from room temperature (25 °C) to 600 °C for $Ho(NO_3)_3{\cdot}5H_2O$.

Table 4.1. Thermal processes of $Ho(NO_3)_3 \cdot 5H_2O$; experimental and theoretical weight losses, corresponding temperature point, and composition proposed in each process.

Process	Accumulated weight losses (%) [observed]	Accumulated weight losses (%) [theoretical]	Temperature (°C)	Composition
Start	-	-	-	$Ho(NO_3)_3 \cdot 5H_2O$
1	-	Melting	55	$Ho(NO_3)_3 \cdot 5H_2O$
2	3.7	4.09	84	$Ho(NO_3)_3 \cdot 4H_2O$
3	8.3	8.34	132	$Ho(NO_3)_3 \cdot 3H_2O$
4	11.2	12.79	153	$Ho(NO_3)_3 \cdot 2H_2O$
5	17.9	17.45	230	$Ho(NO_3)_3 \cdot H_2O$
6	22.2	22.33	254	$Ho(NO_3)_3$
7	43.1	44.56	353	$HoNO_2(NO_3)$
8	54.2	55.55	479	$HoO(NO_3)$
9	59.0	58.84	535	$HoO_{0.5}(NO_3)$
10	> 59.0	> 58.84	> 535	Ho_2O_3

4.3.2 Thermogravimetric and differential thermal analysis (TG-DTA) of $ZnO:TiO_2$ = 1:1 (in mole) doped with 0.03 mol% Ho^{3+} and 9 mol% Yb^{3+} dried at 90 °C

To verify the thermal stability of $ZnO\text{-}TiO_2$ doped with $Ho^{3+}$and Yb^{3+}, the TG-DTA was conducted using the raw mixture dried at 90 °C. As shown in Figure 4.4, there were four endothermic peaks at 37.8 °C, 80.8 °C, 112.1 °C, and 174.8 °C (No.1 to 4) in the DTA curve, and the corresponding weight loss was about 0.30%, 1.32%, 2.25%, and 4.95%, respectively, which it could be inferred that the surface-absorbed water of the dried mixture was evaporated. This phenomenon agreed with the TG-DTA results of raw materials mentioned previously. Further, in the temperature range from 175-320 °C, there was a process which might be classified as endothermic process and the weight loss in this temperature range was around 6%. According to the TG-DTA results of raw materials, the process that was responsible for this weight loss was the dehydration and decomposition processes that, in this analysis, it would take place at the same time. Later, there was one exothermic peak (No.5) which might come from the surfactant decomposition process that was mentioned previously in the case of TG-DTA of TiO_2 sol solution (Chapter III, section 3.3.1.2) because it showed the similar weight loss (around 2%) at the similar temperature (around 300 °C). Focusing on the TG-DTA results of $Yb(NO_3)_3 \cdot 5H_2O$ (Chapter III, section 3.3.1.3) and $Ho(NO_3)_3 \cdot 5H_2O$, there were at least two

peaks related to the NO_x by-product formation during the thermal process in the temperature range from 250-480 °C, but this analysis did not show the obvious peak of that process because of the low content of nitrate. Under between 480-600 °C, a very small change in the weight loss was observed, indicating that the decomposition of this mixture almost completed at this stage. From all TG-DTA results, it can be concluded that the significant point is the total weight losses of ZnO and TiO_2 contents in the temperature range from room temperature to 600 °C around 1.2% and 4%, respectively. These weight losses may have the influences on the formation of target host material and a little change in stoichiometric of ZnO/TiO_2 mixing ratio.

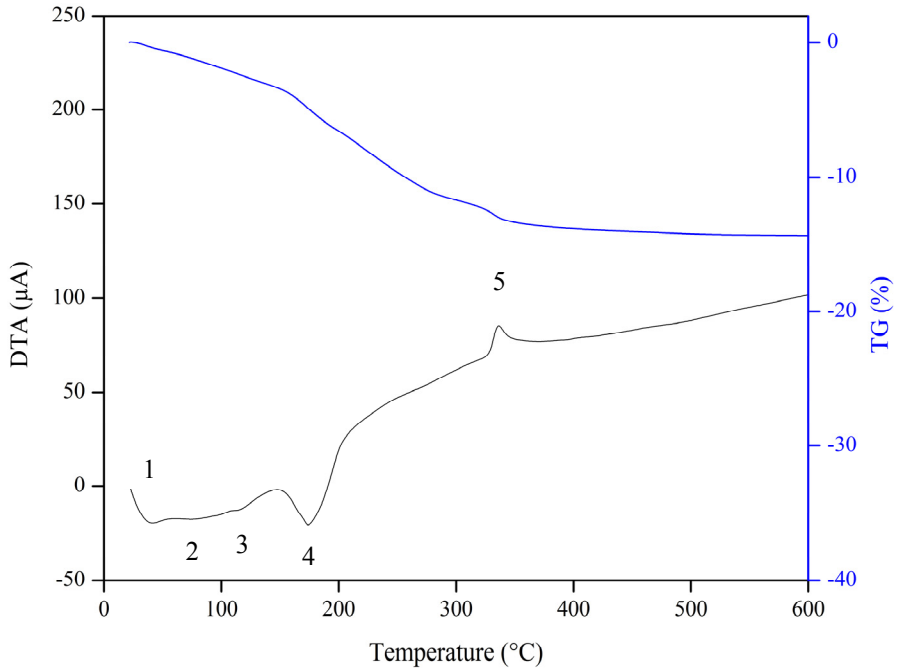

Figure 4.4. TG-DTA curves in the temperature range from room temperature (25 °C) to 600 °C for ZnO:TiO_2 = 1:1 (in mole) doped with 0.03 mol% Ho^{3+} and 9 mol% Yb^{3+} dried at 90 °C.

4.3.3 Effect of firing temperature on crystalline phase

The crystalline phase of the products, $ZnO:TiO_2$ = 1:1 (in mole) doped with 0.03 mol% Ho^{3+} and 9 mol% Yb^{3+} dried and fired at various temperatures (90-1400 °C), was identified using XRD analysis. To comprehend how to obtain the optimum firing temperature, the explanation is separated into two sets based on the temperature used and the physical appearance of the products; from 90 to 1300 °C (Figure 4.5) and 1300 to 1400 °C (Figure 4.7).

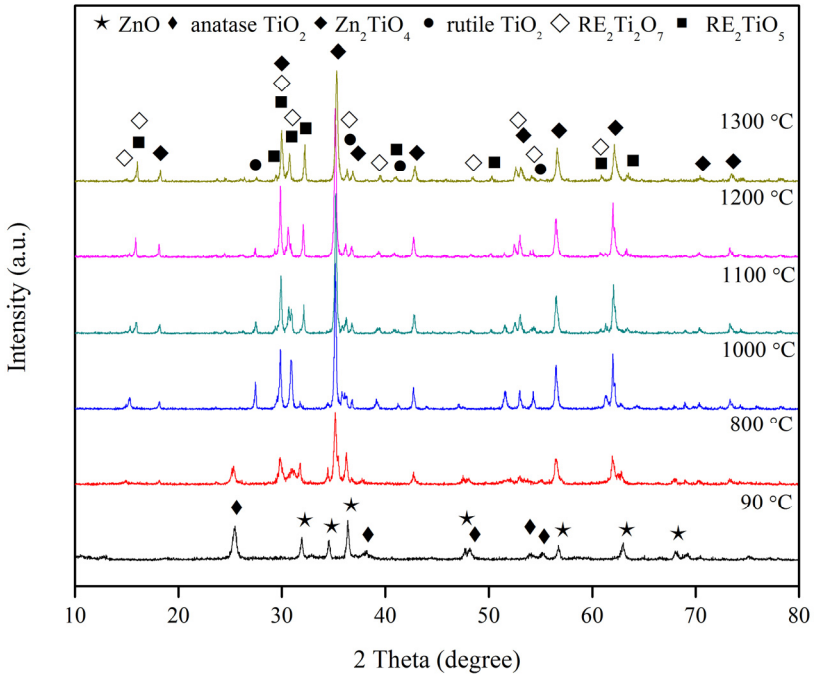

Figure 4.5. XRD patterns of $ZnO:TiO_2$ = 1:1 (in mole) doped with 0.03 mol% Ho^{3+} and 9 mol% Yb^{3+} dried and fired at various temperatures (90-1300 °C).

According to Figure 4.5, the raw mixture (prepared at 90 °C) composed of two phases, ZnO (JCPDS: 36-1451) and anatase TiO_2 (JCPDS: 21-1272). Further increasing temperature, at 800 °C, Zn_2TiO_4 phase (JCPDS: 25-1164) occurred as the dominant peak together with the decrease in ZnO and anatase TiO_2 phase contents. Subsequently, at 1000 °C, Zn_2TiO_4 phase kept in the main peak, but ZnO and anatase TiO_2 phases disappeared. In the meantime, the small peak of rutile TiO_2 (JCPDS: 21-1276) phase was in sight. At higher firing temperature (1100-1300 °C), the final product of all samples consisted of four phases; Zn_2TiO_4, rutile TiO_2, $RE_2Ti_2O_7$ ($Ho_2Ti_2O_7$, JCPDS: 23-0283 and/or $Yb_2Ti_2O_7$, JCPDS: 17-0454), and RE_2TiO_5 (Ho_2TiO_5 and/or Yb_2TiO_5) [22]. The SEM analysis of these six processed phosphor powders is shown in Figure 4.6. It was observed that all samples had different morphological structures, depending on each temperature used. In the figure, these observed microstructures are similar to the case of ZnO-TiO_2:Er^{3+}/Yb^{3+} phosphor presented in Chapter III. Therefore, the explanation about these morphologies can be referred to as mentioned earlier in Chapter III, section 3.3.4.

The XRD patterns of the samples fired at higher temperature (1350-1400 °C) are shown in Figure 4.7. At 1350 °C, the dominant Zn_2TiO_4 phase was still observed along with rutile TiO_2, $RE_2Ti_2O_7$, and RE_2TiO_5 phases. Moreover, two phases of aluminium compound, Al_2O_3 [22] and Al_2TiO_5 phases (JCPDS: 26-0040), were detected. Further increasing firing temperature (1400 °C), Al_2O_3 became the main phase and at the same time, Zn_2TiO_4, rutile TiO_2, $RE_2Ti_2O_7$, RE_2TiO_5, and Al_2TiO_5 phase contents decreased. Corresponding photograph of the sample fired at 1300 °C, 1350 °C, and 1400 °C is presented in Figure 4.8.

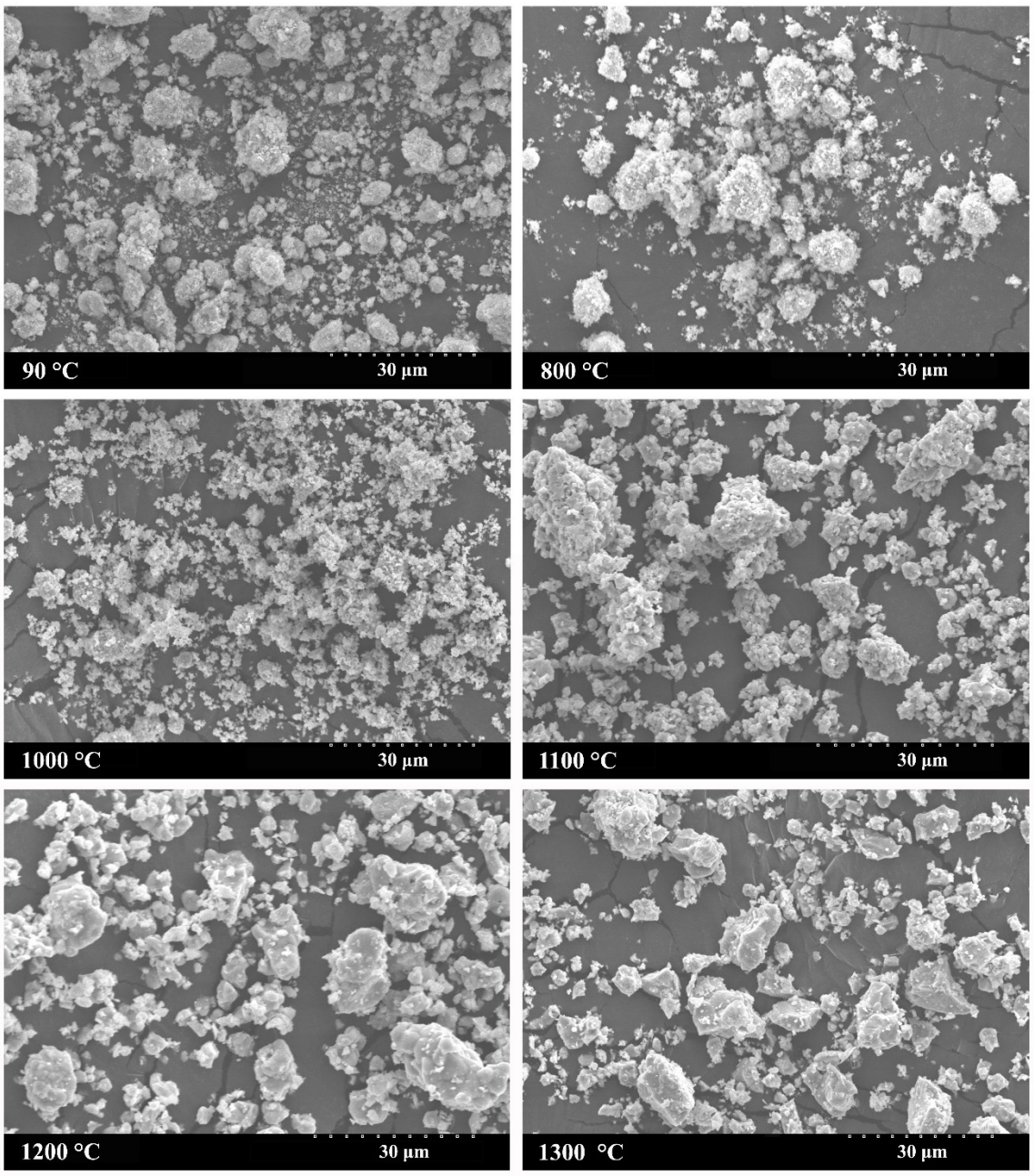

Figure 4.6. SEM images of $ZnO:TiO_2$ = 1:1 (in mole) doped with 0.03 mol% Ho^{3+} and 9 mol% Yb^{3+} dried and fired at various temperatures (90-1300 °C).

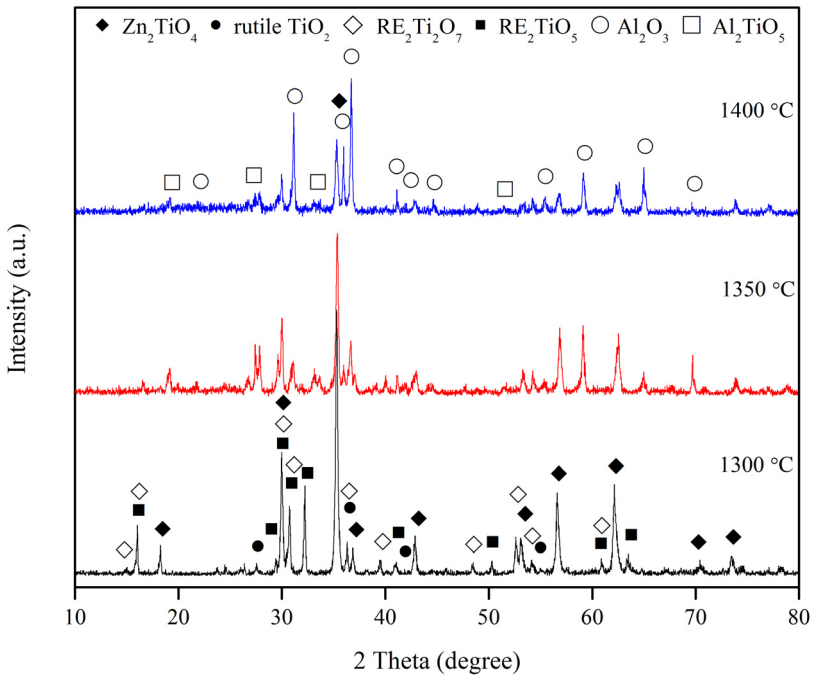

Figure 4.7. XRD patterns of ZnO:TiO_2 = 1:1 (in mole) doped with 0.03 mol% Ho^{3+} and 9 mol% Yb^{3+} fired at various temperatures (1300-1400 °C).

Figure 4.8. Photograph of ZnO:TiO_2 = 1:1 (in mole) doped with 0.03 mol% Ho^{3+} and 9 mol% Yb^{3+} fired at (a) 1300 °C, (b) 1350 °C, and (c) 1400 °C.

This photo shows the difference of physical characteristics of the samples. Taking into account the color of samples, it was clear that the color was different; white, dark purple, and purple for the sample fired at 1300 °C, 1350 °C, and 1400 °C, respectively. Considering the external structure of each sample, the sample fired at 1300 °C kept the powder state and was easily removed from the combustion boat. However, at 1350 °C and 1400 °C, both samples became very stiff and could not be removed from the combustion boat. These samples turn into the solid body because they are in the form of liquid phase at high temperature, afterward the rigid body is generated during the cooling down. The explanation about these behaviors can be referred to as mentioned previously in Chapter III, section 3.3.4.

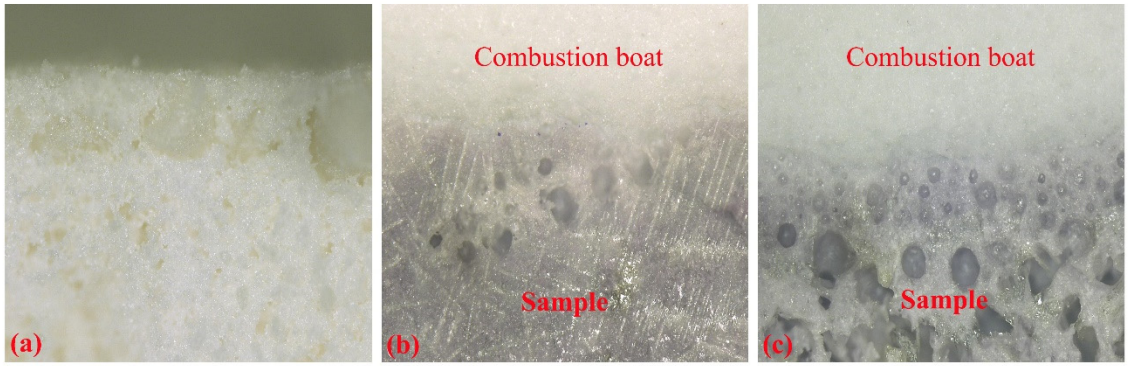

Figure 4.9. Digital microscopes (200x magnification) of $ZnO:TiO_2$ = 1:1 (in mole) doped with 0.03 mol% Ho^{3+} and 9 mol% Yb^{3+} fired at (a) 1300 °C, (b) 1350 °C, and (c) 1400 °C.

Figure 4.9 shows the digital microscope (200x magnification) of the products fired at 1300 °C, 1350 °C, and 1400 °C. Photograph (a) showed that the sample did not combine with the combustion boat, but photograph (b) and (c), the sample merged with the combustion boat. Besides, there were holes that would be generated during the melting of sample at 1350 °C and 1400 °C. With these physical characteristics of the samples fired at 1350 °C and 1400 °C, it was clear that the combustion boat of sample fired at 1400 °C melted more than that of the sample fired at 1350 °C. Besides, these phenomena can be used to confirm the explanation described previously in Chapter III, section 3.3.4 about the formation of Al_2O_3 and Al_2TiO_5 phases.

According to the results and explanations about the digital microscopes (200x magnification) of the sample, $ZnO:TiO_2$ = 1:1 (in mole) doped with 3 mol% Er^{3+} and 9 mol% Yb^{3+} fired at 1300 °C, 1350 °C, and 1400 °C (Chapter III, section 3.3.4), and the digital microscopes (Figure 4.9) in this chapter, it would indicate that the glassy phase occurs at firing temperature 1350 °C and 1400 °C for all ZnO-TiO_2 composite doped with rare earth elements system under the use of Mullite-based combustion boat as a container because of the variation in operating temperature caused by the interaction between the sample and combustion boat at very high temperature. With the existence of glassy phase, it can be concluded that this is one of the possibilities which causes the decrease in Zn_2TiO_4 phase content and directly influences to the change in UCL properties of the product.

4.3.4 Effect of ZnO/TiO_2 mixing ratio on crystalline phase

The effect of various ZnO/TiO_2 mixing ratios, as mentioned as Z*x*T1, on crystalline phase are shown in Figure 4.10. It was observed that all products showed dominant Zn_2TiO_4 phase (JCPDS: 25-1164). This behavior can be explained by considering the phase diagram of ZnO-TiO_2 system [23]. There are two noteworthy phases, $ZnTiO_3$ and Zn_2TiO_4, but $ZnTiO_3$ phase is unstable at high temperature (> 945 °C). On the other hand, Zn_2TiO_4 phase is easily produced, even if the system is in the low ZnO amount state, and it is stable at high temperature range (945-1418 °C). Taking into account the lowest amount of ZnO (x = 0.5), the product consisted of four phases; Zn_2TiO_4, rutile TiO_2, $RE_2Ti_2O_7$, and RE_2TiO_5. Subsequently, to easily understand the tendency of phase changes with varying x-values, the relative phase content of the products was calculated using equation 4.1 and the results are shown in Figure 4.11.

With increase of x-value up to 1.25, Zn_2TiO_4 content increased and at the same time, TiO_2 content decreased and then disappeared at x = 1.25. For $RE_2Ti_2O_7$ and RE_2TiO_5 contents, these two phases were almost constant under $0.5 \leq x \leq 1$. After that, $RE_2Ti_2O_7$ content initially increased, but RE_2TiO_5 content decreased. At $x > 1.25$, Zn_2TiO_4 and $RE_2Ti_2O_7$ contents gradually increased, but RE_2TiO_5 content continuously decreased and almost disappeared at x = 1.5. These phase changes can be interpreted with the consideration of the reaction between base compositions of each compound and the formation energy of the existed phases.

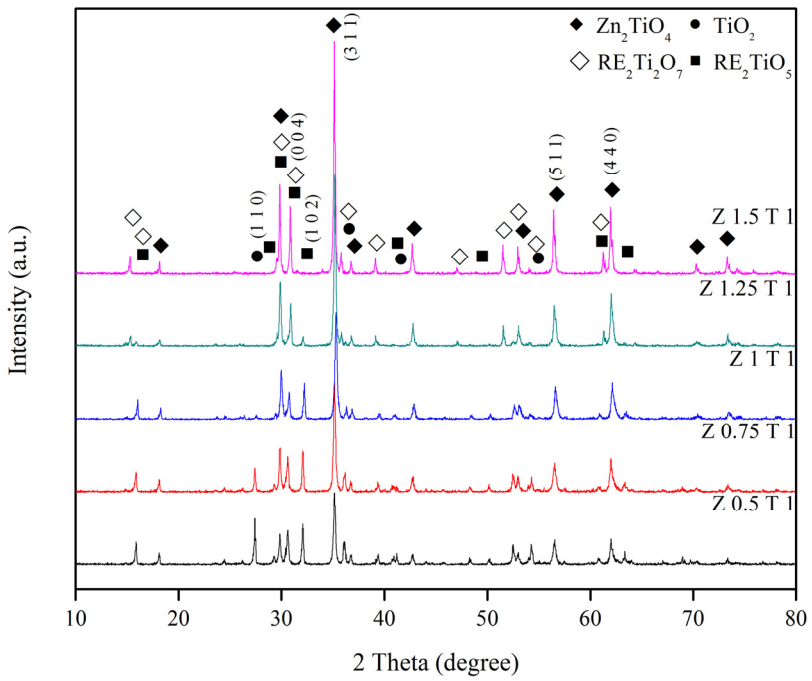

Figure 4.10. XRD patterns of various ZnO/TiO_2 mixing ratios doped with 0.03 mol% Ho^{3+} and 9 mol% Yb^{3+} fired at 1300 °C. Adapted with permission from Kobwittaya *et al*., *Mater. Sci. Forum*, **922** (2018) 32-39. Copyright (2018) Trans Tech Publications.

Typically, Zn_2TiO_4 phase is formed by the reaction between 2 ZnO and 1 TiO_2 (in mole). Hence, as increasing ZnO amount while keeping TiO_2 amount at 1 mole, Zn_2TiO_4 content increases absolutely. Afterward, the remaining TiO_2 reacts with RE_2O_3 and then $RE_2Ti_2O_7$ and RE_2TiO_5 phases are formed. These formation reactions are the competitive ones that depend on the amount of remaining TiO_2 and RE_2O_3, including the formation energy of each compound; Zn_2TiO_4 (-2.88 eV), $RE_2Ti_2O_7$ (-3.8 eV), and RE_2TiO_5 (-3.79 eV) [24]. In the case of TiO_2 content, its diminution is not only from the reaction with ZnO and/or RE_2O_3, but also from the solid solubility of TiO_2 into Zn_2TiO_4 crystal [25]. The SEM images of these processed powders is shown in Figure 4.12. It was observed that all samples had the same physical characteristics; micron-scale particles in irregular shapes and different sizes which they were caused by milling process. Besides, this kind of morphology was apparently due to the agglomeration of particles that was in accordance with the high firing temperature used in the final stage of preparation. Nevertheless, it is worth noting that, for the powder-solution mixing method, ZnO particle size may has little effect on the final products formed, for example non-uniformity of the product morphology due to the irregular particle sizes and shapes of ZnO powder. Besides, by using

ZnO powder which approaches to nanoscale and fine TiO_2 in the form of solution, more homogeneous crystalline powder of the product can be obtained.

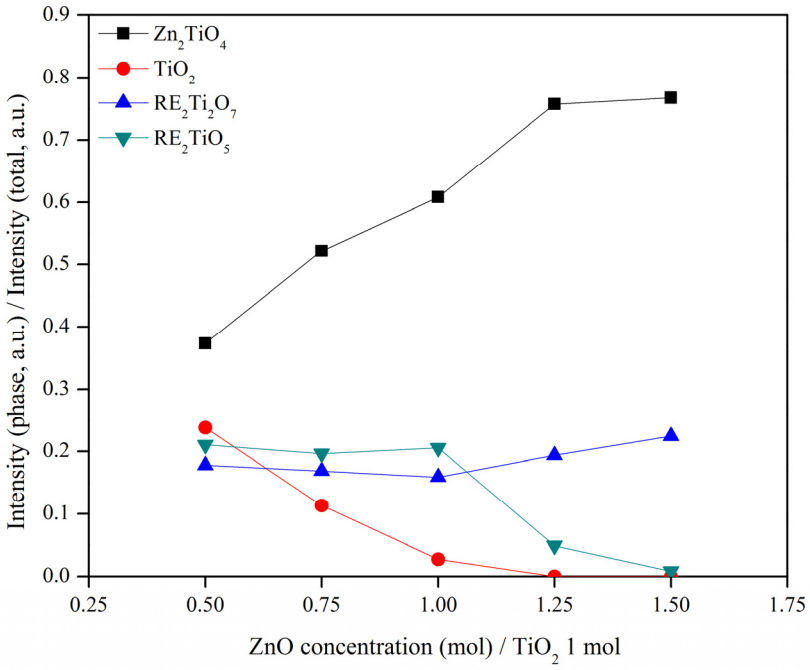

Figure 4.11. Calculated relative phase contents of Zn_2TiO_4, TiO_2, $RE_2Ti_2O_7$, and RE_2TiO_5 phases according to the compositions in Figure 4.10. Reproduced with permission from Kobwittaya *et al.*, *Mater. Sci. Forum*, **922** (2018) 32-39. Copyright (2018) Trans Tech Publications.

.

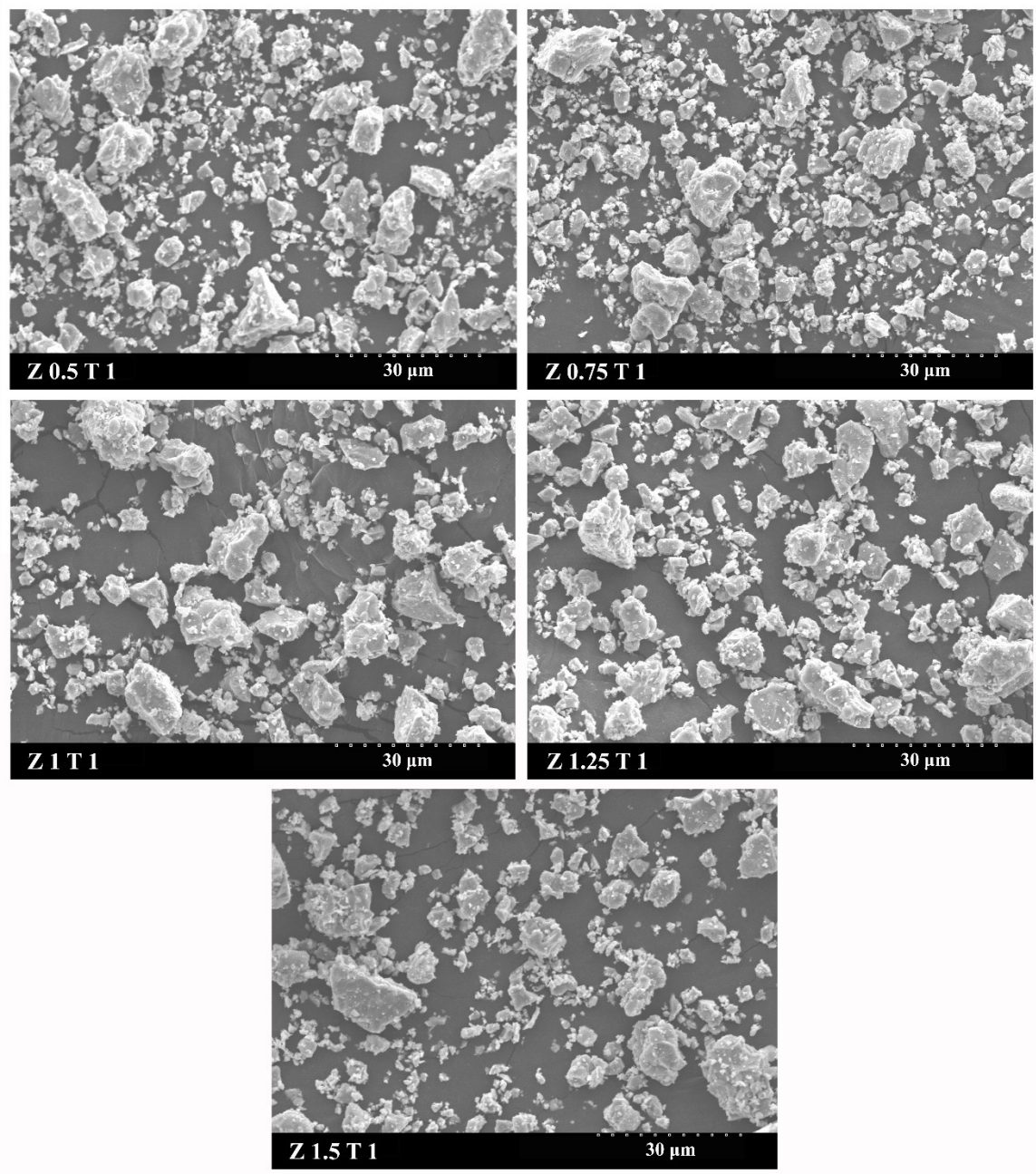

Figure 4.12. SEM images of various ZnO/TiO_2 mixing ratios doped with 0.03 mol% Ho^{3+} and 9 mol% Yb^{3+} fired at 1300 °C.

4.3.5 Effect of firing temperature on upconversion luminescence (UCL)

The luminescence emission photographs of ZnO:TiO_2 = 1:1 (in mole) doped with 0.03 mol% Ho^{3+} and 9 mol% Yb^{3+} samples fired at different temperatures are shown in Figure 4.13. The photograph showed that the initial emission color at 800 °C and 1000 °C was not clear and they

can be summarized as very weak emission. With increasing temperature up to 1300 °C, the emission color appeared as greenish, changing from normal to strong brightness. Additionally, the central area of the samples fired at 1200 °C to 1300 °C seemed to be white which was caused by the strong emission. Further increase of temperature (1350 °C and 1400 °C), the samples showed very weak or no emission.

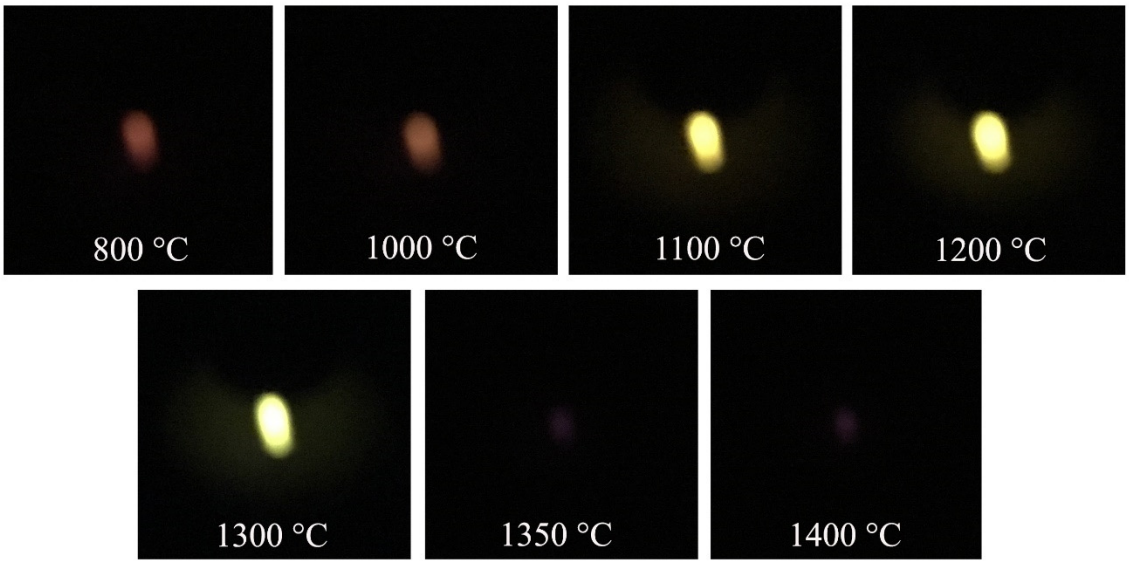

Figure 4.13. UC emission color of $ZnO:TiO_2$ = 1:1 (in mole) doped with 0.03 mol% Ho^{3+} and 9 mol% Yb^{3+} fired at various temperatures, and irradiated with a 980-nm 125 mW laser.

According to the UCL spectra in Figure 4.14, the samples heated below 1100 °C and above 1300 °C exhibited weak emission intensity or no emission spectra, but the samples fired at 1100-1300 °C exhibited strong emission intensity. These emission spectra consisted of two emission bands. The green spectral situated in the range of 532-567 nm which was attributed to $^5F_4$, $^5S_2 \rightarrow {}^5I_8$ transition of Ho^{3+} with the maximum at 538 nm. The red spectral located in the range of 634-677 nm which was ascribed to $^5F_5 \rightarrow {}^5I_8$ transition of Ho^{3+} with the maximum at 669 nm. As shown in Figure 4.13, only green color was clearly observed because the green emission has higher intensity than the red one.

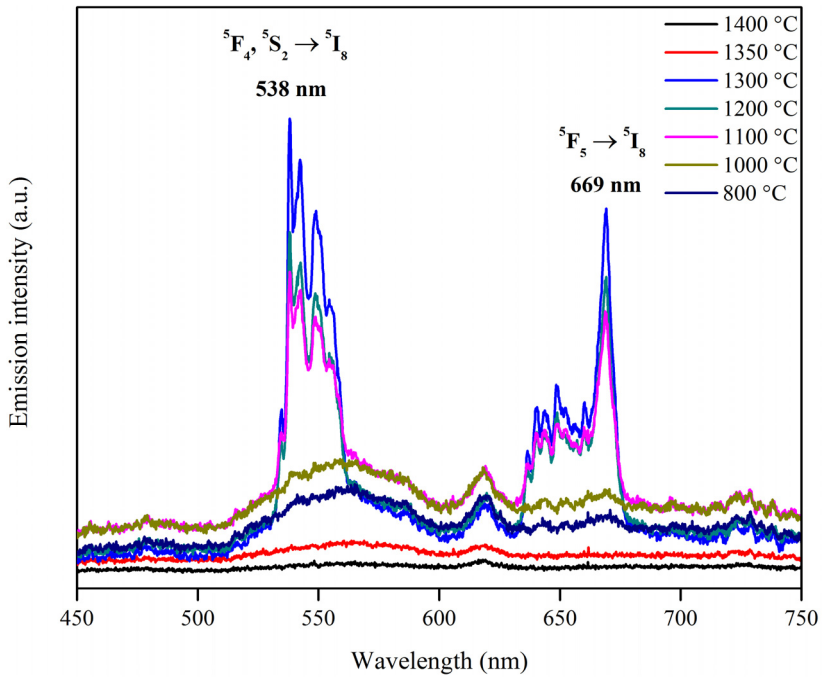

Figure 4.14. UC emission spectra of ZnO:TiO_2 = 1:1 (in mole) doped with 0.03 mol% Ho^{3+} and 9 mol% Yb^{3+} fired at various temperatures, and irradiated with a 980-nm 125 mW laser.

As discussed by Luitel *et al*. in ZnO-TiO_2 composite doped with Er^{3+} and Yb^{3+} prepared by solid-state reaction method [11], Zn^{2+} sites in Zn_2TiO_4 crystal are occupied by RE^{3+} ions. Hence, the increase in the amount of RE^{3+} ions at Zn site affects the change in green (538 nm) and red (669 nm) emission intensities as a function of various firing temperatures (Figure 4.15). This phenomenon can be explained by considering the results in Figure 4.15 together with relative phase contents in Figure 4.11. The explanations about this contemplation can be referred to as mentioned earlier in Chapter III, section 3.3.6. In comparison to the optimum firing temperature for fabricating the most efficient ZnO-TiO_2: Er^{3+}/Yb^{3+} phosphor with the means of powder-solution mixing, the ZnO-TiO_2: Ho^{3+}/Yb^{3+} phosphor system exhibits the brightest green emission under the same optimum firing temperature at 1300 °C and both systems demonstrate identical state of matter (solid and partially liquid) under the same condition of temperature.

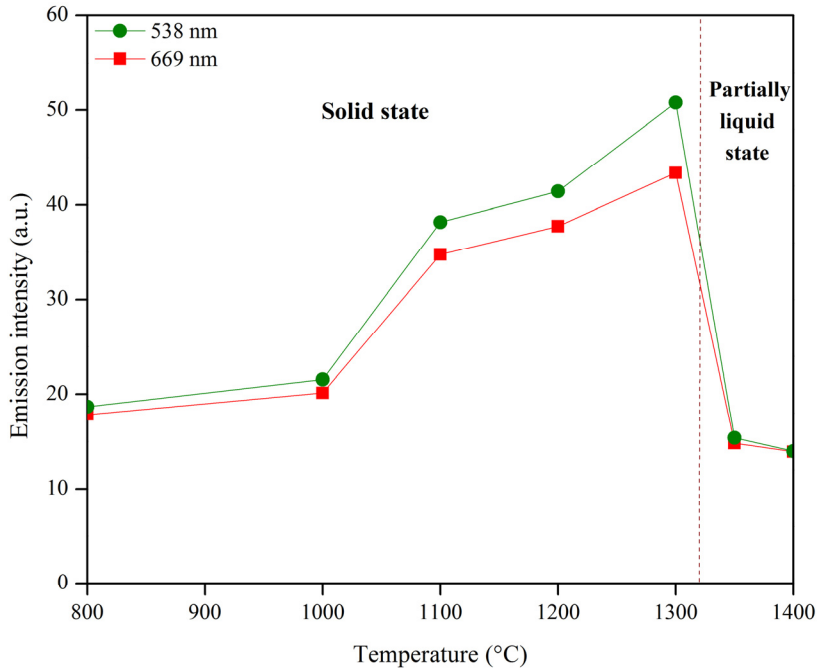

Figure 4.15. The green (538 nm) and red (669 nm) emission intensities versus various firing temperatures according to the details in Figure 4.14.

4.3.6 Effect of ZnO/TiO_2 mixing ratio on upconversion luminescence (UCL)

The UC emission color of the products is shown in Figure 4.16. The photograph showed that the UC emission color was green when ZnO amount $x = 0.5$. Further increasing ZnO amount $x > 0.5$, the brightness of green emission increased and then decreased, reaching the brightest emission at ZnO amount $x = 1$. Subsequently, the green emission changed to the red emission at ZnO amount $x = 1.5$. Corresponding UC emission spectra are shown in Figure 4.17.

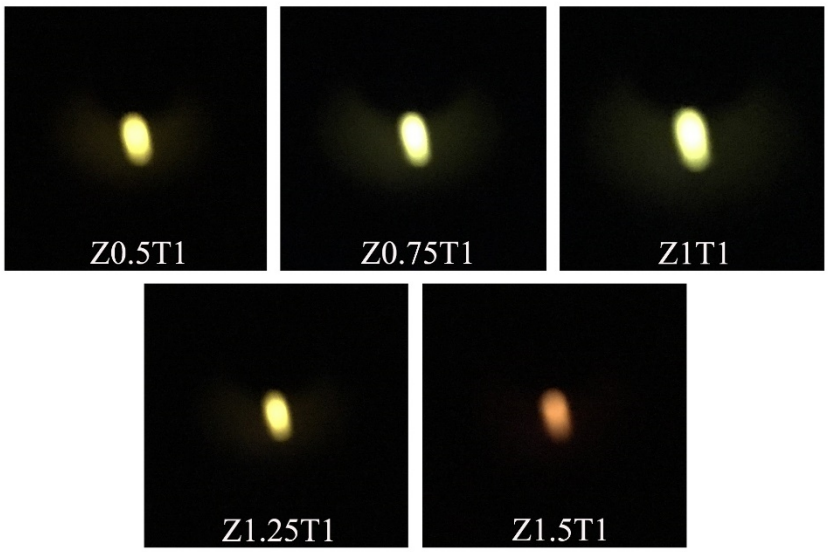

Figure 4.16. UC emission color of various ZnO/TiO_2 mixing ratios doped with 0.03 mol% Ho^{3+} and 9 mol% Yb^{3+} fired at 1300 °C, and irradiated with a 980-nm 125 mW laser. Adapted with permission from Kobwittaya *et al*., *Mater. Sci. Forum*, **922** (2018) 32-39. Copyright (2018) Trans Tech Publications.

The emission color brightness and emission intensity increased with the augmentation of ZnO amount up to $x = 1$. Further increase of ZnO amount ($x = 1.25$ and 1.5), the brightness and emission intensity decreased. Hence, it is clear that the emission intensity changed for both green and red emission bands with changing ZnO contents and the brightest emission was observed for the sample Z1T1. The effect of x-value on the maximum emission intensity of green (538 nm) and red (669 nm) bands of various ZnO/TiO_2 mixing ratios doped with 0.03 mol% Ho^{3+} and 9 mol% Yb^{3+} is shown in Figure 4.18. This result can be explained by dividing the trend line into two sections based on ZnO amount. In the lower x-value ($x < 1$), the increment of ZnO amount up to $x = 1$, the emission intensity for both bands increased. In the case of higher x-value ($x > 1$), further increasing amount of ZnO, the emission intensity for both bands decreased. Taking into account the line patterns of emission intensity between green and red emission bands, they showed similar direction for all the samples studied. These patterns can be explained by considering the solubility of RE^{3+} ions into Zn_2TiO_4 crystal and it is indicated that the amount of soluble Ho^{3+} and Yb^{3+} (in the term of Ho^{3+}/Yb^{3+} ratio) in Zn_2TiO_4 crystal may be equivalent. When the $ZnO:TiO_2 = 1:1$ (in mole), the strongest emission intensity was observed on both green and red emission bands. This behavior can be described by considering

the relative phase contents of the products as presented in Figure 4.11. When the emission intensity increased ($x = 0.5$ to 1), the system consisted of four phases; Zn_2TiO_4, TiO_2, $RE_2Ti_2O_7$, and RE_2TiO_5. Further, when emission intensity decreased ($x > 1$), Zn_2TiO_4, $RE_2Ti_2O_7$, and RE_2TiO_5 phases were observed without TiO_2 phase. So, the difference between these two sections is the existence of TiO_2 phase which may directly affect the UC emission intensity. Hence, the brightest UC emission is obtained by the Ho^{3+} transitions in the mixed phases system that comprises of Zn_2TiO_4, TiO_2, $RE_2Ti_2O_7$, and RE_2TiO_5 phases.

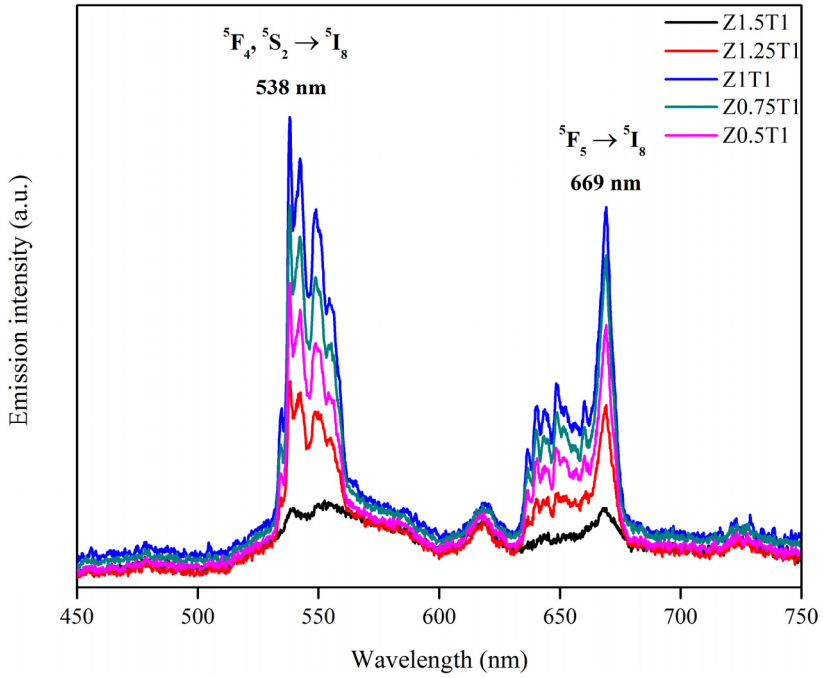

Figure 4.17. UC emission spectra of various ZnO/TiO_2 mixing ratios doped with 0.03 mol% Ho^{3+} and 9 mol% Yb^{3+} fired at 1300 °C, and irradiated with a 980-nm 125 mW laser. Reproduced with permission from Kobwittaya *et al.*, *Mater. Sci. Forum*, **922** (2018) 32-39. Copyright (2018) Trans Tech Publications.

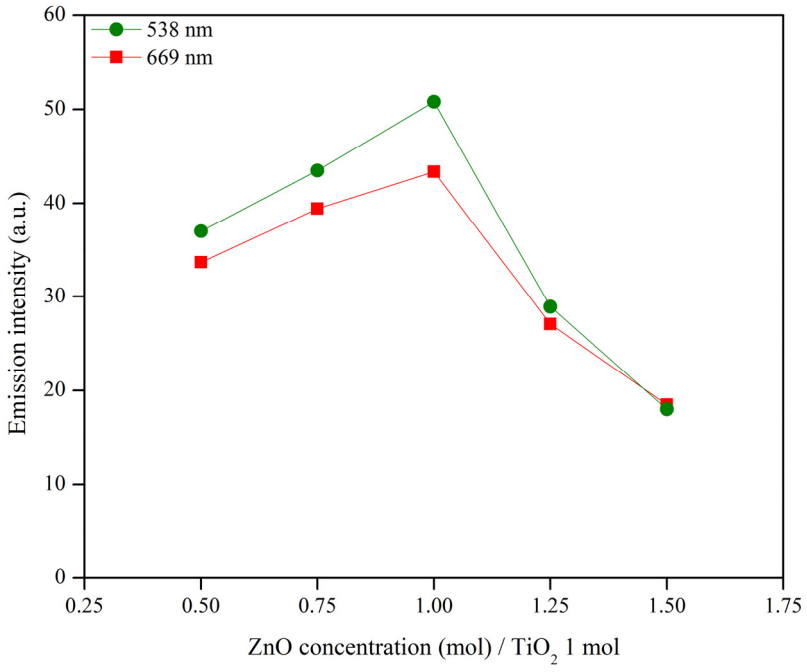

Figure 4.18. The green (538 nm) and red (669 nm) emission intensities versus various ZnO/TiO_2 mixing ratios according to the detail in Figure 4.17. Reproduced with permission from Kobwittaya *et al*., *Mater. Sci. Forum*, **922** (2018) 32-39. Copyright (2018) Trans Tech Publications.

4.3.7 Site preference of Ho^{3+} and Yb^{3+} in Zn_2TiO_4 crystal structure

According to the discussion about this topic in Chapter III, section 3.3.8, in this section, the explanation will be started by the calculation of lattice constant and lattice volume. The crystallographic data of Zn_2TiO_4; lattice constant and lattice volume, according to various ZnO/TiO_2 mixing ratios doped with 0.03 mol% Ho^{3+} and 9 mol% Yb^{3+} are shown in Table 4.2.

Taking into account Zn_2TiO_4 unit cell volume in Table 4.2 and the dependent lattice volumes on various ZnO/TiO_2 mixing ratios in Figure 4.19, The results showed the identical behavior as described in the case of $ZnO\text{-}TiO_2$: Er^{3+}/Yb^{3+} (Chapter III, section 3.3.8). Also, the effect of lattice volume on emission intensity (Figure 4.20) confirmed that the introduction of RE^{3+} ions into the Zn_2TiO_4 crystal is not equal in each sample, resulting in the change in Zn_2TiO_4 lattice volume and influencing to the variation of emission intensity. With these outcomes which are same as the obtained results of $ZnO\text{-}TiO_2$: Er^{3+}/Yb^{3+} (Chapter III, section 3.3.8), therefore, the site preference of Ho^{3+} and Yb^{3+} in Zn_2TiO_4 crystal matrix can be written as follows:

$$Ho_2O_3 + 4TiO_2 \rightarrow 2Ho^{\cdot}_{Zn(oct)} + \frac{3}{2}O_{2(g)} + 6e' + 2Ti^{\cdot\cdot}_{Zn(oct)} + 2Ti_{Ti(oct)} + 8O^{x}_{o} \quad (4.2)$$

$$Yb_2O_3 + 4TiO_2 \rightarrow 2Yb^{\cdot}_{Zn(oct)} + \frac{3}{2}O_{2(g)} + 6e' + 2Ti^{\cdot\cdot}_{Zn(oct)} + 2Ti_{Ti(oct)} + 8O^{x}_{o} \quad (4.3)$$

Table 4.2. The crystallographic data of Zn_2TiO_4; lattice constant and lattice volume of various ZnO/TiO_2 mixing ratios doped with 0.03 mol% Ho^{3+} and 9 mol% Yb^{3+} fired at 1300 °C.

Sample	Lattice constant (Å)	Lattice volume (Å^3)
Zn_2TiO_4 (JCPDS 25-1164)	8.4602	605.54
Z 0.5 T 1	8.4443	602.14
Z 0.75 T 1	8.4399	601.20
Z 1 T 1	8.4300	599.07
Z 1.25 T 1	8.4525	603.89
Z 1.5 T 1	8.4582	605.12

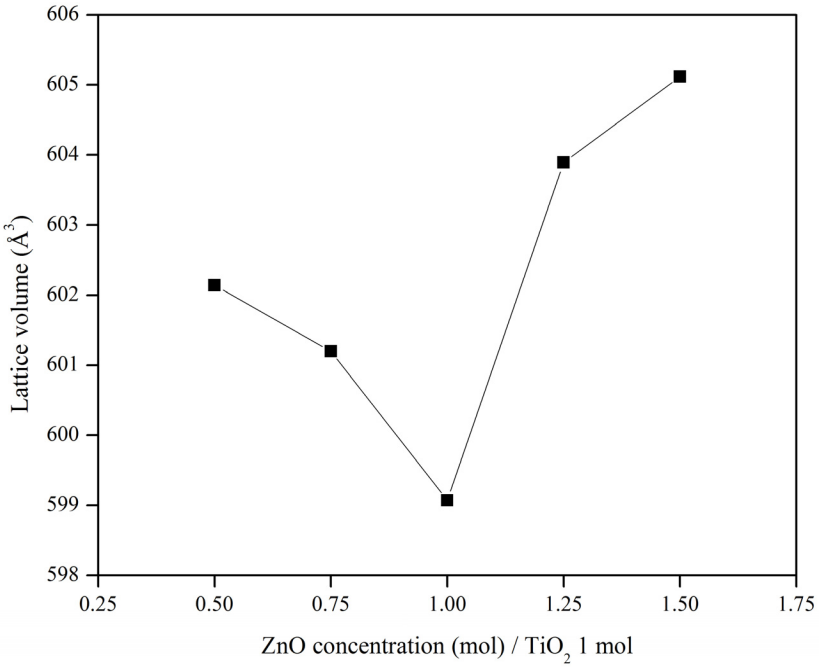

Figure 4.19. The dependent lattice volumes of Zn_2TiO_4 crystal on various ZnO/TiO_2 mixing ratios doped with 0.03 mol% Ho^{3+} and 9 mol% Yb^{3+} fired at 1300 °C.

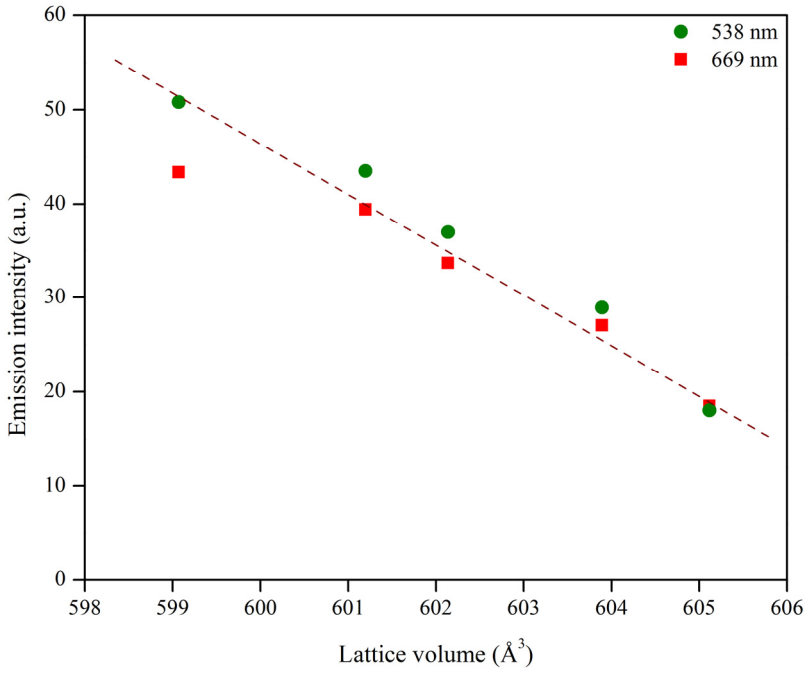

Figure 4.20. The green (538 nm) and red (669 nm) emission intensities of various ZnO/TiO_2 mixing ratios doped with 0.03 mol% Ho^{3+} and 9 mol% Yb^{3+} fired at 1300 °C versus various lattice volumes of Zn_2TiO_4 crystal according to the details in Figure 4.18 and Table 4.2.

4.3.8 Effect of Ho^{3+} and Yb^{3+} concentrations on upconversion luminescence (UCL)

The luminescence emission spectra were examined as a function of Ho^{3+} and Yb^{3+} concentrations. The effect of various Ho^{3+} concentrations, while keeping 9 mol% Yb^{3+} concentration is shown in Figure 4.21, which green (538 nm) and red (669 nm) emission intensities are plotted versus various Ho^{3+} concentrations. These UCL behaviors can be separated into two parts. In the initial part, as increasing Ho^{3+} concentration from 0-0.03 mol%, the emission intensity augmented because the Ho^{3+} activator concentration in the Zn_2TiO_4 crystal increased. Further increase of Ho^{3+} concentration up to 0.05 mol%, the emission intensity decreased because of concentration quenching. Taking into account the UC emission color, the UCL was green and changed from normal to strong brightness with increasing Ho^{3+} concentration from 0.01-0.03 mol%. Further increase of Ho^{3+} concentration more than 0.03 mol%, the brightness of green emission decreased. In addition, when the system did not have Ho^{3+}, no emission color was observed. Hence, the maximum emission intensity is detected on green emission band for Ho^{3+} concentration at 0.03 mol%.

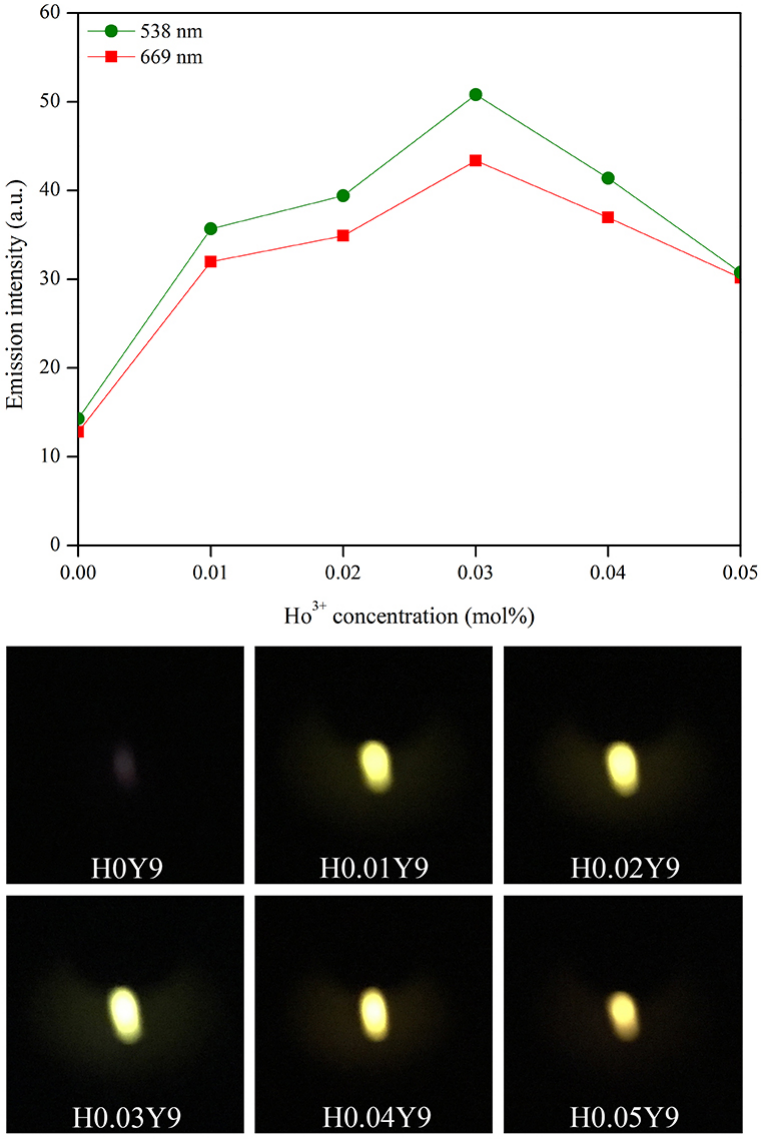

Figure 4.21. The green (538 nm) and red (669 nm) emission intensities versus ZnO:TiO_2 = 1:1 (in mole) doped with various mol% Ho^{3+} and 9 mol% Yb^{3+} fired at 1300 °C, and corresponding photographs of UC emission color irradiated with a 980-nm 125 mW laser. Upper portion is reproduced with permission from Kobwittaya *et al*., *Mater. Sci. Forum*, **922** (2018) 32-39. Copyright (2018) Trans Tech Publications.

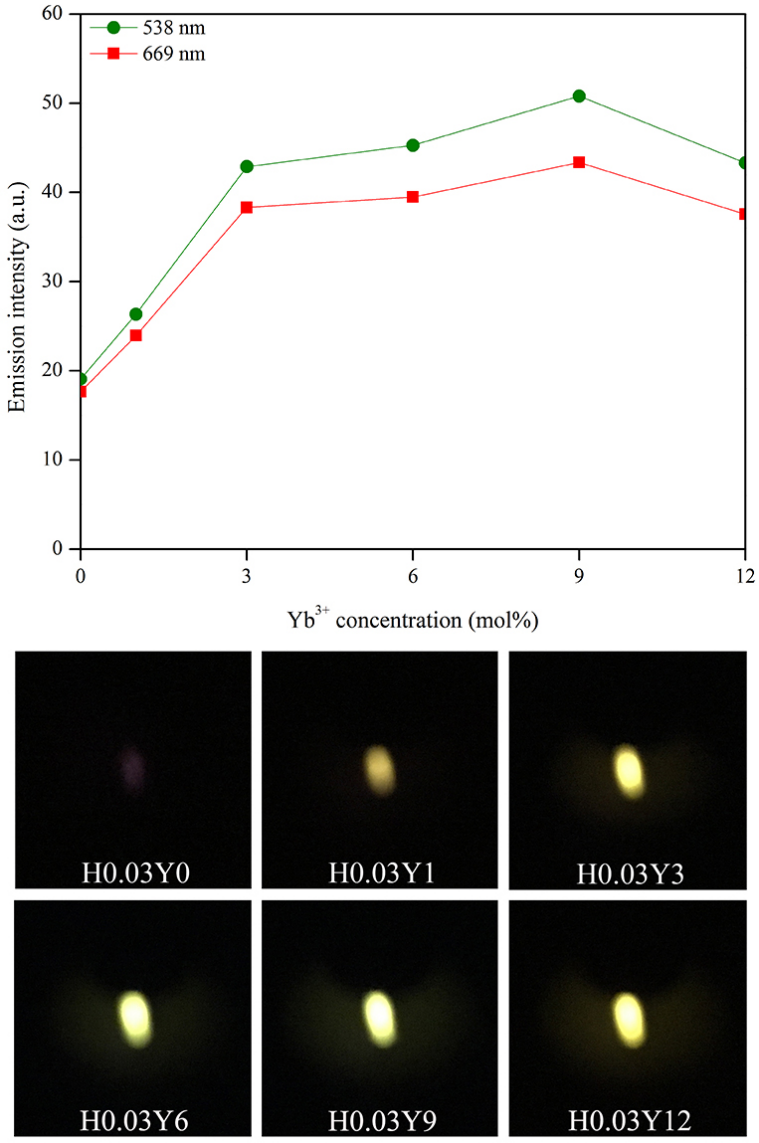

Figure 4.22. The green (538 nm) and red (669 nm) emission intensities versus ZnO:TiO_2 = 1:1 (in mole) doped with 0.03 mol% Ho^{3+} and various mol% Yb^{3+} fired at 1300 °C, and corresponding photographs of UC emission color irradiated with a 980-nm 125 mW laser. Upper portion is reproduced with permission from Kobwittaya *et al.*, *Mater. Sci. Forum*, **922** (2018) 32-39. Copyright (2018) Trans Tech Publications.

The effect of various Yb^{3+} concentrations, while keeping 0.03 mol% Ho^{3+} concentration is shown in Figure 4.22, which the green (538 nm) and red (669 nm) emission intensities are plotted versus various Yb^{3+} concentrations. By keeping Ho^{3+} concentration at 0.03 mol%, the Yb^{3+} concentration influences on the emission intensity of the products. With increasing Yb^{3+}

concentration from 0-12 mol%, the emission intensity increased, reaching maximum at 9 mol% Yb^{3+} doping concentration and then decreased on further increasing it. The increased emission intensity is viable due to higher concentration of dissolved Yb^{3+} concentration into the Zn_2TiO_4 crystal which augmented the number of pump photons and the excited Ho^{3+}. The decreased emission intensity at higher Yb^{3+} concentration corresponded to concentration quenching. Considering the UC emission color, the color changed from weak to strong green with increasing Yb^{3+} concentration. Firstly, when the system did not have Yb^{3+}, no emission color was observed. Further increase of Yb^{3+} concentration from 1-9 mol%, the emission color started with weak green at 1 mol% and gradually changed to stronger green at 3 mol% Yb^{3+}. Then, the brightness of green emission increased and reached maximum brightest at 9 mol%. Subsequently, increasing Yb^{3+} concentration up to 12 mol%, brightness of green emission decreased. With these two results, varying Ho^{3+} and Yb^{3+} concentrations, it is obvious that the optimum Ho^{3+} and Yb^{3+} concentrations for the brightest UC emission are 0.03 and 9 mol%, respectively.

4.3.9 Elemental composition analysis

4.3.9.1 X-ray fluorescence (XRF) of $ZnO:TiO_2$ = 1:1 (in mole) doped with 0.03 mol% Ho^{3+} and 9 mol% Yb^{3+} dried and fired at various temperatures

In this XRF analysis, the Zn and Ti contents of all samples were analyzed by comparing with Zn and Ti standard calibration curves that were mentioned in Chapter III, section 3.3.10.1. For the Ho and Yb contents, their standard calibration curves cannot be created due to the uncertainty of standard samples caused by very low content of both elements. Herein, to analyze Ho and Yb contents, the fundamental parameter (FP) method was used to investigate the content of them. An overview of XRF analysis of the synthesized powder samples, $ZnO:TiO_2$ = 1:1 (in mole) doped with 0.03 mol% Ho^{3+} and 9 mol% Yb^{3+} dried and fired at various temperatures, is given in Table 4.3.

Table 4.3. An overview of XRF analysis of $ZnO:TiO_2$ = 1:1 (in mole) doped with 0.03 mol% Ho^{3+} and 9 mol% Yb^{3+} powder samples dried and fired at various temperatures, their expected mixing ratio values and XRF elemental analysis results (each sample was measured five times at different positions and data were averaged).

Temperature	Zn (mole)		Ti (mole)		Ho (mole)		Yb (mole)	
(°C)	Expected	XRF	Expected	XRF	Expected	XRF	Expected	XRF
90	1.0000	0.9877	1.0000	1.0000	0.0003	0.0000	0.0900	0.0799
800	1.0000	0.9794	1.0000	1.0000	0.0003	0.0000	0.0900	0.0756
1000	1.0000	0.9819	1.0000	1.0000	0.0003	0.0000	0.0900	0.0772
1100	1.0000	0.9801	1.0000	1.0000	0.0003	0.0000	0.0900	0.0763
1200	1.0000	0.9799	1.0000	1.0000	0.0003	0.0000	0.0900	0.0775
1300	1.0000	0.9752	1.0000	1.0000	0.0003	0.0000	0.0900	0.0768

Remark:

1. Atomic weights used to calculate these results are Zn = 65.382, Ti = 47.867, Ho = 164.930, and Yb = 173.045.
2. These results are converted from weight% to mole and followed by keeping 1 mole of Ti.

As shown in Table 4.3, the results showed that all observed values were lower than the expected content. These could be due to many situations, for example the errors during sample preparation and the weight loss of raw material and raw mixture during the thermal process. However, the XRF is only a semi-quantitative technique except a calibration curve is used. So, it should be noted that Ho and Yb contents are too low to detect with precision. Besides, it is worth noting that Ho content that is detected as 0 mole is due to the detection limits such as instrument detection limit and method detection limit. With these results, it could be concluded that the temperature used has little effect on the change in ZnO/TiO_2 mixing ratio, and for the Ho content, it would be in the same way as observed in the XRF analysis of Er and Yb contents (Chapter III, section 3.3.10.2 and 3.3.10.3) that they are similar to the expected content. Therefore, the final mixing ratio of these samples after adjustment based on 1 mole of Ti would be acceptable as Zn:Ti:Ho:Yb = 1:1:0.0003:0.09 (in mole).

4.3.9.2 X-ray fluorescence (XRF) of various ZnO/TiO_2 mixing ratios doped with 0.03 mol% Ho^{3+} and 9 mol% Yb^{3+} fired at 1300 °C

According to the procedures used for XRF analysis in section 4.3.8.1, the analyzed results of the synthesized powder samples, various ZnO/TiO_2 mixing ratios doped with 0.03 mol% Ho^{3+} and 9 mol% Yb^{3+} fired at 1300 °C, is given in Table 4.4.

Table 4.4. An overview of XRF analysis of various ZnO/TiO_2 mixing ratios doped with 0.03 mol% Ho^{3+} and 9 mol% Yb^{3+} powder samples fired at 1300 °C, their expected mixing ratio values and XRF elemental analysis results (each sample was measured five times at different positions and data were averaged).

Mixing ratio	Zn (mole)		Ti (mole)		Ho (mole)		Yb (mole)	
	Expected	XRF	Expected	XRF	Expected	XRF	Expected	XRF
Z 0.5 T 1	0.5000	0.4776	1.0000	1.0000	0.0003	0.0000	0.0900	0.0752
Z 0.75 T 1	0.7500	0.7143	1.0000	1.0000	0.0003	0.0000	0.0900	0.0778
Z 1 T 1	1.0000	0.9752	1.0000	1.0000	0.0003	0.0000	0.0900	0.0768
Z 1.25 T 1	1.2500	1.2208	1.0000	1.0000	0.0003	0.0000	0.0900	0.0771
Z 1.5 T 1	1.5000	1.3291	1.0000	1.0000	0.0003	0.0000	0.0900	0.0769

Remark:

1. Atomic weights used to calculate these results are Zn = 65.382, Ti = 47.867, Ho = 164.930, and Yb = 173.045.
2. These results are converted from weight% to mole and followed by keeping 1 mole of Ti.

As shown in Table 4.4, the results showed that all observed values were lower than the expected content. These could be due to many situations as mentioned in section 4.3.8.1. With these results, it could be summarized that the final mixing ratio of these samples after adjustment based on 1 mole of Ti is in accordance with expected mixing ratio.

4.3.10 Upconversion (UC) mechanism

In the theoretical understanding of UC mechanism, this process can be explained by taking into account the relationship between UC emission intensity (I) and excitation pump power (P). The intensity I is proportional to the n power of P, which can be expressed as $I \propto P^n$, where n is the number of pump photons per one photon emitted [3,26]. To obtain the n-value, a plotting of log I versus log P yields a straight line with slope n as shown in Figure 4.23. In the Figure, the n-values of observed green and red emission bands were 1.13 and 1.10, respectively, under

between P = 15-196 mW. As mentioned earlier in Chapter III, section 3.3.11, even though the observed *n*-value is less than the value two, but it could be suggested that the two-photon process occurs because the system is under the saturation effect in the UCL intensity caused by the competition between linear decay and UC processes for the depletion of the intermediate excited states, resulting in the lower *n*-value [27,28]. To better understand the decrease in *n*-value and the saturation effect, the details can be found in Chapter III, section 3.3.12.

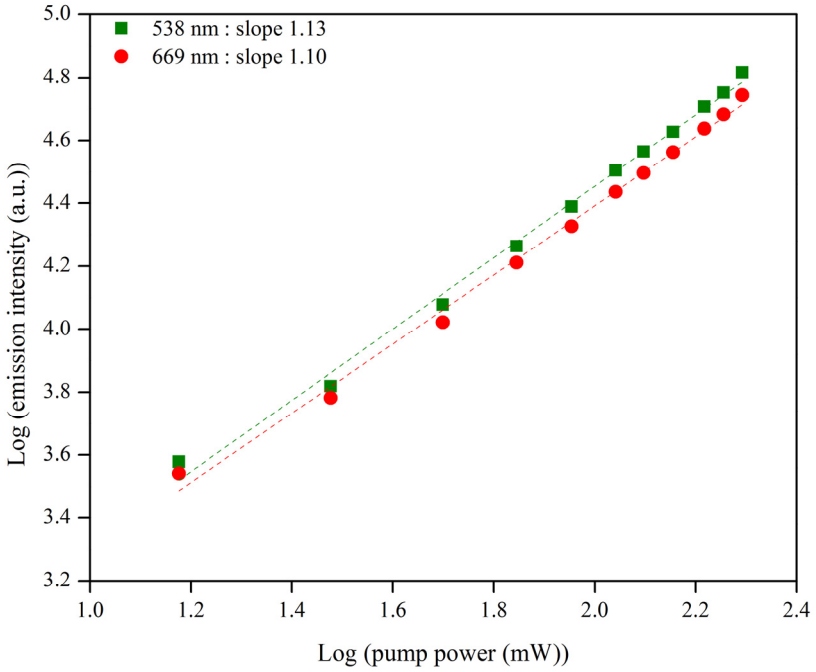

Figure 4.23. Pump power dependent UC of ZnO:TiO_2 = 1:1 (in mole) doped with 0.03 mol% Ho^{3+} and 9 mol% Yb^{3+} fired at 1300 °C, and irradiated with a 980-nm, 15-196 mW laser. Reproduced with permission from Kobwittaya *et al.*, *Mater. Sci. Forum*, **922** (2018) 32-39. Copyright (2018) Trans Tech Publications.

As shown in Figure 4.24, to clearly explain about *n*-value, the *n*-value of various ZnO/TiO_2 mixing ratios doped with 0.03 mol% Ho^{3+} and 9 mol% Yb^{3+} was calculated and then the relationship between them was plotted based on green (538 nm) and red (669 nm) emission bands. With increase of ZnO amount up to $x = 1$, the increase of *n*-value was observed on both green and red bands, and slope of two lines seemed to be parallel. In general, the *n*-value is related to UC mechanism and directly involves with the ratio of Ho^{3+}/Yb^{3+} in Zn_2TiO_4 crystal matrix. Hence, the amount of Ho^{3+} and Yb^{3+} increases equally from the

beginning with the same ratio. Besides, it is possible that the Ho^{3+}/Yb^{3+} pairs of ions are possibly formed in the crystal. Further increase of ZnO amount $x > 1$, the *n*-value for both bands sharply decreased. These situations can be used to confirm that the number of vacant sites in the structure of Zn_2TiO_4 crystal is lower than in the case of $x \leq 1$, causing to the lower performance in the substitution of dopants and influencing to the decrease in energy transfer (*n*-value decreased). It should be noted that, in this case, Ho^{3+} and Yb^{3+} may get into the vacant site in the structure of Zn_2TiO_4 crystal with similar ratio in the case of ZnO amount x = 0.5-1.25 because the change in line pattern seems to be in the same direction. However, when ZnO amount x = 1.5, the line pattern changes. This must be due to the alteration of the ratio of Ho^{3+}/Yb^{3+} at such vacant site.

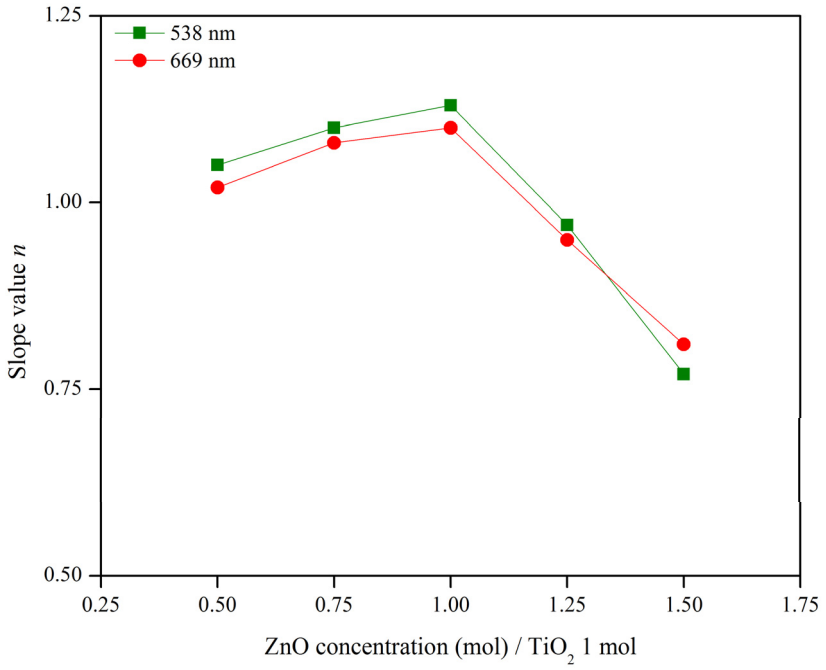

Figure 4.24. The *n*-values of green (538 nm) and red (669 nm) emission bands versus various ZnO/TiO_2 mixing ratios doped with 0.03 mol% Ho^{3+} and 9 mol% Yb^{3+} fired at 1300 °C.

Figure 4.25 shows the proposed UC mechanism of $ZnO\text{-}TiO_2$ composite doped with Ho^{3+} and Yb^{3+} under a 980-nm laser excitation. The mechanism for generating green and red emissions are accomplished as follows. The 980-nm laser excites Yb^{3+} from its ground state $^2F_{7/2}$ level to $^2F_{5/2}$ level, and simultaneously, ground state $^5I_8$ level of Ho^{3+} is excited to the same level as $^2F_{5/2}$ level of Yb^{3+}. These transitions take place via ground state absorption (GSA). Subsequently,

the excess energy returns to the lower energy level in the form of non-radiative (NR) transition, $^2F_{5/2} \rightarrow {}^2F_{7/2}$ and virtual $^2F_{5/2} \rightarrow {}^5I_6$ transitions. In the case of Ho^{3+}, after the NR transition, the exciting from $^5I_6$ to $^5F_4$, $^5S_2$ occurs via the excited state absorption 1 (ESA1). Later, the green and red emissions are observed by the following processes. For the green emission, Yb^{3+} transfers its energy to Ho^{3+} in two possible ways, ET1 and ET2. Herein, the pathways, $^2F_{5/2}$ $(Yb^{3+}) + {}^5I_8$ $(Ho^{3+}) \rightarrow {}^2F_{7/2}$ $(Yb^{3+}) + {}^5I_6$ (Ho^{3+}) and $^2F_{5/2}$ $(Yb^{3+}) + {}^5I_6$ $(Ho^{3+}) \rightarrow {}^2F_{7/2}$ $(Yb^{3+}) + {}^5F_4$, $^5S_2$ (Ho^{3+}) lead to green emission with radiative transition from $^5F_4$, $^5S_2 \rightarrow {}^5I_8$. For the red emission, this emission is associated with $^5F_5 \rightarrow {}^5I_8$ transition which is accomplished by two different channels. First is from the NR ($^5F_4$, $^5S_2 \rightarrow {}^5F_5$) and second is $^5I_7 \rightarrow {}^5F_5$ transition (ESA2) that is populated by NR ($^5I_6 \rightarrow {}^5I_7$) + ET3 [29-31]. Thus, the green and red emission, which show highest emission intensity at 538 nm and 669 nm, respectively, are detected due to the $^5F_4$, $^5S_2 \rightarrow {}^5I_8$ and $^5F_5 \rightarrow {}^5I_8$ transitions of Ho^{3+}.

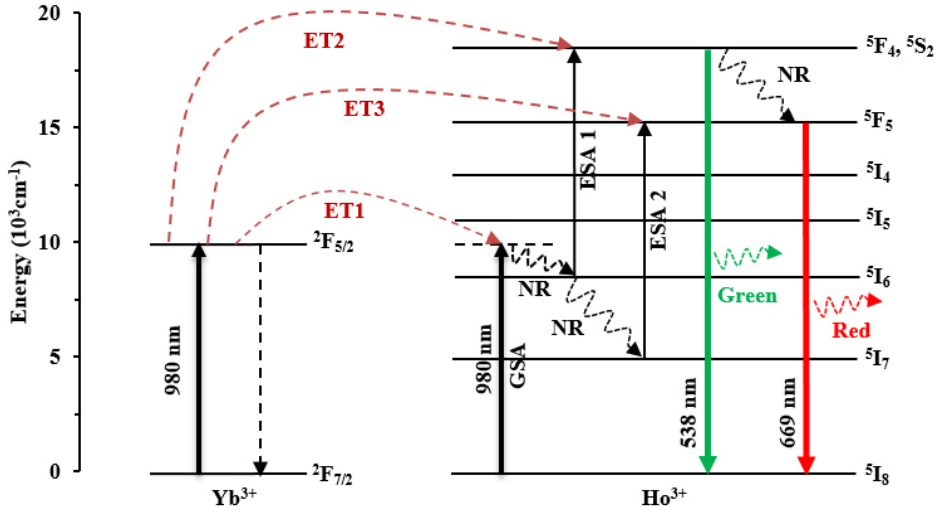

Figure 4.25. Schematic energy level diagram of Ho^{3+} and Yb^{3+} and proposed UC mechanism of ZnO-TiO_2 doped with 0.03 mol% Ho^{3+} and 9 mol% Yb^{3+} under a 980-nm laser excitation.

In this study, the *n*-value for green emission was around 1.13, while *n*-value for the red emission was around 1.10. This could be ascribed to the difference of the intermediate excited state between the green and red emissions. For the green emission, the intermediate excited state is $^5I_6$ of Ho^{3+}, and the UC process and linear decay at this excited state are ESA1 ($^5I_6 \rightarrow {}^5F_4$,$^5S_2$) and NR ($^5I_6 \rightarrow {}^5I_7$), respectively. Because of the *n*-value that is approximately one for the green emission, therefore, the UC process (ESA1) is the dominant depletion mechanism which causes

the saturation effect in UCL intensity and the decrease in *n*-value. In the case of red emission, the intermediate excited state is $^5I_7$ of Ho^{3+} and the reduced *n*-value is related to the competition between UC process (ESA2: $^5I_7 \rightarrow {}^5F_5$) and linear decay ($^5I_7 \rightarrow {}^5I_8$). Also, the *n*-value for red emission was nearly one, therefore, the UC process is dominant mechanism for the depletion of the intermediate state $^5I_7$ of Ho^{3+}, leading to the diminution of *n*-value and the saturation effect in UCL intensity. However, there are minor possibilities which would have influence on the decrease in *n*-value such as the ET processes to impurity defects, cross-relaxation, or other complicated processes, which can also give rise to the depletion of the intermediate excited states of Ho^{3+} and Yb^{3+} [27,28,32,33].

4.3.11 Comparison of upconversion (UC) emission intensity of phosphors prepared by solid-state reaction and powder-solution mixing methods

According to the explanations and details about these two methods provided in Chapter III, section 3.3.13, herein, the ZnO-TiO_2:Ho^{3+}/Yb^{3+} phosphors prepared by SSR and PSM methods will also be compared by considering the products with the same physical characteristic (pellet (SSR) / pellet (PSM) and powder (SSR) / powder (PSM)) and their UC emission intensity. The phosphor pellets were prepared with the optimum condition presented in Chapter II, ZnO:TiO_2 = 1:1 (in mole) doped with 0.05 mol% Ho^{3+} and 9 mol% Yb^{3+} fired at 1200 °C for 4 h, for both SSR and PSM methods. The phosphor powders were prepared with the optimum condition presented in this chapter; ZnO:TiO_2 = 1:1 (in mole) doped with 0.03 mol% Ho^{3+} and 9 mol% Yb^{3+} fired at 1300 °C for 1 h, for both SSR and PSM methods. Besides, to obtain the dependable result, the UC emission intensity of each sample was measured at different positions of its surface. The results of these comparisons will be discussed below.

For the phosphor pellet, according to the photograph in Figure 4.26, the physical characteristics of the samples prepared by SSR and PSM were different. After firing at 1200 °C for 4 h, the SSR sample showed small decrease in the size of the pellet, while the PSM sample showed larger decrease. Also, each sample demonstrated dissimilar colors, white and cream, for SSR and PSM samples, respectively. These miscellaneous changes are caused by the complex and dissimilar reaction mechanisms of each preparation method. To understand these changes, the explanations can be found in the Chapter III, section 3.3.13.

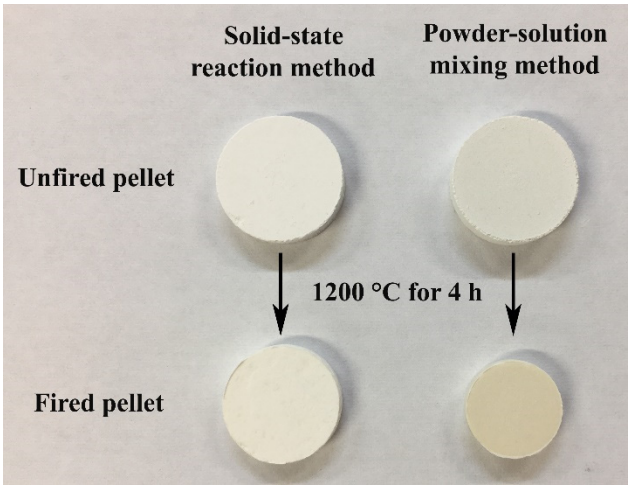

Figure 4.26. Photograph of ZnO:TiO_2 = 1:1 (in mole) doped with 0.05 mol% Ho^{3+} and 9 mol% Yb^{3+} phosphor pellets (before and after firing) prepared by solid-state reaction and powder-solution mixing methods.

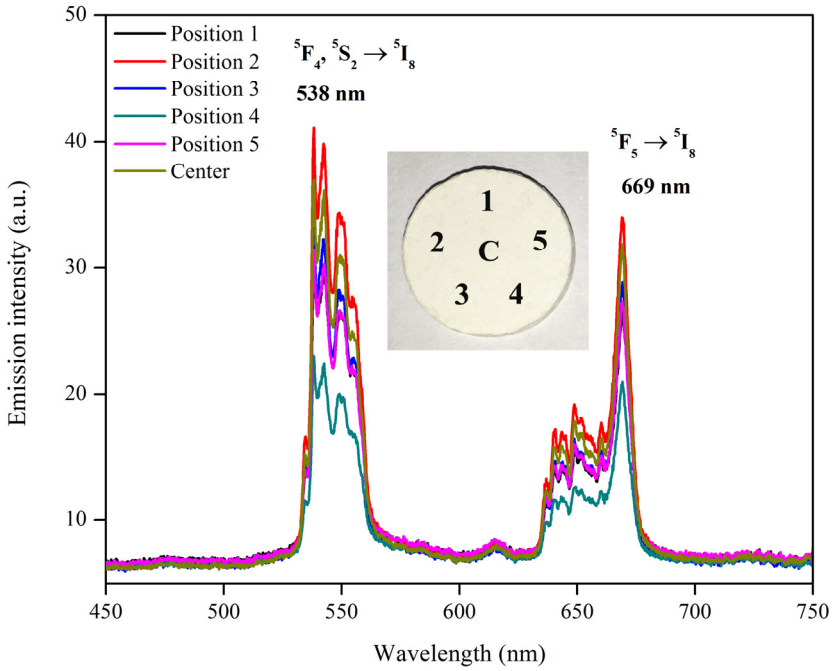

Figure 4.27. UC emission spectra at different positions of pellet surface of the phosphor (ZnO:TiO_2 = 1:1 (in mole) doped with 0.05 mol% Ho^{3+} and 9 mol% Yb^{3+} fired at 1200 °C for 4 h) prepared by solid-state reaction method, and irradiated with a 980-nm 70 mW laser. The inset shows the photograph of the corresponding measured positions as labeled.

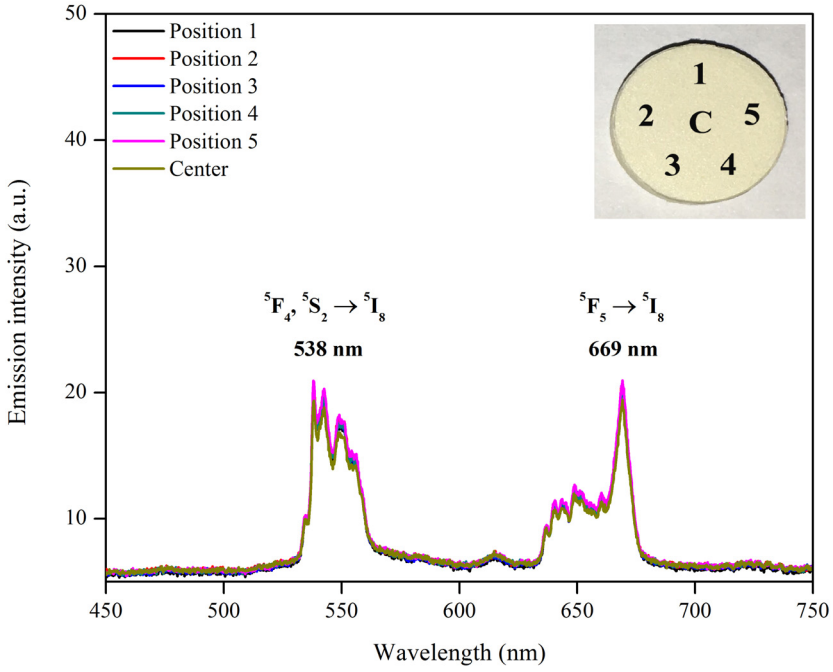

Figure 4.28. UC emission spectra at different positions of pellet surface of the phosphor ($ZnO:TiO_2$ = 1:1 (in mole) doped with 0.05 mol% Ho^{3+} and 9 mol% Yb^{3+} fired at 1200 °C for 4 h) prepared by powder-solution mixing method, and irradiated with a 980-nm 70 mW laser. The inset shows the photograph of the corresponding measured positions as labeled.

The UC emission spectra of both fired samples are measured at different positions of its surface and the results are shown in Figure 4.27 and Figure 4.28. The inset shows the photograph of the measured positions. The results showed that both samples exhibited the same peak emission wavelengths which were at 538 nm for green region and 669 nm for red region. In the case of $ZnO\text{-}TiO_2$: Er^{3+}/Yb^{3+} phosphor pellets prepared by SSR and PSM, the maximum emission intensity of both samples is almost at the same level. But, in this case, SSR sample shows higher emission intensity than PSM sample under the same laser intensity because, in very low concentration state of Ho^{3+} activator, the distribution of Ho^{3+} over the entire sample may be different and this directly affects the insertion of Ho^{3+} into host crystal matrix. In addition, the different formation processes may strongly influence to this behavior. Focusing on the UC emission intensity at various measured positions of each phosphor pellet, it is obvious that the emission intensity of PSM sample is more well-distributed over the whole surface than that of SSR sample. The explanation of this behavior can be found in the Chapter III, section 3.3.13.

For the phosphor powder, the UC emission spectra of both fired samples are also measured at different positions of its surface and the results are shown in Figure 4.29 and Figure 4.30. The inset shows the photograph of the measured positions. The results showed that both samples showed the same peak emission wavelengths as phosphor pellet which were at 538 nm for green region and 669 nm for red region. These can be used to confirm that ZnO-TiO_2 composite doped with Ho^{3+} and Yb^{3+} exhibits the particular emission wavelength for green and red bands, even if the preparation method and physical characteristics are different. In addition, it is clear that the emission intensity of PSM sample is more well-distributed than that of SSR sample either. This must be due to the same reason as mentioned above about phosphor pellet. However, the emission intensity of phosphor powder is usually lower than that of phosphor pellet because the bulk density of powder mixture, which relies on how intimately individual particles pack together, directly affects the formation process of phosphor powder. The explanation of this behavior can also be found in the Chapter III, section 3.3.13.

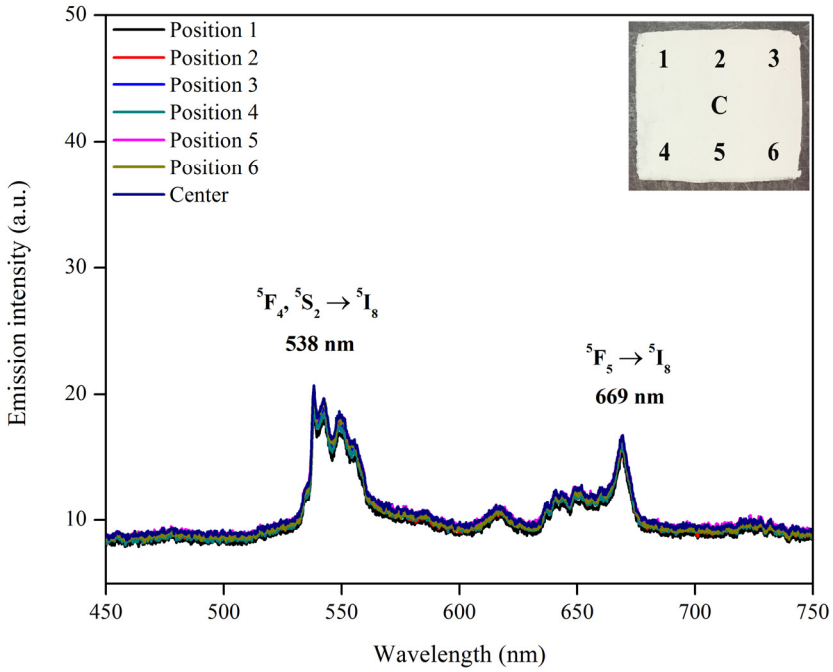

Figure 4.29. UC emission spectra at different positions of powder surface of the phosphor (ZnO:TiO_2 = 1:1 (in mole) doped with 0.03 mol% Ho^{3+} and 9 mol% Yb^{3+} fired at 1300 °C for 1 h) prepared by solid-state reaction method, and irradiated with a 980-nm 110 mW laser. The inset shows the photograph of the corresponding measured positions as labeled.

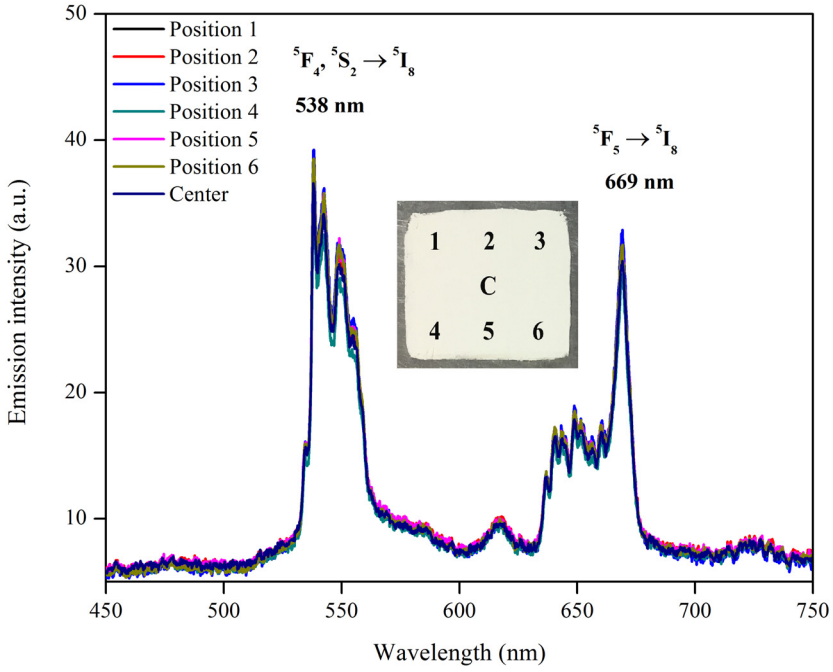

Figure 4.30. UC emission spectra at different positions of powder surface of the phosphor ($ZnO:TiO_2$ = 1:1 (in mole) doped with 0.03 mol% Ho^{3+} and 9 mol% Yb^{3+} fired at 1300 °C for 1 h) prepared by powder-solution mixing method, and irradiated with a 980-nm 110 mW laser. The inset shows the photograph of the corresponding measured positions as labeled.

Significantly, it should be noted that these comparisons focus only on the homogeneity of the phosphor by considering the UC emission intensity of the sample under the same physical characteristic and condition. However, the conditions used for PSM phosphor pellet and SSR phosphor powder are not the optimum condition for them to emit the strongest emission intensity. Moreover, it must be noted that the phosphor powder produced by crushing phosphor pellet shows lower emission intensity than directly preparing phosphor powder and phosphor pellet due to the variation in their bulk density. For the phosphor pellet produced by packing phosphor powder, it shows the instability of the product because the phosphor powder cannot attach to form the phosphor pellet. So, this means is not suitable for fabricating phosphor pellet.

Finally, it can be summarized that, for the Ho^{3+}/Yb^{3+} co-doped $ZnO-TiO_2$ composite phosphor, these two methods show the same optimum ZnO/TiO_2 mixing ratio = 1:1 (in mole), even if the optimum firing temperature, preparation time, and dopant concentration are different; 1200 °C for 4 h (SSR) and 1300 °C for 1 h (PSM), 0.05 mol% Ho^{3+}/9 mol% Yb^{3+} (SSR) and 0.03 mol%

Ho^{3+}/9 mol% Yb^{3+} (PSM). The dissimilar formation processes of the products and the process of incorporation of RE^{3+} ions into the host material may cause these differences. In general, Ho^{3+} and Yb^{3+} enter the host material by diffusion-based and dissolution/diffusion-based processes for SSR and PSM methods, respectively. In addition, it is clearly understandable that, for ZnO-TiO_2:Ho^{3+}/Yb^{3+} phosphor, the product prepared by PSM method presents great potential for enhancing the UC phosphor to be more homogenous phase than SSR method, becoming the leading cause of the improvement of efficiency of Ho^{3+}/Yb^{3+} system-based UC phosphors.

4.4 Conclusion

The ZnO-TiO_2 composite system containing Ho^{3+} and Yb^{3+} was successfully synthesized by powder-solution mixing method. The UCL behavior of this composite phosphor powder was studied under a 980-nm laser excitation. The emission spectra showed green and red emission bands which centered at 538 and 669 nm, respectively. These two emission bands occurred due to the $^5F_4$, $^5S_2 \rightarrow {}^5I_8$ and $^5F_5 \rightarrow {}^5I_8$ transitions of Ho^{3+}. Pump power dependent UC revealed that two-photon process was responsible for both green and red emissions. The green and red emission intensities demonstrated maximum value in the sample that contained 0.03 mol% Ho^{3+} and 9 mol% Yb^{3+}. The optimum ZnO/TiO_2 mixing ratio was ZnO:TiO_2 = 1:1 (in mole), even if the host material was Zn_2TiO_4 (ZnO:TiO_2 = 2:1 (in mole)). Furthermore, ZnO:TiO_2 = 1:1 (in mole): 0.03 mol% Ho^{3+}, 9 mol% Yb^{3+} composite phosphor powder fired at 1300 °C exhibited green UC emission when the system consisted of four phases co-existence; Zn_2TiO_4, TiO_2, $RE_2Ti_2O_7$, and RE_2TiO_5 (RE = Ho^{3+} and/or Yb^{3+}).

The most possibility of site preference of Ho^{3+} and Yb^{3+} in Zn_2TiO_4 host crystal matrix should be at the vacant Zn site in octahedral ($V''_{Zn(oct)}$) that would appear when there were excess TiO_2 in the system and followed by the incorporation of RE^{3+} ions into Zn_2TiO_4 matrix. This phenomenon is mostly expressed in the variations of unit cell parameter of Zn_2TiO_4 crystal, which leads to the decrease in its lattice constant and lattice volume. In addition, the comparison of the optimum mixing ratio and dopant concentration of ZnO-TiO_2:Ho^{3+}/Yb^{3+} phosphors prepared by solid-state reaction method and powder-solution mixing method was discussed in detail. Albeit the optimum firing temperature and preparation time were different, 1200 °C for 4 h (solid-state reaction method) and 1300 °C for 1 h (powder-solution mixing method), but

these two methods showed the same optimum ZnO/TiO_2 mixing ratio = 1:1 (in mole). The most effective product that was synthesized by solid-state reaction method showed the optimum dopant concentrations at 0.05 mol% Ho^{3+} and 9 mol% Yb^{3+}, while using powder-solution mixing method, the optimum dopant concentrations were 0.03 mol% Ho^{3+} and 9 mol% Yb^{3+}. The dissimilar formation processes of the products and the process of incorporation of RE^{3+} ions into the host material may cause these differences. In general, Ho^{3+} and Yb^{3+} enter the host material by diffusion-based and dissolution/diffusion-based processes for SSR and PSM methods, respectively. In addition, it is clearly understandable that, for $ZnO\text{-}TiO_2$:Ho^{3+}/Yb^{3+} phosphor, the product prepared by PSM method presents great potential for enhancing the UC phosphor to be more homogenous phase than SSR method, becoming the leading cause of the improvement of efficiency of Ho^{3+}/Yb^{3+} system-based UC phosphors.

4.5 Acknowledgements

This chapter contains contributions from co-authors and some portions were published in: K. Kobwittaya, Y. Oishi, T. Torikai, M. Yada, T. Watari, Upconversion luminescence of $ZnO\text{-}TiO_2$: Ho^{3+}/Yb^{3+} phosphor powder, *Materials Science Forum*, **922** (2018) 32-39.

4.6 Copyright permission

References

[1] L. Wang, M. Lan, Z. Liu, G. Qin, C. Wu, X. Wang, W. Qin, W. Huang, L. Huang, *J. Mater. Chem. C*, **1** (2013) 2485-2490.

[2] K. Yamamoto, M. Fujii, S. Sowa, K. Imakita, K. Aoki, *J. Phys. Chem. C*, **119** (2015) 1175-1179.

[3] F. Auzel, *Chem. Rev.*, **104** (2004) 139-174.

[4] H.X. Yang, H. Lin, L. Lin, Y.Y. Zhang, B. Zhai, E.Y.B. Pun, *J. Alloy. Compd.*, **453** (2008) 493-498.

[5] H. Lin, G. Meredith, S. Jiang, X. Peng, T. Luo, N. Peyghambarian, E.Y.B. Pun, *J. Appl. Phys.*, **93** (2003) 186-191.
[6] X. Wang, S. Xiao, Y. Bu, J.W. Ding, *J. Alloy. Compd.*, **477** (2009) 941-945.
[7] F. Wang, X. Liu, *Chem. Soc. Rev.*, **38** (2009) 976-989.
[8] H. Huang, H. Zhou, J. Zhou, T. Wang, D. Huang, Y. Wu, L. Sun, G. Zhou, J. Zhan, J. Hu, *RSC Adv.*, **7** (2017) 16777-16786.
[9] L. Li, Y. Fan, D. Wang, G. Feng, D. Xu, *Cryst. Res. Technol.*, **46** (2011) 475-479.
[10] L. Li, F. Li, T. Cui, Q. Zhou, D. Xu, *Phys. Status Solidi A*, **209** (2012) 2596-2599.
[11] H.N. Luitel, K. Ikeue, R. Okuda, R. Chand, T. Torikai, M. Yada, T. Watari, *Opt. Mater.*, **36** (2014) 591-595.
[12] S.-I. Yamamoto, K. Ohyama, T. Nonaka, T. Kanamori, 21st International Workshop on Active-Matrix Flatpanel Displays and Devices (AM-FPD) (2014) 271-272.
[13] K. Ohyama, T. Nonaka, T. Kanamori, S.-I. Yamamoto, 22nd International Workshop on Active-Matrix Flatpanel Displays and Devices (AM-FPD) (2015) 89-90.
[14] T. Nonaka, T. Kanamori, K. Ohyama, S.-I. Yamamoto, *Jpn. J. Appl. Phys.*, **54** (2015) 03CA02.
[15] W.M. Yen, S. Shionoya, H. Yamamoto, Phosphor Handbook, Second Edition, CRC Press, Boca Raton, Florida (2006).
[16] T.J. Bruno, P.D.N. Svoronos, CRC Handbook of Fundamental Spectroscopic Correlation Charts, CRC Press, Boca Raton, Florida (2005).
[17] X. Li, J. Zhu, Z. Man, Y. Ao, H. Chen, *Sci. Rep.*, **4** (2014) 4446.
[18] A. Kumar, S.P. Tiwari, A.K. Singh, K. Kumar, *Appl. Phys. B*, **122** (2016) 190.
[19] B.A.A. Balboul, *Thermochim. Acta*, **419** (2004) 173-179.
[20] B.A.A.A. Balboul, *Powder Technol.*, **107** (2000) 168-174.
[21] B.A.A. Balboul, *Thermochim. Acta*, **351** (2000) 55-60.
[22] Y. Xu, M. Yamazaki, P. Villars, *Jpn. J. Appl. Phys.*, **50** (2011) 11RH02.
[23] E.M. Levin, C.R. Robbins, H.F. McMurdie, Phase Diagram for Chemists Volume I (Figures 1-2066), The American Ceramic Society, Inc., Columbus, Ohio (1964).
[24] A. Jain, G. Hautier, S.P. Ong, C.J. Moore, C.C. Fischer, K.A. Persson, G. Ceder, *Phys. Rev. B*, **84** (2011) 045115.
[25] H.T. Kim, Y. Kim, M. Valant, D. Suvorov, *J. Am. Ceram. Soc.*, **84** (2001) 1081-1086.

[26] E. De la Rosa, P. Salas, H. Desirena, C. Angeles, R.A. Rodríguez, *Appl. Phys. Lett.*, **87** (2005) 241912.

[27] M. Pollnau, D.R. Gamelin, S.R. Lüthi, H.U. Güdel, M.P. Hehlen, *Phys. Rev. B*, **61** (2000) 3337-3346.

[28] J.F. Suyver, A. Aebischer, S. García-Revilla, P. Gerner, H.U. Güdel, *Phys. Rev. B*, **71** (2005) 125123.

[29] X. Yu, S. Liang, Z. Sun, Y. Duan, Y. Qin, L. Duan, H. Xia, P. Zhao, D. Li, *Opt. Commun.*, **313** (2014) 90-93.

[30] J. Xie, L. Mei, L. Liao, M. Guan, H. Liu, *J. Phys. Chem. Solids*, **83** (2015) 152-156.

[31] B. Xu, P. Wang, X. Meng, K. Zou, J. Liu, *J. Lumin.*, **175** (2016) 78-81.

[32] L. Agazzi, K. Wörhoff, M. Pollnau, *J. Phys. Chem. C*, **117** (2013) 6759-6776.

[33] G.C. Righini, M. Ferrari, *Riv. Nuovo Cimento*, **28** (2005) 1-50.

Chapter V

Nearly pure NIR to NIR upconversion luminescence in Tm^{3+}, Yb^{3+} co-doped ZnO-TiO_2 composite phosphor powder

5.1 Introduction

Trivalent rare earth (RE^{3+}) ions doped near-infrared (NIR) to near-infrared (NIR) upconversion (UC) phosphors have received much attention in recent years since the investigations have shown great potential for many applications in biomedical fields, especially biomedical optical bioimaging technologies which they use the NIR biological transparency windows (NIR window, 650-1450 nm) for biological tissues because the traditional visible imaging range (400-750 nm) has limited observation depth due to very low penetration depth caused by the body tissues and water molecules, leading to the attenuation of signal proportional to the depth of the interest targeting [1,2].

To date, the Tm^{3+}/Yb^{3+} system is recognized as one of the most efficient activator-sensitizer pairs of ions for generating NIR emission when it is introduced into a suitable host material because the intense NIR emission can be obtained by the $^3H_4 \rightarrow {}^3H_6$ transition of Tm^{3+} activator. Besides, it has been considered as one of the important and useful choices for fabricating NIR UC phosphors and infrared materials [3-5]. According to many researches regarding UC phosphors, the most effective UC host material is fluoride-based material because fluorides usually exhibit low phonon energies of less than 350 cm^{-1} and high chemical stability [6-8]. However, they are hygroscopic and are of limited use. In comparison, oxide-based materials demonstrate higher chemical and thermal stability, therefore, oxides with low phonon energy may have more promising applications [9]. At present, composite materials have gained much attention due to their properties such as light weight, flexible, high corrosion resistance, and impact strength. Because of these properties, composite materials have been considered as a replacement of classical materials used in aerospace industry, construction, and electrical and electronics [10]. Among various oxide-based composite materials, ZnO-TiO_2 composite is

thought of as a promising host material because it is inexpensive, non-toxic, thermally and chemically stable, and environmental friendliness [8]. Additionally, the noteworthy product of ZnO-TiO_2 composite is Zn_2TiO_4 that is a high thermal stability phase due to its inverse spinel structure. In addition, Zn_2TiO_4 shows great potential for being the good optical host because it has high value of refractive index n = 2.1 [11] and low phonon energy around 721 cm^{-1} [12]. Hence, ZnO-TiO_2 composite could be one of the proper hosts for the fabrication of UC phosphor.

In a series of reports regarding UCL from ZnO-TiO_2 composite phosphors, the reports showed only the results in the visible region (e.g. orange and red emissions) which were observed from Er^{3+}/Yb^{3+} co-doped ZnO-TiO_2 composite prepared by solid-state reaction method [13,14] and metal-organic decomposition method [15-17]. Until now, there is no any result concerning NIR UCL from ZnO-TiO_2 composite phosphor. Therefore, in this study, the systematic analysis of the NIR to NIR UCL properties of ZnO-TiO_2 composite doped with Tm^{3+} and Yb^{3+} prepared by the new simple method, powder-solution mixing method were proposed. The effect of ZnO/TiO_2 mixing ratio, Tm^{3+} and Yb^{3+} doping concentrations, and UCL characteristics were methodically investigated. In addition, the interesting and important results about the site preference of Tm^{3+} and Yb^{3+} in the host crystal matrix were anticipated and described to comprehend how RE^{3+} ions incorporate into complex inorganic crystal structure. Lastly, this new preparation method was comparatively discussed with those two methods in detail.

5.2 Experimental

Tm^{3+} and Yb^{3+} co-doped with ZnO-TiO_2 composite system was synthesized by powder-solution mixing method using zinc oxide (ZnO; NanoTek, ~34 nm, 99%), titanium dioxide sol solution (TiO_2; Ishihara Sangyo Kaisha, 39.5 wt.%), thulium (III) nitrate pentahydrate ($Tm(NO_3)_3{\cdot}5H_2O$; Aldrich, 99.9%), and ytterbium (III) nitrate pentahydrate ($Yb(NO_3)_3{\cdot}5H_2O$; Aldrich, 99.9%). All raw materials were thoroughly mixed in a beaker with deionized water by constant stirring with a high-power mixer. Each starting material changed as follows. Various ZnO-TiO_2 composite samples were prepared by different ZnO/TiO_2 mixing ratios, changing ZnO amounts from 0.5-1.5 (*x*-value; mole), while keeping constant TiO_2 (1 mole) and the sample was named as Z*x*T1. Tm^{3+} and Yb^{3+} concentrations varied from 0-0.15 mol% and 0-18 mol%, respectively. After completely mixed, the sample was dried at 90 °C in drying oven for

12 h and subsequently fired in an air atmosphere at 1300 °C for 1 h. The fired product was crushed by vibration mill for 30 s to obtain the final product in powder form. The complete preparation scheme is shown in Figure 5.1. It is worth noting that, to avoid the surface adsorption of moisture, all samples were kept continuously in a vacuum desiccator over silica gel at room temperature for 6 h before carrying out the optical measurement.

The crystal structure of the samples was characterized by X-ray diffraction (XRD), a Shimadzu XRD-6300 instrument with CuKα radiation in the range of 2θ = 10-80°. Herein, to describe the crystallization process results, the relative phase contents calculated based on pseudo-quantitative analysis of each specific phase were estimated from the XRD patterns using equation (5.1):

$$\text{Relative phase content} = I_{(\text{phase})} / I_{(\text{total})} \quad (5.1)$$

where $I_{(\text{phase})}$ is the intensity of selected peak from a main peak position that consists of only one phase; $I_{(311)}$ for Zn_2TiO_4, $I_{(110)}$ for TiO_2, $I_{(004)}$ for $RE_2Ti_2O_7$, and $I_{(102)}$ for RE_2TiO_5; and $I_{(\text{total})}$ is the intensity summation of all selected peaks.

The microstructure of the samples was characterized by scanning electron microscopy (SEM), a Hitachi S-3000N instrument. Before SEM measurement, the sample was mounted securely by means of conductive carbon tape. Subsequently, the sample was coated with a thin layer of Pt-Pd (coating time of 90 s, around 5 nm thickness) under vacuum condition (vacuum-argon gas flushing) by ion sputter (Hitachi, E-1030).

The UC emission spectra excited by a 980-nm laser was recorded from 250-800 nm spectral range using USB 4000 UV-VIS-NIR fiber optic spectrometer (Ocean optics), having spectral resolution 1.34 nm (full width at half maximum, FWHM) and slit width 25 mm. The change in the maximum emission intensity on the laser power (0-200 mW) was measured for considering the potential UC mechanism. All measurements were performed at room temperature.

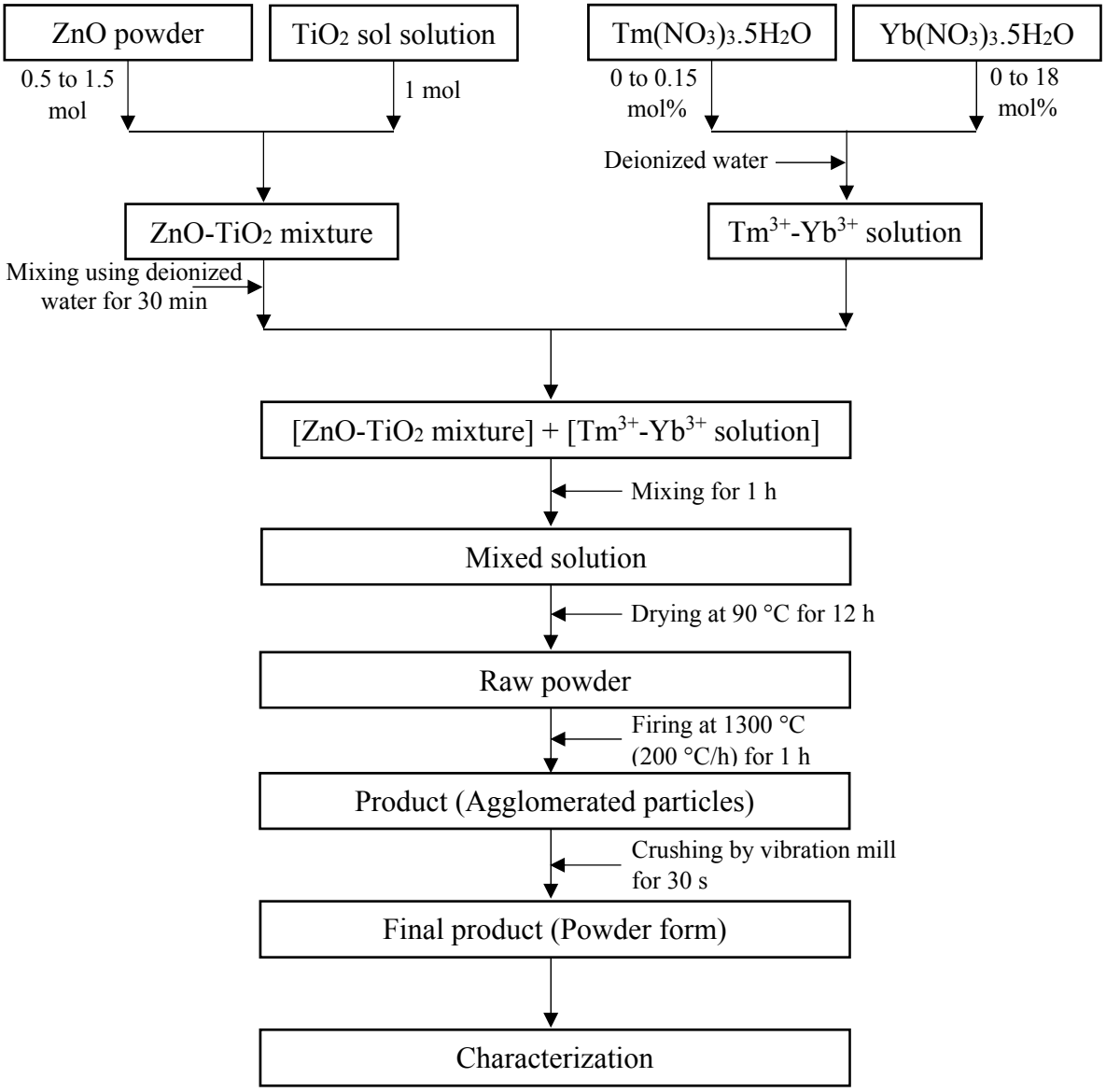

Figure 5.1. Flow chart for the preparation of ZnO-TiO_2:Tm^{3+}/Yb^{3+} phosphor by powder-solution mixing method.

5.3 Results and discussion

5.3.1. Effect of ZnO/TiO_2 mixing ratio on crystalline phase

XRD patterns of various Z*x*T1 samples doped with 0.125 mol % Tm^{3+} and 15 mol% Yb^{3+} are shown in Figure 5.2. The diffraction patterns of the prepared samples can be well indexed with four phases; Zn_2TiO_4 (JCPDS: 25-1164), rutile TiO_2 (JCPDS: 21-1276), $RE_2Ti_2O_7$ ($Tm_2Ti_2O_7$, JCPDS: 23-0590 and/or $Yb_2Ti_2O_7$, JCPDS:17-0454), and RE_2TiO_5 (Tm_2TiO_5 and/or Yb_2TiO_5) [18]. Nevertheless, the information of RE_2TiO_5 phase is ambiguous due to the lack of information of hkl planes, therefore, its crystal structure has been still unclear since it was first published [19], causing to the incomplete quantitative phase analysis via Rietveld refinement.

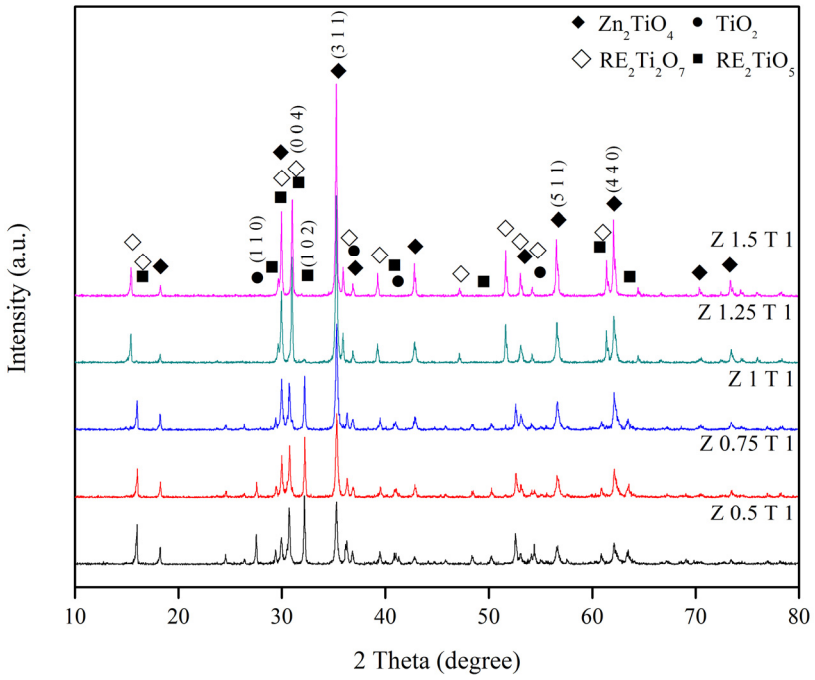

Figure 5.2. XRD patterns of various ZnO/TiO_2 mixing ratios doped with 0.125 mol% Tm^{3+} and 15 mol% Yb^{3+}. Reproduced with permission from Kobwittaya *et al*., *Vacuum*, **148** (2018) 286-295. Copyright (2017) Elsevier Ltd.

However, the content of each phase can be estimated using pseudo-quantitative phase analysis in the term of relative phase content (equation (5.1)) and the calculated results are shown in Figure 5.3. It was obvious that almost all samples showed the dominant Zn_2TiO_4 phase. According to the phase diagram of ZnO-TiO_2 system [20], it should be noted that Zn_2TiO_4 phase is a stable phase and easily formed by the reaction between ZnO and TiO_2, even if the system has low amount of ZnO. As shown in Figure 5.3, with increasing ZnO amount up to x = 1, the content of Zn_2TiO_4 phase increased and at the same time, TiO_2, $RE_2Ti_2O_7$, and RE_2TiO_5 contents gradually decreased. Further increase of ZnO amount x > 1, Zn_2TiO_4 content continuously increased and still was the dominant phase, and TiO_2 phase disappeared at x = 1.25. As increasing ZnO amount up to x = 1.5, $RE_2Ti_2O_7$ content initially increased, but RE_2TiO_5 content sharply decreased and then disappeared at x = 1.5. Focusing on the variation of both RE titanate contents under $1 < x \leq 1.25$, it is possible that there are indistinct and complicated reactions for the formation of RE titanate phases, resulting in the increase in $RE_2Ti_2O_7$ content and sharp decrease in RE_2TiO_5 content.

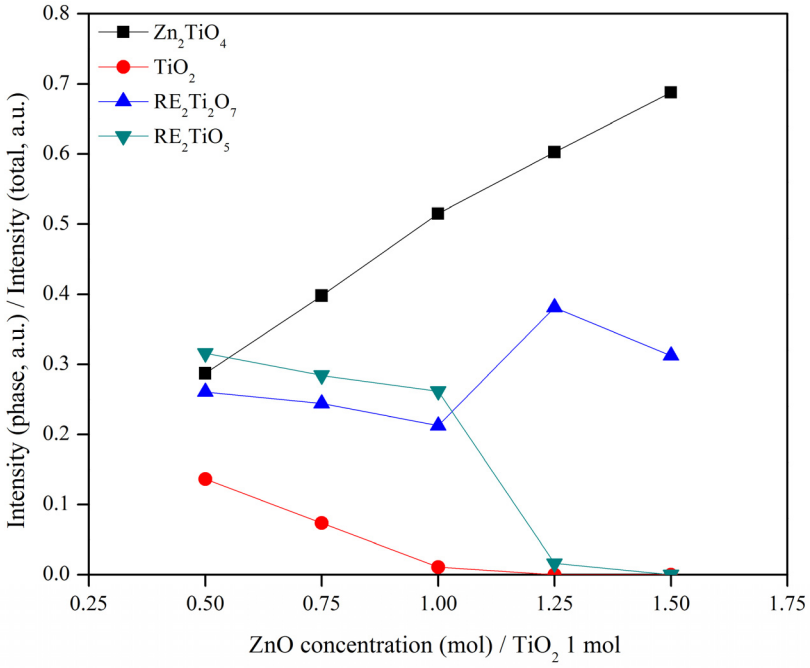

Figure 5.3. Calculated relative phase contents of Zn_2TiO_4, TiO_2, $RE_2Ti_2O_7$, and RE_2TiO_5 phases according to the compositions in Figure 5.2. Reproduced with permission from Kobwittaya *et al*., *Vacuum*, **148** (2018) 286-295. Copyright (2017) Elsevier Ltd.

These phase changes can be described as follows. The Zn_2TiO_4 phase is formed by the reaction between 2 moles of ZnO and 1 mole of TiO_2. Thus, as increasing ZnO amount *x* from 0.5-1.5, Zn_2TiO_4 content increases. For the formation of RE titanate phases, both phases correspond to the reaction between TiO_2 phase and RE_2O_3 phase (the final product of hydrated rare earth nitrate decomposition under high temperature [21-23]). In this phosphor system, the formation of Zn_2TiO_4, $RE_2Ti_2O_7$, and RE_2TiO_5 phases are the competitive reaction which can be clarified by taking into account theoretical formation energy of each phase. The Zn_2TiO_4 phase is first formed since its formation energy (-2.88 eV) is more positive than that of $RE_2Ti_2O_7$ (-3.8 eV) and RE_2TiO_5 (-3.79 eV) phases. It is worth noting that these theoretical formation energies are computed at 0 K and 0 atm, and neglect zero-point effects because heat capacity and density differences between solid phases are normally rather small, leading to only slight effects of temperature and pressure [24]. Furthermore, the Zn_2TiO_4 content and the amount of RE^{3+} ions in the Zn_2TiO_4 crystal matrix directly affect the changes in phase contents. On this basis, as increasing ZnO amount up to $x = 1$, the Zn_2TiO_4 content increases and the amount of RE^{3+} ions in its structure also increases, resulting in the diminution of $RE_2Ti_2O_7$ and RE_2TiO_5 contents. In the case of TiO_2 content, its reduction involves not only the reactions with ZnO and RE_2O_3, but also the solid solubility of TiO_2 into Zn_2TiO_4 crystal structure (maximum at 0.33 mole over stoichiometry) [25]. The microstructure of all processed powders is shown in Figure 5.4. It was observed that all samples had the same physical characteristics; micron-scale particles in irregular shapes and different sizes which they were caused by milling process. Besides, this kind of morphology was obviously due to the agglomeration of particles that corresponded with the high firing temperature used in the final stage of preparation.

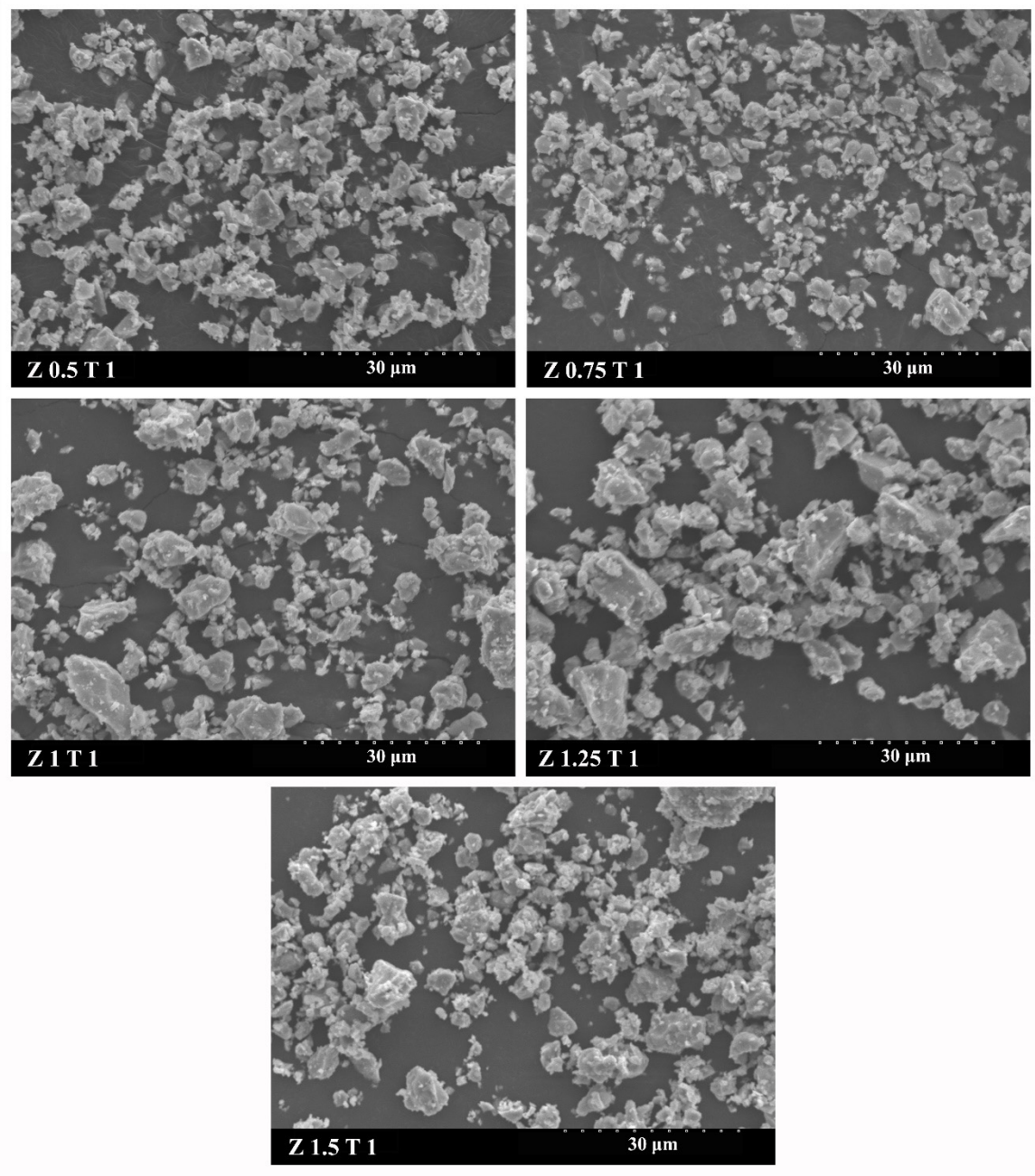

Figure 5.4. SEM images of various ZnO/TiO_2 mixing ratios doped with 0.125 mol% Tm^{3+} and 15 mol% Yb^{3+}. Reproduced with permission from Kobwittaya *et al*., *Vacuum*, **148** (2018) 286-295. Copyright (2017) Elsevier Ltd.

5.3.2. Effect of ZnO/TiO_2 mixing ratio on upconversion luminescence (UCL)

UCL spectra of various ZnO/TiO_2 mixing ratios doped with 0.125 mol% Tm^{3+} and 15 mol% Yb^{3+} are shown in Figure 5.5. The results showed that the UC emission spectra of these products were dominated by NIR emission and they also exhibited very weak red emission. For the other emission peaks observed, they would be a specific characteristic that come from Zn_2TiO_4 crystal structure which was in accordance with the sample, undoped Z1T1. The NIR spectral situated in the range of 774-831 nm and was attributed to $^3H_4 \rightarrow {}^3H_6$ transition of Tm^{3+} with the maximum at 795 nm. For the obscure red spectral, it was estimated that this region located in the range of 675-700 nm and was ascribed to $^3F_2 \rightarrow {}^3H_6$ transition of Tm^{3+}. The strongest peak position in the red region could not be designated due to the equivocal peak positions (Figure 5.6) and identical UC emission color (Figure 5.7).

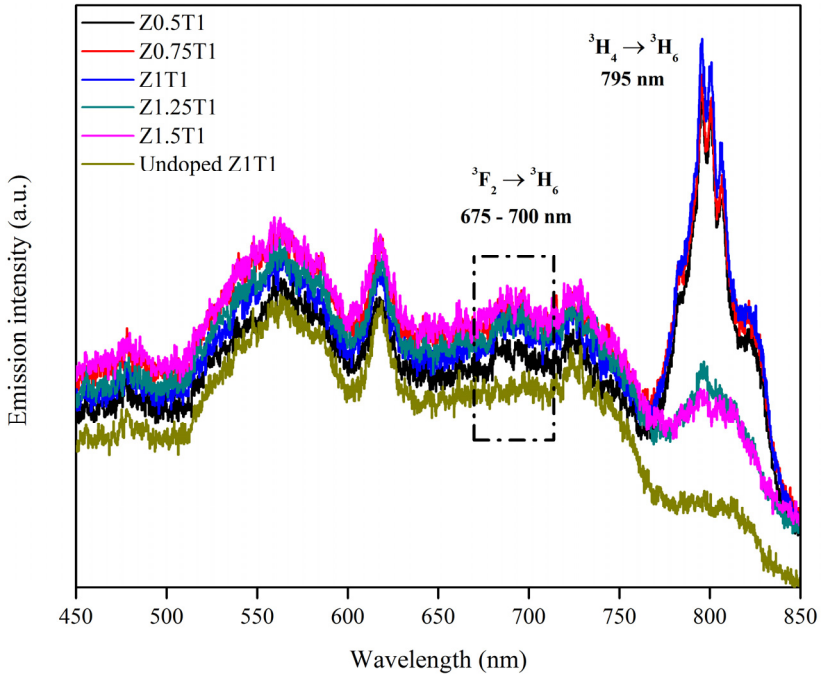

Figure 5.5. UC emission spectra of various ZnO/TiO_2 mixing ratios doped with 0.125 mol% Tm^{3+} and 15 mol% Yb^{3+}, and irradiated with a 980-nm 165 mW laser. Reproduced with permission from Kobwittaya *et al.*, *Vacuum*, **148** (2018) 286-295. Copyright (2017) Elsevier Ltd.

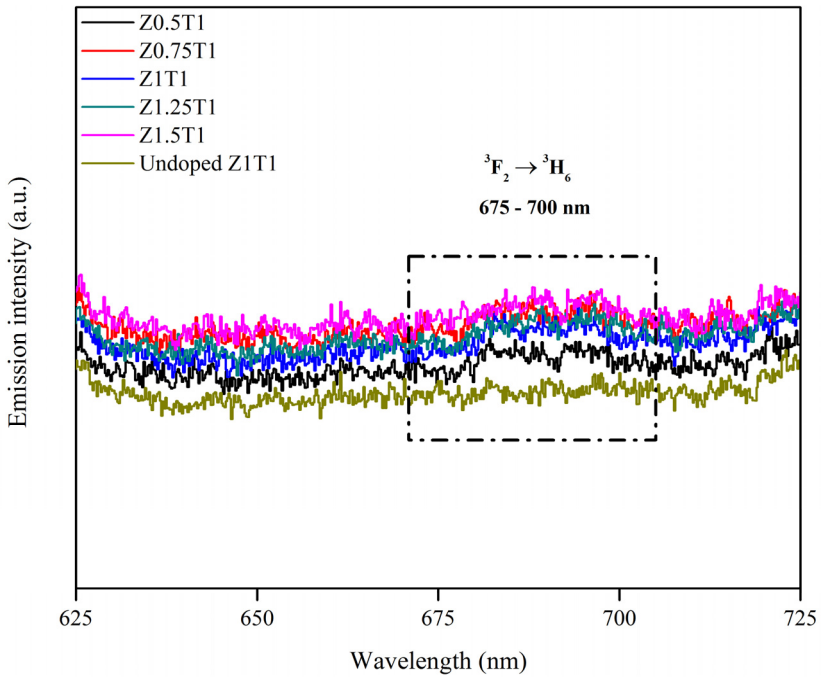

Figure 5.6. The magnified UC emission spectra of Figure 5.5, focusing on the ambiguous red emission region located around 675-700 nm wavelengths. Reproduced with permission from Kobwittaya *et al*., *Vacuum*, **148** (2018) 286-295. Copyright (2017) Elsevier Ltd.

As shown in Figure 5.7, it was clear that the samples that contained RE^{3+} ions showed very weak red emission and their color was a little bit brighter than that of the sample without RE^{3+} ions. This phenomenon will be discussed later by considering UC mechanism. Due to the apparent NIR emission peak and indistinct red emission peak, the following explanations about the effect of ZnO/TiO_2 mixing ratio on UCL will be explained based on the NIR emission only.

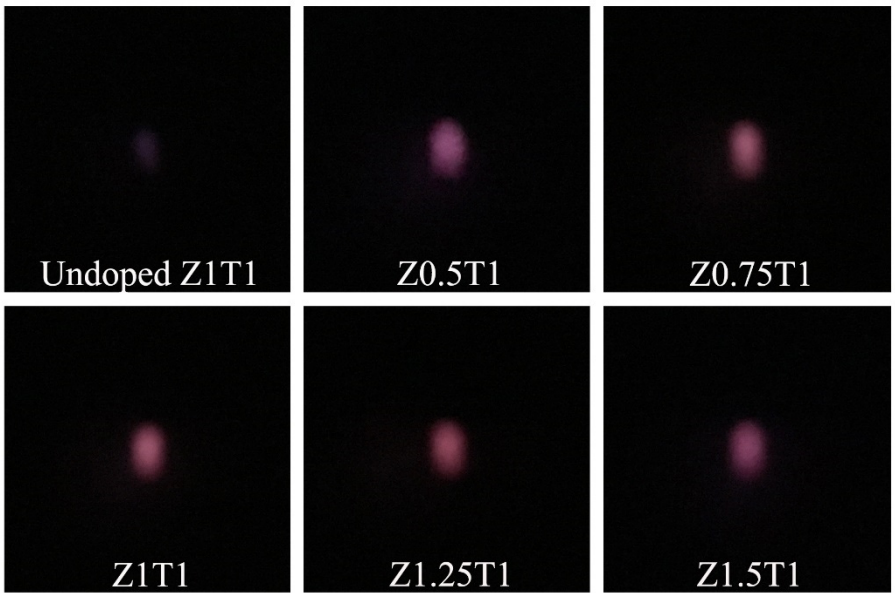

Figure 5.7. UC emission color of undoped ZnO:TiO_2 = 1:1 (in mole), and various ZnO/TiO_2 mixing ratios doped with 0.125 mol% Tm^{3+} and 15 mol% Yb^{3+}, and irradiated with a 980-nm 165 mW laser. Reproduced with permission from Kobwittaya *et al*., *Vacuum*, **148** (2018) 286-295. Copyright (2017) Elsevier Ltd.

The effect of *x*-value on the maximum NIR emission intensity (at 795 nm wavelength) of the products is shown in Figure 5.8. This behavior can be separated into two parts. In the lower *x*-value ($x \leq 1$), with increase of ZnO amount up to $x = 1$, the emission intensity gradually increased. Further increasing ZnO amount at higher *x*-value ($x > 1$), the emission intensity dramatically decreased. Hence, the optimum ZnO/TiO_2 mixing ratio is ZnO:TiO_2 = 1:1 (in mole). To understand the dependent emission intensity on various ZnO/TiO_2 mixing ratios, the relative phase contents (Figure 5.3) were used to explain these phenomena. When the emission intensity increased (ZnO amount x = 0.5-1), the system consisted of four phases; Zn_2TiO_4, TiO_2, $RE_2Ti_2O_7$, and RE_2TiO_5. Subsequently, when the emission intensity primarily decreased and had a sharp inclination ($1 < x \leq 1.25$), Zn_2TiO_4, $RE_2Ti_2O_7$, and RE_2TiO_5 phases were observed without TiO_2 phase. With higher ZnO amount ($1.25 < x \leq 1.5$), the emission intensity continuously decreased, and the system comprised of only two phases; Zn_2TiO_4 and $RE_2Ti_2O_7$. With these three sections of ZnO amount, the difference is the available of TiO_2 phase, whose solubility into Zn_2TiO_4 crystal matrix may affect the UC emission intensity.

Therefore, the strongest NIR emission is obtained by the Tm^{3+} transitions in the mixed phases system, containing Zn_2TiO_4, TiO_2, $RE_2Ti_2O_7$, and RE_2TiO_5 phases.

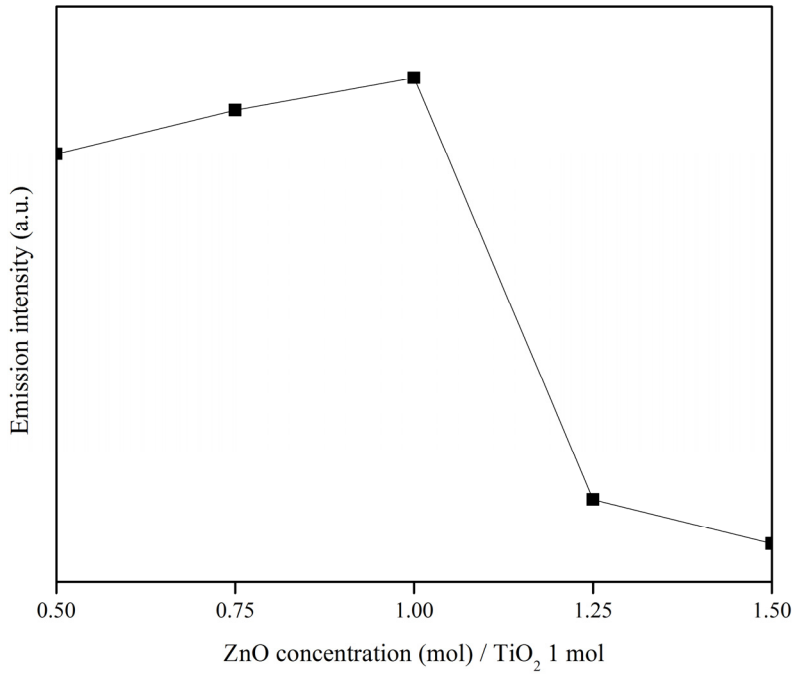

Figure 5.8. The NIR (795 nm) emission intensity versus various ZnO/TiO_2 mixing ratios according to the details in Figure 5.5. Reproduced with permission from Kobwittaya *et al*., *Vacuum*, **148** (2018) 286-295. Copyright (2017) Elsevier Ltd.

5.3.3 Site preference of Tm^{3+} and Yb^{3+} in Zn_2TiO_4 crystal structure

According to the discussion about this topic in Chapter III, section 3.3.8, in this chapter, the explanation will be started by the calculation of lattice constant and lattice volume. The crystallographic data of Zn_2TiO_4; lattice constant and lattice volume, according to various ZnO/TiO_2 mixing ratios doped with 0.125 mol% Tm^{3+} and 15 mol% Yb^{3+} are shown in Table 5.1.

Table 5.1. The crystallographic data of Zn_2TiO_4; lattice constant and lattice volume of various ZnO/TiO_2 mixing ratios doped with 0.125 mol% Tm^{3+} and 15 mol% Yb^{3+}. Reproduced with permission from Kobwittaya *et al*., *Vacuum*, **148** (2018) 286-295. Copyright (2017) Elsevier Ltd.

Sample	Lattice constant (Å)	Lattice volume (Å^3)
Zn_2TiO_4 (JCPDS 25-1164)	8.4602	605.54
Z 0.5 T 1	8.4384	600.87
Z 0.75 T 1	8.4352	600.18
Z 1 T 1	8.4329	599.70
Z 1.25 T 1	8.4390	600.99
Z 1.5 T 1	8.4424	601.72

Taking into account Zn_2TiO_4 unit cell volume in Table 5.1 and the dependent lattice volumes on various ZnO/TiO_2 mixing ratios in Figure 5.9, they showed the identical behavior as described in the case of $ZnO\text{-}TiO_2$: Er^{3+}/Yb^{3+} (Chapter III, section 3.3.8) and $ZnO\text{-}TiO_2$: Ho^{3+}/Yb^{3+} (Chapter IV, section 4.3.6). Also, the effect of lattice volume on emission intensity (Figure 5.10) confirmed that the introduction of RE^{3+} ions into the Zn_2TiO_4 crystal is not equal in each sample, resulting in the change in Zn_2TiO_4 lattice volume and influencing to the variation of emission intensity. With these outcomes which are same as the obtained results of $ZnO\text{-}TiO_2$: Er^{3+}/Yb^{3+} (Chapter III, section 3.3.8) and $ZnO\text{-}TiO_2$: Ho^{3+}/Yb^{3+} (Chapter IV, section 4.3.6), therefore, the site preference of Tm^{3+} and Yb^{3+} in Zn_2TiO_4 crystal can be written as follows:

$$Tm_2O_3 + 4TiO_2 \rightarrow 2Tm^{\cdot}_{Zn(oct)} + \frac{3}{2}O_{2(g)} + 6e' + 2Ti^{\cdot\cdot}_{Zn(oct)} + 2Ti_{Ti(oct)} + 8O^{x}_{o} \quad (5.2)$$

$$Yb_2O_3 + 4TiO_2 \rightarrow 2Yb^{\cdot}_{Zn(oct)} + \frac{3}{2}O_{2(g)} + 6e' + 2Ti^{\cdot\cdot}_{Zn(oct)} + 2Ti_{Ti(oct)} + 8O^{x}_{o} \quad (5.3)$$

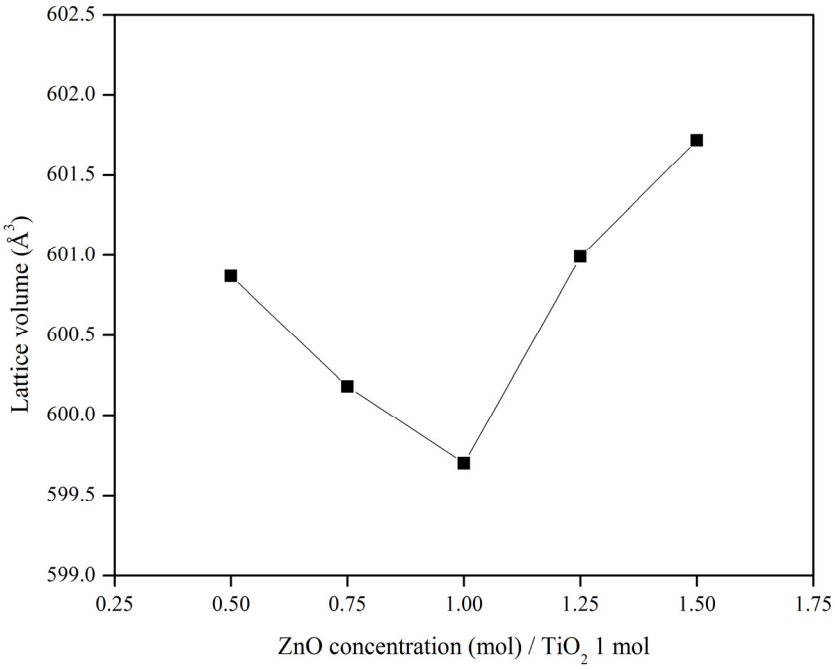

Figure 5.9. The dependent lattice volumes of Zn_2TiO_4 crystal on various ZnO/TiO_2 mixing ratios doped with 0.125 mol% Tm^{3+} and 15 mol% Yb^{3+}.

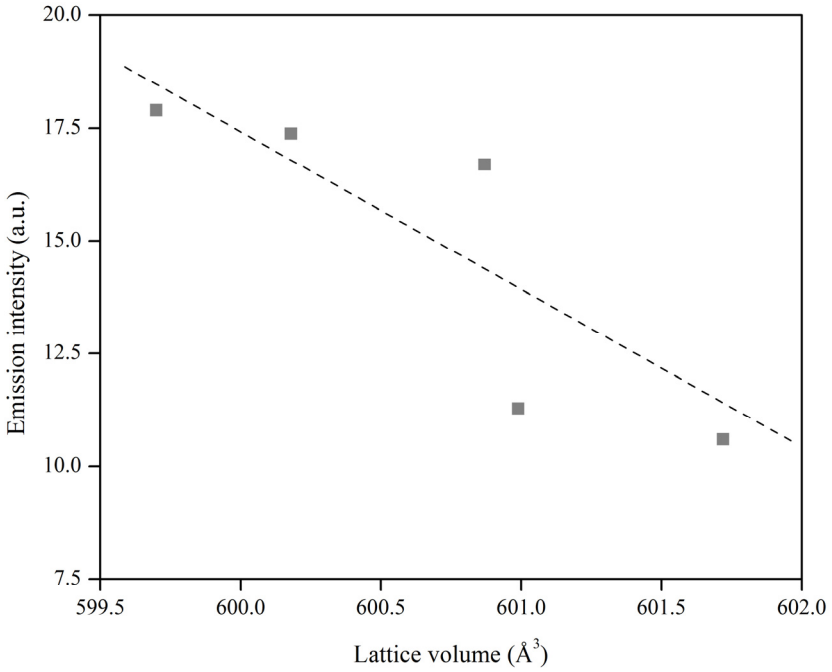

Figure 5.10. The NIR (795 nm) emission intensity of various ZnO/TiO_2 mixing ratios doped with 0.125 mol% Tm^{3+} and 15 mol% Yb^{3+} versus various lattice volumes of Zn_2TiO_4 crystal according to the details in Figure 5.5 and Table 5.1.

5.3.4. Effect of Tm^{3+} and Yb^{3+} concentrations on upconversion luminescence (UCL)

Figure 5.11 and 5.12 present the effect of various Tm^{3+} concentrations, while keeping 15 mol% Yb^{3+} concentration on the Z1T1 sample. As increasing Tm^{3+} concentration up to 0.125 mol%, the emission intensity increased because the Tm^{3+} activator concentration in the Zn_2TiO_4 crystal augmented. Further increase of Tm^{3+} concentration over 0.125 mol%, the emission intensity decreased because of concentration quenching.

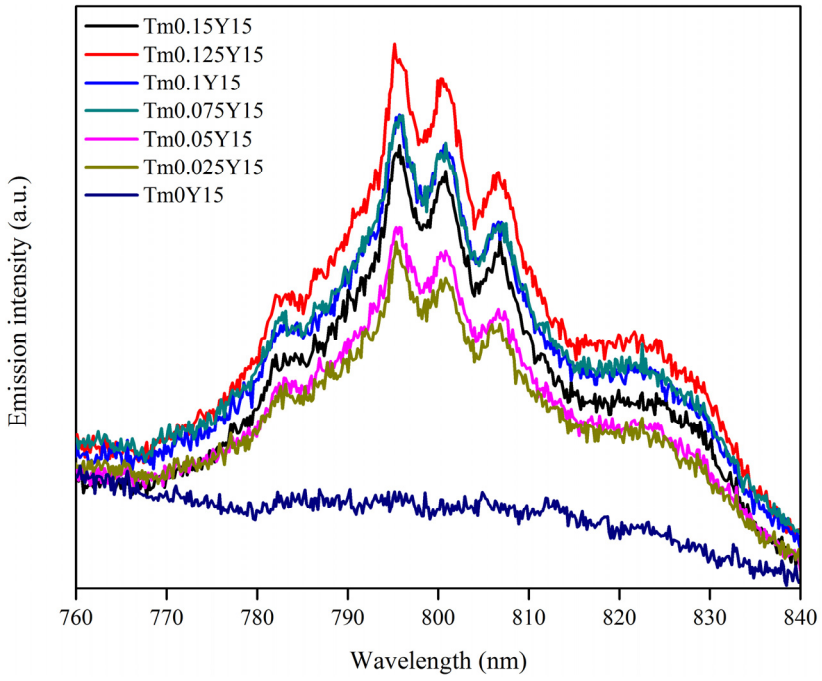

Figure 5.11. UC emission spectra of ZnO:TiO_2 = 1:1 (in mole) doped with various mol% Tm^{3+} and 15 mol% Yb^{3+}, and irradiated with a 980-nm 165 mW laser. Reproduced with permission from Kobwittaya *et al*., *Vacuum*, **148** (2018) 286-295. Copyright (2017) Elsevier Ltd.

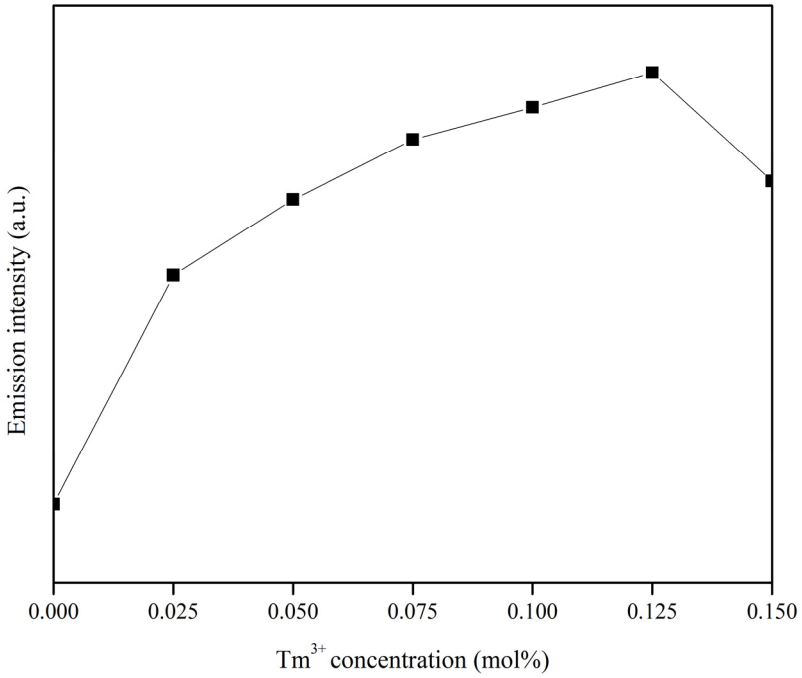

Figure 5.12. The dependence of NIR (795 nm) emission intensity in Figure 5.11 on various Tm^{3+} concentrations. Reproduced with permission from Kobwittaya *et al*., *Vacuum*, **148** (2018) 286-295. Copyright (2017) Elsevier Ltd.

Figure 5.13 and 5.14 demonstrate the effect of various Yb^{3+} concentrations, while keeping 0.125 mol% Tm^{3+} concentration on the Z1T1 sample. With increasing Yb^{3+} concentration up to 18 mol%, the emission intensity first increased, and then decreased at the concentration over 15 mol%. The increased emission intensity is viable because of the higher concentration of dissolved Yb^{3+} concentration in the Zn_2TiO_4 phase which increases the number of pump photons and the excited Tm^{3+}. The decreased emission intensity at higher Yb^{3+} concentration is in accordance with concentration quenching.

Considering the quenching process, this effect could be described by the energy transfer between the two nearest neighbor dopant ions, either activator-activator or sensitizer-activator. As increasing dopant concentration, the distance between two ions is shortened, leading to the energy losses by the non-radiative energy transfers such as exchange energy process and multi-phonon relaxation. Hence, the optimum Tm^{3+} and Yb^{3+} concentrations for generating strongest NIR emission are 0.125 and 15 mol%, respectively. Moreover, it is clear that the NIR emission intensity produced by ZnO-TiO_2: Tm^{3+}/Yb^{3+} phosphor relies mainly on the amount of Yb^{3+} in

the Zn_2TiO_4 host matrix more than that of Tm^{3+} which may have little effect on the NIR emission intensity.

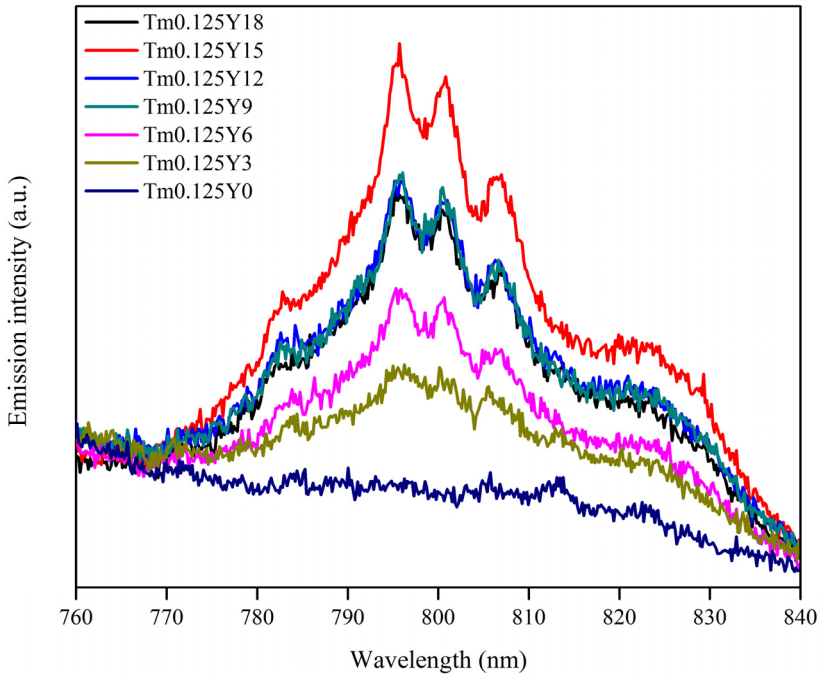

Figure 5.13. UC emission spectra of ZnO:TiO_2 = 1:1 (in mole) doped with 0.125 mol% Tm^{3+} and various mol% Yb^{3+}, and irradiated with a 980-nm 165 mW laser. Reproduced with permission from Kobwittaya *et al*., *Vacuum*, **148** (2018) 286-295. Copyright (2017) Elsevier Ltd.

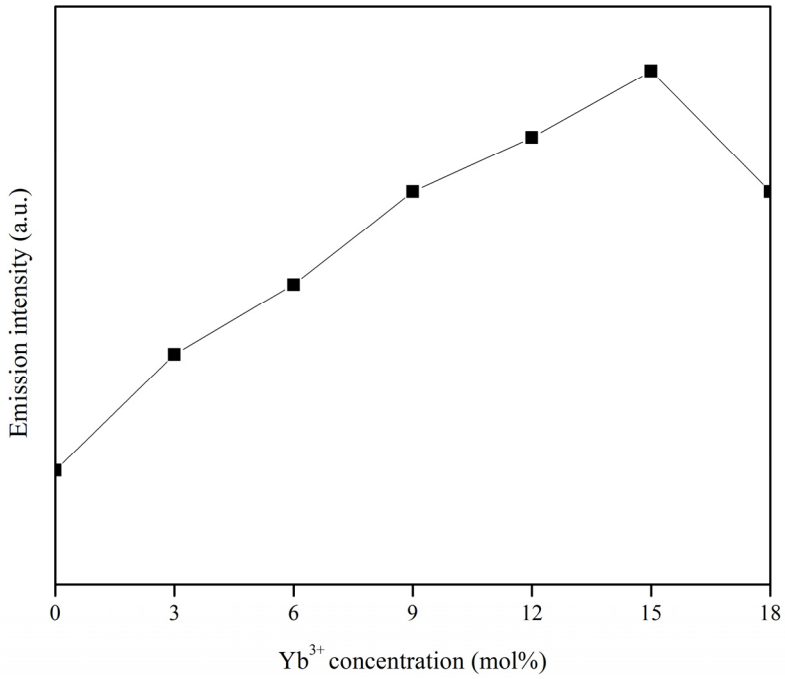

Figure 5.14. The dependence of NIR (795 nm) emission intensity in Figure 5.13 on various Yb^{3+} concentrations. Reproduced with permission from Kobwittaya *et al*., *Vacuum*, **148** (2018) 286-295. Copyright (2017) Elsevier Ltd.

Nevertheless, the optimum concentration of Tm^{3+} was relatively low, therefore, the incorporation of Tm^{3+} including Yb^{3+} into Zn_2TiO_4 host matrix is the noteworthy point. This can be simply proved and clarified by considering the XRD patterns of controlled variables based on the best condition for generating strongest NIR emission, comprising of undoped Z1T1, 0.125 mol% Tm^{3+} doped Z1T1, 15 mol% Yb^{3+} doped Z1T1, and 0.125 mol% Tm^{3+}/15 mol% Yb^{3+} co-doped Z1T1. As shown in Figure 5.15(a), the result showed that when the system consisted of single dopant, $RE_2Ti_2O_7$ and RE_2TiO_5 phases appeared. So, a certain amount of Tm^{3+} and Yb^{3+} exists in the form of RE titanate compounds, even if the system had very low amount of RE^{3+}. Besides, the XRD peaks were found to shift to higher angle with increasing RE^{3+} concentration. As shown in Figure 5.15(b), the expanded XRD patterns of Figure 5.15(a) around $2\theta = 35.2°$ (main peak position of Zn_2TiO_4 phase) showed the single peak with a shift toward higher angles. The shift establishes the substitution effects and indicates a structural modification due to the lattice distortion caused by the dopants. Therefore, both Tm^{3+} and Yb^{3+} assuredly get into the lattice of Zn_2TiO_4 phase, even if the optimum Tm^{3+} concentration was very low.

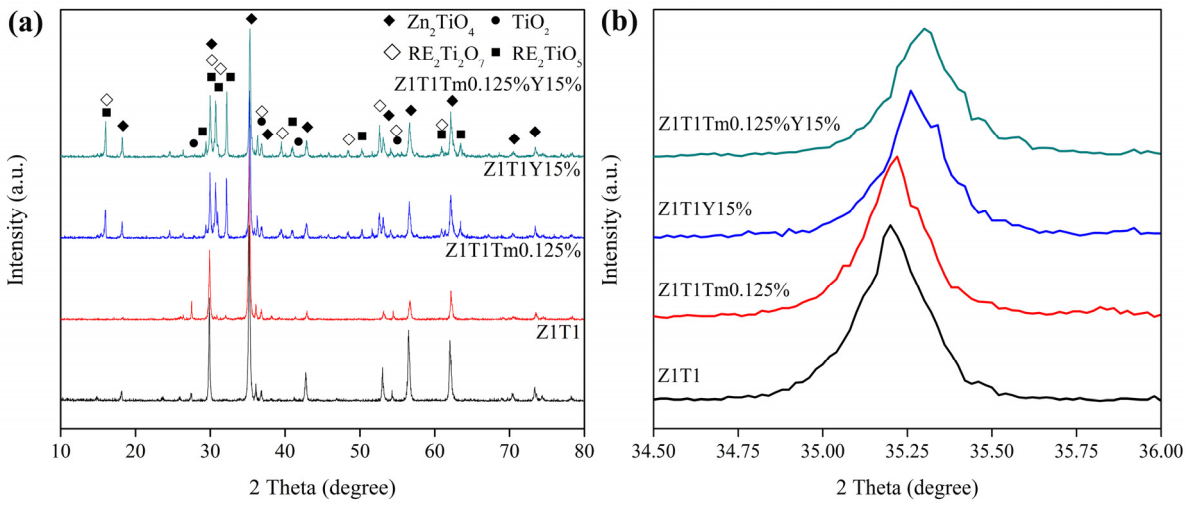

Figure 5.15. (a) XRD patterns of various controlled variables, and (b) the magnified XRD patterns of (a) around 2θ = 35.2°. Reproduced with permission from Kobwittaya *et al*., *Vacuum*, **148** (2018) 286-295. Copyright (2017) Elsevier Ltd.

5.3.5. Upconversion (UC) mechanism

To understand the UC mechanism, it is well-known that, in the unsaturated UC processes, the number of photons which is required to populate the upper emitting state can be obtained by simple relationship, $I \propto P^n$, where I is the UCL intensity, P is pump laser power, and n is the number of the pumped photons per the emitted photon [26]. As shown in Figure 5.16, the result indicated that the slope was 1.01 for NIR emission under between P = 15-196 mW. Typically, the experimental n-value is in the specific range of values and less than the maximum theoretical n-value for each possible UC mechanism; two-photon process ($1 < n \leq 2$) or three-photon process ($2 < n \leq 3$), because of the saturation effect in the UCL intensity mainly caused by the competition between linear decay and UC processes for the depletion of the intermediate excited states [27,28]. Thus, it may suggest that the two-photon process is responsible for NIR emission from ZnO-TiO_2: Tm^{3+}/Yb^{3+} phosphor.

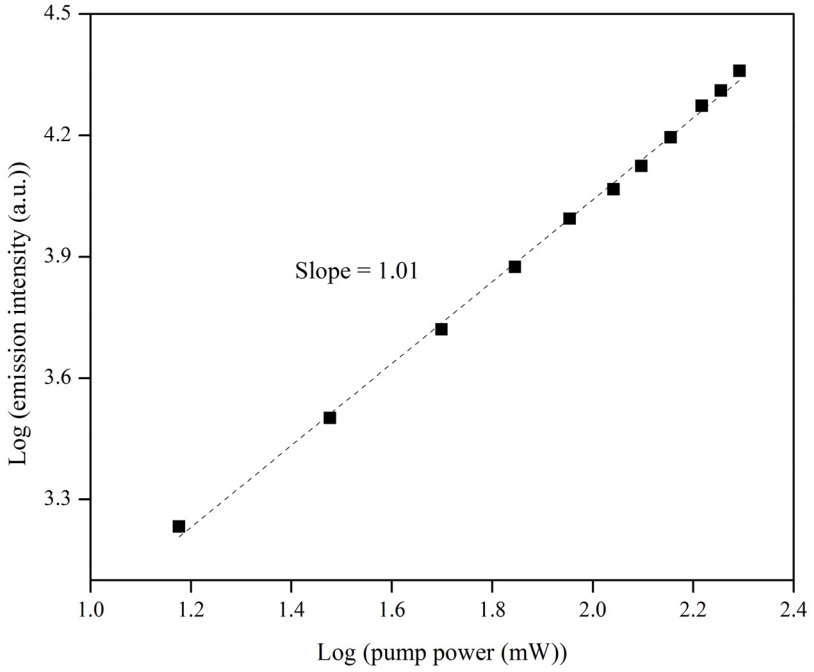

Figure 5.16. Pump power dependent UC of ZnO:TiO_2 = 1:1 (in mole) doped with 0.125 mol% Tm^{3+} and 15 mol% Yb^{3+}, and irradiated with a 980-nm, 15-196 mW laser. Reproduced with permission from Kobwittaya *et al*., *Vacuum*, **148** (2018) 286-295. Copyright (2017) Elsevier Ltd.

According to the result mentioned above, the UC mechanism of ZnO-TiO_2: Tm^{3+}/Yb^{3+} system is proposed and illustrated in Figure 5.17. Under a 980-nm laser excitation, the $^2F_{7/2}$ level of Yb^{3+} and $^3H_6$ level of Tm^{3+} are excited to $^2F_{5/2}$ and $^3H_5$ levels, respectively, by the ground state absorption (GSA) process. Later, the energy in $^2F_{5/2}$ level of Yb^{3+} relaxes back in the form of non- nonradiative transition (NR) to the ground state $^2F_{7/2}$ level due to the excess energy which is in accordance with lattice vibrations of the host material. Take into account the long lifetime of the excited $^2F_{5/2}$ level of Yb^{3+} (typically one millisecond), Yb^{3+} may well transfer the excitation energy (as expressed as ET) to Tm^{3+} with higher probability than decaying the excited energy to its ground state [29]. Thus, the energy is transferred via energy transfer 1 (ET1) to the adjacent Tm^{3+}, leading to the population of $^3H_5$ level of Tm^{3+}. Subsequent $^3H_5 \rightarrow {}^3F_4$ transition can be induced by NR. Through the excited state absorption (ESA) and ET2, the $^3F_4$ level is promoted to $^3F_2$ level. At this state, $^3F_2$ level generates energy in metastable $^3H_4$ level via NR and some part of energy in $^3F_2$ level relaxes back to the ground state of Tm^{3+} via $^3F_2 \rightarrow$

$^3H_6$ transition, resulting in the weak red emission. After that, the NIR emission takes place through the $^3H_4 \rightarrow {}^3H_6$ transition of Tm^{3+} around 795 nm wavelength.

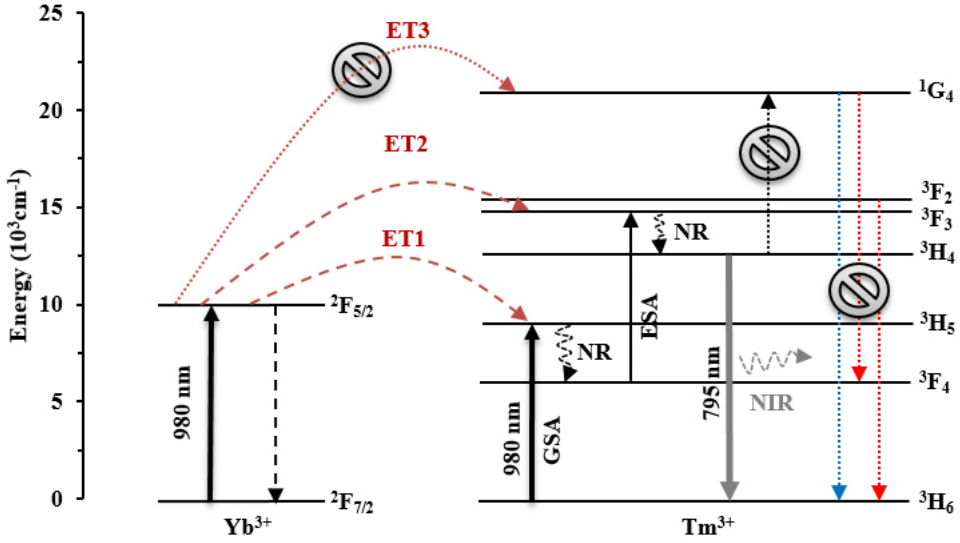

Figure 5.17. Energy level diagram illustrating the proposed energy transfer mechanisms of ZnO-TiO_2 doped with 0.125 mol% Tm^{3+} and 15 mol% Yb^{3+} under a 980-nm laser excitation. Reproduced with permission from Kobwittaya *et al*., *Vacuum*, **148** (2018) 286-295. Copyright (2017) Elsevier Ltd.

Focusing on the energy transfer and observed emissions in this implied UC mechanism, it should be suggested that the $Yb^{3+} \rightarrow Tm^{3+}$ transition in Zn_2TiO_4 host is non-resonant with the involvement of phonon-assisted energy transfer because the energy mismatches between the transitions within Yb^{3+} ($^2F_{7/2} \rightarrow {}^2F_{5/2}$) and Tm^{3+} ($^3H_6 \rightarrow {}^3H_5$ and $^3F_4 \rightarrow {}^3F_2$) may require much number of phonons for the latter that the electrons in $^3H_4$ level are more likely to reincorporate with electron acceptors by emitting NIR emission, rather than being recombined in $^3F_2$ level to emit stronger red emission or further provoked into higher excited state ($^1G_4$ level) to generate additional visible emission (blue and more stronger red) [30,31]. For this reason, it would be indicated that the third energy transfer (ET3) from Yb^{3+}/Tm^{3+} is effectively prevented, leading to the lack of blue and strong red emissions (STOP symbol (⃠)). Therefore, it is worth noting that the restriction of ET3 and the mechanism between ET2+ESA and $^3F_2$,$^3F_3$ levels of Tm^{3+} is the keystone for fabricating the pure NIR UCL materials. According to the *n*-value which is 1.01, this could be ascribed to the competition between linear decay and UC processes at the

intermediate excited states $^3F_4$ of Tm^{3+}. The UC process and linear decay at this excited state are $^3F_4 \rightarrow {}^3F_2$ and $^3F_4 \rightarrow {}^3H_6$, respectively. Because of the *n*-value that is approximately one for the NIR emission, therefore, the UC process (ESA) is the dominant depletion mechanism which causes the saturation effect in UCL intensity and the decrease in *n*-value.

5.3.6. Comparison of ZnO-TiO_2 composite UC phosphors prepared by various methods

According to various methods used for preparing ZnO-TiO_2 composite UC phosphors, there are only three methods, including in this study; solid-state reaction (SSR) [13,14], metal-organic decomposition (MOD) [15-17], and powder-solution mixing (PSM). Considering the physical characteristics of final products prepared by these methods, the MOD presents the products in the form of thin films coated on substrate, while the SSR and PSM show the products in the form of pellet and powder. In the case of final firing temperature and firing time used in these methods, the final products are obtained under different conditions, 1200 °C 4 h (SSR), 1000 °C 4 h (MOD), and 1300 °C 1 h (PSM). Even though the physical characteristics of the final products, operating temperature, and reaction time on the synthesis related to these methods are diverse, but they show the same optimum ZnO/TiO_2 mixing ratio = 1:1 (in mole). Additionally, they demonstrate the highest UC emission intensity in the same state that is under multiple phases cooccurrence, for example the products prepared by SSR and MOD exhibit the strongest UC emission intensity under the coexistence of Zn_2TiO_4, rutile TiO_2, $RE_2Ti_2O_7$ phases.

After reviewing these preparation methods, it is clearly observed that there are some disadvantages needed to be improved to obtain higher efficiency of the ZnO-TiO_2 composite UC phosphors. Concerning the drawbacks of each method that influence the effectiveness of UC phosphor, the products prepared by SSR would be incompletely formed because of the diffusion limited, causing to the incomplete reaction, some loss of reactants, and compositional inhomogeneity of the product [8]. For the MOD including general film deposition methods, there are many criteria needed to be controlled, for example deposition rate, film uniformity, quality of film, and type of substrate [32,33], leading to a much wider variation in performance of UC phosphor thin films before obtaining the excellent one. In the case of PSM, the obvious disadvantage is the agglomeration of particles which is the limitation of nanosized materials production. Nevertheless, PSM method is the new method that is first proposed in this study. At this stage, the good points for this new method are the use of water as solvent which offers

simple operation and high efficiency in reactions, possible to obtain the homogenous product, easily understandable method because of a few simple steps, and cost and energy savings due to low cost reactants and shorter preparation time. With these advantages, therefore, the powder-solution mixing method might be one of the appropriate techniques for the fabrication of efficient UC phosphors.

5.4 Conclusion

Tm^{3+}/Yb^{3+} co-doped ZnO-TiO_2 composite UC phosphor was successfully synthesized by the new simple method, powder-solution mixing method. Under a 980-nm laser excitation, the UC spectra demonstrated two emissions, dominant NIR emission centered at 795 nm wavelength in accordance with the $^3H_4 \rightarrow {}^3H_6$ transition of Tm^{3+} and very weak red emission located at around 675-750 nm wavelengths corresponding to $^3F_2 \rightarrow {}^3H_6$ transition of Tm^{3+}. In the case of very weak red emission and its ambiguous emission spectra which it seemed that the red emission did not exist, therefore, it could be summarized that this system exhibited nearly pure NIR emission. The dependence of NIR emission intensity on various pump power from 15-196 mW showed that two-photon process was responsible for NIR emission from ZnO-TiO_2: Tm^{3+}/Yb^{3+} phosphor. The optimum ZnO/TiO_2 mixing ratio was ZnO:TiO_2 = 1:1 (in mole). The NIR emission intensity reached a maximum value for the sample that contained 0.125 mol% Tm^{3+} and 15 mol% Yb^{3+}. Strongest NIR emission intensity of ZnO-TiO_2 composite doped with Tm^{3+} and Yb^{3+} was observed from the product with multiple phases, comprising of Zn_2TiO_4, TiO_2, $RE_2Ti_2O_7$, and RE_2TiO_5 (RE = Tm^{3+} and/or Yb^{3+}).

In the case of site preference of Tm^{3+} and Yb^{3+} in the Zn_2TiO_4 crystal structure, the most possibility of site preference should take place at the vacant Zn site in octahedral ($V''_{Zn(oct)}$) that would appear when the remaining TiO_2 and RE^{3+} ions are introduced into Zn_2TiO_4 crystal matrix. This possibility is confirmed by considering the changes in the unit cell parameter of host material. These changes occur because the amount of RE^{3+} ions that enters Zn_2TiO_4 crystal matrix is not equal in each sample due to the dissimilar number of $V''_{Zn(oct)}$ caused by the different ZnO/TiO_2 mixing ratios and remaining TiO_2, resulting in the varying of lattice constant, lattice volume, including the variation of emission intensity. Based on the results in this study, the benefit experienced from these results is that ZnO-TiO_2 composite doped with

Tm^{3+} and Yb^{3+} has the potential to be an ideal UC phosphor for emitting pure NIR emission which is the considerable radiation used in biomedical imaging for diagnostics.

5.5 Acknowledgements

This section contains contributions from co-authors and was published in: K. Kobwittaya, Y. Oishi, T. Torikai, M. Yada, T. Watari, H.N. Luitel, Nearly pure NIR to NIR upconversion luminescence in Tm^{3+}, Yb^{3+} co-doped ZnO-TiO_2 composite phosphor powder, *Vacuum*, **148** (2018) 286-295.

5.6 Copyright permission

References

[1] X. Liu, Z. Ye, W. Wei, Y. Du, J. Yuan, D. Ma, *Chem. Commun.*, **47** (2011) 8139-8141.

[2] R. Wang, F. Zhang, *J. Mater. Chem. B*, **2** (2014) 2422-2443.

[3] Y. Mita, M. Togashi, Y. Umetsu, H. Yamamoto, *Jpn. J. Appl. Phys.*, **40** (2001) 5925-5929.

[4] T.P. Mokoena, E.C. Linganiso, V. Kumar, H.C. Swart, S.-H. Cho, O.M. Ntwaeaborwa, *J. Colloid Interf. Sci.*, **496** (2017) 87-99.

[5] D. Wu, Z. Hao, W. Xiao, X. Zhang, G.-H. Pan, L. Zhang, Y. Luo, L. Zhang, H. Zhao, J. Zhang, *J. Alloy. Compd.*, **704** (2017) 206-211.

[6] F. Wang, X. Liu, *Chem. Soc. Rev.*, **38** (2009) 976-989.

[7] J. Zhou, Q. Liu, W. Feng, Y. Sun, F. Li, *Chem. Rev.*, **115** (2015) 395-465.

[8] R.-S. Liu, Phosphors, Up conversion Nano Particles, Quantum Dots and Their Applications (Volume 2), Springer Science+Business Media Singapore, Singapore (2016).

[9] H. Huang, H. Zhou, J. Zhou, T. Wang, D. Huang, Y. Wu, L. Sun, G. Zhou, J. Zhan, J. Hu, *RSC Adv.*, **7** (2017) 16777-16786.

[10] K.K. Kar, Composite Materials: Processing, Applications, Characterizations, Springer-Verlag Berlin Heidelberg (2017).

[11] L. Li, Y. Fan, D. Wang, G. Feng, D. Xu, *Cryst. Res. Technol.*, **46** (2011) 475-479.

[12] L. Li, F. Li, T. Cui, Q. Zhou, D. Xu, *Phys. Status Solidi A*, **209** (2012) 2596-2599.
[13] H.N. Luitel, K. Ikeue, R. Okuda, R. Chand, T. Torikai, M. Yada, T. Watari, *Opt. Mater.*, **36** (2014) 591-595.
[14] K. Ohyama, T. Nonaka, T. Kanamori, S.-I. Yamamoto, 22nd International Workshop on Active-Matrix Flatpanel Displays and Devices (AM-FPD) (2015) 89-90.
[15] S.-I. Yamamoto, K. Ohyama, T. Nonaka, T. Kanamori, 21st International Workshop on Active-Matrix Flatpanel Displays and Devices (AM-FPD) (2014) 271-272.
[16] T. Nonaka, T. Kanamori, K. Ohyama, S.-I. Yamamoto, *Jpn. J. Appl. Phys.*, **54** (2015) 03CA02.
[17] T. Nonaka, S.-I. Yamamoto, *T. MRS Jap.*, **42** (2017) 57-60.
[18] Y. Xu, M. Yamazaki, P. Villars, *Jpn. J. Appl. Phys.*, **50** (2011) 11RH02.
[19] L.G. Shcherbakova, A.V. Kolesnikov, O.N. Breusov, *Inorg. Chem.*, **15** (1979) 1724-1729.
[20] E.M. Levin, C.R. Robbins, H.F. McMurdie, Phase Diagram for Chemists Volume I (Figures 1-2066), The American Ceramic Society, Inc., Columbus, Ohio (1964).
[21] B.A.A. Balboul, *Thermochim. Acta*, **351** (2000) 55-60.
[22] B.A.A.A. Balboul, *Powder Technol.*, **107** (2000) 168-174.
[23] B.A.A. Balboul, *Thermochim. Acta*, **419** (2004) 173-179.
[24] A. Jain, G. Hautier, S.P. Ong, C.J. Moore, C.C. Fischer, K.A. Persson, G. Ceder, *Phys. Rev. B*, **84** (2011) 045115.
[25] H.T. Kim, Y. Kim, M. Valant, D. Suvorov, *J. Am. Ceram. Soc.*, **84** (2001) 1081-1086.
[26] F. Auzel, *Chem. Rev.*, **104** (2004) 139-174.
[27] M. Pollnau, D.R. Gamelin, S.R. Lüthi, H.U. Güdel, M.P. Hehlen, *Phys. Rev. B*, **61** (2000) 3337-3346.
[28] J.F. Suyver, A. Aebischer, S. García-Revilla, P. Gerner, H.U. Güdel, *Phys. Rev. B*, **71** (2005) 125123.
[29] I. Hyppänen, J. Hölsä, J. Kankare, M. Lastusaari, L. Pihlgren, *J. Nanomater.*, **Article ID 16391** (2007) 1-8.
[30] Z. Wang, Y. Li, Q. Jiang, H. Zeng, Z. Ci, L. Sun, *J. Mater. Chem. C*, **2** (2014) 4495-4501.
[31] X. Xue, M. Thitsa, T. Cheng, W. Gao, D. Deng, T. Suzuki, Y. Ohishi, *Opt. Express*, **24** (2016) 26307-26321.
[32] M. Serényi, T. Lohner, G. Sáfrán, J. Szívós, *Vacuum*, **128** (2016) 213-218.

[33] Y. Ando, D. Kindole, Y. Noda, R.N. Mbiu, B.K. Kosgey, S.M. Maranga, A. Kobayashi, *Vacuum*, **136** (2017) 203-208.

Chapter VI

Conclusion and Recommendations for future work

6.1 Summary of the results

The core objective of the research presented in this dissertation was the synthesis and characterizations of rare earth elements doped ZnO-TiO_2 composite based upconversion (UC) phosphor using solid-state reaction method and a new proposed method, namely powder-solution mixing method to develop novel efficient UC phosphors and to improve the luminescence properties for various practical applications. The considerable results of the present study are summarized as follows.

At first, the Ho^{3+} and Yb^{3+} co-doped ZnO-TiO_2 composite prepared by solid-state reaction method was successfully synthesized. Under a 980-nm laser excitation, the most efficient product exhibited green color which was in accordance with the UC emission spectra peaks centered at 542 and 670 nm wavelengths from the $^5F_4$, $^5S_2 \rightarrow {}^5I_8$ and $^5F_5 \rightarrow {}^5I_8$ transitions of Ho^{3+}. The optimum condition for obtaining the brightest green UC emission was ZnO:TiO_2 = 1:1 (in mole) doped with 0.05 mol% Ho^{3+}, 9 mol% Yb^{3+} fired at 1200 °C for 4 h. Additionally, this brightest green UC emission occurred when the system consisted of mixed phases, Zn_2TiO_4, TiO_2, $RE_2Ti_2O_7$, and RE_2TiO_5 (RE = Ho^{3+} and/or Yb^{3+}). Pump power dependent UC revealed that two-photon process was responsible for this UC system.

Later, ZnO-TiO_2 composite doped with three pairs of rare earth ions (Er^{3+}/Yb^{3+}, Ho^{3+}/Yb^{3+}, and Tm^{3+}/Yb^{3+}) prepared by a new synthetic method, powder-solution mixing method, was successfully carried out. Under a 980-nm laser excitation, the results of UC luminescence (UCL) measurement of these three systems revealed that, at the strongest UC emission intensity, the products containing Er^{3+}/Yb^{3+}, Ho^{3+}/Yb^{3+}, and Tm^{3+}/Yb^{3+} exhibited bright red, bright green, and nearly pure NIR emissions. Corresponding UCL spectra showed that, for the Er^{3+}/Yb^{3+} system, there were two emission bands detected, weak green band centered at 544 and 559 nm wavelengths, and strong red band centered at 657 and 675 nm wavelengths which

both bands were in accordance with $^2H_{11/2}$, $^4S_{3/2} \rightarrow {}^4I_{15/2}$ and $^4F_{9/2} \rightarrow {}^4I_{15/2}$ transitions of Er^{3+}, respectively. For Ho^{3+}/Yb^{3+} system, the UC emission spectra showed green and red emission bands centered at 538 and 669 nm wavelengths, respectively. These two emission bands occurred due to the $^5F_4$, $^5S_2 \rightarrow {}^5I_8$ and $^5F_5 \rightarrow {}^5I_8$ transitions of Ho^{3+}, respectively. And, for Tm^{3+}/Yb^{3+} system, the UC emission spectra demonstrated two emissions, dominant NIR emission centered at 795 nm wavelength which it was in accordance with the $^3H_4 \rightarrow {}^3H_6$ transition of Tm^{3+} and very weak red emission located at around 675-750 nm wavelengths corresponding to $^3F_2 \rightarrow {}^3H_6$ transition of Tm^{3+}. These results were observed in the samples fired at 1300 °C for 1 h and at the ZnO/TiO_2 mixing ratio of 1:1 (in mole). Also, the XRD results revealed that all efficient samples were under the mixed phases condition, consisting of Zn_2TiO_4, TiO_2, $RE_2Ti_2O_7$, and RE_2TiO_5 (RE is the dopants which can be either one or both, e.g. Er^{3+} and/or Yb^{3+}). For the dopant concentration, the optimum content (at mol%) was 3/9 for Er^{3+}/Yb^{3+}, 0.03/9 for Ho^{3+}/Yb^{3+}, and 0.125/15 for Tm^{3+}/Yb^{3+}. The dependence of UC emission intensity on various excitation pump power (980-nm laser, 15-196 mW laser) indicated that the two-photon process was responsible for these UC systems.

The simple chemical formula equations, for explaining the site preference of rare earth ions in host crystal matrix, were generated by considering the target host crystal structure, its crystal properties, and the effect of dopant ions to its crystal matrix. The results showed that the most possibility of site preference of RE^{3+} ions in the host crystal matrix of Zn_2TiO_4 should be at the vacant Zn site in octahedral ($V''_{Zn(oct)}$) according to the equation below;

$$RE_2O_3 + 4TiO_2 \rightarrow 2RE^{\cdot}_{Zn(oct)} + \frac{3}{2}O_{2(g)} + 6e' + 2Ti^{\cdot\cdot}_{Zn(oct)} + 2Ti_{Ti(oct)} + 8O^{x}_{o}$$

where RE is trivalent rare earth (RE^{3+}) ions used in each system.

This $V''_{Zn(oct)}$ would appear when there were excess TiO_2 in the system (this caused the existence of $V''_{Zn(tet)}$) and followed by the incorporation of RE^{3+} ions into Zn_2TiO_4 matrix (this caused the change in position of Zn^{2+}, moving from octahedral site to $V''_{Zn(tet)}$ because of bigger ionic radii of RE^{3+} ions forcing them). This process is related to the assumption that the RE^{3+} ions go to $V''_{Zn(oct)}$ easier than occupy Zn^{2+} or Ti^{4+} sites, and vacant Zn site in tetrahedral ($V''_{Zn(tet)}$) due to the mismatch ionic radii and electronic charge of RE^{3+} ions, and Zn^{2+} or Ti^{4+} ions, including

inappropriate radius of ($V''_{Zn(tet)}$). Additionally, this proposed site preference equation is also verified by considering A and B-sites of Zn_2TiO_4 crystal structure. The tetrahedral (A-site) corresponds to $2Zn_{Zn}$ due to the $2Zn^{2+}$ from the occurrence of $2V''_{Zn(oct)}$ and octahedral (B-site) conforms to $(2RE^{\cdot}_{Zn} + 2Ti^{\cdot\cdot}_{Zn}) + 2Ti_{Ti}$. Therefore, the possible site preference of RE^{3+} ions in Zn_2TiO_4 matrix is $(Zn_{Zn})_{2(tet)}((RE^{\cdot}_{Zn} + Ti^{\cdot\cdot}_{Zn}) + Ti_{Ti})_{4(oct)}(O^{x}_{o})_8$ that equals to theoretical site AB_2O_4 type of Zn_2TiO_4 crystal structure. Besides, this phenomenon is mostly expressed in the changes in unit cell parameter of Zn_2TiO_4 crystal, which lead to the decrease in its lattice constant and lattice volume.

The changes in unit cell volume of Zn_2TiO_4 host crystal corresponds to the positive charge that occurs when $V''_{Zn(oct)}$ is generated and then substituted by RE^{3+} ions. In the equation, this is in accordance with $2RE^{\cdot}_{Zn(oct)}$. Also, the positive charge in all cation positions is higher than the negative charge of oxygen. So, according to Coulomb force, the positive charge would attract the negative charge, leading to the abatement of Zn_2TiO_4 lattice volume. With this behavior, it can be summarized that the change in Zn_2TiO_4 lattice volume is based on the amount of $V''_{Zn(oct)}$ and RE^{3+} ions incorporated into Zn_2TiO_4 crystal matrix. Hence, it can be indicated that, in the $ZnO\text{-}TiO_2$ doped with rare earth elements, the relation between luminescence emission intensity and lattice volume is reverse variation.

In addition, the phosphors prepared by solid-state reaction (SSR) and powder-solution mixing (PSM) methods were compared by considering the products with the same physical characteristic (pellet (SSR) / pellet (PSM) and powder (SSR) / powder (PSM)) and their UC emission intensity. The results revealed that the emission intensity of PSM sample was more well-distributed over the whole surface than that of SSR sample for both pellet and powder forms. This can be explained as follows. The SSR method provides the direct reaction between the reactants (solid-solid reaction) at high temperature via diffusion process, therefore, the inhomogeneity of the product may take place due to the incomplete mixing of raw materials and the formation process. On the other hand, the PSM method involves various blending steps based on the mixing of nitrate-based compounds, sol solution, and solid particles in deionized water. Due to the use of dopants in the form of solution and the preparation via liquid-phase mixing, the PSM method results in the complete mixing of raw materials and the homogeneity

of raw mixture. For this reason, in the case of PSM sample, the dopants are well-distributed over the raw mixture and they easily get into the host material more than in the case of SSR sample. Hence, higher homogeneity of the product can be obtained.

According to the existed preparation methods used for preparing ZnO-TiO_2 composite UC phosphors, there are only three methods, including in this study; solid-state reaction (SSR), metal-organic decomposition (MOD), and powder-solution mixing (PSM). Considering the physical characteristics of final products prepared by these methods, the MOD presents the products in the form of thin films coated on substrate, while the SSR and PSM show the products in the form of pellet and powder. In the case of final firing temperature and firing time used in these methods, the final products are obtained under different conditions, 1200 °C 4 h (SSR), 1000 °C 4 h (MOD), and 1300 °C 1 h (PSM). Even though the physical characteristics of the final products, operating temperature, and reaction time on the synthesis related to these methods are diverse, but they show the same optimum ZnO/TiO_2 mixing ratio = 1:1 (in mole). Additionally, they demonstrate the highest UC emission intensity in the same state that is under multiple phases cooccurrence, for example the products prepared by SSR and MOD exhibit the strongest UC emission intensity under the coexistence of Zn_2TiO_4, rutile TiO_2, $RE_2Ti_2O_7$ phases.

After reviewing these preparation methods, it is clearly observed that there are some disadvantages needed to be improved to obtain higher efficiency of the ZnO-TiO_2 composite UC phosphors. Concerning the drawbacks of each method that influence the effectiveness of UC phosphor, the products prepared by SSR would be incompletely formed because of the diffusion limited, causing to the incomplete reaction, some loss of reactants, and compositional inhomogeneity of the product. For the MOD including general film deposition methods, there are many criteria needed to be controlled, for example deposition rate, film uniformity, quality of film, and the type of substrates, leading to a much wider variation in performance of UC phosphor thin films before obtaining the excellent one. In the case of PSM, the obvious disadvantage is the agglomeration of particles which is the limitation of nanosized materials production. However, PSM method is the new method that is first proposed in this study. At this stage, the good points for this new method are the use of water as solvent which offers simple operation and high efficiency in reactions, possible to obtain the homogenous product,

easily understandable method because of a few simple steps, and cost and energy savings due to low cost reactants and shorter preparation time. With these advantages and the results summarized previously, therefore, the powder-solution mixing method might be one of the appropriate techniques for the fabrication of efficient UC phosphors.

6.2 Recommendations for future work

The research directions for the future work related to this dissertation are suggested and discussed as follows.

1. To enhance the UCL properties of rare earth elements doped ZnO-TiO_2 composite phosphors, the adding of metal ions such as Li^+, K^+, and B^{3+} may be considered as co-dopant, working together with sensitizer-activator pairs of ions.
2. To complete the RGB (Red, Green, Blue) color model of ZnO-TiO_2 composite UC phosphor, the blue emission color exhibited by this phosphor is necessary to be investigated by exploring the decent dopants.
3. The 980-nm laser excitation used in this study provides continuous waveform. So, the other types of waveform such as pulse wave and ultra-pulse wave may be examined.
4. Color-tunable UCL from rare earth elements tri-doped ZnO-TiO_2 composite may be investigated.
5. To overcome the limitation of powder-solution mixing method that the nanosized product cannot be obtained, the development of this preparation method should be considered.
6. The ZnO-TiO_2 composite phosphor prepared by other techniques especially the methods that can produce nanosized products may be studied.

Appendix A

Refined crystallographic parameters
(Rietveld refinement)

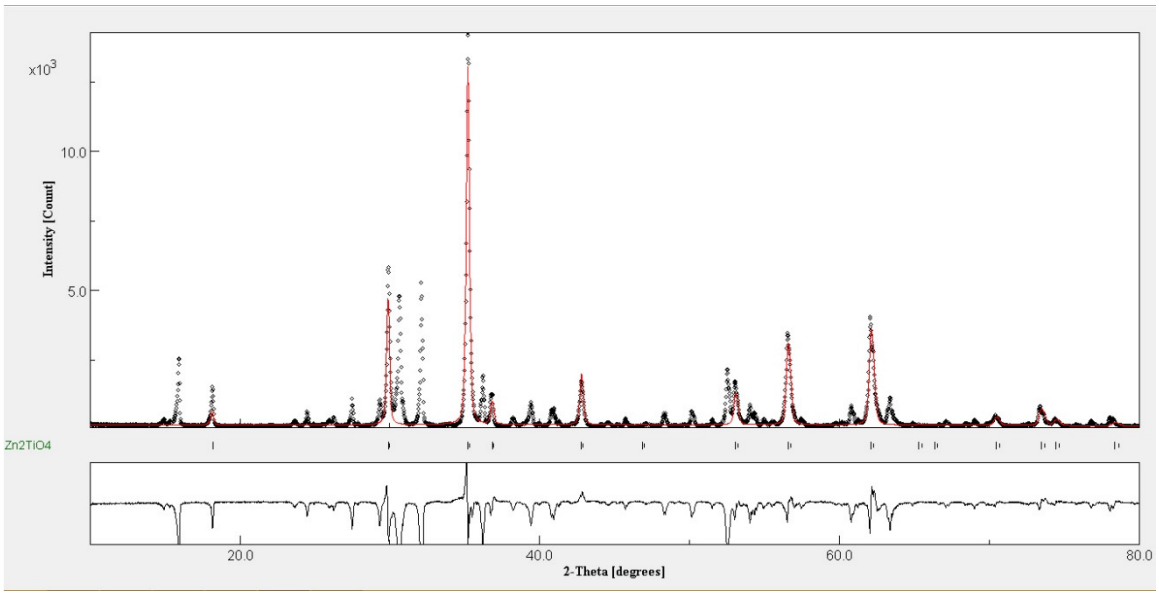

Figure A1. Rietveld plot of ZnO:TiO_2 = 1:1 (in mole) doped with 3 mol% Er^{3+} and 9 mol% Yb^{3+} fired at 1300 °C, site occupancy: 0.001 RE^{3+} at Zn^{2+} position in tetrahedral site. (R_{wp} = 46.530%, R_p = 35.675%).

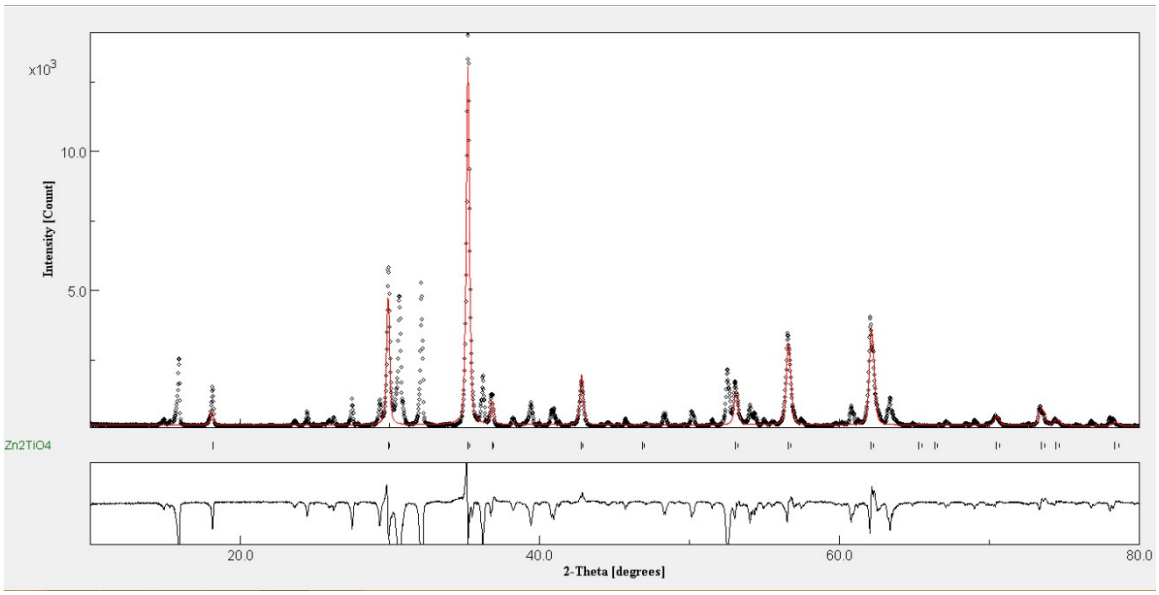

Figure A2. Rietveld plot of ZnO:TiO_2 = 1:1 (in mole) doped with 3 mol% Er^{3+} and 9 mol% Yb^{3+} fired at 1300 °C, site occupancy: 0.01 RE^{3+} at Zn^{2+} position in tetrahedral site. (R_{wp} = 46.502%, R_p = 35.607%).

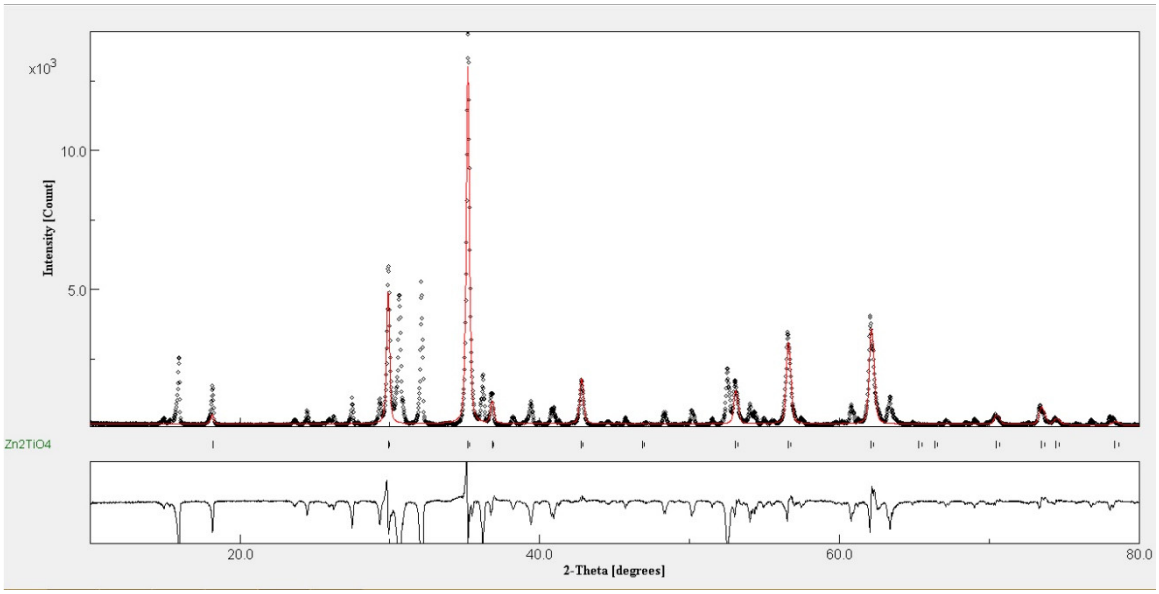

Figure A3. Rietveld plot of ZnO:TiO_2 = 1:1 (in mole) doped with 3 mol% Er^{3+} and 9 mol% Yb^{3+} fired at 1300 °C, site occupancy: 0.05 RE^{3+} at Zn^{2+} position in tetrahedral site. (R_{wp} = 46.462%, R_p = 35.369%).

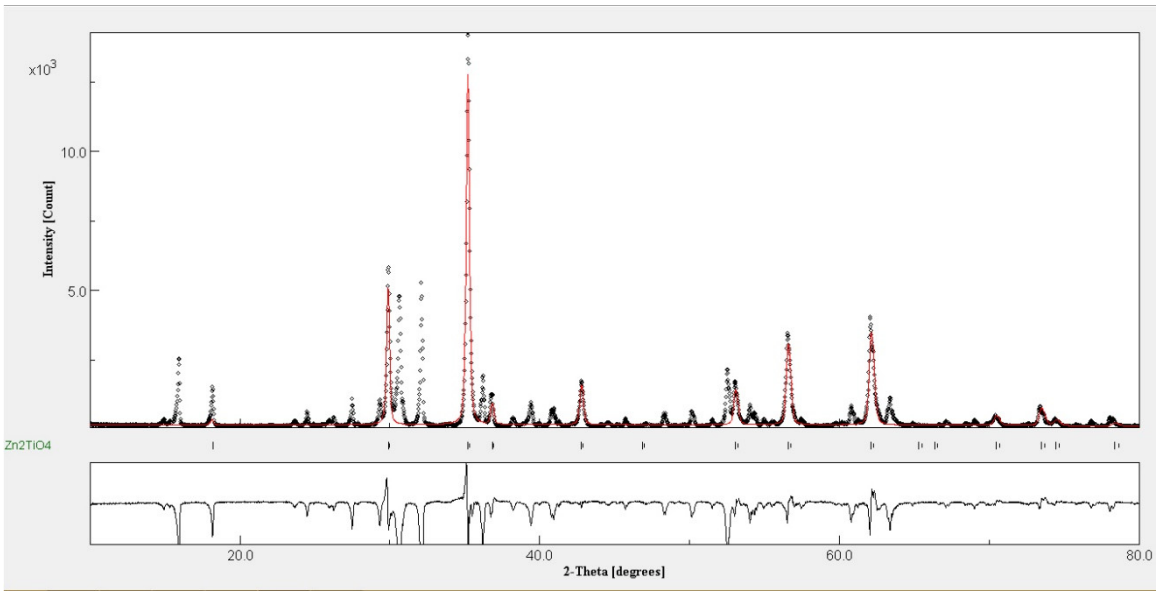

Figure A4. Rietveld plot of ZnO:TiO_2 = 1:1 (in mole) doped with 3 mol% Er^{3+} and 9 mol% Yb^{3+} fired at 1300 °C, site occupancy: 0.1 RE^{3+} at Zn^{2+} position in tetrahedral site. (R_{wp} = 46.514%, R_p = 35.279%).

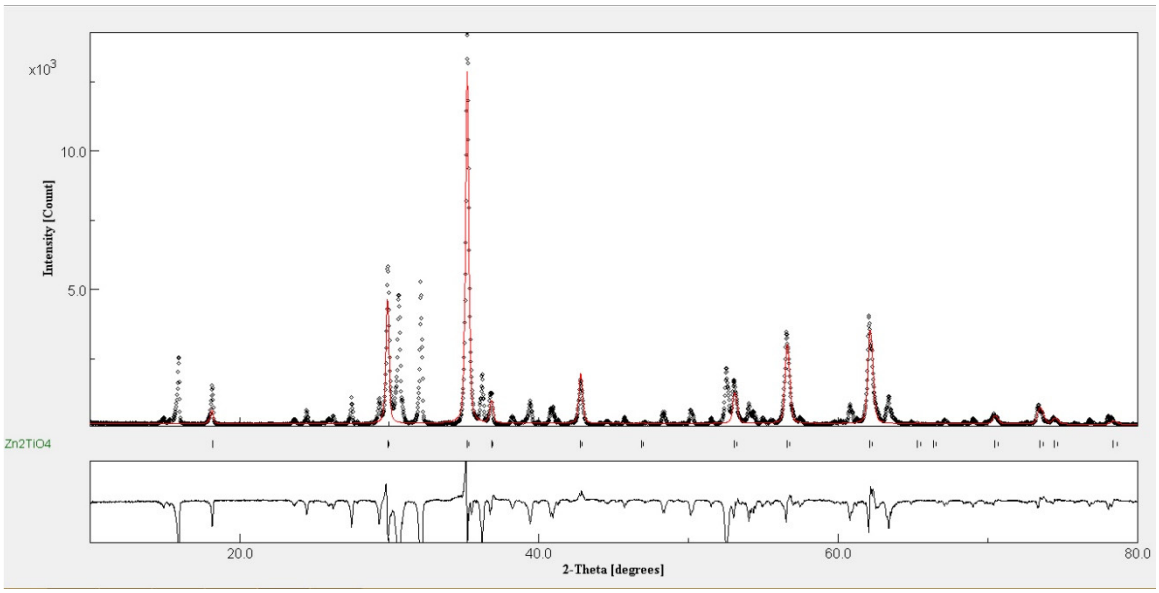

Figure A5. Rietveld plot of ZnO:TiO_2 = 1:1 (in mole) doped with 3 mol% Er^{3+} and 9 mol% Yb^{3+} fired at 1300 °C, site occupancy: 0.001 RE^{3+} at Zn^{2+} position in octahedral site. (R_{wp} = 46.516%, R_p = 35.637%).

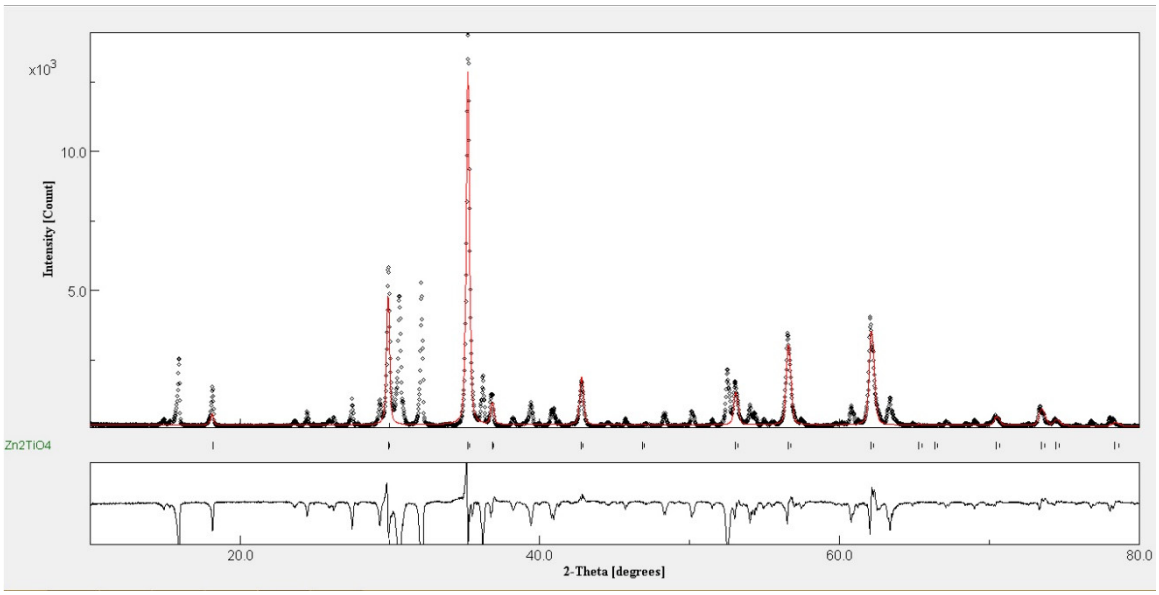

Figure A6. Rietveld plot of ZnO:TiO_2 = 1:1 (in mole) doped with 3 mol% Er^{3+} and 9 mol% Yb^{3+} fired at 1300 °C, site occupancy: 0.01 RE^{3+} at Zn^{2+} position in octahedral site. (R_{wp} = 46.468%, R_p = 35.503%).

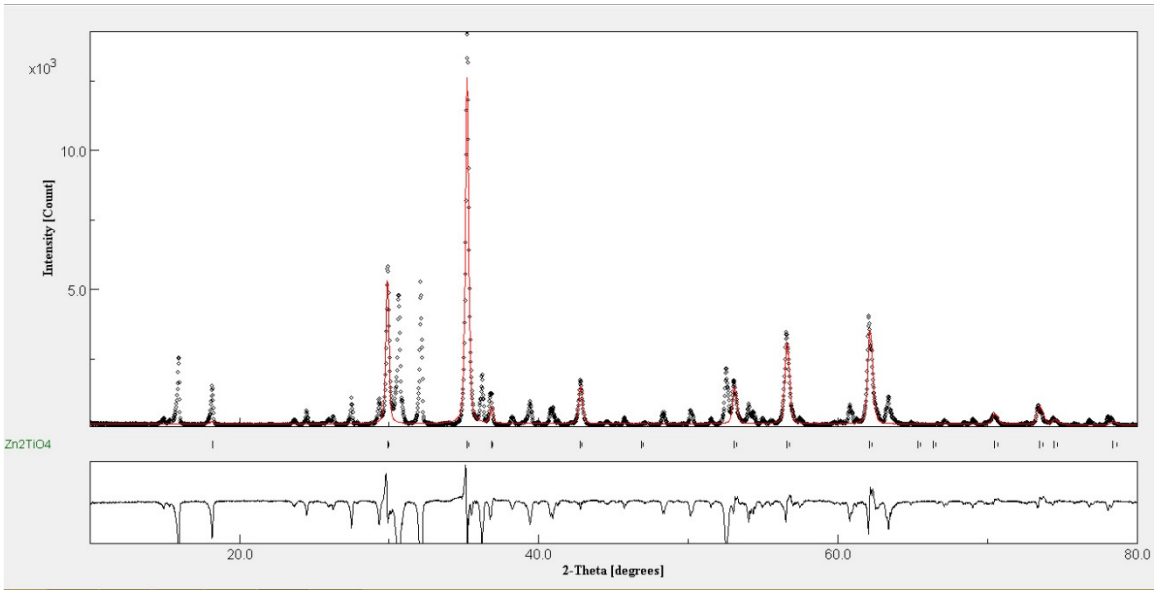

Figure A7. Rietveld plot of ZnO:TiO_2 = 1:1 (in mole) doped with 3 mol% Er^{3+} and 9 mol% Yb^{3+} fired at 1300 °C, site occupancy: 0.05 RE^{3+} at Zn^{2+} position in octahedral site. (R_{wp} = 46.657%, R_p = 35.427%).

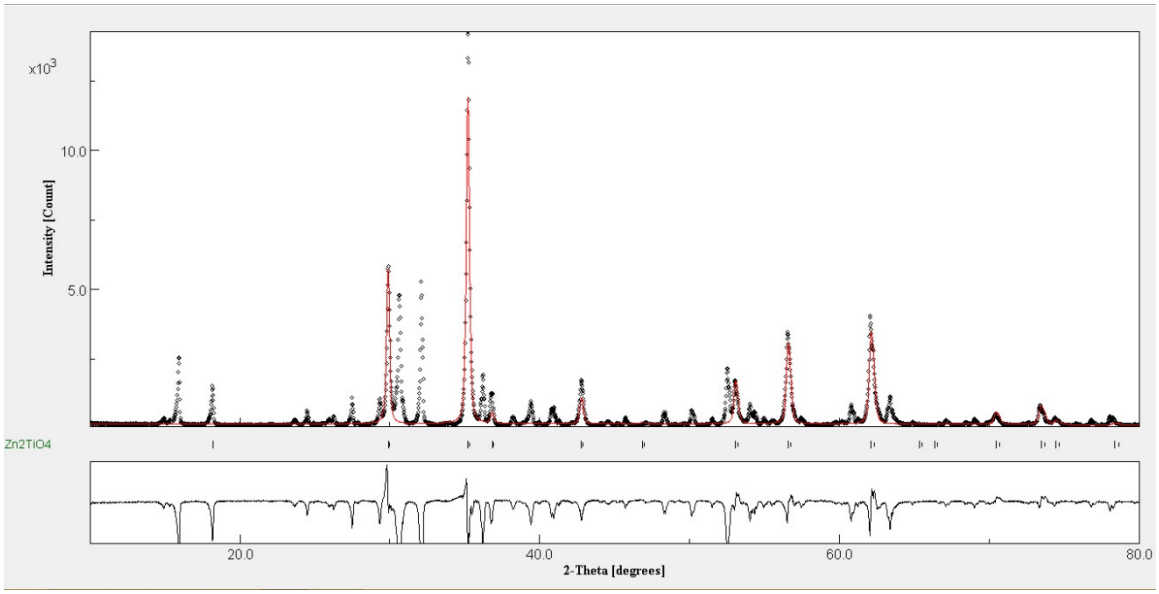

Figure A8. Rietveld plot of ZnO:TiO_2 = 1:1 (in mole) doped with 3 mol% Er^{3+} and 9 mol% Yb^{3+} fired at 1300 °C, site occupancy: 0.1 RE^{3+} at Zn^{2+} position in octahedral site. (R_{wp} = 47.293%, R_p = 36.371%).

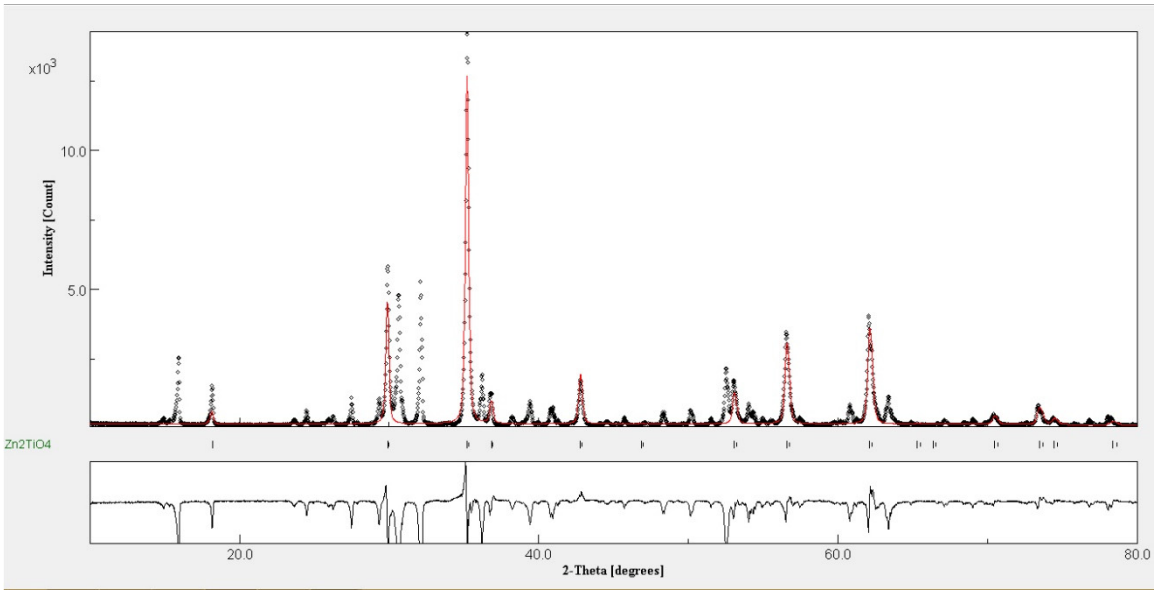

Figure A9. Rietveld plot of $ZnO:TiO_2$ = 1:1 (in mole) doped with 3 mol% Er^{3+} and 9 mol% Yb^{3+} fired at 1300 °C, site occupancy: 0.001 RE^{3+} at Ti^{4+} position in octahedral site. (R_{wp} = 46.561%, R_p = 35.726%).

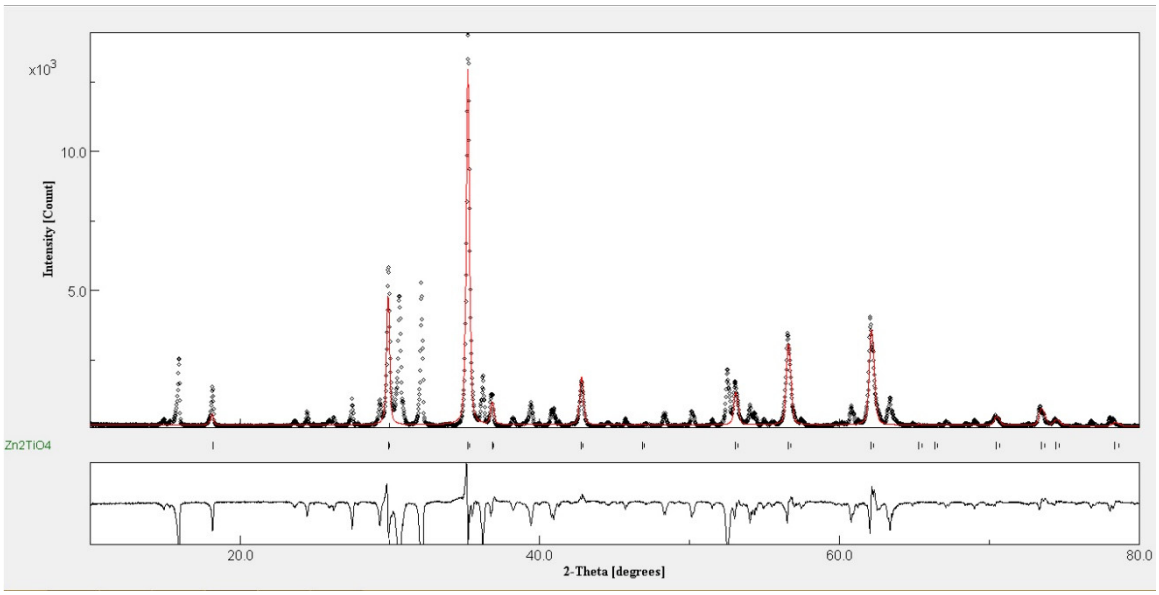

Figure A10. Rietveld plot of $ZnO:TiO_2$ = 1:1 (in mole) doped with 3 mol% Er^{3+} and 9 mol% Yb^{3+} fired at 1300 °C, site occupancy: 0.01 RE^{3+} at Ti^{4+} position in octahedral site. (R_{wp} = 46.476%, R_p = 35.523%).

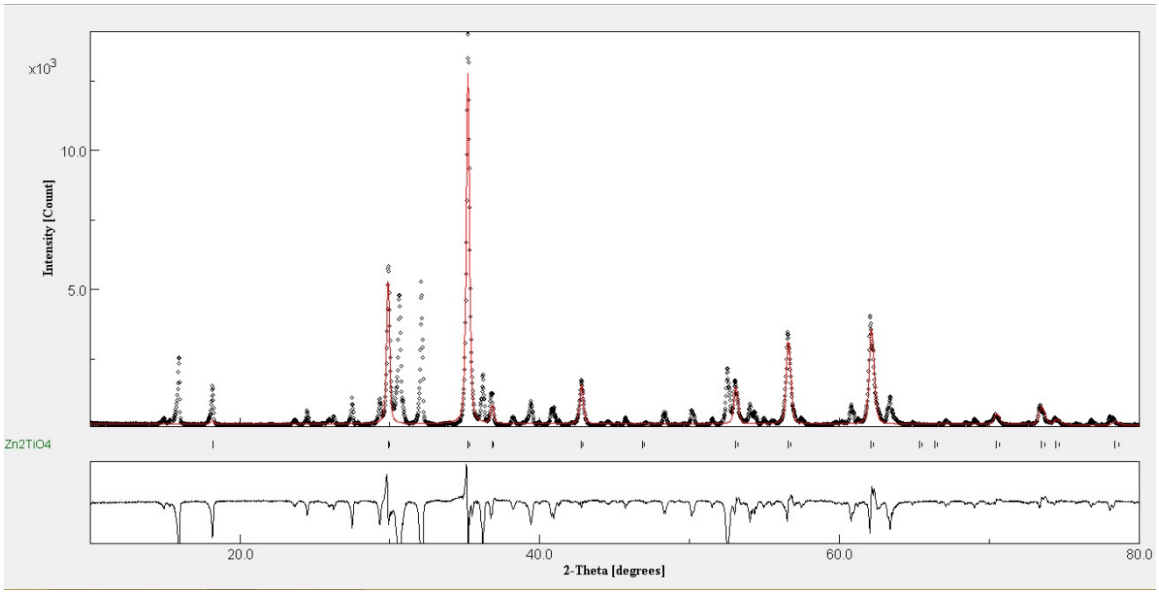

Figure A11. Rietveld plot of ZnO:TiO_2 = 1:1 (in mole) doped with 3 mol% Er^{3+} and 9 mol% Yb^{3+} fired at 1300 °C, site occupancy: 0.05 RE^{3+} at Ti^{4+} position in octahedral site. (R_{wp} = 46.612%, R_p = 35.379%).

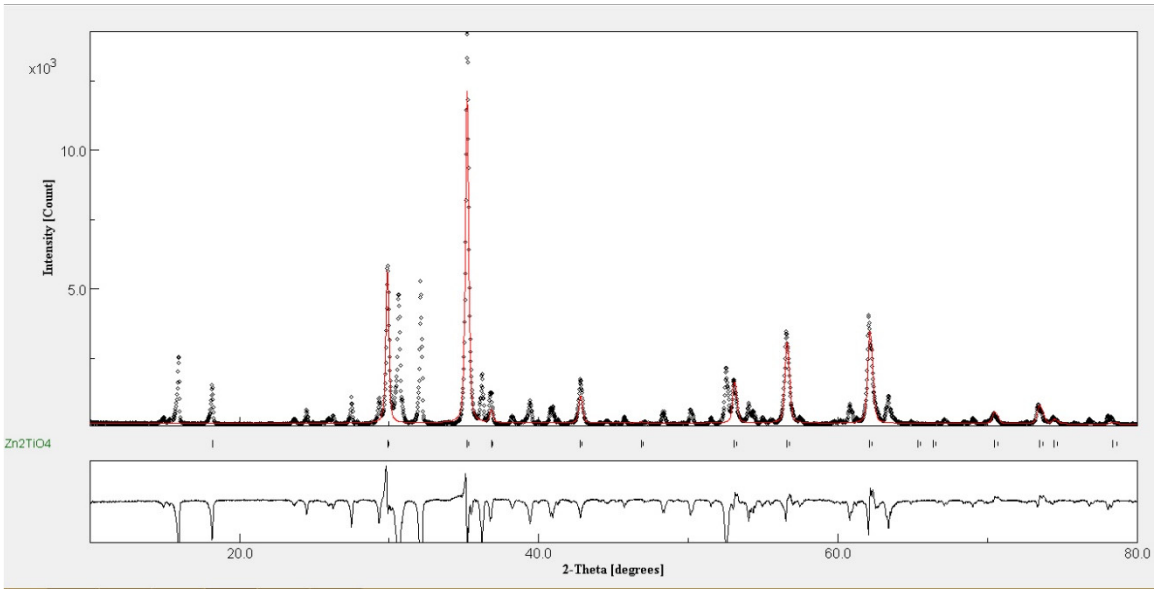

Figure A12. Rietveld plot of ZnO:TiO_2 = 1:1 (in mole) doped with 3 mol% Er^{3+} and 9 mol% Yb^{3+} fired at 1300 °C, site occupancy: 0.1 RE^{3+} at Ti^{4+} position in octahedral site. (R_{wp} = 47.120%, R_p = 36.141%).

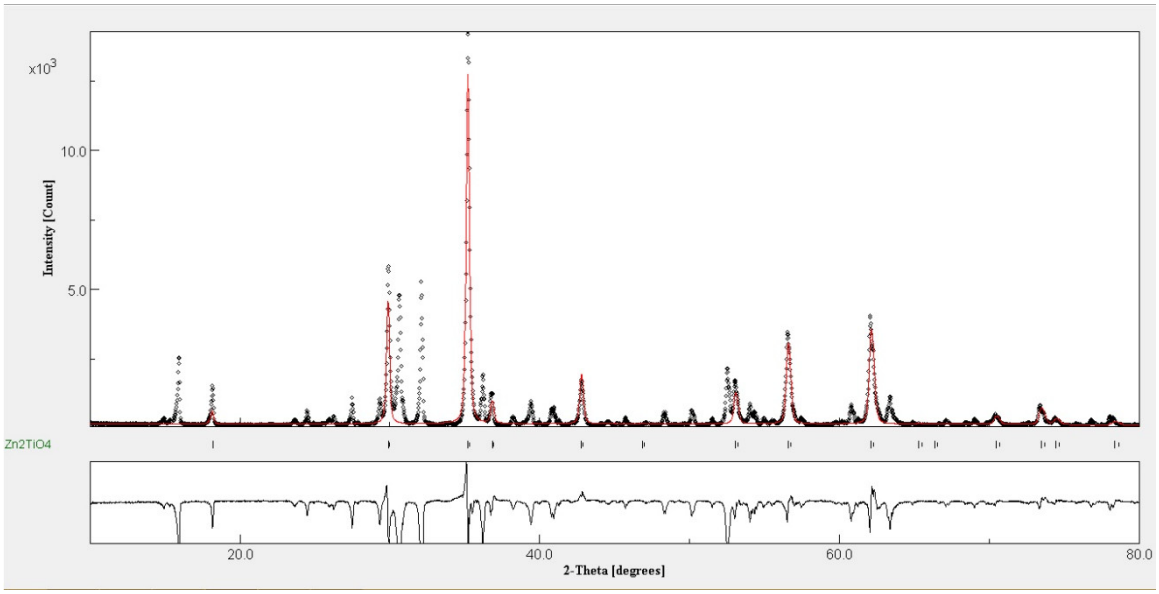

Figure A13. Rietveld plot of ZnO:TiO_2 = 1:1 (in mole) doped with 3 mol% Er^{3+} and 9 mol% Yb^{3+} fired at 1300 °C, site occupancy: 0.001 RE^{3+} at Zn^{2+} and Ti^{4+} positions in octahedral site. (R_{wp} = 46.537%, R_p = 35.698%).

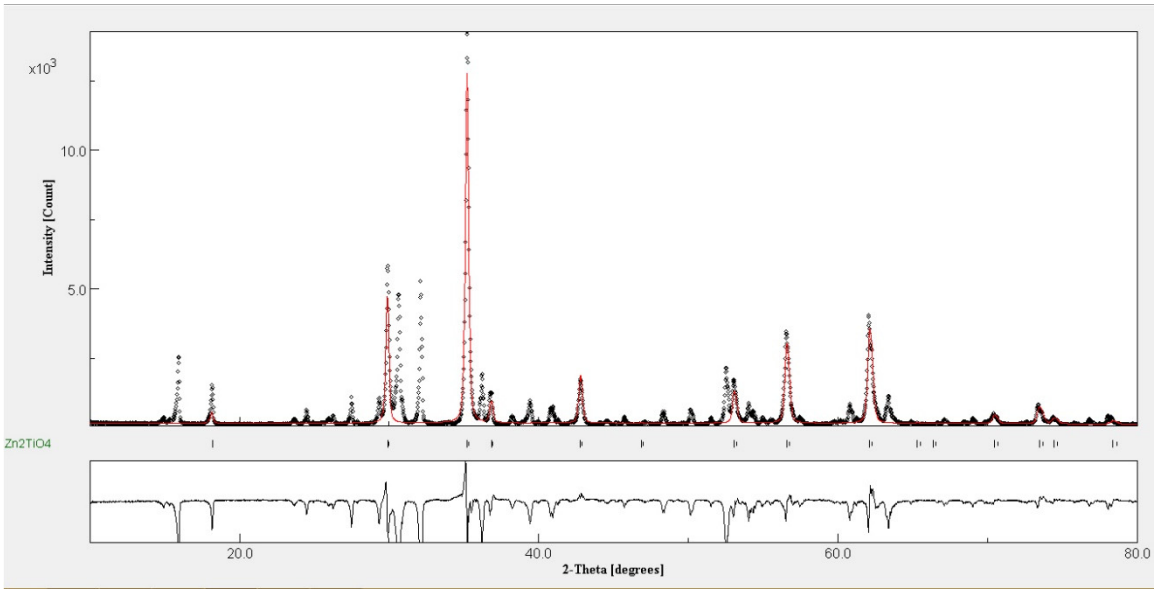

Figure A14. Rietveld plot of ZnO:TiO_2 = 1:1 (in mole) doped with 3 mol% Er^{3+} and 9 mol% Yb^{3+} fired at 1300 °C, site occupancy: 0.01 RE^{3+} at Zn^{2+} and Ti^{4+} positions in octahedral site. (R_{wp} = 46.485%, R_p = 35.537%).

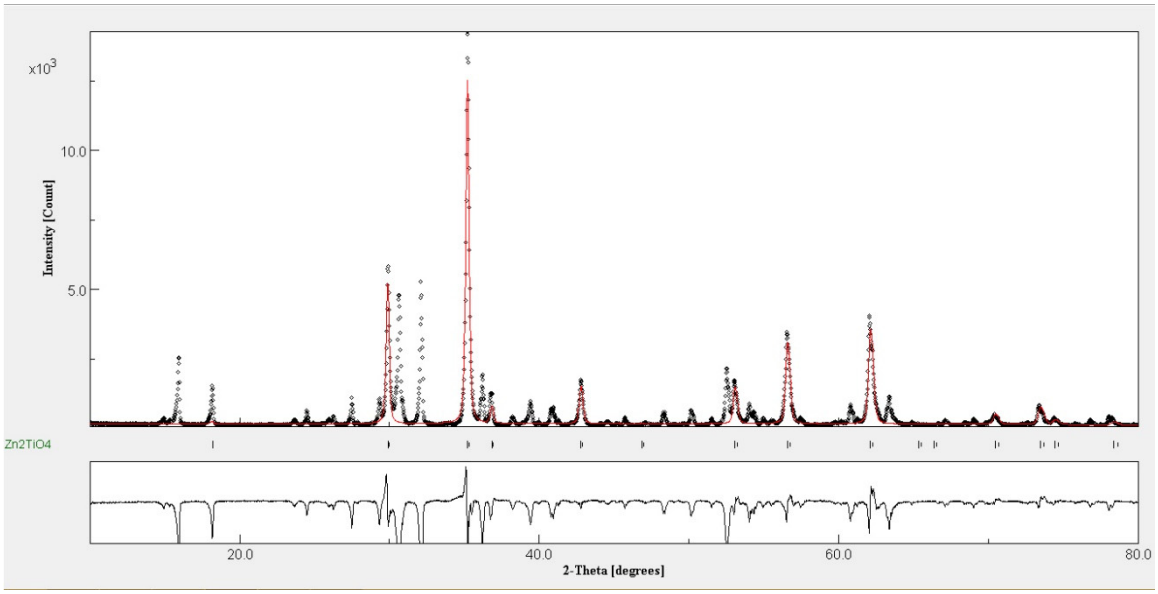

Figure A15. Rietveld plot of ZnO:TiO_2 = 1:1 (in mole) doped with 3 mol% Er^{3+} and 9 mol% Yb^{3+} fired at 1300 °C, site occupancy: 0.05 RE^{3+} at Zn^{2+} and Ti^{4+} positions in octahedral site. (R_{wp} = 46.601%, R_p = 35.428%).

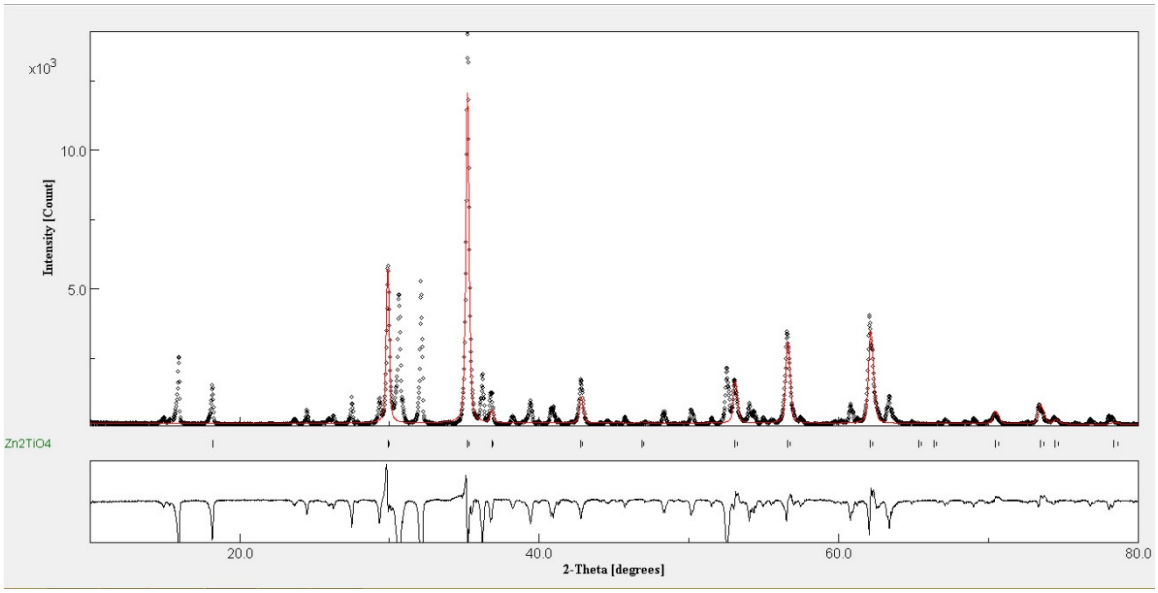

Figure A16. Rietveld plot of ZnO:TiO_2 = 1:1 (in mole) doped with 3 mol% Er^{3+} and 9 mol% Yb^{3+} fired at 1300 °C, site occupancy: 0.1 RE^{3+} at Zn^{2+} and Ti^{4+} positions in octahedral site. (R_{wp} = 47.204%, R_p = 36.240%).

Table A1. Original Zn_2TiO_4 crystal structure parameters.

Atom	Site	x	y	z	Occupancy
Ti	Ti**B**	0.625	0.625	0.625	0.500
Zn	Zn**B**	0.625	0.625	0.625	0.500
Zn	Zn**A**	0.000	0.000	0.000	1.000
O	O	0.380	0.380	0.380	1.000

Remark: **A** is A-site of Zn_2TiO_4 crystal referred to tetrahedral site.
B is B-site of Zn_2TiO_4 crystal referred to octahedral site.
x, y, z is crystallographic coordinate system.
Occupancy is the proportion of site occupancy of each atom at such position (e.g. 1.000 = 100%).

Table A2. Zn_2TiO_4 crystal structure parameters corresponding to Figure A1.

Atom	Site	x	y	z	Occupancy
Ti	Ti**B**	0.625	0.625	0.625	0.500
Zn	Zn**B**	0.625	0.625	0.625	0.500
Zn	Zn**A**	0.000	0.000	0.000	0.999
O	O	0.380	0.380	0.380	1.000
REs	RE**A**	0.000	0.000	0.000	0.001

Remark: REs is Er^{3+} and/or Yb^{3+}.

Table A3. Zn_2TiO_4 crystal structure parameters corresponding to Figure A2.

Atom	Site	x	y	z	Occupancy
Ti	Ti**B**	0.625	0.625	0.625	0.500
Zn	Zn**B**	0.625	0.625	0.625	0.500
Zn	Zn**A**	0.000	0.000	0.000	0.990
O	O	0.380	0.380	0.380	1.000
REs	RE**A**	0.000	0.000	0.000	0.010

Table A4. Zn_2TiO_4 crystal structure parameters corresponding to Figure A3.

Atom	Site	x	y	z	Occupancy
Ti	Ti**B**	0.625	0.625	0.625	0.500
Zn	Zn**B**	0.625	0.625	0.625	0.500
Zn	Zn**A**	0.000	0.000	0.000	0.950
O	O	0.380	0.380	0.380	1.000
REs	RE**A**	0.000	0.000	0.000	0.050

Table A5. Zn_2TiO_4 crystal structure parameters corresponding to Figure A4.

Atom	Site	x	y	z	Occupancy
Ti	Ti**B**	0.625	0.625	0.625	0.500
Zn	Zn**B**	0.625	0.625	0.625	0.500
Zn	Zn**A**	0.000	0.000	0.000	0.900
O	O	0.380	0.380	0.380	1.000
REs	RE**A**	0.000	0.000	0.000	0.100

Table A6. Zn_2TiO_4 crystal structure parameters corresponding to Figure A5.

Atom	Site	x	y	z	Occupancy
Ti	Ti**B**	0.625	0.625	0.625	0.500
Zn	Zn**B**	0.625	0.625	0.625	0.499
Zn	Zn**A**	0.000	0.000	0.000	1.000
O	O	0.380	0.380	0.380	1.000
REs	RE**B**	0.000	0.000	0.000	0.001

Table A7. Zn_2TiO_4 crystal structure parameters corresponding to Figure A6.

Atom	Site	x	y	z	Occupancy
Ti	Ti**B**	0.625	0.625	0.625	0.500
Zn	Zn**B**	0.625	0.625	0.625	0.490
Zn	Zn**A**	0.000	0.000	0.000	1.000
O	O	0.380	0.380	0.380	1.000
REs	RE**B**	0.000	0.000	0.000	0.010

Table A8. Zn_2TiO_4 crystal structure parameters corresponding to Figure A7.

Atom	Site	x	y	z	Occupancy
Ti	Ti**B**	0.625	0.625	0.625	0.500
Zn	Zn**B**	0.625	0.625	0.625	0.450
Zn	Zn**A**	0.000	0.000	0.000	1.000
O	O	0.380	0.380	0.380	1.000
REs	RE**B**	0.000	0.000	0.000	0.050

Table A9. Zn_2TiO_4 crystal structure parameters corresponding to Figure A8.

Atom	Site	x	y	z	Occupancy
Ti	Ti**B**	0.625	0.625	0.625	0.500
Zn	Zn**B**	0.625	0.625	0.625	0.400
Zn	Zn**A**	0.000	0.000	0.000	1.000
O	O	0.380	0.380	0.380	1.000
REs	RE**B**	0.000	0.000	0.000	0.100

Table A10. Zn_2TiO_4 crystal structure parameters corresponding to Figure A9.

Atom	Site	x	y	z	Occupancy
Ti	Ti**B**	0.625	0.625	0.625	0.499
Zn	Zn**B**	0.625	0.625	0.625	0.500
Zn	Zn**A**	0.000	0.000	0.000	1.000
O	O	0.380	0.380	0.380	1.000
REs	RE**B**	0.000	0.000	0.000	0.001

Table A11. Zn_2TiO_4 crystal structure parameters corresponding to Figure A10.

Atom	Site	x	y	z	Occupancy
Ti	Ti**B**	0.625	0.625	0.625	0.490
Zn	Zn**B**	0.625	0.625	0.625	0.500
Zn	Zn**A**	0.000	0.000	0.000	1.000
O	O	0.380	0.380	0.380	1.000
REs	RE**B**	0.000	0.000	0.000	0.010

Table A12. Zn_2TiO_4 crystal structure parameters corresponding to Figure A11.

Atom	Site	x	y	z	Occupancy
Ti	Ti**B**	0.625	0.625	0.625	0.450
Zn	Zn**B**	0.625	0.625	0.625	0.500
Zn	Zn**A**	0.000	0.000	0.000	1.000
O	O	0.380	0.380	0.380	1.000
REs	RE**B**	0.000	0.000	0.000	0.050

Table A13. Zn_2TiO_4 crystal structure parameters corresponding to Figure A12.

Atom	Site	x	y	z	Occupancy
Ti	Ti**B**	0.625	0.625	0.625	0.400
Zn	Zn**B**	0.625	0.625	0.625	0.500
Zn	Zn**A**	0.000	0.000	0.000	1.000
O	O	0.380	0.380	0.380	1.000
REs	RE**B**	0.000	0.000	0.000	0.100

Table A14. Zn_2TiO_4 crystal structure parameters corresponding to Figure A13.

Atom	Site	x	y	z	Occupancy
Ti	Ti**B**	0.625	0.625	0.625	0.4995
Zn	Zn**B**	0.625	0.625	0.625	0.4995
Zn	Zn**A**	0.000	0.000	0.000	1.000
O	O	0.380	0.380	0.380	1.000
REs	RE**B**	0.000	0.000	0.000	0.001

Table A15. Zn_2TiO_4 crystal structure parameters corresponding to Figure A14.

Atom	Site	x	y	z	Occupancy
Ti	Ti**B**	0.625	0.625	0.625	0.495
Zn	Zn**B**	0.625	0.625	0.625	0.495
Zn	Zn**A**	0.000	0.000	0.000	1.000
O	O	0.380	0.380	0.380	1.000
REs	RE**B**	0.000	0.000	0.000	0.010

Table A16. Zn_2TiO_4 crystal structure parameters corresponding to Figure A15.

Atom	Site	x	y	z	Occupancy
Ti	Ti**B**	0.625	0.625	0.625	0.475
Zn	Zn**B**	0.625	0.625	0.625	0.475
Zn	Zn**A**	0.000	0.000	0.000	1.000
O	O	0.380	0.380	0.380	1.000
REs	RE**B**	0.000	0.000	0.000	0.050

Table A17. Zn_2TiO_4 crystal structure parameters corresponding to Figure A16.

Atom	Site	x	y	z	Occupancy
Ti	Ti**B**	0.625	0.625	0.625	0.450
Zn	Zn**B**	0.625	0.625	0.625	0.450
Zn	Zn**A**	0.000	0.000	0.000	1.000
O	O	0.380	0.380	0.380	1.000
REs	RE**B**	0.000	0.000	0.000	0.100

Appendix B

Summary of permission for third party copyright works

Page number (Work)	Source work	Copyright holder and year	Permission
Page 12 (Figure 1.4)	G. Liu, B. Jacquier, *Spectroscopic Properties of Rare Earths in Optical Materials*, F. Auzel, Chapter 5 Up-conversion in RE-doped solids, Figure 5.1, Page 269.	© 2005 Springer-Verlag Berlin Heidelberg	Granted
Page 14 (Figure 1.5)	F. Wang, X. Liu, *Chem. Soc. Rev.*, **38** (2009) 976-989. Figure 1, Page 977.	© 2009 The Royal Society of Chemistry	Granted
Page 19 (Table 1.1)	W.M. Yen, S. Shionoya, H. Yamamoto, *Phosphor Handbook Second Edition*, T. Kano, Chapter 3 - Section 3 Luminescence centers of rare-earth ions, Table 12, Page 192.	© 2006 Taylor and Francis Group LLC	Granted
Page 20 (Figure 1.6)	L. Aboshyan-Sorgho, M. Cantuel, S. Petoud, A. Hauser, C. Piguet, *Coordin. Chem. Rev.*, **256** (2012) 1644-1663. Figure 1, Page 1645.	© 2011 Elsevier B.V.	Granted
Page 22 (Figure 1.7)	J. Zhou, Q. Liu, W. Feng, Y. Sun, F. Li, *Chem. Rev.*, **115** (2015) 395-465. Scheme 3, Page 400.	© 2015 American Chemical Society	Granted
Page 30 (Figure 1.8)	E.M. Levin, C.R. Robbins, H.F. McMurdie, *Phase Diagram for Chemists Volume I (Figures 1-2066)*, Figure 303, Page 120.	© 1964 The American Ceramic Society, Inc.	Granted
Page 30 (Figure 1.9)	K. Kobwittaya, Y. Oishi, T. Torikai, M. Yada, T. Watari, H.N. Luitel, *Ceram. Int.*, **43** (2017) 13505-13515. Figure 9, 13509.	© 2017 Elsevier Ltd and Techna Group S.r.l.	Granted

Continued…

Page number (Work)	Source work	Copyright holder and year	Permission
Page 55-71 (Chapter II)	K. Kobwittaya**,** Y. Oishi, T. Torikai, M. Yada, T. Watari, H.N. Luitel, *J. Ceram. Soc. Jpn.*, **125** (2017) 559-564. Whole Paper	© 2017 The Ceramic Society of Japan	CC BY-ND 4.0 (https://creativecommons.org/licenses/by-nd/4.0/)
Page 72-140 (Chapter III)	K. Kobwittaya**,** Y. Oishi, T. Torikai, M. Yada, T. Watari, H.N. Luitel, *Ceram. Int.*, **43** (2017) 13505-13515. Whole Paper	© 2017 Elsevier Ltd and Techna Group S.r.l.	Granted
Page 94 (Figure 3.14)	E.M. Levin, C.R. Robbins, H.F. McMurdie, *Phase Diagram for Chemists Volume I (Figures 1-2066)*, Figure 314, Page 123.	© 1964 The American Ceramic Society, Inc.	Granted
Page 141-183 (Chapter IV)	K. Kobwittaya**,** Y. Oishi, T. Torikai, M. Yada, T. Watari, *Mater. Sci. Forum*, **922** (2018) 32-39. Whole Paper	© 2018 Trans Tech Publications	Granted
Page 184-209 (Chapter V)	K. Kobwittaya**,** Y. Oishi, T. Torikai, M. Yada, T. Watari, H.N. Luitel, *Vacuum*, **148** (2018) 286-295. Whole Paper	© 2017 Elsevier Ltd	Granted

Appendix C

Copyright permission letters

Copyright Clearance Center

Note: Copyright.com supplies permissions but not the copyrighted content itself.

1 PAYMENT — 2 REVIEW — 3 CONFIRMATION

Step 3: Order Confirmation

Thank you for your order! A confirmation for your order will be sent to your account email address. If you have questions about your order, you can call us 24 hrs/day, M-F at +1.855.239.3415 Toll Free, or write to us at info@copyright.com. This is not an invoice.

Confirmation Number: 11716358
Order Date: 05/08/2018

If you paid by credit card, your order will be finalized and your card will be charged within 24 hours. If you choose to be invoiced, you can change or cancel your order until the invoice is generated.

Payment Information

Krisana Kobwittaya
kobwittaya.k@gmail.com
+81 8090626522
Payment Method: n/a

Order Details

Spectroscopic properties of rare earths in optical materials

Order detail ID:	71169458
Order License Id:	4344020831390
ISBN:	978-3-540-28209-9
Publication Type:	e-Book
Volume:	
Issue:	
Start page:	
Publisher:	SPRINGER-VERLAG BERLIN/HEIDELBERG
Author/Editor:	JACQUIER, BERNARD ; SpringerLink (Online service)

Permission Status: Granted

Permission type: Republish or display content
Type of use: Thesis/Dissertation

Requestor type	Academic institution
Format	Print, Electronic
Portion	chart/graph/table/figure
Number of charts/graphs/tables/figures	1
The requesting person/organization	Krisana Kobwittaya
Title or numeric reference of the portion(s)	Figure 5.1
Title of the article or chapter the portion is from	5 Up-conversion in RE-doped Solids
Editor of portion(s)	N/A

Author of portion(s)	F. Auzel
Volume of serial or monograph	N/A
Page range of portion	269
Publication date of portion	2005
Rights for	Main product and any product related to main product
Duration of use	Life of current edition
Creation of copies for the disabled	no
With minor editing privileges	no
For distribution to	Worldwide
In the following language(s)	Original language of publication
With incidental promotional use	no
Lifetime unit quantity of new product	Up to 499
Title	Upconversion luminescence in ZnO-TiO2 composite doped with rare earth elements
Instructor name	Krisana Kobwittaya
Institution name	Saga University
Expected presentation date	Sep 2018
Attachment	

Note: This item will be invoiced or charged separately through CCC's **RightsLink** service. More info **$ 0.00**

Total order items: 1

This is not an invoice.

Order Total: 0.00 USD

Confirmation Number: 11716358

Special Rightsholder Terms & Conditions

The following terms & conditions apply to the specific publication under which they are listed

Spectroscopic properties of rare earths in optical materials
Permission type: Republish or display content
Type of use: Thesis/Dissertation

TERMS AND CONDITIONS

The following terms are individual to this publisher:

A maximum of 10% of the content may be licensed for republication.

The user is responsible for identifying and seeking separate licenses for any third party materials that are identified anywhere in the work. Without a separate license, such third party materials may not be reused.

Other Terms and Conditions:

STANDARD TERMS AND CONDITIONS

1. Description of Service; Defined Terms. This Republication License enables the User to obtain licenses for republication of one or more copyrighted works as described in detail on the relevant Order Confirmation (the "Work(s)"). Copyright Clearance Center, Inc. ("CCC") grants licenses through the Service on behalf of the rightsholder identified on the Order Confirmation (the "Rightsholder"). "Republication", as used herein, generally means the inclusion of a Work, in whole or in part, in a new work or works, also as described on the Order Confirmation. "User", as used herein, means the person or entity making such republication.

2. The terms set forth in the relevant Order Confirmation, and any terms set by the Rightsholder with respect to a particular Work, govern the terms of use of Works in connection with the Service. By using the Service, the person transacting for a republication license on behalf of the User represents and warrants that he/she/it (a) has been duly authorized by the User to accept, and hereby does accept, all such terms and conditions on behalf of User, and (b) shall inform User of all such terms and conditions. In the event such person is a "freelancer" or other third party independent of User and CCC, such party shall be deemed jointly a "User" for purposes of these terms and conditions. In any event, User shall be deemed to have accepted and agreed to all such terms and conditions if User republishes the Work in any fashion.

3. Scope of License; Limitations and Obligations.

3.1 All Works and all rights therein, including copyright rights, remain the sole and exclusive property of the Rightsholder. The license created by the exchange of an Order Confirmation (and/or any invoice) and payment by User of the full amount set forth on that document includes only those rights expressly set forth in the Order Confirmation and in these terms and conditions, and conveys no other rights in the Work(s) to User. All rights not expressly granted are hereby reserved.

3.2 General Payment Terms: You may pay by credit card or through an account with us payable at the end of the month. If you and we agree that you may establish a standing account with CCC, then the following terms apply: Remit Payment to: Copyright Clearance Center, 29118 Network Place, Chicago, IL 60673-1291. Payments Due: Invoices are payable upon their delivery to you (or upon our notice to you that they are available to you for downloading). After 30 days, outstanding amounts will be subject to a service charge of 1-1/2% per month or, if less, the maximum rate allowed by applicable law. Unless otherwise specifically set forth in the Order Confirmation or in a separate written agreement signed by CCC, invoices are due and payable on "net 30" terms. While User may exercise the rights licensed immediately upon issuance of the Order Confirmation, the license is automatically revoked and is null and void, as if it had never been issued, if complete payment for the license is not received on a timely basis either from User directly or through a payment agent, such as a credit card company.

3.3 Unless otherwise provided in the Order Confirmation, any grant of rights to User (i) is "one-time" (including the editions and product family specified in the license), (ii) is non-exclusive and non-transferable and (iii) is subject to any and all limitations and restrictions (such as, but not limited to, limitations on duration of use or circulation) included in the Order Confirmation or invoice and/or in these terms and conditions. Upon completion of the licensed use, User shall either secure a new permission for further use of the Work(s) or immediately cease any new use of the Work(s) and shall render inaccessible (such as by deleting or by removing or severing links or other locators) any further copies of the Work (except for copies printed on paper in accordance with this license and still in User's stock at the end of such period).

3.4 In the event that the material for which a republication license is sought includes third party materials (such as photographs, illustrations, graphs, inserts and similar materials) which are identified in such material as having been used by permission, User is responsible for identifying, and seeking separate licenses (under this Service or otherwise) for, any of such third party materials; without a separate license, such third party materials may not be used.

3.5 Use of proper copyright notice for a Work is required as a condition of any license granted under the Service. Unless otherwise provided in the Order Confirmation, a proper copyright notice will read substantially as follows: "Republished with permission of [Rightsholder's name], from [Work's title, author, volume, edition number and year of copyright];

permission conveyed through Copyright Clearance Center, Inc. ” Such notice must be provided in a reasonably legible font size and must be placed either immediately adjacent to the Work as used (for example, as part of a by-line or footnote but not as a separate electronic link) or in the place where substantially all other credits or notices for the new work containing the republished Work are located. Failure to include the required notice results in loss to the Rightsholder and CCC, and the User shall be liable to pay liquidated damages for each such failure equal to twice the use fee specified in the Order Confirmation, in addition to the use fee itself and any other fees and charges specified.

3.6 User may only make alterations to the Work if and as expressly set forth in the Order Confirmation. No Work may be used in any way that is defamatory, violates the rights of third parties (including such third parties' rights of copyright, privacy, publicity, or other tangible or intangible property), or is otherwise illegal, sexually explicit or obscene. In addition, User may not conjoin a Work with any other material that may result in damage to the reputation of the Rightsholder. User agrees to inform CCC if it becomes aware of any infringement of any rights in a Work and to cooperate with any reasonable request of CCC or the Rightsholder in connection therewith.

4. Indemnity. User hereby indemnifies and agrees to defend the Rightsholder and CCC, and their respective employees and directors, against all claims, liability, damages, costs and expenses, including legal fees and expenses, arising out of any use of a Work beyond the scope of the rights granted herein, or any use of a Work which has been altered in any unauthorized way by User, including claims of defamation or infringement of rights of copyright, publicity, privacy or other tangible or intangible property.

5. Limitation of Liability. UNDER NO CIRCUMSTANCES WILL CCC OR THE RIGHTSHOLDER BE LIABLE FOR ANY DIRECT, INDIRECT, CONSEQUENTIAL OR INCIDENTAL DAMAGES (INCLUDING WITHOUT LIMITATION DAMAGES FOR LOSS OF BUSINESS PROFITS OR INFORMATION, OR FOR BUSINESS INTERRUPTION) ARISING OUT OF THE USE OR INABILITY TO USE A WORK, EVEN IF ONE OF THEM HAS BEEN ADVISED OF THE POSSIBILITY OF SUCH DAMAGES. In any event, the total liability of the Rightsholder and CCC (including their respective employees and directors) shall not exceed the total amount actually paid by User for this license. User assumes full liability for the actions and omissions of its principals, employees, agents, affiliates, successors and assigns.

6. Limited Warranties. THE WORK(S) AND RIGHT(S) ARE PROVIDED “AS IS”. CCC HAS THE RIGHT TO GRANT TO USER THE RIGHTS GRANTED IN THE ORDER CONFIRMATION DOCUMENT. CCC AND THE RIGHTSHOLDER DISCLAIM ALL OTHER WARRANTIES RELATING TO THE WORK(S) AND RIGHT(S), EITHER EXPRESS OR IMPLIED, INCLUDING WITHOUT LIMITATION IMPLIED WARRANTIES OF MERCHANTABILITY OR FITNESS FOR A PARTICULAR PURPOSE. ADDITIONAL RIGHTS MAY BE REQUIRED TO USE ILLUSTRATIONS, GRAPHS, PHOTOGRAPHS, ABSTRACTS, INSERTS OR OTHER PORTIONS OF THE WORK (AS OPPOSED TO THE ENTIRE WORK) IN A MANNER CONTEMPLATED BY USER; USER UNDERSTANDS AND AGREES THAT NEITHER CCC NOR THE RIGHTSHOLDER MAY HAVE SUCH ADDITIONAL RIGHTS TO GRANT.

7. Effect of Breach. Any failure by User to pay any amount when due, or any use by User of a Work beyond the scope of the license set forth in the Order Confirmation and/or these terms and conditions, shall be a material breach of the license created by the Order Confirmation and these terms and conditions. Any breach not cured within 30 days of written notice thereof shall result in immediate termination of such license without further notice. Any unauthorized (but licensable) use of a Work that is terminated immediately upon notice thereof may be liquidated by payment of the Rightsholder's ordinary license price therefor; any unauthorized (and unlicensable) use that is not terminated immediately for any reason (including, for example, because materials containing the Work cannot reasonably be recalled) will be subject to all remedies available at law or in equity, but in no event to a payment of less than three times the Rightsholder's ordinary license price for the most closely analogous licensable use plus Rightsholder's and/or CCC's costs and expenses incurred in collecting such payment.

8. **Miscellaneous.**

8.1 User acknowledges that CCC may, from time to time, make changes or additions to the Service or to these terms and conditions, and CCC reserves the right to send notice to the User by electronic mail or otherwise for the purposes of notifying User of such changes or additions; provided that any such changes or additions shall not apply to permissions already secured and paid for.

8.2 Use of User-related information collected through the Service is governed by CCC’s privacy policy, available online here: http://www.copyright.com/content/cc3/en/tools/footer/privacypolicy.html.

8.3 The licensing transaction described in the Order Confirmation is personal to User. Therefore, User may not assign or transfer to any other person (whether a natural person or an organization of any kind) the license created by the Order Confirmation and these terms and conditions or any rights granted hereunder; provided, however, that User may assign such license in its entirety on written notice to CCC in the event of a transfer of all or substantially all of User’s rights in the new material which includes the Work(s) licensed under this Service.

8.4 No amendment or waiver of any terms is binding unless set forth in writing and signed by the parties. The Rightsholder and CCC hereby object to any terms contained in any writing prepared by the User or its principals, employees, agents or affiliates and purporting to govern or otherwise relate to the licensing transaction described in the Order Confirmation, which terms are in any way inconsistent with any terms set forth in the Order Confirmation and/or in these terms and conditions or CCC's standard operating procedures, whether such writing is prepared prior to, simultaneously with or subsequent to the Order Confirmation, and whether such writing appears on a copy of the Order Confirmation or in a separate instrument.

8.5 The licensing transaction described in the Order Confirmation document shall be governed by and construed under the law of the State of New York, USA, without regard to the principles thereof of conflicts of law. Any case, controversy, suit, action, or proceeding arising out of, in connection with, or related to such licensing transaction shall be brought, at CCC's sole discretion, in any federal or state court located in the County of New York, State of New York, USA, or in any federal or state court whose geographical jurisdiction covers the location of the Rightsholder set forth in the Order Confirmation. The parties expressly submit to the personal jurisdiction and venue of each such federal or state court.If

you have any comments or questions about the Service or Copyright Clearance Center, please contact us at 978-750-8400 or send an e-mail to info@copyright.com.

v 1.1

Close

Confirmation Number: 11716358

Citation Information

Order Detail ID: 71169458

Spectroscopic properties of rare earths in optical materials by JACQUIER, BERNARD ; SpringerLink (Online service) Reproduced with permission of SPRINGER-VERLAG BERLIN/HEIDELBERG in the format Thesis/Dissertation via Copyright Clearance Center.

Close

Title: Recent advances in the chemistry of lanthanide-doped upconversion nanocrystals
Author: Feng Wang,Xiaogang Liu
Publication: Chemical Society Reviews
Publisher: Royal Society of Chemistry
Date: Feb 12, 2009

Order Completed

Thank you for your order.

This Agreement between Krisana Kobwittaya ("You") and Royal Society of Chemistry ("Royal Society of Chemistry") consists of your license details and the terms and conditions provided by Royal Society of Chemistry and Copyright Clearance Center.

Your confirmation email will contain your order number for future reference.

printable details

License Number	4344030031662
License date	May 08, 2018
Licensed Content Publisher	Royal Society of Chemistry
Licensed Content Publication	Chemical Society Reviews
Licensed Content Title	Recent advances in the chemistry of lanthanide-doped upconversion nanocrystals
Licensed Content Author	Feng Wang,Xiaogang Liu
Licensed Content Date	Feb 12, 2009
Licensed Content Volume	38
Licensed Content Issue	4
Type of Use	Thesis/Dissertation
Requestor type	academic/educational
Portion	figures/tables/images
Number of figures/tables/images	1
Distribution quantity	50
Format	print and electronic
Will you be translating?	no
Order reference number	
Title of the thesis/dissertation	Upconversion luminescence in ZnO-TiO2 composite doped with rare earth elements
Expected completion date	Sep 2018
Estimated size	250
Attachment	
Requestor Location	Krisana Kobwittaya Department of Science and Advanced Technology Graduate School of Science and Engineering Saga University Saga, other 840-8502 Japan Attn:
Billing Type	Invoice

Billing address	Krisana Kobwittaya Department of Science and Advanced Technology Graduate School of Science and Engineering Saga University Saga, Japan 840-8502 Attn: Krisana Kobwittaya
Total	0.00 USD

ORDER MORE CLOSE WINDOW

Copyright Clearance Center

Confirmation Number: 11716365
Order Date: 05/08/2018

Customer Information

Customer: Krisana Kobwittaya
Account Number: 3001165384
Organization: Krisana Kobwittaya
Email: kobwittaya.k@gmail.com
Phone: +81 8090626522
Payment Method: Invoice

This is not an invoice

Order Details

Phosphor handbook

Billing Status: **N/A**

Order detail ID: 71169469
ISBN: 9780849335648
Publication Type: Book
Publisher: TAYLOR & FRANCIS GROUP LLC
Author/Editor: YEN, WILLIAM M.

Permission Status: **Granted**
Permission type: Republish or display content
Type of use: Thesis/Dissertation
Job Ticket: 501397952
Order License Id: 4344150019394

Requestor type	Academic institution
Format	Print, Electronic
Portion	chart/graph/table/figure
Number of charts/graphs/tables/figures	1
The requesting person/organization	Krisana Kobwittaya
Title or numeric reference of the portion(s)	Chapter 3, Section 3, Table 12
Title of the article or chapter the portion is from	Principle phosphor materials and their optical properties, Luminescence centers of rare-earth ions
Editor of portion(s)	N/A
Author of portion(s)	Tsuyoshi Kano
Volume of serial or monograph	N/A
Page range of portion	192
Publication date of portion	2006
Rights for	Main product and any product related to main product
Duration of use	Life of current edition
Creation of copies for the disabled	no
With minor editing privileges	yes

For distribution to	Worldwide
In the following language(s)	Original language of publication
With incidental promotional use	no
Lifetime unit quantity of new product	Up to 499
Title	Upconversion luminescence in ZnO-TiO2 composite doped with rare earth elements
Instructor name	Krisana Kobwittaya
Institution name	Saga University
Expected presentation date	Sep 2018
Attachment	

Note: This item was invoiced through CCC'S **RightsLink service.** More info **$ 0.00**

Total order items: 1 **Order Total: $0.00**

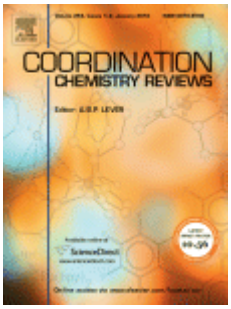

Title: Optical sensitization and upconversion in discrete polynuclear chromium–lanthanide complexes

Author: Lilit Aboshyan-Sorgho,Martine Cantuel,Stephane Petoud,Andreas Hauser,Claude Piguet

Publication: Coordination Chemistry Reviews

Publisher: Elsevier

Date: August 2012

Order Completed

Thank you for your order.

This Agreement between Krisana Kobwittaya ("You") and Elsevier ("Elsevier") consists of your license details and the terms and conditions provided by Elsevier and Copyright Clearance Center.

Your confirmation email will contain your order number for future reference.

printable details

License Number	4344031155632
License date	May 08, 2018
Licensed Content Publisher	Elsevier
Licensed Content Publication	Coordination Chemistry Reviews
Licensed Content Title	Optical sensitization and upconversion in discrete polynuclear chromium–lanthanide complexes
Licensed Content Author	Lilit Aboshyan-Sorgho,Martine Cantuel,Stephane Petoud,Andreas Hauser,Claude Piguet
Licensed Content Date	Aug 1, 2012
Licensed Content Volume	256
Licensed Content Issue	15-16
Licensed Content Pages	20
Type of Use	reuse in a thesis/dissertation
Portion	figures/tables/illustrations
Number of figures/tables/illustrations	1
Format	both print and electronic
Are you the author of this Elsevier article?	No
Will you be translating?	No
Original figure numbers	Figure 1
Title of your thesis/dissertation	Upconversion luminescence in ZnO-TiO2 composite doped with rare earth elements
Publisher of new work	Saga University
Author of new work	Krisana Kobwittaya
Expected completion date	Sep 2018
Estimated size (number of pages)	250
Attachment	
Requestor Location	Krisana Kobwittaya Department of Science and Advanced Technology Graduate School of Science and Engineering Saga University Saga, other 840-8502

	Japan Attn:
Publisher Tax ID	JP00022
Total	0 JPY

ORDER MORE CLOSE WINDOW

Title: Upconversion Luminescent Materials: Advances and Applications

Author: Jing Zhou, Qian Liu, Wei Feng, et al

Publication: Chemical Reviews

Publisher: American Chemical Society

Date: Jan 1, 2015

PERMISSION/LICENSE IS GRANTED FOR YOUR ORDER AT NO CHARGE

This type of permission/license, instead of the standard Terms & Conditions, is sent to you because no fee is being charged for your order. Please note the following:

- Permission is granted for your request in both print and electronic formats, and translations.
- If figures and/or tables were requested, they may be adapted or used in part.
- Please print this page for your records and send a copy of it to your publisher/graduate school.
- Appropriate credit for the requested material should be given as follows: "Reprinted (adapted) with permission from (COMPLETE REFERENCE CITATION). Copyright (YEAR) American Chemical Society." Insert appropriate information in place of the capitalized words.
- One-time permission is granted only for the use specified in your request. No additional uses are granted (such as derivative works or other editions). For any other uses, please submit a new request.

If credit is given to another source for the material you requested, permission must be obtained from that source.

Copyright Clearance Center

Note: Copyright.com supplies permissions but not the copyrighted content itself.

1 PAYMENT — 2 REVIEW — 3 CONFIRMATION

Step 3: Order Confirmation

Thank you for your order! A confirmation for your order will be sent to your account email address. If you have questions about your order, you can call us 24 hrs/day, M-F at +1.855.239.3415 Toll Free, or write to us at info@copyright.com. This is not an invoice.

Confirmation Number: 11716366
Order Date: 05/08/2018

If you paid by credit card, your order will be finalized and your card will be charged within 24 hours. If you choose to be invoiced, you can change or cancel your order until the invoice is generated.

Payment Information

Krisana Kobwittaya
kobwittaya.k@gmail.com
+81 8090626522
Payment Method: n/a

Order Details

Phase diagrams for ceramists. 1, (Figures 1 - 2066)

Order detail ID: 71169470
Order License Id: 4344040531674

ISBN: 9780916094041
Publication Type: Book
Publisher: AM CERAMIC SOC INC
Author/Editor: LEVIN, ERNEST M.

Permission Status: Granted

Permission type: Republish or display content
Type of use: Thesis/Dissertation

Hide details

Requestor type	Academic institution
Format	Print, Electronic
Portion	chart/graph/table/figure
Number of charts/graphs/tables/figures	2
The requesting person/organization	Krisana Kobwittaya
Title or numeric reference of the portion(s)	Figure 303, Figure 314
Title of the article or chapter the portion is from	B. METAL OXIDE SYSTEMS, II. Two Oxides
Editor of portion(s)	M.K. Reser
Author of portion(s)	E.M. Levin, C.R. Robbins, H.F. McMurdie
Volume of serial or monograph	N/A
Page range of portion	120, 123
Publication date of portion	Fifth Printing 1985

Rights for	Main product and any product related to main product
Duration of use	Life of current edition
Creation of copies for the disabled	no
With minor editing privileges	no
For distribution to	Worldwide
In the following language(s)	Original language of publication
With incidental promotional use	no
Lifetime unit quantity of new product	Up to 499
Title	Upconversion luminescence in ZnO-TiO2 composite doped with rare earth elements
Instructor name	Krisana Kobwittaya
Institution name	Saga University
Expected presentation date	Sep 2018
Attachment	

Note: This item will be invoiced or charged separately through CCC's **RightsLink** service. More info **$ 0.00**

Total order items: 1

This is not an invoice.

Order Total: 0.00 USD

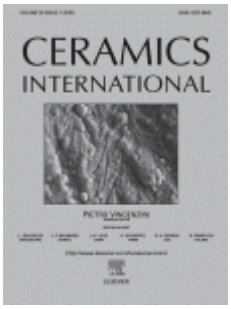

Title: Bright red upconversion luminescence from Er3+ and Yb3+ co-doped ZnO-TiO2 composite phosphor powder

Author: Krisana Kobwittaya,Yushi Oishi,Toshio Torikai,Mitsunori Yada,Takanori Watari,Hom Nath Luitel

Publication: Ceramics International

Publisher: Elsevier

Date: November 2017

Creative Commons Legal Code

Attribution-NoDerivatives 4.0 International

Official translations of this license are available in other languages.

Creative Commons Corporation (“Creative Commons”) is not a law firm and does not provide legal services or legal advice. Distribution of Creative Commons public licenses does not create a lawyer-client or other relationship. Creative Commons makes its licenses and related information available on an “as-is” basis. Creative Commons gives no warranties regarding its licenses, any material licensed under their terms and conditions, or any related information. Creative Commons disclaims all liability for damages resulting from their use to the fullest extent possible.

Using Creative Commons Public Licenses

Creative Commons public licenses provide a standard set of terms and conditions that creators and other rights holders may use to share original works of authorship and other material subject to copyright and certain other rights specified in the public license below. The following considerations are for informational purposes only, are not exhaustive, and do not form part of our licenses.

Considerations for licensors: *Our public licenses are intended for use by those authorized to give the public permission to use material in ways otherwise restricted by copyright and certain other rights. Our licenses are irrevocable. Licensors should read and understand the terms and conditions of the license they choose before applying it. Licensors should also secure all rights necessary before applying our licenses so that the public can reuse the material as expected. Licensors should clearly mark any material not subject to the license. This includes other CC-licensed material, or material used under an exception or limitation to copyright. More considerations for licensors.*

Considerations for the public: *By using one of our public licenses, a licensor grants the public permission to use the licensed material under specified terms and conditions. If the licensor’s permission is not necessary for any reason–for example, because of any applicable exception or limitation to copyright–then that use is not regulated by the license. Our licenses grant only permissions under copyright and certain other rights that a licensor has authority to grant. Use of the licensed material may still be restricted for other reasons, including because others have copyright or other rights in the material. A licensor may make special requests, such as asking that all changes be marked or described. Although not required by our licenses, you are encouraged to respect those requests where reasonable. More considerations for the public.*

Creative Commons Attribution-NoDerivatives 4.0 International Public License

By exercising the Licensed Rights (defined below), You accept and agree to be bound by the terms and conditions of this Creative Commons Attribution-NoDerivatives 4.0 International Public License ("Public License"). To the extent this Public License may be interpreted as a contract, You are granted the Licensed Rights in consideration of Your acceptance of these terms and conditions, and the Licensor grants You such rights in consideration of benefits the Licensor receives from making the Licensed Material available under these terms and conditions.

Section 1 – Definitions.

a. **Adapted Material** means material subject to Copyright and Similar Rights that is derived from or based upon the Licensed Material and in which the Licensed Material is translated, altered, arranged, transformed, or otherwise modified in a manner requiring permission under the Copyright and Similar Rights held by the Licensor. For purposes of this Public License, where the Licensed Material is a musical work, performance, or sound recording, Adapted Material is always produced where the Licensed Material is synched in timed relation with a moving image.
b. **Copyright and Similar Rights** means copyright and/or similar rights closely related to copyright including, without limitation, performance, broadcast, sound recording, and Sui Generis Database Rights, without regard to how the rights are labeled or categorized. For purposes of this Public License, the rights specified in Section 2(b)(1)-(2) are not Copyright and Similar Rights.
c. **Effective Technological Measures** means those measures that, in the absence of proper authority, may not be circumvented under laws fulfilling obligations under Article 11 of the WIPO Copyright Treaty adopted on December 20, 1996, and/or similar international agreements.
d. **Exceptions and Limitations** means fair use, fair dealing, and/or any other exception or limitation to Copyright and Similar Rights that applies to Your use of the Licensed Material.
e. **Licensed Material** means the artistic or literary work, database, or other material to which the Licensor applied this Public License.
f. **Licensed Rights** means the rights granted to You subject to the terms and conditions of this Public License, which are limited to all Copyright and Similar Rights that apply to Your use of the Licensed Material and that the Licensor has authority to license.
g. **Licensor** means the individual(s) or entity(ies) granting rights under this Public License.
h. **Share** means to provide material to the public by any means or process that requires permission under the Licensed Rights, such as reproduction, public display, public performance, distribution, dissemination, communication, or importation, and to make material available to the public including in ways that members of the public may access the material from a place and at a time individually chosen by them.
i. **Sui Generis Database Rights** means rights other than copyright resulting from Directive 96/9/EC of the European Parliament and of the Council of 11 March 1996 on the legal protection of databases, as amended and/or succeeded, as well as other essentially equivalent rights anywhere in the world.
j. **You** means the individual or entity exercising the Licensed Rights under this Public License. **Your** has a corresponding meaning.

Section 2 – Scope.

a. **License grant**.
    1. Subject to the terms and conditions of this Public License, the Licensor hereby grants You a worldwide, royalty-free, non-sublicensable, non-exclusive, irrevocable license to exercise the Licensed Rights in the Licensed Material to:
        A. reproduce and Share the Licensed Material, in whole or in part; and
        B. produce and reproduce, but not Share, Adapted Material.
    2. Exceptions and Limitations. For the avoidance of doubt, where Exceptions and Limitations apply to Your use, this Public License does not apply, and You do not need to comply with its terms and conditions.
    3. Term. The term of this Public License is specified in Section 6(a).
    4. Media and formats; technical modifications allowed. The Licensor authorizes You to exercise the Licensed Rights in all media and formats whether now known or hereafter created, and to make technical modifications necessary to do so. The Licensor waives and/or agrees not to assert any right or authority to forbid You from making technical modifications necessary to exercise the Licensed Rights, including technical modifications necessary to circumvent Effective Technological Measures. For purposes of this Public License, simply making modifications authorized by this Section 2(a)(4) never produces Adapted Material.
    5. Downstream recipients.
        A. Offer from the Licensor – Licensed Material. Every recipient of the Licensed Material automatically receives an offer from the Licensor to exercise the Licensed Rights under the terms and conditions of this Public License.
        B. No downstream restrictions. You may not offer or impose any additional or different terms or conditions on, or apply any Effective Technological Measures to, the

Licensed Material if doing so restricts exercise of the Licensed Rights by any recipient of the Licensed Material.

6. No endorsement. Nothing in this Public License constitutes or may be construed as permission to assert or imply that You are, or that Your use of the Licensed Material is, connected with, or sponsored, endorsed, or granted official status by, the Licensor or others designated to receive attribution as provided in Section 3(a)(1)(A)(i).

b. **Other rights**.

1. Moral rights, such as the right of integrity, are not licensed under this Public License, nor are publicity, privacy, and/or other similar personality rights; however, to the extent possible, the Licensor waives and/or agrees not to assert any such rights held by the Licensor to the limited extent necessary to allow You to exercise the Licensed Rights, but not otherwise.
2. Patent and trademark rights are not licensed under this Public License.
3. To the extent possible, the Licensor waives any right to collect royalties from You for the exercise of the Licensed Rights, whether directly or through a collecting society under any voluntary or waivable statutory or compulsory licensing scheme. In all other cases the Licensor expressly reserves any right to collect such royalties.

Section 3 – License Conditions.

Your exercise of the Licensed Rights is expressly made subject to the following conditions.

a. **Attribution**.

1. If You Share the Licensed Material, You must:

A. retain the following if it is supplied by the Licensor with the Licensed Material:
i. identification of the creator(s) of the Licensed Material and any others designated to receive attribution, in any reasonable manner requested by the Licensor (including by pseudonym if designated);
ii. a copyright notice;
iii. a notice that refers to this Public License;
iv. a notice that refers to the disclaimer of warranties;
v. a URI or hyperlink to the Licensed Material to the extent reasonably practicable;
B. indicate if You modified the Licensed Material and retain an indication of any previous modifications; and
C. indicate the Licensed Material is licensed under this Public License, and include the text of, or the URI or hyperlink to, this Public License.

For the avoidance of doubt, You do not have permission under this Public License to Share Adapted Material.

2. You may satisfy the conditions in Section 3(a)(1) in any reasonable manner based on the medium, means, and context in which You Share the Licensed Material. For example, it may be reasonable to satisfy the conditions by providing a URI or hyperlink to a resource that includes the required information.
3. If requested by the Licensor, You must remove any of the information required by Section 3(a)(1)(A) to the extent reasonably practicable.

Section 4 – Sui Generis Database Rights.

Where the Licensed Rights include Sui Generis Database Rights that apply to Your use of the Licensed Material:

a. for the avoidance of doubt, Section 2(a)(1) grants You the right to extract, reuse, reproduce, and Share all or a substantial portion of the contents of the database, provided You do not Share Adapted Material;
b. if You include all or a substantial portion of the database contents in a database in which You have Sui Generis Database Rights, then the database in which You have Sui Generis Database Rights (but not its individual contents) is Adapted Material; and
c. You must comply with the conditions in Section 3(a) if You Share all or a substantial portion of the contents of the database.

For the avoidance of doubt, this Section 4 supplements and does not replace Your obligations under this Public License where the Licensed Rights include other Copyright and Similar Rights.

Section 5 – Disclaimer of Warranties and Limitation of Liability.

a. **Unless otherwise separately undertaken by the Licensor, to the extent possible, the Licensor offers the Licensed Material as-is and as-available, and makes no representations or warranties of any kind concerning the Licensed Material, whether express, implied, statutory, or other. This includes, without limitation, warranties of title, merchantability, fitness for a particular purpose, non-infringement, absence of latent or other defects, accuracy, or the presence or absence of errors, whether or not known or discoverable. Where disclaimers of warranties are not allowed in full or in part, this disclaimer may not apply to You.**
b. **To the extent possible, in no event will the Licensor be liable to You on any legal theory (including, without limitation, negligence) or otherwise for any direct, special, indirect, incidental, consequential, punitive, exemplary, or other losses, costs, expenses, or damages arising out of this Public License or use of the Licensed Material, even if the Licensor has been advised of the possibility of such losses, costs, expenses, or damages. Where a limitation of liability is not allowed in full or in part, this limitation may not apply to You.**

c. The disclaimer of warranties and limitation of liability provided above shall be interpreted in a manner that, to the extent possible, most closely approximates an absolute disclaimer and waiver of all liability.

Section 6 – Term and Termination.

a. This Public License applies for the term of the Copyright and Similar Rights licensed here. However, if You fail to comply with this Public License, then Your rights under this Public License terminate automatically.

b. Where Your right to use the Licensed Material has terminated under Section 6(a), it reinstates:

    1. automatically as of the date the violation is cured, provided it is cured within 30 days of Your discovery of the violation; or
    2. upon express reinstatement by the Licensor.

    For the avoidance of doubt, this Section 6(b) does not affect any right the Licensor may have to seek remedies for Your violations of this Public License.
c. For the avoidance of doubt, the Licensor may also offer the Licensed Material under separate terms or conditions or stop distributing the Licensed Material at any time; however, doing so will not terminate this Public License.
d. Sections 1, 5, 6, 7, and 8 survive termination of this Public License.

Section 7 – Other Terms and Conditions.

a. The Licensor shall not be bound by any additional or different terms or conditions communicated by You unless expressly agreed.
b. Any arrangements, understandings, or agreements regarding the Licensed Material not stated herein are separate from and independent of the terms and conditions of this Public License.

Section 8 – Interpretation.

a. For the avoidance of doubt, this Public License does not, and shall not be interpreted to, reduce, limit, restrict, or impose conditions on any use of the Licensed Material that could lawfully be made without permission under this Public License.
b. To the extent possible, if any provision of this Public License is deemed unenforceable, it shall be automatically reformed to the minimum extent necessary to make it enforceable. If the provision cannot be reformed, it shall be severed from this Public License without affecting the enforceability of the remaining terms and conditions.
c. No term or condition of this Public License will be waived and no failure to comply consented to unless expressly agreed to by the Licensor.
d. Nothing in this Public License constitutes or may be interpreted as a limitation upon, or waiver of, any privileges and immunities that apply to the Licensor or You, including from the legal processes

of any jurisdiction or authority.

Copyright Clearance Center

Note: Copyright.com supplies permissions but not the copyrighted content itself.

1 PAYMENT — 2 REVIEW — 3 CONFIRMATION

Step 3: Order Confirmation

Thank you for your order! A confirmation for your order will be sent to your account email address. If you have questions about your order, you can call us 24 hrs/day, M-F at +1.855.239.3415 Toll Free, or write to us at info@copyright.com. This is not an invoice.

Confirmation Number: 11722171
Order Date: 06/06/2018

If you paid by credit card, your order will be finalized and your card will be charged within 24 hours. If you choose to be invoiced, you can change or cancel your order until the invoice is generated.

Payment Information

Krisana Kobwittaya
kobwittaya.k@gmail.com
+81 8090626522
Payment Method: n/a

Order Details

Materials science forum

Order detail ID:	71232231
Order License Id:	4362941247722
ISSN:	1662-9752
Publication Type:	Monographic Series
Volume:	
Issue:	
Start page:	
Publisher:	Trans Tech Publications

Permission Status: Granted
Permission type: Republish or display content
Type of use: Thesis/Dissertation

Requestor type	Academic institution
Format	Print, Electronic
Portion	chapter/article
Number of pages in chapter/article	8
The requesting person/organization	Krisana Kobwittaya
Title or numeric reference of the portion(s)	Materials Science Forum Volume 922, Eco-Materials Processing and Design XVIII.
Title of the article or chapter the portion is from	Upconversion Luminescence of ZnO-TiO2: Ho3+/Yb3+ Phosphor Powder
Editor of portion(s)	J. Hojo, T. Sekino, J.F. Yang, H.S. Kim, W.B. Cao
Author of portion(s)	K. Kobwittaya, Y. Oishi, T. Torikai, M. Yada, T. Watari

Volume of serial or monograph	922
Page range of portion	32-39
Publication date of portion	May 2018
Rights for	Main product and any product related to main product
Duration of use	Life of current edition
Creation of copies for the disabled	no
With minor editing privileges	yes
For distribution to	Worldwide
In the following language(s)	Original language of publication
With incidental promotional use	no
Lifetime unit quantity of new product	Up to 499
Title	Upconversion luminescence in ZnO-TiO2 composite doped with rare earth elements
Instructor name	Krisana Kobwittaya
Institution name	Saga University
Expected presentation date	Sep 2018

Note: This item will be invoiced or charged separately through CCC's **RightsLink** service. More info **$ 0.00**

Total order items: 1

This is not an invoice.

Order Total: 0.00 USD

Confirmation Number: 11722171

Special Rightsholder Terms & Conditions

The following terms & conditions apply to the specific publication under which they are listed

Materials science forum
Permission type: Republish or display content
Type of use: Thesis/Dissertation

TERMS AND CONDITIONS

The following terms are individual to this publisher:

None

Other Terms and Conditions:

STANDARD TERMS AND CONDITIONS

1. Description of Service; Defined Terms. This Republication License enables the User to obtain licenses for republication of one or more copyrighted works as described in detail on the relevant Order Confirmation (the "Work(s)"). Copyright Clearance Center, Inc. ("CCC") grants licenses through the Service on behalf of the rightsholder identified on the Order Confirmation (the "Rightsholder"). "Republication", as used herein, generally means the inclusion of a Work, in whole or in part, in a new work or works, also as described on the Order Confirmation. "User", as used herein, means the person or entity making such republication.

2. The terms set forth in the relevant Order Confirmation, and any terms set by the Rightsholder with respect to a particular Work, govern the terms of use of Works in connection with the Service. By using the Service, the person transacting for a republication license on behalf of the User represents and warrants that he/she/it (a) has been duly authorized by the User to accept, and hereby does accept, all such terms and conditions on behalf of User, and (b) shall inform User of all such terms and conditions. In the event such person is a "freelancer" or other third party independent of User and CCC, such party shall be deemed jointly a "User" for purposes of these terms and conditions. In any event, User shall be deemed to have accepted and agreed to all such terms and conditions if User republishes the Work in any fashion.

3. Scope of License; Limitations and Obligations.

3.1 All Works and all rights therein, including copyright rights, remain the sole and exclusive property of the Rightsholder. The license created by the exchange of an Order Confirmation (and/or any invoice) and payment by User of the full amount set forth on that document includes only those rights expressly set forth in the Order Confirmation and in these terms and conditions, and conveys no other rights in the Work(s) to User. All rights not expressly granted are hereby reserved.

3.2 General Payment Terms: You may pay by credit card or through an account with us payable at the end of the month. If you and we agree that you may establish a standing account with CCC, then the following terms apply: Remit Payment to: Copyright Clearance Center, 29118 Network Place, Chicago, IL 60673-1291. Payments Due: Invoices are payable upon their delivery to you (or upon our notice to you that they are available to you for downloading). After 30 days, outstanding amounts will be subject to a service charge of 1-1/2% per month or, if less, the maximum rate allowed by applicable law. Unless otherwise specifically set forth in the Order Confirmation or in a separate written agreement signed by CCC, invoices are due and payable on "net 30" terms. While User may exercise the rights licensed immediately upon issuance of the Order Confirmation, the license is automatically revoked and is null and void, as if it had never been issued, if complete payment for the license is not received on a timely basis either from User directly or through a payment agent, such as a credit card company.

3.3 Unless otherwise provided in the Order Confirmation, any grant of rights to User (i) is "one-time" (including the editions and product family specified in the license), (ii) is non-exclusive and non-transferable and (iii) is subject to any and all limitations and restrictions (such as, but not limited to, limitations on duration of use or circulation) included in the Order Confirmation or invoice and/or in these terms and conditions. Upon completion of the licensed use, User shall either secure a new permission for further use of the Work(s) or immediately cease any new use of the Work(s) and shall render inaccessible (such as by deleting or by removing or severing links or other locators) any further copies of the Work (except for copies printed on paper in accordance with this license and still in User's stock at the end of such period).

3.4 In the event that the material for which a republication license is sought includes third party materials (such as photographs, illustrations, graphs, inserts and similar materials) which are identified in such material as having been used by permission, User is responsible for identifying, and seeking separate licenses (under this Service or otherwise) for, any of such third party materials; without a separate license, such third party materials may not be used.

3.5 Use of proper copyright notice for a Work is required as a condition of any license granted under the Service. Unless otherwise provided in the Order Confirmation, a proper copyright notice will read substantially as follows: "Republished with permission of [Rightsholder's name], from [Work's title, author, volume, edition number and year of copyright]; permission conveyed through Copyright Clearance Center, Inc. " Such notice must be provided in a reasonably legible font size and must be placed either immediately adjacent to the Work as used (for example, as part of a by-line or footnote but not as a separate electronic link) or in the place where substantially all other credits or notices for the new work containing the republished Work are located. Failure to include the required notice results in loss to the Rightsholder and CCC, and the User shall be liable to pay liquidated damages for each such failure equal to twice the use fee specified in the Order Confirmation, in addition to the use fee itself and any other fees and charges specified.

3.6 User may only make alterations to the Work if and as expressly set forth in the Order Confirmation. No Work may be used in any way that is defamatory, violates the rights of third parties (including such third parties' rights of copyright, privacy, publicity, or other tangible or intangible property), or is otherwise illegal, sexually explicit or obscene. In addition, User may not conjoin a Work with any other material that may result in damage to the reputation of the Rightsholder. User agrees to inform CCC if it becomes aware of any infringement of any rights in a Work and to cooperate with any reasonable request of CCC or the Rightsholder in connection therewith.

4. Indemnity. User hereby indemnifies and agrees to defend the Rightsholder and CCC, and their respective employees and directors, against all claims, liability, damages, costs and expenses, including legal fees and expenses, arising out of any use of a Work beyond the scope of the rights granted herein, or any use of a Work which has been altered in any unauthorized way by User, including claims of defamation or infringement of rights of copyright, publicity, privacy or other tangible or intangible property.

5. Limitation of Liability. UNDER NO CIRCUMSTANCES WILL CCC OR THE RIGHTSHOLDER BE LIABLE FOR ANY DIRECT, INDIRECT, CONSEQUENTIAL OR INCIDENTAL DAMAGES (INCLUDING WITHOUT LIMITATION DAMAGES FOR LOSS OF BUSINESS PROFITS OR INFORMATION, OR FOR BUSINESS INTERRUPTION) ARISING OUT OF THE USE OR INABILITY TO USE A WORK, EVEN IF ONE OF THEM HAS BEEN ADVISED OF THE POSSIBILITY OF SUCH DAMAGES. In any event, the total liability of the Rightsholder and CCC (including their respective employees and directors) shall not exceed the total amount actually paid by User for this license. User assumes full liability for the actions and omissions of its principals, employees, agents, affiliates, successors and assigns.

6. Limited Warranties. THE WORK(S) AND RIGHT(S) ARE PROVIDED "AS IS". CCC HAS THE RIGHT TO GRANT TO USER THE RIGHTS GRANTED IN THE ORDER CONFIRMATION DOCUMENT. CCC AND THE RIGHTSHOLDER DISCLAIM ALL OTHER WARRANTIES RELATING TO THE WORK(S) AND RIGHT(S), EITHER EXPRESS OR IMPLIED, INCLUDING WITHOUT LIMITATION IMPLIED WARRANTIES OF MERCHANTABILITY OR FITNESS FOR A PARTICULAR PURPOSE. ADDITIONAL RIGHTS MAY BE REQUIRED TO USE ILLUSTRATIONS, GRAPHS, PHOTOGRAPHS, ABSTRACTS, INSERTS OR OTHER PORTIONS OF THE WORK (AS OPPOSED TO THE ENTIRE WORK) IN A MANNER CONTEMPLATED BY USER; USER UNDERSTANDS AND AGREES THAT NEITHER CCC NOR THE RIGHTSHOLDER MAY HAVE SUCH ADDITIONAL RIGHTS TO GRANT.

7. Effect of Breach. Any failure by User to pay any amount when due, or any use by User of a Work beyond the scope of the license set forth in the Order Confirmation and/or these terms and conditions, shall be a material breach of the license created by the Order Confirmation and these terms and conditions. Any breach not cured within 30 days of written notice thereof shall result in immediate termination of such license without further notice. Any unauthorized (but licensable) use of a Work that is terminated immediately upon notice thereof may be liquidated by payment of the Rightsholder's ordinary license price therefor; any unauthorized (and unlicensable) use that is not terminated immediately for any reason (including, for example, because materials containing the Work cannot reasonably be recalled) will be subject to all remedies available at law or in equity, but in no event to a payment of less than three times the Rightsholder's ordinary license price for the most closely analogous licensable use plus Rightsholder's and/or CCC's costs and expenses incurred in collecting such payment.

8. **Miscellaneous.**

8.1 User acknowledges that CCC may, from time to time, make changes or additions to the Service or to these terms and conditions, and CCC reserves the right to send notice to the User by electronic mail or otherwise for the purposes of notifying User of such changes or additions; provided that any such changes or additions shall not apply to permissions already secured and paid for.

8.2 Use of User-related information collected through the Service is governed by CCC's privacy policy, available online here: http://www.copyright.com/content/cc3/en/tools/footer/privacypolicy.html.

8.3 The licensing transaction described in the Order Confirmation is personal to User. Therefore, User may not assign or transfer to any other person (whether a natural person or an organization of any kind) the license created by the Order Confirmation and these terms and conditions or any rights granted hereunder; provided, however, that User may assign such license in its entirety on written notice to CCC in the event of a transfer of all or substantially all of User's rights in the new material which includes the Work(s) licensed under this Service.

8.4 No amendment or waiver of any terms is binding unless set forth in writing and signed by the parties. The Rightsholder and CCC hereby object to any terms contained in any writing prepared by the User or its principals, employees, agents or affiliates and purporting to govern or otherwise relate to the licensing transaction described in the Order Confirmation, which terms are in any way inconsistent with any terms set forth in the Order Confirmation and/or in these terms and conditions or CCC's standard operating procedures, whether such writing is prepared prior to, simultaneously with or subsequent to the Order Confirmation, and whether such writing appears on a copy of the Order Confirmation or in a separate instrument.

8.5 The licensing transaction described in the Order Confirmation document shall be governed by and construed under the law of the State of New York, USA, without regard to the principles thereof of conflicts of law. Any case, controversy, suit, action, or proceeding arising out of, in connection with, or related to such licensing transaction shall be brought, at CCC's sole discretion, in any federal or state court located in the County of New York, State of New York, USA, or in any federal or state court whose geographical jurisdiction covers the location of the Rightsholder set forth in the Order Confirmation. The parties expressly submit to the personal jurisdiction and venue of each such federal or state court.If you have any comments or questions about the Service or Copyright Clearance Center, please contact us at 978-750-8400 or send an e-mail to info@copyright.com.

v 1.1

Close

Confirmation Number: 11722171

Citation Information

Order Detail ID: 71232231

Materials science forum by Trans Tech Publications. Reproduced with permission of Trans Tech Publications in the format Thesis/Dissertation via Copyright Clearance Center.

Close

Title: Nearly pure NIR to NIR upconversion luminescence in Tm3+, Yb3+ co-doped ZnO-TiO2 composite phosphor powder

Author: Krisana Kobwittaya,Yushi Oishi,Toshio Torikai,Mitsunori Yada,Takanori Watari,Hom Nath Luitel

Publication: Vacuum

Publisher: Elsevier

Date: February 2018

Appendix D

List of publications

Book Chapter

1 **Krisana Kobwittaya**, Takanori Watari, Chapter 9 Optical Properties of Ceramics, *Materials Chemistry of Ceramics*, Ed. Junichi Hojo, Springer, 2018, in Press.

Peer-Reviewed Journal Articles

1 **Krisana Kobwittaya**, Yushi Oishi, Toshio Torikai, Mitsunori Yada, Takanori Watari, Upconversion luminescence of ZnO-TiO_2: Ho^{3+}/Yb^{3+} phosphor powder, *Materials Science Forum*, **922** (2018) 32-39.

2 **Krisana Kobwittaya**, Yushi Oishi, Toshio Torikai, Mitsunori Yada, Takanori Watari, Hom Nath Luitel, Nearly pure NIR to NIR upconversion luminescence in Tm^{3+}, Yb^{3+} co-doped ZnO-TiO_2 composite phosphor powder, *Vacuum*, **148** (2018) 286-295.

3 **Krisana Kobwittaya**, Yushi Oishi, Toshio Torikai, Mitsunori Yada, Takanori Watari, Hom Nath Luitel, Bright red upconversion luminescence from Er^{3+} and Yb^{3+} co-doped ZnO-TiO_2 composite phosphor powder, *Ceramics International*, **43**(16) (2017) 13505-13515.

4 **Krisana Kobwittaya**, Yushi Oishi, Toshio Torikai, Mitsunori Yada, Takanori Watari, Hom Nath Luitel, Synthesis and upconversion luminescence properties of ZnO-TiO_2 containing Ho^{3+} and Yb^{3+}, *Journal of the Ceramic Society of Japan*, **125**(7) (2017) 559-564.

Conference Presentations and Proceedings

1 **Krisana Kobwittaya**, Yushi Oishi, Toshio Torikai, Mitsunori Yada, Takanori Watari, Upconversion luminescence in Ho^{3+}/Yb^{3+} co-doped ZnO-TiO_2 system, *The 18th International Symposium on Eco-materials Processing and Design (ISEPD 2017)* Okinawa, Japan, February 17-20, 2017. [ORAL] (Abstract)

2 **Krisana Kobwittaya**, Yushi Oishi, Toshio Torikai, Mitsunori Yada, Takanori Watari, Upconversion luminescence of ZnO-TiO_2 composite doped with Er^{3+} and Yb^{3+}, *The 33rd International Korea-Japan Seminar on Ceramics (K-J Ceramics 33)*, Daejeon, Korea, November 16-19, 2016. [ORAL] (Abstract)